Analysis and Evaluation of Single Piles in Laterally Spreading Soil

Christopher McGann

A thesis submitted in partial fulfillment
of the requirements for the degree of

Master of Science in Civil Engineering

University of Washington

2009

Program Authorized to Offer Degree: Civil and Environmental Engineering

University of Washington
Graduate School

This is to certify that I have examined this copy of a master's thesis by

Christopher McGann

and have found that it is complete and satisfactory in all respects,
and that any and all revisions required by the final
examining committee have been made.

Committee Members:

_____
Pedro Arduino

_____
Peter Mackenzie–Helnwein

Date: _____

Signature_____

Date_____

University of Washington

Abstract

Analysis and Evaluation of Single Piles in Laterally Spreading Soil

Christopher McGann

Co-Chairs of the Supervisory Committee:
Associate Professor Pedro Arduino
Civil and Environmental Engineering

Research Assistant Professor Peter Mackenzie–Helnwein
Civil and Environmental Engineering

Liquefaction–induced lateral spreading is an important load case for pile–founded bridges and port facilities located in seismically active regions. This work presents a kinematic analysis of the effects of lateral spreading on a single pile embedded in a layered soil profile and discusses the applicability of conventional analysis methods to the lateral spreading problem.

A series of three–dimensional finite element models are created and analyzed using the OpenSees finite element analysis platform developed at the Pacific Earthquake Engineering Research (PEER) Center. The developed FEA considers a single pile (modeled using beam elements) embedded in a soil continuum (modeled using brick elements). Beam–Solid contact elements are utilized to define the interface between the pile and soil elements. Three distinct reinforced concrete pile designs are considered in the models. Elastoplastic behavior is considered in both the pile and the soil through the use of fiber sections and a Drucker–Prager constitutive model, respectively. Each individual component in the model is validated through a series of simple analyses, ensuring that the desired behavior is captured. Force density–displacement ($p-y$) curves are extracted from the finite element models and compared to several conventional methods for establishing these curves. The characteristic parameters used in this comparison are initial stiffness and ultimate resistance. Additional,

one–dimensional models are created which utilize the same beam elements and consider the soil response through the use of $p-y$ curves generated using both the FEA results and conventional means.

The results for the lateral spreading models show that elastoplastic soil behavior must be considered in order to determine appropriate maximum moment demands for piles. Through the extraction of $p-y$ curves from the 3D models, it is determined that the kinematics of the pile greatly influence the extracted curves. A rigid pile undergoing a uniform displacement with depth is the most suitable method for obtaining sensible $p-y$ curves from the models. It is shown that the methods commonly used to establish the characteristic parameters for $p-y$ curves at large overburden pressure (greater depth) estimate values which are in excess of those returned by the finite element models, especially for large pile diameters. In the one–dimensional models, the extracted $p-y$ curves produce moment–curvature demands in piles which are similar to the results of the three–dimensional simulations, while the conventional curves produce demands which do not correlate well with the 3D modeling effort. It is determined that the conventionally–used methods are most applicable for moderately–sized piles subject to loads applied at or above the ground surface, but misrepresent a deeper event such as lateral spreading.

TABLE OF CONTENTS

LIST OF FIGURES

LIST OF TABLES

ACKNOWLEDGMENTS

I would like to express my sincere appreciation of Professors Pedro Arduino and Peter Mackenzie–Helnwein for their support and guidance during my research. I have learned much more than simply what is written in the pages of this document, and they are the primary reason. I am also very grateful for the opportunities I have been accorded during my time in the department of Civil and Environmental Engineering. I would also like to acknowledge everyone who dedicates themselves to the learning of others. The world is a better place for your efforts.

Partial support for this research was provided by the Pacific Earthquake Engineering Research (PEER) Center under Subagreement No. 00006405. This support is appreciated very much.

Finally, I would like to thank my parents, Steve and Ruth, and my girlfriend Kelly, for all of the support and encouragement they have provided during my educational career.

Chapter 1
INTRODUCTION

The behavior of pile foundations in response to lateral loading is an important item to consider during the design of a deep foundation system, as well as an interesting area for research. An aspect of this behavior that is of significant interest is the case of a pile embedded in a layered soil system that is subject to a liquefaction–induced lateral spreading event. During such an event, considerable bending demands are placed upon an embedded pile. In order to withstand these demands, the pile must be designed to have sufficient capacity and ductility. Due to the challenges presented by this problem, current methods for accomplishing the design of such piles often lead to overdesigned and overly expensive solutions.

The purpose of this study is to investigate the pile and soil responses to the lateral spreading load case as well as to evaluate the applicability of conventional analysis methods to this load case. This evaluation is conducted with respect to one of the current state–of–the–practice design paradigms for the analysis of laterally–loaded piles, the $p-y$ method (McClelland and Focht, 1958 [18], Matlock and Reese, 1960 [16], and Reese and Van Impe, 2001 [23]), as well as with respect to other conventional analysis tools. These goals will be accomplished through investigation of a single pile's simulated response to a lateral spreading event using the OpenSees finite element analysis platform developed at the Pacific Earthquake Engineering Research (PEER) Center. The investigation will involve several sizes of piles embedded in soil systems consisting of varying soil parameters and layer thicknesses, and will utilize both one–, two–, and three–dimensional finite element models. This work is an extension of past lateral spreading research conducted using OpenSees by Lam, Arduino, and Mackenzie–Helnwein (2009) [15], who used linear elastic three–dimensional finite element models to develop a simplified design procedure.

It is hypothesized that one–dimensional soil response curves reflecting the kinematic loading, the effects of depth, and the interaction between the soil layers occurring during a lateral spreading event can be generated using three–dimensional finite element models incorporating elastic pile elements, nonlinear soil and beam–solid contact elements. The resulting force density–displacement ($p-y$) curves, along with conventionally–defined curves, can then be applied to a parametric study using one–dimensional beam–spring models. The relative merits of the two sets of curves can then be evaluated through comparisons with three–dimensional lateral spreading models. This thesis describes the development of all of the necessary models, discusses all of the findings made, and draws several conclusions on the applicability of conventional analysis methods to the lateral spreading kinematic case.

1.1 Background

The problem of liquefaction–induced lateral spreading is very important in the design of deep foundation systems in certain situations. Common scenarios for which this phenomenon must be considered include bridge piers and foundations for port facilities that lie in seismically active regions. Often, in the areas in which these structures are constructed, layered soil systems will be encountered in which a potentially liquefiable layer is sandwiched between two layers which have a lower liquefaction potential. The system presented in Figure 1.1 is an example of one such situation. In this soil system, a relatively loose sand layer separates two denser layers of sand. The potential for liquefaction is much greater in the loose layer than it is in the more dense layers of sand.

During or slightly after a seismic event, a liquefied condition can develop in the middle layer of less dense sand. Once liquefied, the shear strength of the soil is greatly reduced and there is the potential for lateral displacement of the upper, still solid, layer with respect to the bottom layer. If a pile is embedded in such a soil system during this type of event, the displacement of the surrounding upper layer of soil will cause the pile to displace in a manner similar to that depicted in Figure 1.1. If the pile is embedded to a sufficient depth, the base of the pile will remain essentially fixed in the lower solid layer of soil while the upper portion of the pile is displaced laterally, resulting in large bending moment and shear force demands within the pile.

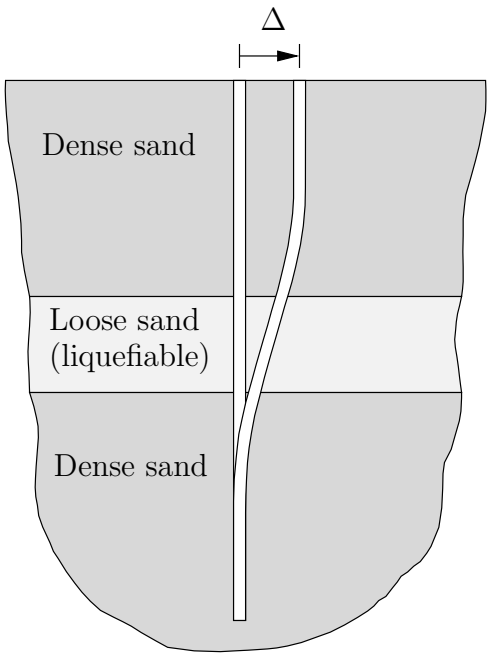

Figure 1.1: Schematic depicting the type of layered soil system of primary interest and the deflected shape of an embedded pile subject to a lateral spreading event in which the upper layer has displaced relative to the lower layer by a distance Δ

There are many challenges that arise when modeling the response of a pile to lateral loads. Due to these challenges, the most common method employed during numerical analysis of piles is the $p-y$ method (McClelland and Focht, 1958 [18], Matlock and Reese, 1960 [16], and Reese and Van Impe, 2001 [23]). In this approach, the three–dimensional laterally–loaded pile problem is emulated using one–dimensional, empirically–derived, nonlinear force density–displacement $(p-y)$[1] curves to describe the interaction between the soil and the pile. This method is used extensively in lateral pile design and has been extended for use in layered soils (Georgiadis, 1983 [11]), as well as liquefied and laterally spreading

[1]In the usually employed nomenclature, which appears to date from the 1950's, the symbol p is used to denote the pressure acting on the pile in units of FL^{-2}, although in the final curves it usually represents the reaction force per unit length of the pile, FL^{-1}, and the pile deflection is given by the symbol y. To be consistent with solid mechanics convention, the displacement should be taken as u, y is a coordinate direction, however, the original symbols p and y will be used to remain consistent with practical usage (Scott, 1981 [24]).

soils (Wang and Reese, 1998 [25]). There are other simplified approaches that may be employed in designing piles to resist lateral loads, but with the advent of easily–implemented computer programs based on the $p-y$ method, it has become the most prevalent.

The $p-y$ method is often utilized very successfully, however, there are documented problems that arise from potential oversimplifications inherent to the method. These problems include:

1. The tendency for the springs to be too stiff with depth.

2. The reliance upon empirical results that are not always applicable to the particular type of loading that is being considered.

3. The uncoupled behavior of the individual $p-y$ curves with depth.

Most of these problems can usually be circumvented through careful modeling decisions. However, when the method is applied to the problem of laterally spreading soil, certain inadequacies become apparent.

The approach of Georgiadis (1983) [11] is commonly used to account for layering effects in the $p-y$ method. This approach accounts for the effect of the upper soil layers on the lower layers, but does not consider any effects that the lower layers may have on the upper layers. Using 3D finite element models, Yang and Jeremic (2005) [27], as well as Petek (2006) [21], showed that for layered soils, not only are the lower layers affected by the presence of the upper layers, the upper layers are affected by the adjacent lower layers as well. This is something that most current $p-y$ curves do not consider, and a result that may become even more prevalent when dealing with unliquefied layers overlaying liquefied soils.

The majority of the $p-y$ curves currently employed in design practice for cohesionless soils are based upon the results of pile tests conducted with the application of lateral loads at the top of the pile (Reese et al., 1974 [22]). In this type of loading, below a certain depth, the soil is able to effectively restrain the pile from lateral motion. This method fairly accurately captures the response of the soil near the surface, but leads to $p-y$ curves at

depth that may not be applicable to other loading cases. This suggests that curves generated using surface loading are inconsistent with the type of kinematic demand placed upon a pile during a lateral spreading event, leading to potentially non–optimal design solutions.

1.2 Scope of Work

This thesis details the work related to the development of a set of three–dimensional lateral spreading models and the evaluation of $p-y$ curves extracted from these models. The work encompasses the development of all necessary finite element models, along with the accompanying validation work, a lateral spreading analysis using 3D finite element models, the extraction of representative $p-y$ curves from the models, and an evaluation of conventional analysis methods.

Finite Element Model Development

- A template three–dimensional soil–pile interaction model is created for the lateral spreading case. This model employs beam–column elements to model the piles, solid brick elements for the soils, and beam–solid contact elements to define the soil–pile interaction.

- Fiber section models are developed for a series of template reinforced concrete piles. The nonlinearity of the template piles is captured through these fiber sections, which define the behavior of the piles at a cross–sectional level, while standard beam–column elements can still be employed.

- A Drucker–Prager elastoplastic constitutive model is explored for the soil elements.

- It is important to ensure that computer models exhibit verifiably–correct behavior when applied to simple load cases. Validating simulations are performed to ensure that all components of the models display predictable responses.

- From the template model, specialized cases with various element types and input parameters are generated for use in this study.

Lateral Spreading Analysis

- The bending response of piles subject to a lateral spreading event is evaluated through a parametric study conducted using the developed three–dimensional models.

- Several parameters are considered such as the diameter of the pile, the constitutive models for both the pile and the soil, and the support conditions of the pile head.

- Further analysis of observed pile behavioral mechanisms is accomplished in order to verify observations made, and all accompanying results are summarized.

Representative $p-y$ Curve Extraction

- Using the developed three–dimensional finite element models and considering elastic pile elements and an elastoplastic soil constitutive model, $p-y$ curves for all depths and layers are generated.

- The extraction process is discussed and the various factors which can influence the extracted $p-y$ curves are identified.

Evaluation of Conventional Analysis Methods

- The extracted $p-y$ curves are compared to several conventional means for estimating the soil response for a given soil profile.

- The $p-y$ curves obtained from the three–dimensional models are extended for use in a one–dimensional beam on nonlinear support model, similar to a Winkler–beam, which is analyzed for the lateral spreading load case. A set of conventionally–derived $p-y$ curves are also utilized in this model.

- Using the 1D beam model, a parametric study investigating the relative responses obtained using the two sets of $p-y$ curves is conducted. The parameter study considers both elastic and elastoplastic pile elements in combination with the previously defined $p-y$ curves.

- The pile demands obtained from the one–dimensional beam–spring models are compared to equivalent results obtained in the three–dimensional modeling effort.

1.3 Thesis Organization

The work pertaining to this research is organized in the following manner:

Chapter 2 discusses the three–dimensional finite element model used to model the case of a laterally spreading layered soil system. All of the decisions and assumptions made during the creation of the model are examined and explained, including the loading and boundary conditions applied to the model and the methods in which the model is generated. A new surface load element is developed for use in OpenSees to meet the goals of this research. The formulation and validation of this element is also discussed in this chapter.

Chapters 3 and 4 describe the models used for the piles and the soil, respectively, in all aspects of this research. These models are examined in detail, including discussions into the generation and application of each pile and soil model. All of the models are verified and validated via simple tests to ensure that they have been created correctly and can be implemented in the desired manner.

Chapter 5 presents the results obtained from the three–dimensional lateral spreading parametric study. Several simple beam models are evaluated in order to validate observations made during this effort. The effects of the various considered parameters are discussed.

The $p-y$ curve extraction process is described in detail in Chapter 6. A least squares curve–fitting procedure is introduced in order to obtain smooth functions from the recorded data points. Findings related to the effects of pile kinematics on the soil response are discussed. Several model–specific phenomena which can influence the quality of the extracted curves are identified.

Chapter 7 discusses the meaning of the extracted curves and compares these curves to several conventional methods commonly used to estimate the response of a given soil to an applied lateral load. One–dimensional beam–spring models are created. A parametric study using these models is discussed.

Chapter 8 summarizes and presents the conclusions of this research, along with recommendations for future research.

Chapter 2

THREE–DIMENSIONAL LATERAL SPREADING MODEL

2.1 Introduction

To investigate the response of a single pile embedded in laterally spreading soil, there are essentially two options. First, to create a physical model of the system and then record data as this physical model is subjected to a loading event, or second, to create a numerical model that is able to simulate the response of the system to said event using a numerical technique such as the finite element method. Each option has its merits, but for this research, the latter option is more appropriate. Running such a large parameter study consisting of actual tests would be prohibitively expensive, especially when compared to the cost of running the study numerically.

During liquefaction–induced lateral spreading, complex events occur, especially at the soil–pile interface and at the boundaries of the individual soil layers. Due to this complexity, it becomes difficult to accurately capture all aspects of the behavior using one– or two–dimensional models. For the purposes of this research, it was important to account for the fundamentally three–dimensional nature of the problem; leading to the creation of a 3D model of the soil–pile system.

2.1.1 Finite Element Analysis Platform

The open–source finite element framework OpenSees (`http://opensees.berkeley.edu`) is used in this research for all finite element analyses. OpenSees was developed at the Pacific Earthquake Engineering Research (PEER) Center for use in structural and geotechnical simulations in one–, two–, and three–dimensions. OpenSees has a programming framework that uses object oriented programming in C++. The software architecture is created in a manner such that there is separation of the materials and elements, thus, new materials or elements can be added without modification to existing material and element classes.

2.1.2 Pre– and Post–processing of Simulated Data

The commercial program GiD (`http://gid.cimne.upc.es/`) is used during this research as a graphical pre– and post–processor for OpenSees. All of the input information for the problem, including everything from mesh generation to material and element assignments, is performed using this tool. This information is then transferred to an input file and run in OpenSees. After reformatting, the OpenSees recorder data can be interpreted by GiD, allowing for the program to function as a visual post–processor for OpenSees, which while perfectly functional as a finite element solver, has only limited visual capabilities. The ability of GiD to function in this capacity greatly simplifies the creation of the input files and the visualization of the results.

2.2 Model Overview

A typical finite element mesh used in this study is provided in Figure 2.1. Following the model of liquefaction–induced lateral spreading introduced in Section 1.1 and depicted in Figure 1.1, the finite element model shown in Figure 2.1 includes three distinct layers of soil. These soil layers consist of two thick layers of solid, unliquefiable, soil (depicted as orange in Figure 2.1), between which a relatively thin layer of liquefiable soil is located (depicted as white in Figure 2.1). The elements of the embedded pile are located in the middle of the soil system (depicted in green in Figure 2.1). This model takes advantage of the inherent symmetry of the problem, only modeling the soil on one side of the pile and replacing the missing soil with appropriate boundary conditions. In addition to reducing computational time by eliminating unnecessary calculations, this also provides superior visual access to the pile and the surrounding soil, important to interpreting results.

As is discussed in Chapter 3, there are three pile designs considered in this research. The size and layout of the layers in the lateral spreading model are dependent upon the diameter of the embedded pile, leading to the creation of three separate base models differing only in their dimensions. In these models, the thickness of the upper and lower soil layers are set arbitrarily equal to ten pile diameters. This thickness is adequate to essentially hold the base of the pile fixed in place relative to the top of the pile. The thickness of the liquefiable

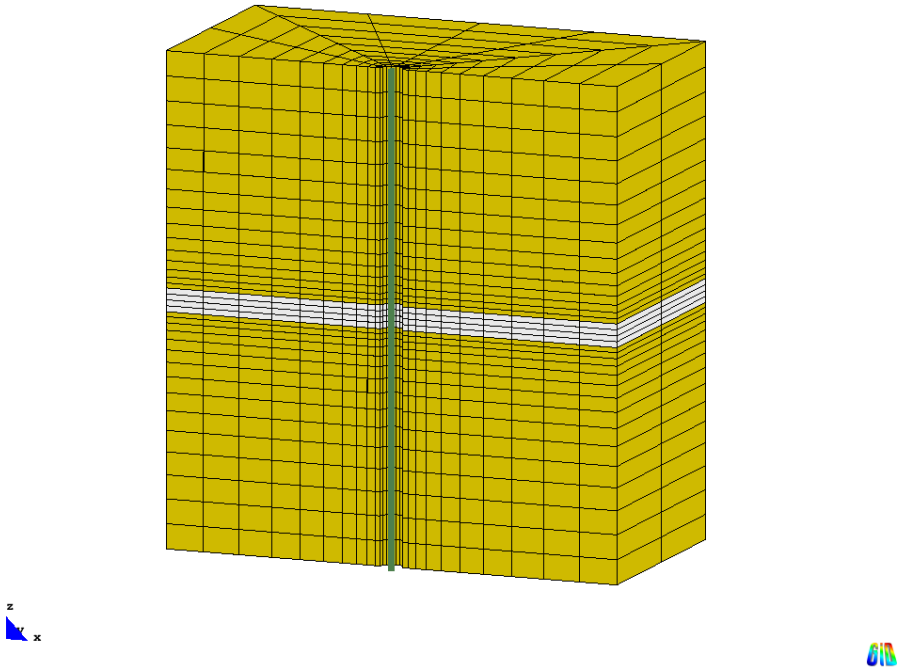

Figure 2.1: Typical finite element mesh for soil–pile system.

layer is arbitrarily set as one pile diameter in this study.

It is critical to define a sensible horizontal extent for the soil in the model, to ensure that boundary effects do not affect the results. Past work with laterally loaded piles found in the literature (Yang and Jeremic, 2002 [27] and Brown et al., 1990 [7]) used thirteen and eleven pile diameters on either side of the pile, respectively. Using this information, and past modeling experience, the models include a horizontal extent of ten pile diameters from the pile centerline. The ten–diameter lateral distance is considered to be wide enough to allow for the effective reduction of the free–field kinematic demand imposed upon the soil system in the areas surrounding the pile. Additionally, this distance is deemed sufficiently wide so as to remove the pile from any effects imposed by the applied boundary conditions at the extents of the model. However, as will be discussed in Chapter 6, it is determined that when using an associative plasticity formulation for the soil, the specified ten–pile–diameter distance is not wide enough to eliminate the effects of the fixed boundary on the results of the simulations.

Chapters 3 and 4 will discuss the pile and soil models incorporated into the three–dimensional lateral spreading model as well as the motivations behind their selections. All further information pertaining to these components of the model can be found there.

2.3 Boundary and Loading Conditions

In order for a finite element model to be effective in modeling a specific case, appropriate boundary conditions must be defined. The lateral spreading model requires boundary conditions that offer support to the elements as well as those that restrict unnecessary motions. As shown in Figure 2.1, symmetry is employed in the model, and only the soil on one side of the pile is considered. This use of symmetry introduces additional boundary conditions into the model.

The boundary conditions on the soil nodes are relatively simple. These nodes are created with only three translational degrees–of–freedom. To support the model against gravity loading, the soil nodes on the base of the model are held fixed against displacements in the vertical direction (the direction parallel to the axis of the pile). To enforce the symmetry condition, all of the nodes on the symmetry plane are held fixed against translation normal to this plane. The pile requires fixing of the torsional rotation and out–of–plane rotations (rotation axis in–plane) to enforce the symmetry of the model. Additionally, all of the soil nodes lying on the outer surfaces of the model are held fixed against horizontal in–plane translations and translations normal to their surface to enhance the stability of the model.

Further details on boundary and symmetry conditions applied to the piles in this model are discussed in Section 3.3.2.

2.3.1 Loading Conditions

The first step in the analysis of the lateral spreading model is to apply gravity loads. All of the soil elements are assigned a unit weight of $\gamma = 17$ kN/m^3. During the self–weight analysis, gravity is switched on and the soil elements generate a linearly increasing stress profile with depth. This procedure creates an appropriate distribution of confining pressures in the model, critical to determining the effective strength of the soil elements and to obtaining sensible results. The self–weight of the pile are neglected as it provides

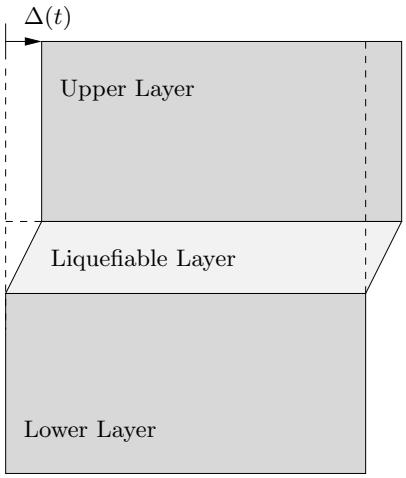

Figure 2.2: A depiction of the imposed displacement profile for the lateral spreading model.

no additional benefit to the model. Only after the self–weight analysis has successfully converged does the model move on to the lateral analysis.

During a simulated lateral spreading event, the lower unliquefied layer is assumed to remain stationary while the upper unliquefied layer and the liquefied middle layer experience lateral translations relative to the lower layer. This kinematic loading is achieved in the model by gradually imposing a set displacement profile to the soil nodes on all outer surfaces of the model excluding the symmetry face. This displacement profile represents the far–field kinematic demands on the soil system, with the upper layer translating relative to the lower layer. The presence of the pile alters the behavior of the soil, creating a near–field kinematic demand to which the pile will be subjected. The imposed profile is only applied to the boundary nodes in order to allow ample distance over which the far–field kinematic demand can be reduced to the more manageable near–field demand.

The horizontal displacement is imposed as constant upon the entire height of the upper solid layer, and as linearly–increasing over the height of the liquefiable layer. No displacements are imposed upon the lower unliquefied layer. The imposed displacement profile is shown in Figure 2.2. Excepting those restrictions, all other soil nodes are free to move in any direction. The magnitude of the constant horizontal displacement in the upper layer is taken to be one pile radius.

2.4 Modeling the Soil–Pile Interface

It is important to recognize that the behavior of a laterally loaded pile embedded in a soil system is governed, in part, by the complex interaction between the soil and the pile. Before the pile begins to move, the stresses applied by the soil should be uniform (for a given depth) and normal to the pile surface. After the pile has deflected laterally, the stresses on the leading side of the pile increase, while the stresses on the following side of the pile decrease. Additionally, these stresses may now have both normal and shear components, depending upon the particular loading conditions (Reese and Van Impe, 2001 [23]). The amount of resistance provided by the soil depends upon the amount of pile deflection that has occurred, which in turn depends upon the amount of resistance provided by the soil (among other factors). This interactive relationship between the soil and the pile is crucial to the lateral spreading problem and must be accounted for in the finite element model.

One suitable means to account for the interaction between soil elements and any embedded structural components is the use of contact elements. In this study, the interaction between the soil and the embedded pile is defined through beam–solid contact elements developed and implemented in OpenSees by Petek (2006) [21].

2.4.1 Contact Elements

As shown in Figure 2.3, the orange soil elements form a semi–circle of blank space around the green pile elements. Because standard beam–column elements have no physical size, this blank space is included to represent the extents of the pile. Existing between the single row of pile elements and the adjacent perimeter of soil elements are contact elements that define both the physical size of the pile and the ways in which the pile and soil elements interact.

The contact element developed by Petek (2006) [21] is formulated to create a link between the pile, modeled using beam–column elements, and the solid brick elements of the surrounding soil. The ability to use beam–column elements is highly advantageous from a modeling standpoint, enabling the use of fiber sections for the pile elements, and providing access to the wide variety of available beam–column element formulations. The contact ele-

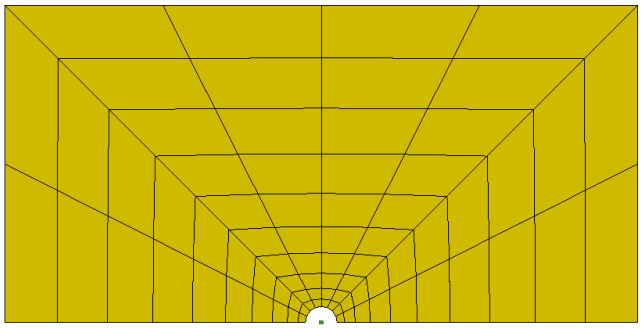

Figure 2.3: A top view of the finite element mesh for the soil mass. The pile is the green dot in the center of the lower edge.

ment creates a frictional interface allowing for sticking, slip, and separation which is capable of modeling the coupling between vertical and horizontal displacements. Figure 2.4 provides an example of how these elements function within the lateral spreading model, showing the way in which the soil elements deform around the pile as it moves laterally. The ability of these elements to create a gap between the trailing edge of the pile and the surrounding soil elements is visible at the top of Figure 2.4(a). Further information into the development and formulation of these beam–to–solid contact elements is available in Petek (2006) [21].

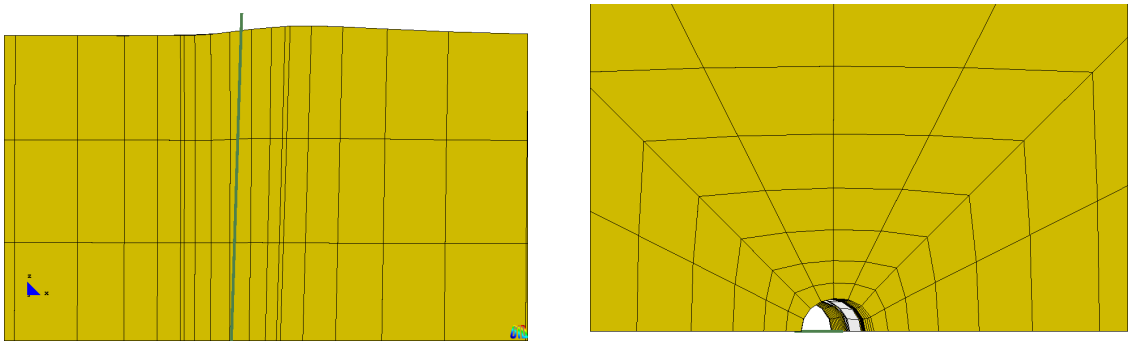

(a) (b)

Figure 2.4: Details of the deformation in the soil elements around the pile using beam–solid contact elements.

2.5 Surface Load Elements

In order to achieve the goals of this research, it is necessary to have models in which the liquefied layer is located at varying depths within the soil system. Due to the computational limitations induced by working with three–dimensional finite element models, the mesh is selectively refined in the area of the liquefied layer as opposed to a uniform refinement. This strategy, while sensible for computational optimization, necessitates the creation of customized meshes and input files for each case. In lieu of laboriously creating a series of models for each pile for liquefied layers at various depths, a uniform overburden pressure is applied to the ground (free) surface of the soil elements in the model. This overburden pressure, applied as a surface load, creates stress conditions in the soil which are equivalent to moving the liquefied layer to a deeper location.

In OpenSees, there is no built–in surface loading capability, forces can only be applied at a nodal level. Due to the irregular shape of elements in the lateral spreading model, as shown in Figures 2.3 and 2.4, determination of the equivalent nodal forces for a uniform surface load is a tedious task. One that would need to be performed for every increment of overburden pressure in every model. Instead of pursuing that somewhat tedious strategy for the application of overburden pressure in the finite element model, a new element is developed in OpenSees which is able to determine the appropriate nodal forces for a given magnitude of uniform pressure in a quadrilateral element. No additional stiffness is provided by these surface load elements, and the increase in computational cost is minimal, as only the assembly phase is affected. This new element eases the implementation of surface loads for the purpose of this research, while also increasing the capabilities of the OpenSees platform.

2.5.1 Formulation of Surface Load Elements

The developed surface load element is based upon a relatively simple strategy. The internal force vector for each element is replaced by the external force vector that would result from the application of a uniform surface loading. By creating a force imbalance in the elements, for equilibrium to be satisfied, there must exist an equal–but–opposite set of external forces which is applied to each of the elements on the surface. This set of external

forces is manifested in the application of energetically conjugate nodal forces representing the uniform surface loading.

The formulation of the surface load elements begins with the weak form of the principle of virtual displacements

$$-\int_V \boldsymbol{\sigma} : \boldsymbol{\nabla}^s \boldsymbol{\eta}\, dV + \int_V \mathbf{b} \cdot \boldsymbol{\eta}\, dV + \int_{\partial V_\sigma} \overline{\mathbf{t}} \cdot \boldsymbol{\eta}\, d\mathcal{S} = \mathbf{0} \tag{2.1}$$

where $\boldsymbol{\sigma}$ is the stress tensor, $\boldsymbol{\nabla}^s$ is the symmetric vector operator, $\boldsymbol{\eta}$ is an arbitrary displacement function, V is the volume of the body, $\mathbf{b}$ is the body force acting on the body, $\overline{\mathbf{t}}$ is the surface traction vector, ∂V_σ is the portion of the surface of the body with prescribed stresses, and $\mathcal{S}$ is the surface of the body.

Equation (2.1) expresses equilibrium for the system in terms of an arbitrary displacement function $\boldsymbol{\eta}$. The vector of external forces, which follows from the third term of (2.1), can be determined by, first, expressing the arbitrary displacement as

$$\boldsymbol{\eta} = \sum_I N_I(\xi, \eta) \cdot \boldsymbol{\eta}_I \tag{2.2}$$

where N_I are the (linear) shape functions, the subscript I refers to each of the four nodes for the element, and $\boldsymbol{\eta}_I$ are arbitrary nodal displacements. The linear shape functions, N_I, can be expressed for these quadrilateral elements as

$$N_I = \frac{1}{4}(1 + \overline{\xi_I}\,\xi)(1 + \overline{\eta_I}\,\eta) \tag{2.3}$$

by mapping a bi–unit square onto the quadrilateral surface patch. The normalized coordinates ξ and η, where $\overline{\xi_I}$ and $\overline{\eta_I}$ represent the nodal coordinates on the bi–unit square.

Applying (2.2) to the external force term of (2.1) results in

$$\sum_I \left(\int \overline{\mathbf{t}} \cdot N_I(\xi, \eta) J d\xi d\eta \right) \cdot \boldsymbol{\eta}_I =: \sum_I \mathbf{f}_I^{ext} \cdot \boldsymbol{\eta}_I \tag{2.4}$$

which must hold for any arbitrary nodal displacement $\boldsymbol{\eta}_I$, thus uniquely defining the nodal force

$$\mathbf{f}_I^{ext} = \int \overline{\mathbf{t}} \cdot N_I(\xi, \eta) J d\xi d\eta \tag{2.5}$$

where J is the Jacobian determinant necessary for the coordinate transformation to ξ and η, and the integration is performed over the bi–unit square to which the element has been mapped.

For a uniform surface pressure applied perpendicular to a given surface, the traction vector, $\overline{\mathbf{t}}$, is

$$\overline{\mathbf{t}} = -p\,\mathbf{n}(\xi,\eta) \tag{2.6}$$

in which p is the scalar magnitude of the pressure and $\mathbf{n}$ is the unit vector defining the outward normal of the surface. To establish the outward normal for the surface elements, general base vectors are defined for each element. There are two general base vectors, one in the ξ direction, $\mathbf{g}_\xi$, and the other in the η direction on the element, $\mathbf{g}_\eta$. This general base can be found from the nodal position vector as

$$\mathbf{x}(\xi,\eta) = \sum_I N_I(\xi,\eta)\cdot\mathbf{x}_I \tag{2.7}$$

where $\mathbf{x}_I$ are the nodal position vectors. The base vectors follow as

$$\mathbf{g}_\xi = \frac{\partial\mathbf{x}}{\partial\xi} = \sum_I \frac{\partial N_I}{\partial\xi}\cdot\mathbf{x}_I = \sum_I \frac{\overline{\xi_I}}{4}(1+\overline{\eta_I}\,\eta)\cdot\mathbf{x}_I \tag{2.8}$$

and

$$\mathbf{g}_\eta = \frac{\partial\mathbf{x}}{\partial\eta} = \sum_I \frac{\partial N_I}{\partial\eta}\cdot\mathbf{x}_I = \sum_I \frac{\overline{\eta_I}}{4}(1+\overline{\xi_I}\,\xi)\cdot\mathbf{x}_I \tag{2.9}$$

A local normal vector, $\hat{\mathbf{n}}$, for each element is defined by the cross product of the two base vectors as

$$\hat{\mathbf{n}} = \mathbf{g}_\xi \times \mathbf{g}_\eta \tag{2.10}$$

This vector contains information about both the area and the direction of the outward normal for its respective element. It can be shown that the norm of $\hat{\mathbf{n}}$ is equal to the surface Jacobian determinant, J. Thus, the relationship between $\hat{\mathbf{n}}$ and $\mathbf{n}$ can be expressed as

$$\mathbf{n} = \frac{1}{J}\hat{\mathbf{n}} \tag{2.11}$$

This relation is used to express the surface traction (2.6) in terms of the local normal vector as

$$\overline{\mathbf{t}} = -\frac{p}{J}\hat{\mathbf{n}} \tag{2.12}$$

where p is the magnitude of the surface pressure and J is the Jacobian determinant.

Applying (2.12) to (2.5), the external force acting at node I is obtained as

$$\mathbf{f}_I^{ext} = -p \int \hat{\mathbf{n}}(\xi,\eta) N_I(\xi,\eta) d\xi d\eta \tag{2.13}$$

The integral of (2.13) is evaluated using four–point Gaussian integration of the form

$$\mathbf{f}_I^{ext} = \sum_{\alpha=1}^{2}\sum_{\beta=1}^{2} -p\,\hat{\mathbf{n}}(\xi_\alpha,\eta_\beta) N_I(\xi_\alpha,\eta_\beta) w_\alpha w_\beta \tag{2.14}$$

in which the Gaussian quadrature and weights are $(\xi_\alpha, w_\alpha) = (\eta_\beta, w_\beta) = (\pm\frac{1}{\sqrt{3}}, 1)$.

In each surface element, the internal force vector is set equal to the vector of forces resulting from a uniform surface traction as determined by (2.14). To satisfy equilibrium, the elements must be subject to a set of nodal forces in opposition to the prescribed external force.

2.5.2 Validation of Surface Elements

A simple model is created in order to validate the successful implementation of the surface load elements in OpenSees. The model is meshed using irregularly–shaped elements as depicted in Figure 2.5. The newly created surface load elements are applied to the upper surface of this model over four layers of linear–elastic isotropic brick elements. The irregular shape of the mesh allows the elements to be tested for generality, as they should create energetically consistent nodal loads across the surface regardless of the shape of the quadrilateral elements, and thus create a constant stress in the solid.

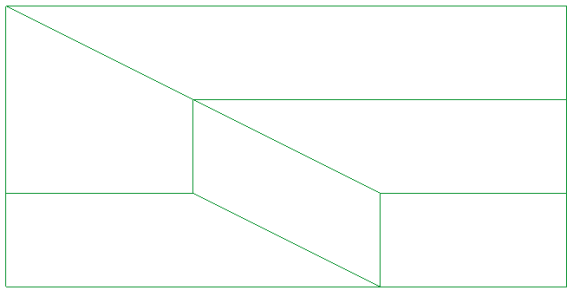

Figure 2.5: Irregularly–shaped mesh used for surface load element validation.

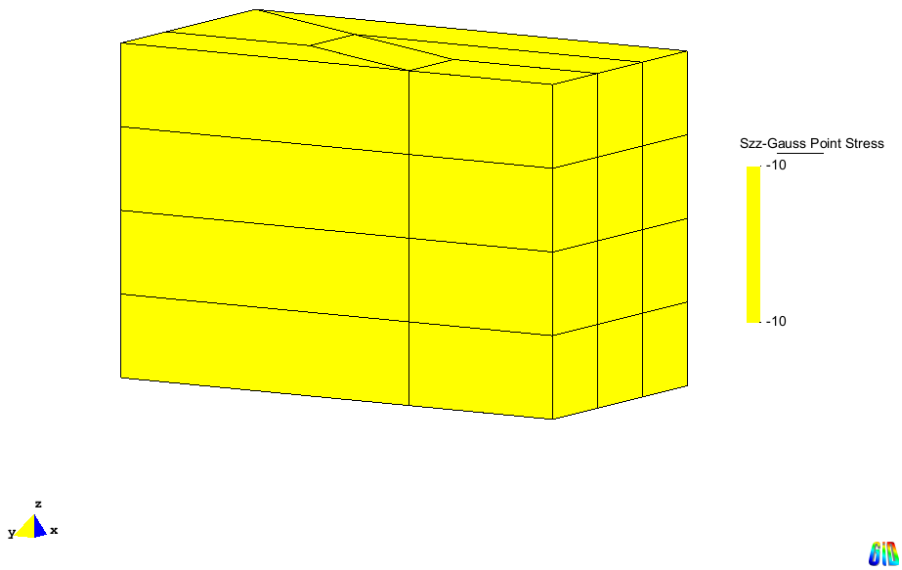

Figure 2.6: Distribution of vertical stress in the surface load element validation model.

The validation test used for the surface load elements, consists of the application a uniform loading of 10 kPa to the upper surface of the model. The base of the model is held fixed against translation in the direction of the loading. As shown in Figure 2.6, which shows a three–dimensional view of the validation model, the surface load elements are able to create nodal forces which create an equivalent loading to the assumed uniform load, resulting in a constant vertical stress distribution of -10 kPa. This result validates that the surface load elements created for use in OpenSees perform as intended.

Chapter 3

MODELING THE PILES

3.1 Introduction

Three separate pile models are used in this study. In an effort to obtain results from the models that are valid in a practical sense, each pile model is based upon a template reinforced concrete pile known to have been used in practice. These template piles are discussed further in the following sections of this chapter. An effort was made to faithfully model the actual pile cross–sections, but since the models were needed merely as benchmarks for this study, certain modifications are made to ease the modeling process.

The three piles selected are chosen such that they represent a reasonable variation in size and stiffness; thus providing data that is relevant to the range of sizes and stiffnesses where most practical pile designs fall. All three pile designs are modeled with circular cross–sections. The study includes a small pile (0.6096 m in diameter), a mid–sized pile (1.3716 m in diameter), and a large pile (2.5 m in diameter). Further details into the actual pile designs selected are available in Section 3.2. For ease of notation, the three pile designs chosen are referred to hereafter with reference to their individual diameters (i.e. the 2.5 m pile).

As discussed in Section 1.2, this research consists of several phases in which differing levels of complexity exist within each individual aspect of the model. This necessity for varying levels of complexity manifests itself with respect to the piles in the need for two separate models for each of the three template piles. Certain aspects of the research require piles with linear elastic behavior, while other aspects necessitate nonlinear elastoplastic pile models. The two models differ mainly in their constitutive behavior, though there are certain other differences in the modeling process that are discussed in the subsequent sections.

3.2 Template Pile Designs

It is important to note that the piles used in the study not only have realistic sizes and stiffnesses, but they also define a reasonable range that includes most practical pile designs. Figure 3.1 shows the three piles in section, drawn to scale to emphasize the relative sizes of the piles. The majority of piles that are commonly used in practice to withstand lateral spreading events have cross–sectional areas falling somewhere in the range defined by these three piles.

The 0.6096 m (2 ft) pile is a design common to the Port of Los Angeles, where piles of this type are employed in wharf foundations. The Port of L.A. pile design is included in the study as it is representative of one of the smallest pile designs that would commonly be encountered in applications where potentially liquefiable soils are present. The actual pile used by the Port of L.A. has a 0.6096 m wide octagonal cross–section. To ease implementation into OpenSees, an area–equivalent, 0.626 m diameter, circular cross–section is created. The amount and location of the longitudinal and spiral reinforcement found in the actual octagonal pile is left unchanged in the equivalent circular model.

In contrast to the relatively small Port of L.A. pile, a 2.5 m diameter pile recently used for the Bay Bridge in the San Francisco Bay is included in the study to be representative of one of the largest and stiffest pile designs that would be encountered in practice. Thus

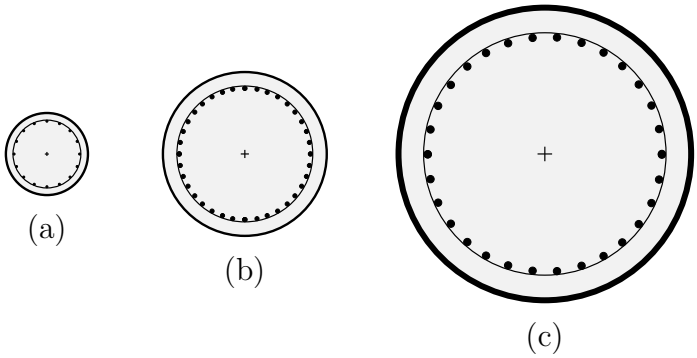

Figure 3.1: Template pile designs used in this study (to scale). (a) 0.6096 m pile. (b) 1.3716 m pile. (c) 2.5 m pile.

Table 3.1: Cross–sectional steel details for the three template pile designs.

	0.6096 m pile	1.3716 m pile	2.5 m pile
Number of longitudinal bars	16	36	30
Longitudinal bar diameter (mm)	15.24	15.24	57.3
Steel casing thickness (mm)	–	–	64
Spiral reinforcement diameter (mm)	9.525	9.525	22.2
Spiral reinforcement spacing (mm)	76.2	76.2	200

establishing the higher end of the range of practical piles. A unique characteristic of the 2.5 m pile is the inclusion of the steel casing surrounding the concrete. This added steel greatly increases the bending stiffness of the cross–section as compared to the other template piles, even more so than the increased size.

The 1.3716 m diameter pile is included in the study to establish an intermediate case that has a size and stiffness larger than the Port of L.A. pile, but also smaller than the Bay Bridge pile. This pile design was employed on the Dumbarton Bridge (Menlo Park to Fremont, CA) replacement completed in the early 1980's. The actual piles used on the Dumbarton Bridge project included a precast reinforced concrete ring which was filled with plain concrete after the piles had been driven. Once the infill has cured, it can be assumed that the piles act as a solid circular cross–section. For ease of modeling, no consideration is made with respect to the two separate concrete portions of the 1.3716 m pile. Instead, the pile model considers only one solid mass of concrete filling the entire circular cross–section.

A summary of the relevant dimensions of each of the three template pile designs is provided in Figure 3.2, in which the equivalent circular version of the 0.6096 m pile is depicted along with the unaltered 2.5 m and 1.3716 m template pile designs. As is the case with the 0.6096 m pile, the layout of the reinforcing steel was left unaltered in the conversion from the 2.5 m and 1.3716 m templates to the pile models. For further details pertaining to the steel provided in each template pile cross–section, refer to Table 3.1. A discussion of the relevant material properties for all three pile designs is provided in Section 3.4.

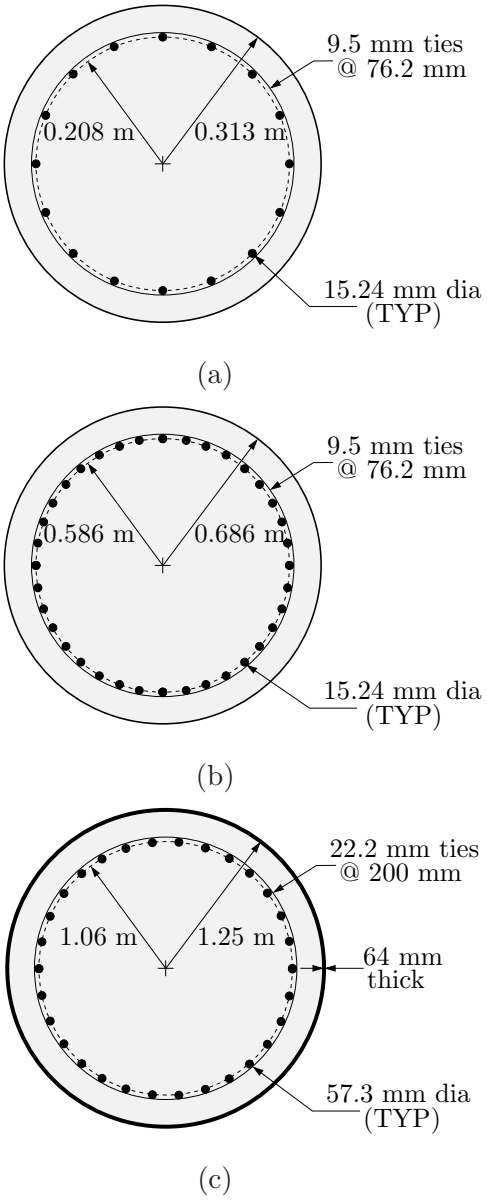

Figure 3.2: Dimensions and details of the three template piles. (a) 0.6096 m pile. (b) 1.3716 m pile. (c) 2.5 m pile.

3.3 Pile Elements

The piles are all modeled using OpenSees' standard beam–column elements with a displacement–based formulation. The OpenSees designation for the beam–column elements used in the model is *dispBeamColumn*. These elements are able to include distributed plasticity. Integration within the elements is based on the Gauss–Legendre quadrature rule (Mazzoni et al., 2007 [17]). For the elastoplastic pile models, the material nonlinearity of each pile is included in the elements through the use of fiber section models, based upon the template pile cross–sections. The elastic pile models use elastic section models along with the *dispBeamColumn* elements. These elastic section models are also based off of the template pile cross–sections. No geometric nonlinearity is considered as it is assumed that the deformations are not sufficiently large as to introduce any significant geometric effects into the behavior of the piles. All of the pile nodes have six degrees–of–freedom (3 translational, 3 rotational), of which three (1 translational, 2 rotational) are restrained due to symmetry conditions.

3.3.1 Fiber Section Models

Each of the three pile designs display moment–curvature behavior based upon the strength, distribution, and size of the concrete and steel available in their cross–section. In order to incorporate the unique behavior of each pile into a finite element model, fiber section models were created for each pile design. These fiber section models incorporate all of the relevant aspects of the individual pile designs, and define the behavior of each pile model at a cross–sectional level. In order to obtain consistent results for the symmetry conditions imposed upon the soil mesh in the 3D lateral spreading model, only one–half of each pile is incorporated, resulting in semi–circular fiber section models. The reasoning behind this decision is discussed further in Section 3.3.2.

Fiber section models are effective when modeling composite materials, such as reinforced concrete piles, hence their employment in this study. Fiber sections have a geometry defined in two levels; an overall geometry, in this case semi–circular, within which exists many smaller subregions of regular shape. A circular shape, or any sector thereof, lends itself

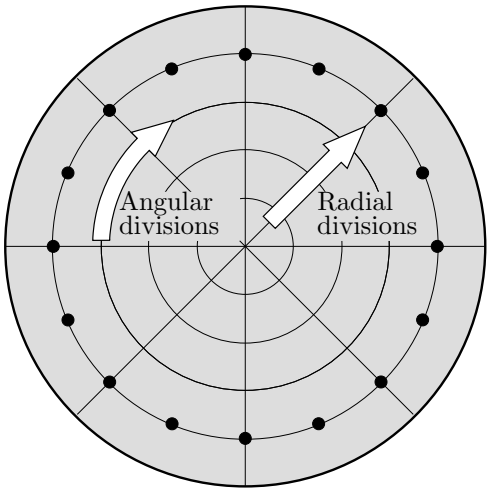

Figure 3.3: Typical fiber discretization for a circular fiber section model.

well to the type of discretization framework shown in Figure 3.3 which includes a set of divisions set at even intervals along the radius of the circle, as well as divisions that are set at equal angular increments. Reinforcement steel can be included in the fiber model as individual fiber regions with appropriate areas and locations. This type of fiber discretization is employed in all of the fiber models created for this research.

Each subregion of the fiber model can be assigned its own unique uniaxial constitutive model. In the case of reinforced concrete, it would follow that the subregions representing the reinforcement are given the material behavior of steel and the surrounding subregions representing the concrete portion of the cross–section are assigned constitutive behavior based upon that of concrete. Through defining the cross–section in this manner, a composite constitutive behavior is achieved for the pile elements. For a given increment of displacement in an element defined using fiber section models, the axial strain and stress in each subregion are calculated based upon location and material properties. These values are combined with the results from the other subregions within the fiber element in order to return the force and moment vectors and axial and rotational tangent stiffness at each Gauss point to the element for use in the next iteration. This modeling technique approximates the three–dimensional behavior of an actual pile while still enabling the use of standard beam elements.

3.3.2 Pile Symmetry and Boundary Conditions

A single, circular, pile embedded in a mass of soil is an inherently symmetric problem. Whenever modeling a problem where symmetry is involved, it is computationally efficient to create a model that takes advantage of this fact. As shown in Figure 2.1, this method is employed in the 3D lateral spreading model. Only one–half of the soil mass surrounding the pile is included in the model, the other half is replaced by appropriate boundary conditions on the soil nodes located where the interface between the two halves would be. This approach greatly reduces the amount of computational effort required to solve the system of equations, without compromising the validity in the results.

In order to create consistency in the results of the model, the fiber section models must account for the symmetry conditions imposed upon the soil. To accomplish this end, each pile model must have one–half of the area and bending stiffness of the corresponding circular pile, assuring that the interaction between the soil and the pile will be appropriate. This is accomplished through the use of semi–circular fiber section models that only consider one half of each pile cross–section. Using this approach, the resulting pile shear and moment data obtained from the simulation correctly reflects the symmetry condition. Results that are applicable to a full, circular, pile can be obtained by simply multiplying the semi–circular pile forces and moments by a factor of two.

As for boundaries, the pile nodes are held fixed against translation perpendicular to the symmetry plane. Additionally, since the semi–circular cross–sections are not doubly–symmetric, the pile nodes must be held fixed with respect to rotations about the pile axis to prevent the sections from twisting during loading. All of the pile nodes are fixed against out–of–plane rotations as well (rotation axis lies in the symmetry plane). These are all required symmetry conditions. The base node of the pile is held fixed against translation in the vertical direction (parallel to the pile axis), a required stability condition. The pile is allowed to rotate in the plane of loading at each node with the exception of cases where a fixed support condition is imposed at the head of the pile. Fixing the pile head is representative of a connection to a pile cap or other structural component. Both fixed and free pile head conditions are considered.

3.4 Elastoplastic Pile Constitutive Behavior

In order to meet the goals of this research, it was important to select constitutive models that introduce material nonlinearity into the piles, but are not overly complex so as to slow down the computations with unnecessary features. As discussed in Section 3.3.1, there are two uniaxial constitutive models defined for each fiber section model, one for the concrete portion of the cross–section and one for the steel portion of the cross–section. The total constitutive behavior of the pile model will be a composite of the two assigned models according to factors such as the area and distribution of each cross–sectional component.

OpenSees provides a series of predefined uniaxial constitutive models that can be effectively incorporated into fiber section models. From this index of provided constitutive models, the *Concrete02* and *Steel01* models are chosen to model the concrete and steel portions of the pile cross–sections, respectively. Figure 3.4 shows the general forms of these constitutive models, slightly exaggerated for clarity, along with the input parameters required to properly define the behavior. The corresponding input values for each pile are provided in Tables 3.2 and 3.3.

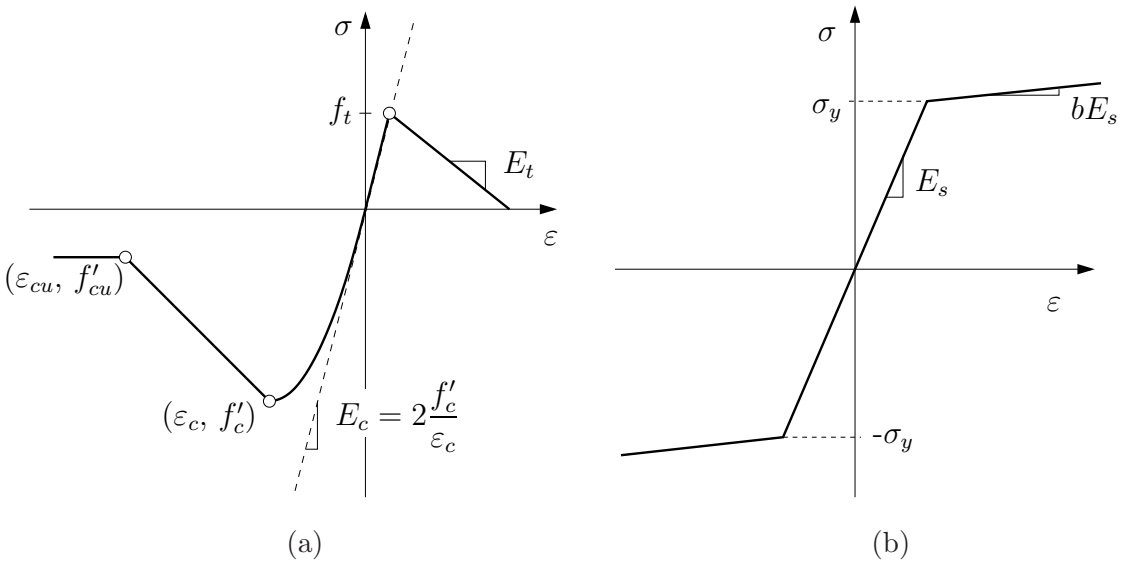

Figure 3.4: Uniaxial constitutive models used in pile fiber section models. (a) *Concrete02* model, (b) *Steel01* model.

Table 3.2: Steel material property input values used in fiber section models.

Pile Model	σ_y (MPa)	E_s (GPa)	b
0.6096 m	1860	200	0.001
1.3716 m	1860	200	0.001
2.5 m	520	200	0.001

Table 3.3: Concrete material property input values used in fiber section models.

Pile Model	f'_c (kPa)	ε_c	f'_{cu} (kPa)	ε_{cu}	f_t (kPa)	E_t (MPa)
0.6096 m	44816	0.003	8960	0.015	4170	-2080
1.3716 m	43170	0.003	8270	0.011	4000	-1400
2.5 m	20684	0.003	4140	0.013	2830	-13800

The chosen constitutive models were selected based upon their ability to incorporate aspects of the pile designs that are influential to the behavior of the piles in bending. The key features that are included in the concrete model are the ability to account for the effects of confinement on the compressive behavior, and the ability to link the tensile behavior to the development of cracks in the pile. For the steel portions of the cross–sections, the desirable features include elastoplastic behavior and a relatively simple set of input parameters. When these individual materials are combined via the fiber models, the resulting constitutive behavior of the pile model is suitably representative of that which would be expected for a reinforced concrete pile.

3.4.1 Steel in Tension and Compression

The chosen steel material model, while not intended solely for use in reinforcement modeling, has many of the salient features that are desirable in a steel constitutive model. As shown in Figure 3.4(b), the *Steel01* model is a bilinear plasticity model that incorporates isotropic strain hardening in the yield behavior. The longitudinal reinforcement fibers in all three pile models, as well as the steel tube in the 2.5 m pile model, are incorporated into the fiber

section models with behavior defined using this constitutive model.

The initial portion of the model is linear elastic, with a slope defined by the modulus of elasticity, E, specified to be 200 GPa for all of the steel in this study. The hardening slope of the curve is defined as the product of the elastic modulus and a specified hardening ratio, b, which was taken as a somewhat arbitrary value of 0.001 for all models. Though this constitutive model is relatively simple, the bilinear model creates a situation in which there is a constant tangent in the plastic region. The chosen approach simplifies the computations without significantly affecting the results.

3.4.2 Concrete in Compression

In compression, the selected constitutive model is based upon the Kent–Park model (Kent and Park, 1971 [14]), which was derived from tests conducted with confined concrete beam–columns. This model has three distinct regions of behavior. These regions define the initial, crushing, and post–crushing relationships between the axial stress and strain in each subregion of the fiber elements. Whenever possible, the material parameters used as input values in the constitutive models are based on the corresponding properties in the template pile designs.

In the initial loading region, from the origin up to the maximum compressive stress and strain, the behavior is parabolic. The maximum strength in compression, f'_c, for each model was taken directly from the template pile designs. The assigned values are given in Table 3.3. Per American Concrete Institute (ACI) recommendations, all three piles are assumed to have a peak strain of $\varepsilon_c = 0.003$ when their maximum compressive stress has been reached (ACI, 2005 [1]). The initial tangent of this region of the model is equal to the modulus of elasticity, E, which is defined as

$$E = 2\,\frac{f'_c}{\varepsilon_c} \tag{3.1}$$

Once the strain in the model begins to exceed the set value of ε_c, the concrete begins to soften due to the onset of crushing. This is represented by the descending linear region of the material behavior. The speed at which this softening occurs is based upon the amount of confinement provided by the longitudinal bars and spiral ties included in each template

pile design. With greater levels of confinement, larger axial strains can be achieved in the concrete core before the contribution of that concrete to the strength of the pile becomes minimal. To account for the influence of the amount of confinement in each pile model, the post–crushing behavior for the respective concrete constitutive models are defined in accordance with a procedure detailed in Park and Paulay (1975) [20]. Using this procedure, ε_{cu}, the strain at which the concrete is considered entirely crushed, can be defined based upon the known geometry of the core and the amount of steel by which it is confined. The crushed strains for each model are provided in Table 3.3.

After the strain in a particular subregion of the fiber model has reached ε_{cu}, the concrete is considered to be completely crushed, however, confined concrete has the documented ability to sustain small levels of stress at very large strains. To account for this, a residual strength is defined for each pile model as shown in Table 3.3. In all cases, the residual concrete strength is set as $f_{cu} = 0.2f'_c$ after recommendations made by Park and Paulay (1975) [20].

3.4.3 Concrete in Tension

When the concrete subregions of the fiber models are subject to tensile strains, it is desirable for there to be a limited amount of tensile strength followed by a region of tension softening due to the onset of cracking in the material. The selected uniaxial constitutive model includes both of these features. An enlargement of the tensile portion of the uniaxial concrete constitutive behavior is provided in Figure 3.5. As shown, the tensile behavior for this model can be fully described through three variables: the tensile strength, f_t, the elastic modulus, E, and the tension softening stiffness, E_t.

The tensile strength of the concrete in each pile model is defined based on the ACI recommended modulus of rupture for concrete in bending

$$f_r = 0.62\sqrt{f'_c} \tag{3.2}$$

with f_r and f'_c in units of MPa (ACI, 2005 [1]). The modulus of rupture is slightly greater than the strength of concrete in uniaxial tension, however, tensile stresses will be generated

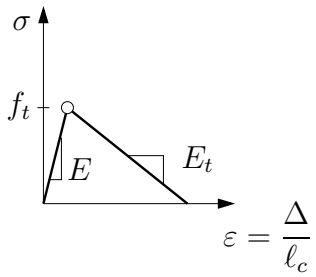

Figure 3.5: Detail of tensile behavior in concrete constitutive model.

in the models due to the application of bending loads, not uniaxial tensile loads. Therefore, defining the tensile strength to be the modulus of rupture may yield more realistic results.

The tension softening stiffness, E_t, which is the slope of the linear softening portion of the tensile stress–strain curve shown in Figure 3.5, defines the rate at which the stress degrades with increasing tensile strains. In this region of the model there is a linear constitutive relation between the stress and the strain is assumed to be

$$d\sigma = -E_t \, d\varepsilon \tag{3.3}$$

Sensible values for E_t are determined for each pile based upon the principles of fracture mechanics as they apply to plain concrete. A discussion of this process is provided in Section 3.4.4.

Eventually, when the tensile strain becomes large enough, the concrete will have cracked sufficiently such that it can no longer provide any resistance to increasing tensile strains. This is represented in Figure 3.5 by the point at which the softening curve crosses the strain axis. This limiting value of strain varies for each model based upon their respective tensile strengths and softening moduli.

3.4.4 1D Fracture Mechanics of Concrete in Tension

When concrete approaches its tensile capacity, defined in this model by the modulus of rupture, cracks will begin to form. Though the cracks may propagate relatively rapidly, the surrounding concrete does not lose all tensile strength instantaneously. Instead, the tensile stress in the region of the crack is assumed to degrade over time as a function of the width

of the crack opening, w. The rate at which this occurs varies depending upon the material in question.

There are models, of varying levels of complexity, that have been developed to describe the relationship between the tensile stress and the rate at which cracks will open in a material. Examples of such models are available in Xu and Zhang (2008) [26], Bazant and Becq–Giraudon (2002) [3], and Kaplan (1961) [13]. For the purposes of this research, a simplified crack propagation model has been adopted. This model is shown in Figure 3.6, where the tensile stress is plotted as a linear function of the crack opening. This assumed relationship between incremental stresses and crack widths is defined by the crack propagation slope, $\overline{E}_t$, and can be written as

$$d\sigma = -\overline{E}_t \, dw \tag{3.4}$$

an expression that is helpful in relating $\overline{E}_t$ to the desired input value of E_t.

As shown in Figure 3.6, there is a certain amount of energy that must be expended before the concrete in the area of the crack loses its tensile strength entirely. This energy is called the fracture energy, or fracture toughness, and is commonly denoted as G_f. Fracture energy is a fundamental material property that can be determined via laboratory tests or from empirical formulas present in the literature. In this study, there are no physical items to test, so the latter approach is employed. The fracture energy for each pile model is defined as shown in Table 3.4; values determined using the empirical procedure developed by Bazant and Becq–Giraudon (2002) [3].

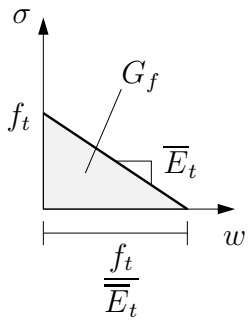

Figure 3.6: Simplified fracture model for concrete showing the relationship between tensile stress, f_t, and crack width, w.

Table 3.4: Concrete fracture energies and crack propagation slopes used to define pile constitutive models.

Pile Diameter	G_f (kJ/m^2)	$\overline{E}_t$ (MN/m^3)
0.6096 m	0.155	55450
1.3716 m	0.150	53100
2.5 m	0.109	36520

In a general sense, the value of the fracture energy for a given material is dependent upon the specific relationship between the tensile stress and the crack opening width, defined by the function $\sigma(w)$. The fracture energy is equal to the following integral

$$G_f = \int_0^{+\infty} \sigma(w)\, dw \tag{3.5}$$

which essentially states that G_f is equal to the area under the curve defined by $\sigma(w)$. Applying this to the simplified model of Figure 3.6, the fracture energy can be related to the tensile stress at the onset of cracking, f_t, and the crack propagation rate, $\overline{E}_t$, as

$$\begin{aligned} G_f &= \frac{1}{2} f_t\, w \\ &= \frac{f_t^2}{2\overline{E}_t} \end{aligned} \tag{3.6}$$

Solving (3.6) for the unknown crack propagation slope results in

$$\overline{E}_t = \frac{f_t^2}{2G_f} \tag{3.7}$$

which defines $\overline{E}_t$ in terms of the known values for concrete fracture energy and tensile strength. The values of $\overline{E}_t$ calculated for each pile model are summarized in Table 3.4.

A consideration of what is happening in a single pile element during cracking is beneficial when attempting to relate the stress degradation slope, $\overline{E}_t$, to the tension softening slope, E_t. Figure 3.7 shows such an element both before ($w = 0$) and after ($w > 0$) cracking. For simplicity it is common to assume that there is a single crack in each element. This assumption defines the characteristic length, ℓ_c, which is the distance between cracks, to be equal to the element length.

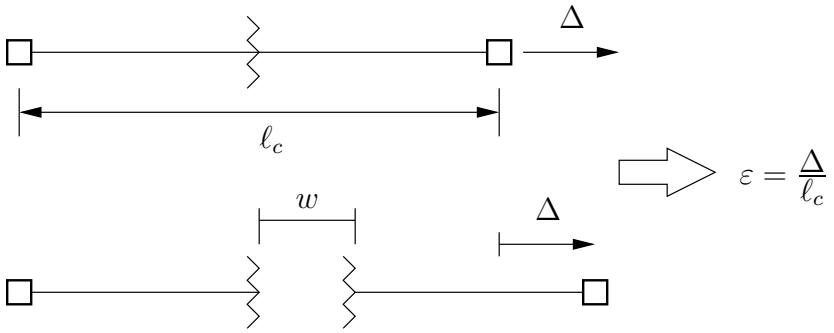

Figure 3.7: Relationship between elongation, crack width, and element length for a single pile element.

As would follow in a typical finite element formulation, the change in length of the element, $d\Delta$, can be related to the change in strain within the element, $d\varepsilon$ by

$$d\Delta = \ell_c \, d\varepsilon \tag{3.8}$$

As implied by Figure 3.7, the addition of a crack with increasing width into the element modifies (3.8) such that

$$d\Delta = \ell_c \, d\varepsilon^e + dw \tag{3.9}$$

where $d\varepsilon^e$ is the change in elastic strain and dw is the change in crack opening width. Assuming linear elastic behavior in the uncracked zone, (3.9) can be written in terms of the stress as

$$d\Delta = \frac{\ell_c}{E} \, d\sigma + dw \tag{3.10}$$

in which E is the elastic modulus. Expanding (3.10) using (3.4) and (3.8) yields

$$\left(1 - \frac{\ell_c \, \overline{E}_t}{E}\right) dw = \ell_c \, d\varepsilon \tag{3.11}$$

and solving (3.11) for the incremental change in crack width yields

$$dw = \frac{\ell_c}{\left(1 - \dfrac{\overline{E}_t \, \ell_c}{E}\right)} \, d\varepsilon \tag{3.12}$$

The constitutive relation defining the behavior of the tension–softening portion of the concrete model follows from (3.4) and (3.12) as

$$d\sigma = -\frac{\overline{E}_t\,\ell_c}{\left(1 - \dfrac{\overline{E}_t\,\ell_c}{E}\right)}\,d\varepsilon \tag{3.13}$$

which when compared with (3.3) defines the tension softening modulus to be

$$E_t = \frac{\overline{E}_t\,\ell_c}{\left(1 - \dfrac{\overline{E}_t\,\ell_c}{E}\right)} \tag{3.14}$$

This result, combined with (3.7), enables the calculation of the tension softening modulus for any finite element discretization using known material parameters and element sizes.

3.4.5 Implementation of Tension Parameters

The resultant tension softening modulus from (3.14) is largely dependent upon the chosen characteristic length, ℓ_c. The other terms are all material–dependent parameters, but the characteristic length is somewhat arbitrary. As was discussed previously, ℓ_c is initially taken to be equal to the element length, thus implying that a single crack develops in each element. As the length of an element increases, this assumption becomes less valid. Assuming that there is an adequate amount of longitudinal and shear reinforcement provided in a pile, it could be expected for cracks to develop at spacings in the range of 5–10 cm. Specifying ℓ_c to be equal to the expected crack spacing can reduce E_t considerably. Reducing the tension softening modulus can result in models that exhibit fewer convergence issues without altering the results in a significant manner.

Preliminary sensitivity studies, performed with the three pile models, have shown that the 0.6096 m and 1.3716 m pile models are very sensitive to the specified input value for E_t. In these models, there is a significant reduction in stiffness when the concrete cracks in tension. If E_t is set at too large a value, the resulting softening behavior is too steep and the elements are unable to converge. An example of this severe softening behavior can be seen inside the circled region of the moment–curvature response shown in Figure 3.8. The convergence issues encountered for these two pile models identified the need for a more

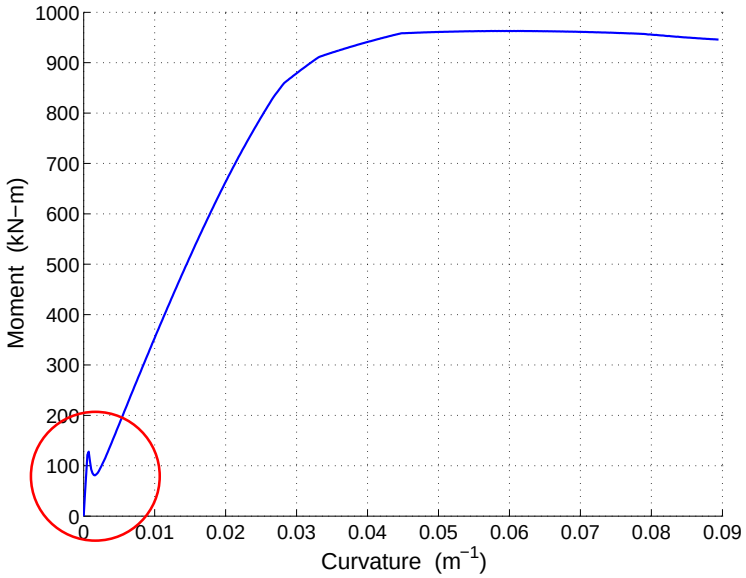

Figure 3.8: Moment–curvature behavior for 0.6096 m pile model illustrating softening behavior resulting from a large characteristic length, ℓ_c.

careful selection of the characteristic length values. Because the 2.5 m pile model is encased in a steel tube, it does not display a similar loss of strength at the onset of tension cracking. This is illustrated by Figure 3.9, which shows the moment–curvature behavior for the 2.5 m pile cross–section for two extreme values of ℓ_c. There is no discernable difference, thus the characteristic length, and the corresponding tension softening stiffness, can be set at any sensible value for this pile model. The behavior of the 2.5 m pile model is not governed by the concrete parameters, but instead is governed by the steel in the cross–section.

Based upon a crack spacing in the range specified previously, a characteristic length of $\ell_c = 7$ cm is selected for the 0.6096 m pile model and a value of $\ell_c = 5$ cm is set for the 1.3716 m pile model. For the 2.5 m pile, ℓ_c is set as the length of the smallest element in this model. Table 3.5 summarizes the characteristic lengths and softening stiffnesses for each pile model.

A reduction in the tension softening modulus for the 0.6096 m and 1.3716 m pile models to the values shown in Table 3.5 results in a less drastic change in strength after the onset of tension cracking. Thus, allowing for a smoother transition between the initial behavior

Table 3.5: Characteristic length and tension softening modulus used in each pile model.

Pile Diameter	ℓ_c (m)	E_t (kPa)
0.6096 m	0.07	-2.08e6
1.3716 m	0.05	-1.40e6
2.5 m	0.42	-1.38e7

and the ultimate behavior of the pile. The moment–curvature responses for each pile's fiber section model are shown in Figures 3.10 and 3.11. They show that the severity of the softening behavior identified with larger values of E_t is lessened as ℓ_c becomes smaller. The convergence issues associated with these pile models disappear when the characteristic length and tension softening stiffness are set to the values of Table 3.5. The validation work performed in order to support the reduction in these parameters is discussed in Section 3.6.2.

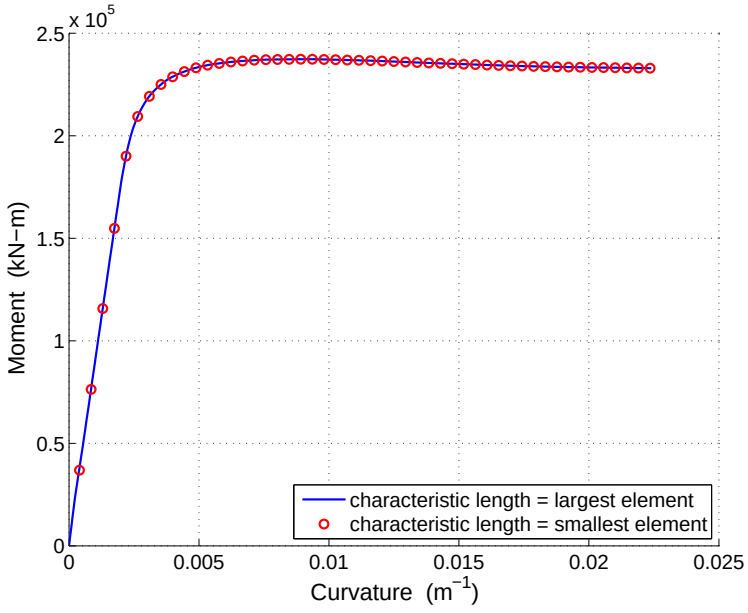

Figure 3.9: Moment–curvature behavior for 2.5 m pile model with two separate values for characteristic length, ℓ_c.

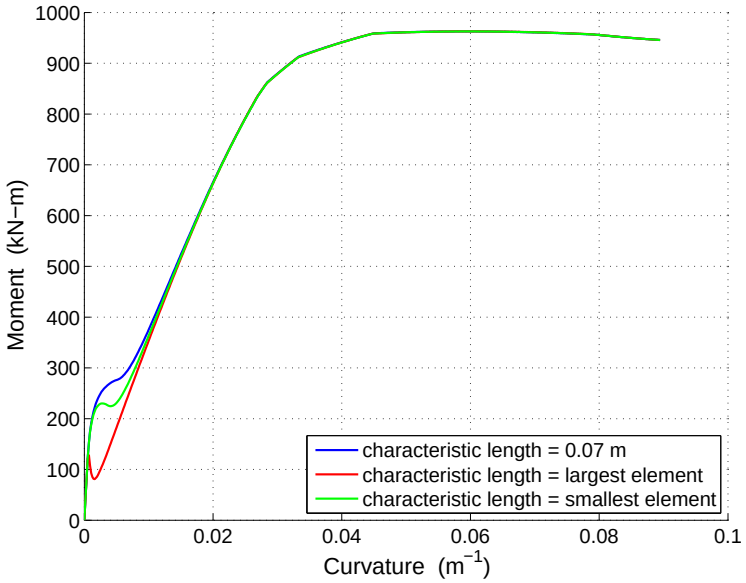

Figure 3.10: Moment–curvature behavior for 0.6096 m pile model with various values of ℓ_c. Largest element length is 0.649 m. Smallest element length is 0.102 m.

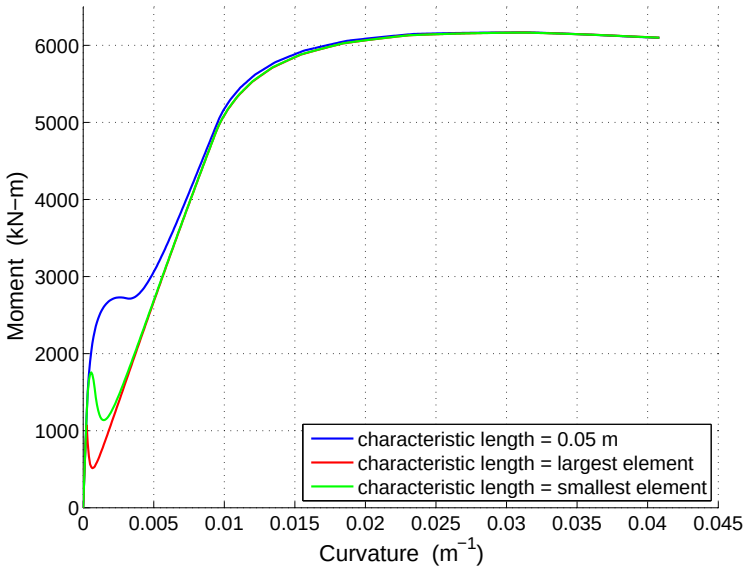

Figure 3.11: Moment–curvature behavior for 1.3716 m pile model with various values of ℓ_c. Largest element length is 1.79 m. Smallest element length is 0.231 m.

3.5 Linear Elastic Pile Constitutive Behavior

In addition to the elastoplastic fiber section pile models, the scope of this research also requires the use of linear elastic pile models. As with the fiber models, the linear elastic pile models are based upon the three template pile designs, however, no material nonlinearity is considered. The linear elastic pile models are introduced into the previously discussed *dispBeamColumn* pile elements by way of elastic section models. These elastic section models define the elastic modulus, cross–sectional area, second moment of the area, polar moment of inertia, and shear modulus for the pile elements. The ability to define the linear elastic behavior in this manner is beneficial as it allows for the use of the same pile elements, mesh, and boundary conditions as employed in the nonlinear pile models.

The properties of each linear elastic pile model are summarized in Table 3.6. It is important to note that the linear elastic models have comparable properties to the nonlinear fiber section models in order for consistent results between the various aspects of this research. To this end, for each template pile model, the area, A, and the second moments of the area, $I_y = I_z$, are determined based upon half–pile cross–sections. A schematic depicting the coordinate axes for the cross–section is provided in Figure 3.12. The polar moment of inertia is a necessary input value for the elastic models, however, due to the boundary conditions imposed upon the piles, the magnitude of J for each pile is superfluous. From the values of I_y for each pile, appropriate elastic moduli are selected such that linear elastic bending stiffness, EI, becomes equal to the initial bending stiffness of the corresponding elastoplastic pile model. The shear moduli are then determined from the elastic moduli by assuming a value of Poisson's ratio, $\nu = 0.25$.

Table 3.6: Material and section property values used in linear elastic pile models.

Pile Diameter	A (m^2)	E (GPa)	G (GPa)	I_y (m^4)	I_z (m^4)	J (m^4)
0.6096 m	0.1539	31.297	12.52	0.00377	0.00377	0.00754
1.3716 m	0.7388	28.688	11.48	0.0869	0.0869	0.1738
2.5 m	2.454	102.4	40.96	0.9587	0.9587	1.9174

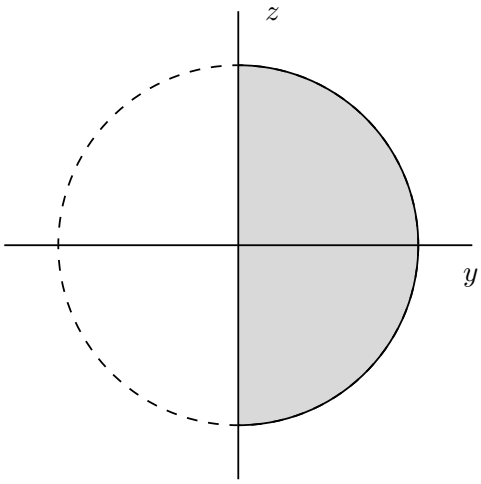

Figure 3.12: Names and locations of the coordinate axes for the half–pile model.

3.6 Validation of Pile Models

In all computer simulations, it is important to ensure that user–created models exhibit reasonable behavior in response to easily verifiable loading conditions. Each step in the creation of the pile models, from the behavior of the cross–section to the overall behavior of the pile models, must first be validated before implementation into the full–scale lateral spreading model. The results of several of the most important verification studies accomplished to meet this end are discussed in the subsequent sections.

3.6.1 Verification of Elastoplastic Fiber Section Models

To ensure that the fiber section models for each pile are created and implemented correctly, the behavior of each is evaluated and verified through a series of simple analyses. In this analysis suite, the first step is to verify the moment–curvature relation for each fiber model, thus providing reassurance that the models are created properly. Unless otherwise noted, all of the fiber section validation work is performed using the half–pile fiber section models (see Section 3.3.2 for details) created for use in the lateral spreading model.

Moment–Curvature Response

Using OpenSees, zero–length element models are created with the previously defined semi–circular fiber section models. One node is held fixed, and the other is left free with respect to rotation. The element is then subjected to, first, a constant axial load to represent the self weight of the pile, and second, a linearly–increasing applied moment. The force and deformation responses of the section are recorded during this process, from which a moment–curvature diagram can be created. This procedure is a relatively simple way to establish the moment–curvature behavior for a fiber section model in OpenSees.

Computer aided hand–calculations are performed to verify that the correct initial tangents and the true moment–curvature behaviors of the cross–section have been captured in the OpenSees analysis. A script is implemented in Matlab utilizing a numeric integration algorithm in combination with a Newton–Raphson iterative procedure.

The Matlab script iteratively solves the following equation

$$\mathbf{R} = \left\{ \begin{array}{c} N - \int_A \sigma dA \\ M - \int_A y\sigma dA \end{array} \right\} = \mathbf{0} \tag{3.15}$$

where $\mathbf{R}$ is the residual, N is the applied normal force, M is the applied moment, σ is the axial stress, A is the area of the cross–section, and y is distance from the neutral axis. Incremental changes in the residual are computed using the following equation

$$d\mathbf{R} = \left[\begin{array}{cc} -\int \partial\sigma/\partial\varepsilon & -\int \partial\sigma/\partial\phi \\ -\int y\partial\sigma/\partial\varepsilon & -\int y\partial\sigma/\partial\phi \end{array} \right] \tag{3.16}$$

in which ε is the axial strain and ϕ is the curvature. In the script, an ultimate curvature is defined. This ultimate value is approached incrementally in constant steps. For each curvature step, the axial strain distribution in the cross–section can be computed as

$$\varepsilon(y) = \varepsilon_{current} + \phi y \tag{3.17}$$

where $\varepsilon(y)$ is the axial strain as a function of position y, ϕ is the curvature at the current step, and $\varepsilon_{current}$ is the mean axial strain at the beginning of each iteration. The distributions of stress resulting from this computed strain distribution are calculated using the appropriate constitutive models for the concrete and steel portions of the cross–section.

The cross–section is divided into subregions. Rectangular and circular subregions are used for the concrete and steel portions of the cross–section, respectively. Each subregion has a particular center position, y_i, and area, A_i. Using these subregions, the internal normal force and moment acting on the cross–section can be approximated using the following sums

$$\int_A \sigma dA \approx \sum \sigma_i A_i \tag{3.18a}$$

$$\int_A y\sigma dA \approx \sum y_i \sigma_i A_i \tag{3.18b}$$

where σ_i is the stress acting at the center of each of i subregions. Additionally, the terms of (3.16) are computed as

$$\int \frac{\partial \sigma}{\partial \varepsilon} \approx \sum E_c A_{ci} + E_s A_{si} \tag{3.19a}$$

$$\int \frac{\partial \sigma}{\partial \phi} \approx \sum E_c y_{ci} A_{ci} + E_s y_{si} A_{si} \tag{3.19b}$$

$$\int y\frac{\partial \sigma}{\partial \varepsilon} \approx \sum E_c y_{ci} A_{ci} + E_s y_{si} A_{si} \tag{3.19c}$$

$$\int y\frac{\partial \sigma}{\partial \phi} \approx \sum E_c I_{ci} + E_s I_{si} \tag{3.19d}$$

in which E_c, y_{ci}, and A_{ci} are the concrete elastic modulus and the center location and area for each concrete subregion, respectively, and E_s, y_{si}, and A_{si} are the corresponding terms for the steel portion of the cross–section.

The internal normal force and moment obtained from (3.18) are used to compute the residual using (3.15). If the residual is not a zero vector, an updated strain distribution is computed using the newly computed residual and the incremental change in the residual determined in (3.19). The process then repeats, iterating until (3.15) is satisfied for the current curvature step before moving on to the next. The moment–curvature response of the cross–section is determined by recording the converged values of the moment for each curvature step.

As a means of validation, the converged final stress and strain distributions acting over the cross–section are recorded for plotting purposes. Figure 3.13 shows the distributions of stress and strain obtained from the Matlab script for the 0.6096 m pile section along

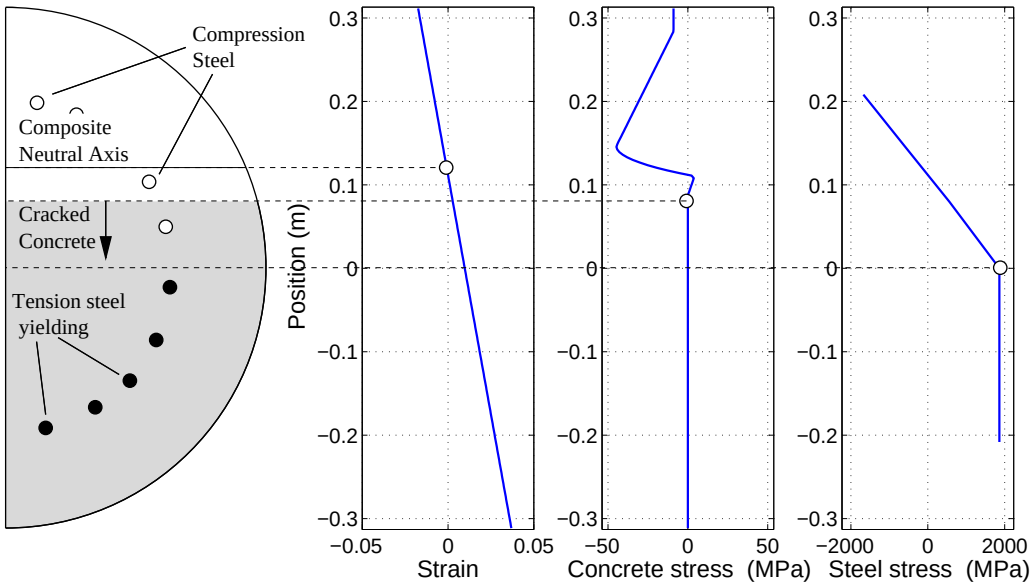

Figure 3.13: Distributions of stress and strain determined from Matlab model for the 0.6096 m pile cross–section. The middle of the section is located at position zero.

with a schematic depicting various conditions within the cross–section. The similarity to the specified constitutive models for the steel and concrete portions of the cross–section discussed in Section 3.4 verifies that the constitutive models are correctly implemented in the Matlab script.

Figures 3.14, 3.16, and 3.18 present the moment–curvature response determined using the zero–length element approach in OpenSees along with the calculated initial tangent, and the calculated moment–curvature response for all three full, circular, fiber section models. Figures 3.15, 3.17, and 3.19 present the same data for the half–pile (semi–circular) models that are employed in the lateral spreading model. As shown in all of the figures, there is considerable agreement between the independently calculated (Matlab) and OpenSees curves for each model; the general shapes are nearly identical and the calculated initial tangents match the OpenSees results. Any differences can be attributed to the differing degrees of accuracy in the discretization of the cross–sections. These analyses provide verification that OpenSees is running as intended and that all three fiber models are displaying predictable, and intended, responses.

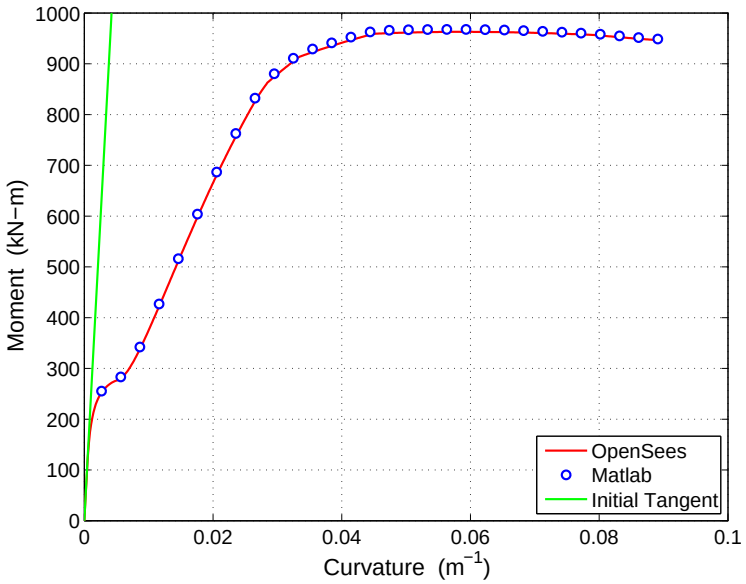

Figure 3.14: Comparison of moment–curvature responses of zero–length elements in OpenSees with independently calculated results for 0.6096 m full (circular) pile model.

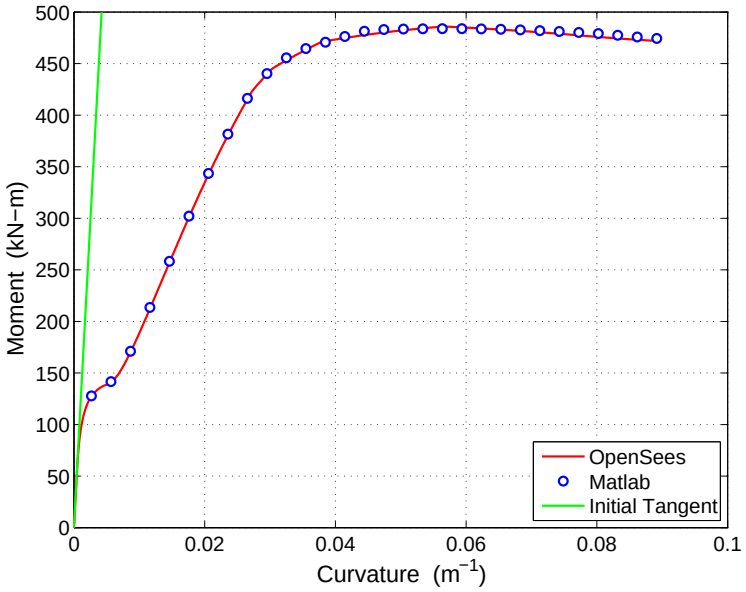

Figure 3.15: Comparison of moment–curvature responses of zero–length elements in OpenSees with independently calculated results for 0.6096 m half–pile (semi–circular) model.

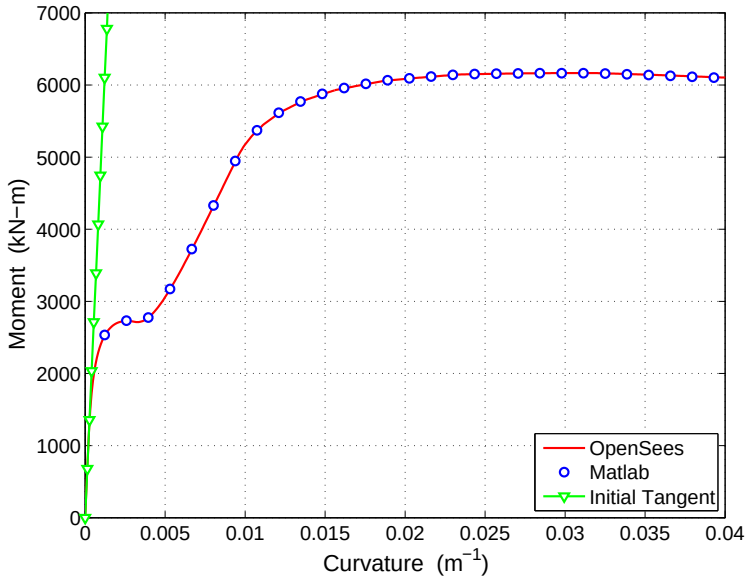

Figure 3.16: Comparison of moment–curvature responses of zero–length elements in OpenSees with independently calculated results for 1.3716 m full (circular) pile model.

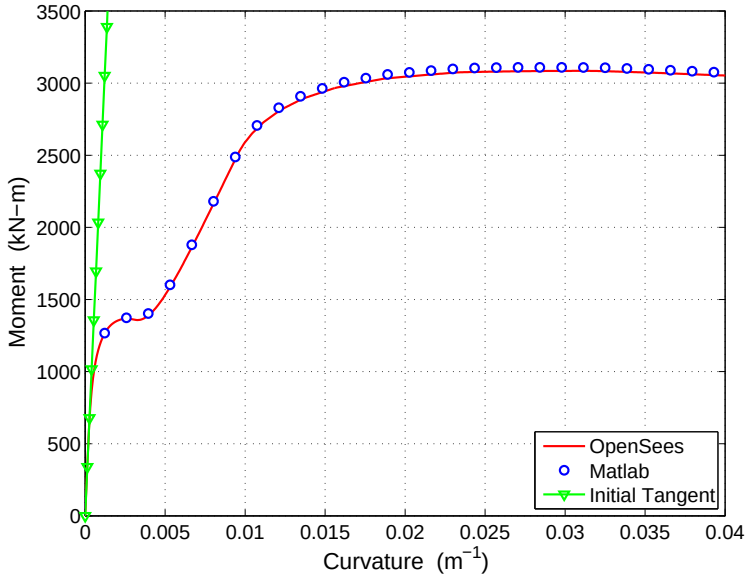

Figure 3.17: Comparison of moment–curvature responses of zero–length elements in OpenSees with independently calculated results for 1.3716 m half–pile (semi–circular) model.

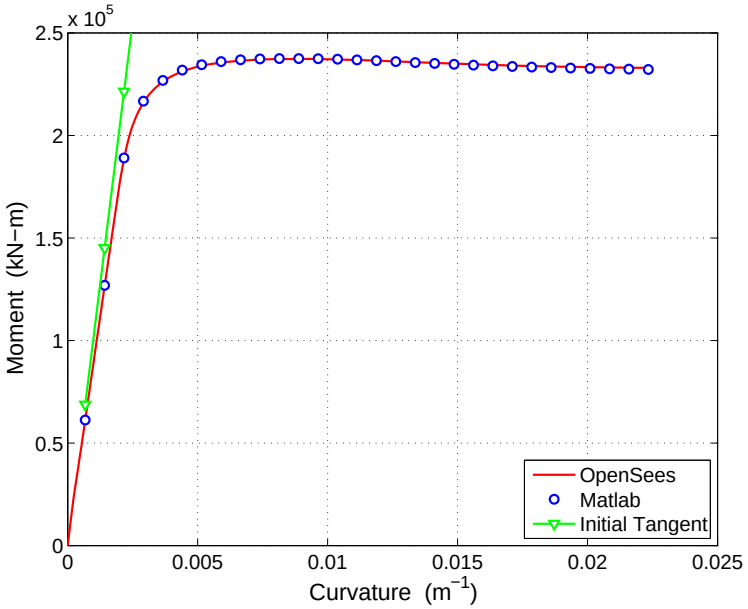

Figure 3.18: Comparison of moment–curvature responses of zero–length elements in OpenSees with independently calculated results for 2.5 m full (circular) pile model.

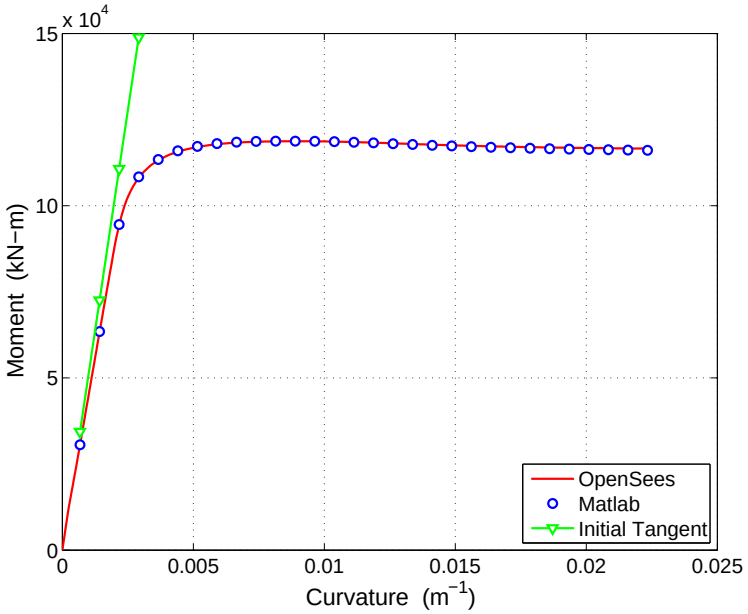

Figure 3.19: Comparison of moment–curvature responses of zero–length elements in OpenSees with independently calculated results for 2.5 m half–pile (semi–circular) model.

As discussed in Section 3.3.2, the symmetry conditions assumed in the lateral spreading model require the piles to be modeled as half–piles. Using this assumption, the resulting pile moments and forces must be multiplied by two in order to obtain the respective values that would exist in a full pile. As expected, the half–pile models (Figures 3.15, 3.17, and 3.19) display moment–curvature behavior in which the moments are exactly one–half of those returned by the full–pile models for a given curvature value. This provides validation that the symmetry condition in the lateral spreading model is correctly implemented.

Cantilever Beam Implementation

One additional verification measure was taken in order to ensure that the behavior of the section models is consistent regardless of the loading configuration. Using a simple cantilever beam model, a schematic of which is provided in Figure 3.20, the resulting moment–curvature responses can be determined and then compared to the results obtained with the zero–length element and Matlab methods. As before, the cantilever beams utilize the fiber section models generated for each pile. The moment–curvature responses for the 0.6096 and 2.5 m piles, in the element adjacent to the fixed base, are shown in Figures 3.21 and 3.22 along with the previously discussed results for the zero–length models. This small study provides verification that the cross–sectional model is successfully and correctly implemented into a 3D simulation.

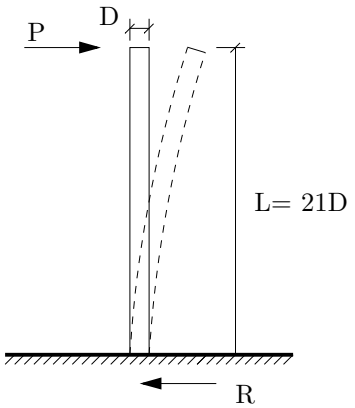

Figure 3.20: Cantilever beam analysis. The horizontal load, P, is increased linearly until the pile tip deflects a distance of one pile radius.

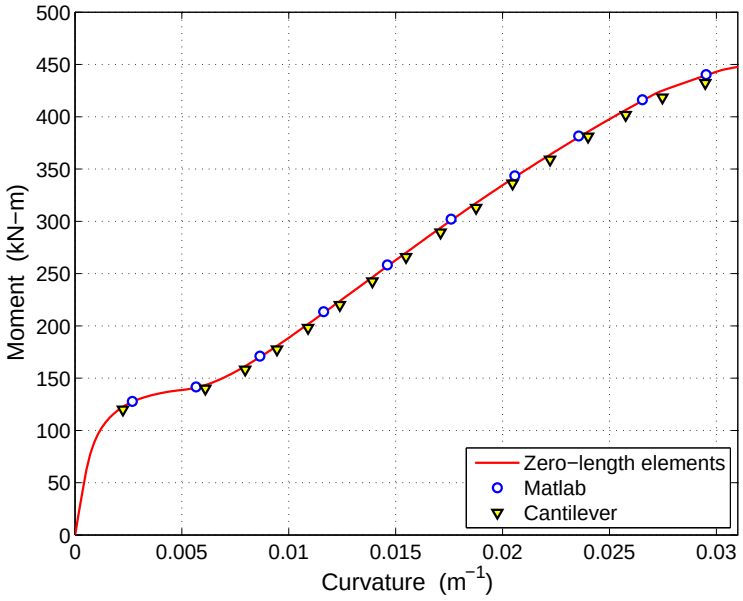

Figure 3.21: Moment–curvature response of the cantilever model compared to zero–length element and independently calculated section responses for the 0.6096 m pile. The cantilever model fails at this level of curvature.

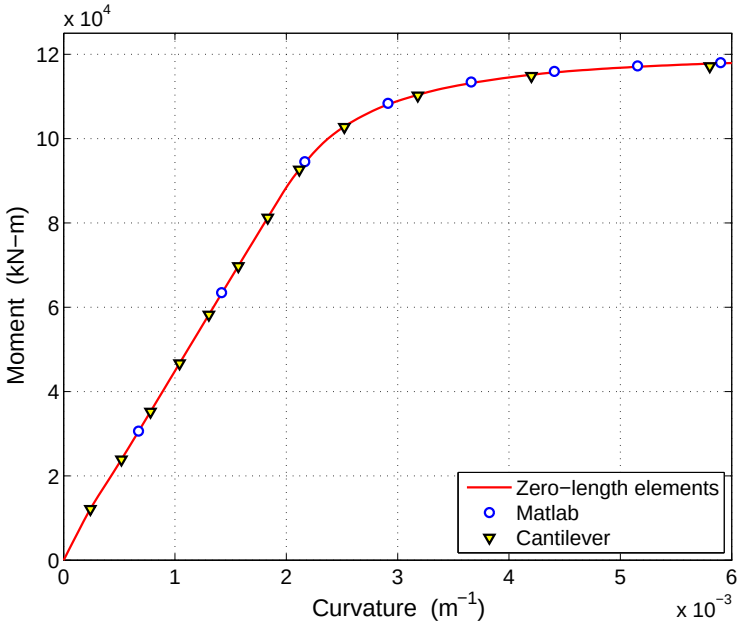

Figure 3.22: Moment–curvature response of the cantilever model compared to zero–length element and independently calculated section responses for the 2.5 m pile.

3.6.2 Validation of Tension Parameters

As discussed in Section 3.4.5, the 0.6096 m and 1.3716 m pile models exhibit convergence problems when assigned large values of the tension softening modulus, E_t. While it is important to select input parameters that allow for convergence, it is equally important to validate that any changes in the parameters are sensible and do not significantly alter the resulting behavior of the pile models. To show that a suitable compromise between accuracy/detail resolution and numerical stability in tension softening parameter does not significantly affect the results, the behavior of the pile models for several values of E_t are compared via two validation studies. These initial validation studies are made in an effort to promote the use of the tension softening stiffnesses that provide the best rate of convergence without compromising results for each pile model (see Table 3.5 on page 38).

In the first validation study, the moment–curvature behavior of the pile models is compared for three separate values of E_t. This behavior is generated for each model using the zero–length element approach as discussed in Section 3.6.1. Two of the three tension softening stiffnesses are based upon characteristic lengths set equal to the sizes of the largest and smallest elements, respectively, in each pile model. These characteristic lengths derive from the assumption that a single crack develops in each element. The third value of E_t is determined by setting the characteristic length to be the assumed crack spacings listed in Table 3.5.

For the lateral spreading model, it is important that the behavior of the pile elements at large curvature and displacement demands remains unaffected by changes in the tension softening modulus. Part of the goal of this research is to evaluate the maximum moments, shear forces, and curvatures that develop in a pile embedded in a laterally spreading soil system. For this reason, the behavior at middling curvature and displacement demands is relatively unimportant. Also, since the stiffness of the pile is crucial in determining how the free–field curvature demand on the soil will affect the embedded pile, it is desirable that changes in E_t leave the initial tangent stiffness of the models similarly unaffected.

As shown in Figures 3.10 and 3.11 on page 39, the initial tangent stiffness of the pile model is not affected by the selected characteristic lengths, validating that altering ℓ_c to

improve the rate of convergence does not alter the initial stiffness of the pile models. These figures also show that at larger curvature demands, above about 0.015 m^{-1} in the 0.6096 m model and about 0.007 m^{-1} in the 1.3716 m model, the moment–curvature behavior is unaltered by the magnitude of the tension softening modulus. Thus, validating that the respective selections of ℓ_c are sensible with respect to the resulting moment–curvature response of the pile models in the range of curvatures that is important to this research.

Further validation of the selected tension softening moduli is made through the second validation study. This second study is an examination of the force–displacement behavior of cantilever beams modeled with the 0.6096 m and 1.317 m pile section elements. A schematic of this model is presented in Figure 3.20 and the results of this validation exercise are shown in Figures 3.23 and 3.24. Each model is a assigned tension softening modulus resulting from characteristic lengths of decreasing magnitude, starting from setting ℓ_c as the smallest element length in the respective models. The cantilever beam models for each pile section model mimic the mesh and geometry of the piles as used in the lateral spreading models exactly.

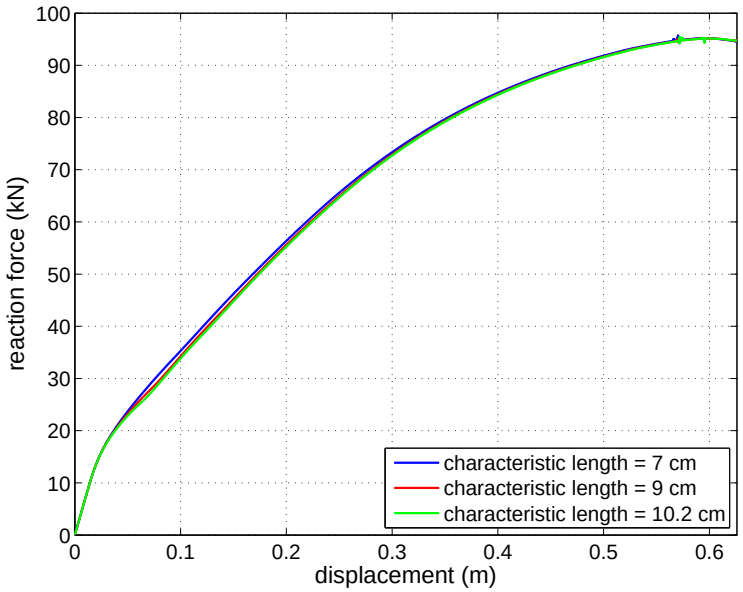

Figure 3.23: Force–displacement behavior for 0.6096 m pile section model as implemented in a cantilever beam model with various values of ℓ_c.

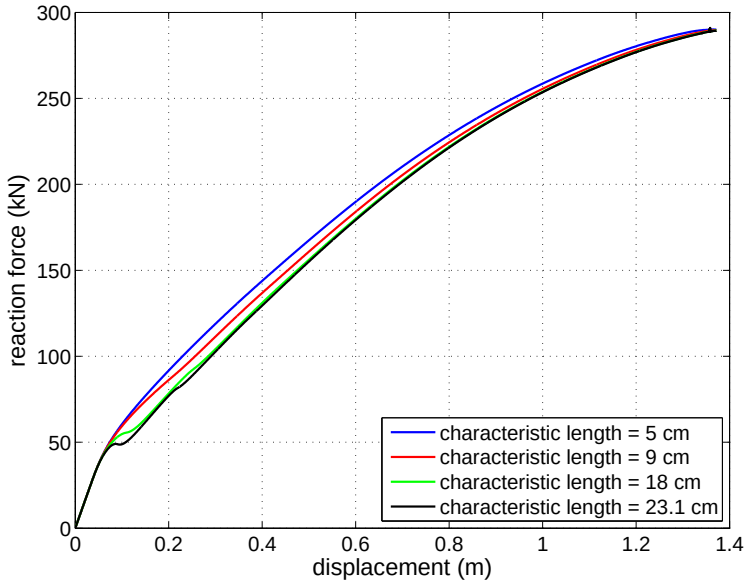

Figure 3.24: Force–displacement behavior for 1.3716 m pile section model as implemented in a cantilever beam model with various values of ℓ_c.

The effects of the changes in magnitude of the tension softening parameter are more apparent in the cantilever model, where the elements have lengths, as compared to the zero–length element approach used to generate the moment–curvature behavior of the models. This is demonstrated by the observation that the cantilever models for both pile models are unable to converge past a few time steps when the characteristic length is set as the largest element length. Once the tensile stress in the cross–section reaches that which signals the onset of cracking, no converged solution can be found. The models display convergence issues even when ℓ_c is set as the smallest element length, though, unlike the case where the characteristic length is equal to the largest element length, the models will converge, albeit with a large number of small load steps. As in the moment–curvature study, the initial behavior is the same regardless of parameter selection, and all of the cases reach essentially the same reaction force at the final displacement.

The selections of ℓ_c summarized in Table 3.5 (page 38), and the resulting tension softening moduli, are made with consideration towards a realistic crack spacing as well as with respect to the convergence behavior of the pile models. The cantilever verification study

provides validation that the selected characteristic length parameter will allow the pile models to reach convergence when implemented in a model with actual geometry, validation that the zero–length elements cannot provide. Additionally, the cantilever study demonstrates that the magnitude of the tension softening modulus only affects the middle range of the models' behavior; the initial and final ranges are unaffected.

Chapter 4

MODELING THE SOIL

4.1 Introduction

The behavior of the soil surrounding the piles is important to the problem of a pile embedded in laterally spreading soils as it is both the source of and the medium through which the kinematic demands of the moving soil mass are transmitted to the embedded pile foundations. In a layered soil system, such as that being considered in this study, the thickness of the liquefied layer and the various material properties of the surrounding soil layers are integral to defining how a pile experiences a lateral spreading event. Seemingly minor changes in the material properties or the configuration of the layers can significantly alter the resultant behavior of an embedded pile. In order for the results of this study to be valid for most piles in different soils, it is critical to select appropriate values for the soil parameters.

The soil system considered in this study consists of three individual soil layers modeled as a 3D continuum surrounding the pile on one side. A global view of the complete finite element model is shown in Figure 2.1 (page 11), in which the various soil layers and the general layout of the soil elements are clearly visible. For all of the models involved in this research, the soil modeling decisions are made based upon the assumption that all three layers are made up entirely of homogenous (within each layer) cohesionless soil.

In the particular three–dimensional lateral spreading models analyzed in this research, two separate soil models are considered. One of these models considers the soil to be linear elastic while the other soil model considers elastoplastic behavior using a Drucker–Prager constitutive model with tension–cutoff developed and implemented for use in OpenSees by Petek (2006) [21].

4.2 Soil Elements

The soil continuum is modeled using eight–node brick elements. The soil nodes defining these elements are created with three translational degrees of freedom. The number of soil elements ranges from 2720 to 3360 depending upon the thickness of the liquefiable layer considered in each particular case. As can be seen in Figure 2.1 (page 11), the degree of mesh refinement is increased in the middle of the model as compared to the regions near the top and bottom of the model. This meshing scheme allows the areas of importance (i.e. the areas near the interface of the liquefiable layer) to have a relatively fine mesh, while leaving the outlying regions with a coarser level of refinement.

The elements of all three soil layers in all of the models are assigned a unit weight, $\gamma = 17$ kN/m^3. The assignment of a unit weight to the soil elements is crucial to creating appropriate confinement pressure at depth for the soil model, which is, in turn, critical to determining the effective strength of each soil element. As detailed in Chapter 2, the first step in the lateral spreading analysis is to apply the self–weight of the soil elements, thus creating a soil system in which the confinement pressure varies with depth. Using this approach, both the soil and the embedded pile will behave in a manner consistent with a real soil–pile system when subjected to the simulated lateral spreading event.

4.3 Linear Elastic Soil Constitutive Modeling

For certain aspects of this research, the elements of soil surrounding the piles are assumed to display isotropic linear elastic behavior. This simplification allows for a means of comparison between elastoplastic pile and elastic soil lateral spreading models with simpler, entirely elastic models, as well as a basic case with which to test the elastoplastic pile models in the global lateral spreading model. In OpenSees, the particular material model selected accepts as input values the elastic modulus, E, and Poisson's ratio, ν, for the material of interest. The values selected for these parameters in each soil layer are shown in Table 4.1.

During liquefaction of the middle layer, the pore water pressure in the layer increases, thus reducing the effective stress in the layer. As the magnitude of the pore water pressure becomes closer to the total mean stress in the layer, the shear strength becomes significantly

Table 4.1: Material input parameters used in isotropic linear elastic soil constitutive models.

Soil Layer	E (kPa)	ν	G (kPa)	k (kPa)
Upper	25000	0.35	9260	27777.8
Liquefiable	2500	0.485	842	27777.8
Lower	25000	0.35	9260	27777.8

smaller. The compressibility of the layer, however, should not change quite as drastically. For this reason, all of the soil material parameters are selected based upon an assumption that the bulk modulus, k, remains consistent throughout the soil mass. The upper and lower solid layers are assigned an elastic modulus, E, equal to 25000 kPa and a Poisson's ratio, $\nu = 0.35$. Both are typical values for cohesionless soils. Using the well known isotropic linear elastic material parameter relations

$$k = \frac{E}{3\,(1-2\nu)} \tag{4.1}$$

and

$$G = \frac{E}{2\,(1+\nu)} \tag{4.2}$$

the bulk modulus and shear modulus can be computed for known values of E and ν. In a fully liquefied state, the middle soil layer should have a Poisson's ratio close to 0.5, matching that of an incompressile fluid. Using a value of $\nu = 0.5$ would create an infinite bulk modulus, and cause a multitude of problems in the solver. To avoid this result, a value of $\nu = 0.485$ is selected for the liquefied middle layer. Using this parameter and a bulk modulus of $k = 27777.8$ kPa computed for all of the solid layers, appropriate values for the elastic and shear moduli are computed for the liquefied layer using (4.1) and (4.2). These values are summarized in Table 4.1.

4.4 Elastoplastic Soil Constitutive Modeling

In order to return $p-y$ curves that are appropriate for use in practice, the soil elements must display material nonlinearity in their constitutive behavior. The material nonlinearity considered in this research is introduced in the soil models through a Drucker–Prager

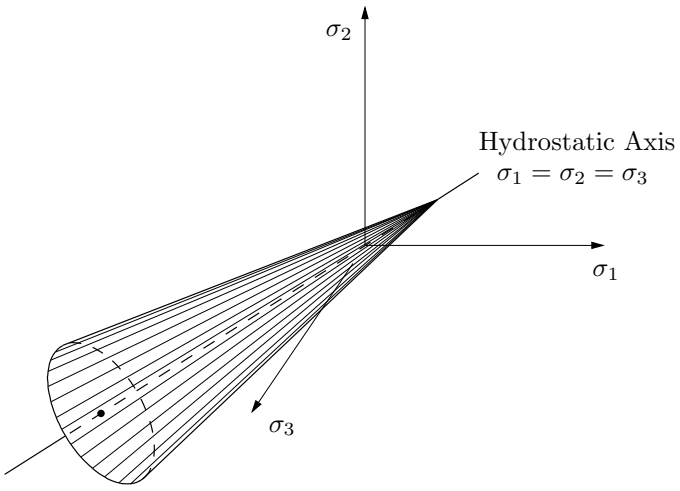

Figure 4.1: Drucker–Prager failure surface plotted in the Haigh–Westergaard stress space.

constitutive model. The Drucker–Prager model is the simplest constitutive model that is appropriate for use with cohesionless soils. Other, more sophisticated constitutive models have been developed, however, the Drucker–Prager model is deemed sufficient to meet the goals of this research. The particular model employed is one that was implemented in OpenSees by Petek (2006) [21]. The following section includes a basic discussion of the various components defining the Drucker–Prager model, as implemented in OpenSees. Section 4.4.2 includes a discussion on the particular material parameters used in the models and the impetus behind their use.

4.4.1 Drucker–Prager Constitutive Model

The Drucker–Prager constitutive model is one of the earliest soil plasticity models, developed as an extension of the von Mises yield criterion from one material parameter to two material parameters by Drucker and Prager (1952) [9]. Whereas the von Mises criterion is useful for metals, where independence from hydrostatic pressure is observed, the Drucker–Prager criterion was developed to account for the effects of hydrostatic pressure on the behavior of soil materials. As with the von Mises criterion, isotropic and kinematic strain hardening laws can be incorporated into the Drucker–Prager model, though it is not a required feature.

In a three–dimensional Haigh–Westergaard principal stress space, the Drucker–Prager yield surface is a circular cone centered around the hydrostatic stress axis ($\sigma_1 = \sigma_2 = \sigma_3$). This surface is shown in Figure 4.1 using a standard continuum mechanics sign convention (i.e. tension positive). The conical shape is the direct visual result of the effects of hydrostatic pressure on the behavior of a Drucker–Prager material. As compressive hydrostatic pressure increases, an increasing amount of deviatoric stress must be applied in order to bring the material to yield.

The material model can be fully defined by the material's free energy function, ψ, state equations, the Drucker–Prager yield condition, $f(\boldsymbol{\sigma}) \leq 0$, and evolution laws (flow rule and hardening law); all of which follow from classical rate–independent plasticity theory. For a 3D formulation, including linear isotropic and kinematic strain hardening, the free energy function can be written as a function of the state variables, which include: the strain, $\boldsymbol{\varepsilon}$, the plastic strain, $\boldsymbol{\varepsilon}^p$, the and the respective isotropic and kinematic hardening parameters, α^{iso} and $\boldsymbol{\alpha}^{kin}$, as

$$\psi\left(\boldsymbol{\varepsilon}, \boldsymbol{\varepsilon}^p, \alpha^{iso}, \boldsymbol{\alpha}^{kin}\right) = \frac{1}{2}\left(\boldsymbol{\varepsilon} - \boldsymbol{\varepsilon}^p\right) : \mathbb{C} : \left(\boldsymbol{\varepsilon} - \boldsymbol{\varepsilon}^p\right) + \frac{1}{2}K\left(\alpha^{iso}\right)^2 + \frac{1}{2}\boldsymbol{\alpha}^{kin} : \mathbb{H} : \boldsymbol{\alpha}^{kin} \tag{4.3}$$

where

$$\mathbb{C} = 3k\mathbb{I}^{vol} + 2G\mathbb{I}^{dev} \tag{4.4}$$

is the elastic tensor, expressed in terms of the bulk and shear moduli (k and G) and the fourth–order volumetric and deviatoric operators, $\mathbb{I}^{vol}$ and $\mathbb{I}^{dev}$. The fourth–order tensor $\mathbb{H}$, characterizing a shift of the yield surface in the deviatoric plane, can be defined in terms of the scalar kinematic hardening variable, H, as

$$\mathbb{H} = \frac{2}{3}H\mathbb{I}^{dev} \tag{4.5}$$

and K is a constant (scalar) isotropic hardening parameter. From the free energy function of (4.3), three state equations, (4.6), (4.7), and (4.8), can be written relating the state variables to the stress

$$\boldsymbol{\sigma} = \frac{\partial \psi}{\partial \boldsymbol{\varepsilon}} = \mathbb{C} : \left(\boldsymbol{\varepsilon} - \boldsymbol{\varepsilon}^p\right) \tag{4.6}$$

isotropic hardening stress

$$q^{iso} = -\frac{\partial \psi}{\partial \alpha^{iso}} = -K\alpha^{iso} \tag{4.7}$$

and kinematic hardening stress (or back–stress)

$$\mathbf{q}^{kin} = -\frac{\partial \psi}{\partial \boldsymbol{\alpha}^{kin}} = -\mathbb{H} : \boldsymbol{\alpha}^{kin} \tag{4.8}$$

When implementing this model in an algorithm using compressed matrix representations for the involved second– and fourth–order tensors, it is important to note the difference between stress–type (contravariant) second–order tensors, such as $\boldsymbol{\sigma}$ and $\mathbf{q}^{kin}$, and strain–type (covariant) second–order tensors such as $\boldsymbol{\varepsilon}$ and $\boldsymbol{\alpha}^{kin}$ (Helnwein, 2001 [12]). Due to these differences, it is often beneficial to express the yield condition entirely in terms of one type of variable. Written in terms of stress–type variables, the yield condition for the Drucker–Prager model can be expressed as

$$f\left(\boldsymbol{\sigma}, q^{iso}, \mathbf{q}^{kin}\right) = \|\mathbf{s} + \mathbf{q}^{kin}\| + \rho I_1 + \sqrt{\frac{2}{3}} q^{iso} - \sqrt{\frac{2}{3}} \sigma_Y \leq 0 \tag{4.9}$$

in which

$$\mathbf{s} = dev(\boldsymbol{\sigma}) = \boldsymbol{\sigma} - \frac{1}{3} I_1 \mathbf{1} \tag{4.10}$$

is the deviatoric stress tensor,

$$I_1 = tr(\boldsymbol{\sigma}) \tag{4.11}$$

is the first invariant of the stress tensor, and the two parameters ρ and σ_Y are positive material constants. It is common to define an additional variable $\boldsymbol{\eta}$ such that

$$\boldsymbol{\eta} = \mathbf{s} + \mathbf{q}^{kin} \tag{4.12}$$

The adoption of this additional variable allows for the expression of (4.9) in the form

$$f = \|\boldsymbol{\eta}\| + \rho I_1 - \sqrt{\frac{2}{3}} \left(\sigma_Y - q^{iso}\right) \leq 0 \tag{4.13}$$

which is useful for its relative simplicity in notation.

The final set of equations characterizing the Drucker–Prager model are the three evolution laws which describe how the state variables $\boldsymbol{\varepsilon}^p$, α^{iso}, and $\boldsymbol{\alpha}^{kin}$ change over time. These laws are defined in terms of various derivatives of the loading function

$$g\left(\boldsymbol{\eta}, I_1, q^{iso}\right) := \|\boldsymbol{\eta}\| + \overline{\rho} I_1 - \sqrt{\frac{2}{3}} \left(\sigma_Y - q^{iso}\right) \tag{4.14}$$

in which $\overline{\rho}$ is a non-associative parameter ranging from $0 \leq \overline{\rho} \leq \rho$, and a nonnegative scalar consistency parameter, γ. The evolution law for plastic strains, known commonly as the flow rule, can be written as

$$\dot{\boldsymbol{\varepsilon}}^p = \gamma \frac{\partial g}{\partial \boldsymbol{\sigma}} = \gamma \left(\frac{\boldsymbol{\eta}}{\|\boldsymbol{\eta}\|} + \overline{\rho}\mathbf{1} \right) \tag{4.15}$$

The parameter $\overline{\rho}$ controls the evolution of plastic volume change. When $\overline{\rho} = \rho$ the plastic flow is said to be fully associative and $g = f$. The evolution laws for the hardening variables, commonly referred to as hardening laws, are expressed as

$$\dot{\alpha}^{iso} = \gamma \frac{\partial g}{\partial q^{iso}} = \gamma \sqrt{\frac{2}{3}} \tag{4.16}$$

$$\dot{\boldsymbol{\alpha}}^{kin} = \gamma \frac{\partial g}{\partial \mathbf{q}^{kin}} = \gamma \left(\frac{\boldsymbol{\eta}}{\|\boldsymbol{\eta}\|} \right) \tag{4.17}$$

The Drucker–Prager model implemented in OpenSees by Petek (2006) [21] also includes a tension–cutoff surface, incorporating tension softening, in addition to the standard Drucker–Prager yield surface. This tension–cutoff better captures the limited tensile capacity of a cohesionless soil. Additionally, the condition of $\|\mathbf{s}\| \geq 0$, which follows from a basic property of norms, requires a second surface.

The tension cutoff surface can be defined by the yield condition

$$f_2\left(\boldsymbol{\sigma}, q^{ten}\right) = I_1 + q^{ten} \leq 0 \tag{4.18}$$

where q^{ten} is a stress–type variable associated with the softening variable, α^{ten}, by the state equation

$$q^{ten} = -T_o \exp\left(-\delta \alpha^{ten}\right) \tag{4.19}$$

in which δ is a softening coefficient and T_o is a constant related to the Drucker–Prager yield surface as

$$T_o = \sqrt{\frac{2}{3}} \frac{\sigma_Y}{\rho} \tag{4.20}$$

The flow rule (4.15) is extended for the tension cutoff surface as

$$\dot{\boldsymbol{\varepsilon}}^p = \gamma_1 \frac{\partial g_1}{\partial \boldsymbol{\sigma}} + \gamma_2 \frac{\partial f_2}{\partial \boldsymbol{\sigma}} = \gamma_1 \left(\frac{\boldsymbol{\eta}}{\|\boldsymbol{\eta}\|} + \overline{\rho}\mathbf{1} \right) + \gamma_2 \mathbf{1} \tag{4.21}$$

and the softening law can be formulated as

$$\dot{\alpha}^{ten} = \gamma_2 \frac{\partial f_2}{\partial q^{ten}} = \gamma_2 \tag{4.22}$$

4.4.2 Determination of Material Parameters

The material constants defining the Drucker–Prager constitutive model are selected carefully such that there is consistency with the elastic soil elements, as well as a degree of realism in the magnitudes used for each soil layer. The elastic constants of bulk and shear moduli defined as input values in the linear elastic soil models are also used as inputs in the elastoplastic models. To create a realistic pressure–dependent elastic stiffness in the elastoplastic model, the elastic parameters are modified to include the ability to update the bulk modulus according to the relation

$$k = k_{ref} \left(1 + \left| \frac{\sigma_m}{\sigma_{ref}} \right| \right)^{0.5} \tag{4.23}$$

in which k_{ref} is the reference bulk modulus listed in Table 4.2 for each layer, $\sigma_m = I_1/3$ is the mean stress in each element, and σ_{ref} is a reference pressure taken to be equal to atmospheric pressure (101 kPa). A matching relation of

$$G = G_{ref} \left(1 + \left| \frac{\sigma_m}{\sigma_{ref}} \right| \right)^{0.5} \tag{4.24}$$

is used to update the shear modulus in the model, in which G_{ref} is the reference shear modulus listed in Table 4.2. The parameter update approach lets the model establish appropriate parameters with depth based upon the mean stress in each element due to the self weight of the soil.

In order to obtain sensible values for the Drucker–Prager material constants ρ and σ_Y, the following correlations have been made with the somewhat more common, and measurable, Mohr–Coulomb material constants of cohesion, c, and friction angle, ϕ, after the discussion detailed in Chen and Saleeb (1994) [8] as follows:

$$\rho = \frac{2\sqrt{2}\sin\phi}{\sqrt{3}\,(3 - \sin\phi)} \tag{4.25}$$

$$\sigma_Y = \frac{6c\cos\phi}{\sqrt{2}\,(3 - \sin\phi)} \tag{4.26}$$

Table 4.2: Material input parameters used in Drucker–Prager soil constitutive models.

Soil Layer	k (kPa)	G (kPa)	σ_Y (kPa)	ρ	K (kPa)	δ
Upper	27777.8	9260	5	0.398	0.0	0.0
Liquefiable	27777.8	842	4.97	0.0	0.0	0.0
Lower	27777.8	9260	5	0.398	0.0	0.0

Assuming a small amount of cohesion for numerical stability and friction angles of $\phi = 36^\circ$ in the unliquefied layers and $\phi = 0^\circ$ in the liquefied layer, the Drucker–Prager material constants are computed for each layer using (4.25) and (4.26) and summarized in Table 4.2. With respect to associative and non-associative plastic flow, several combinations are explored. Models are run with the non-associative parameter $\overline{\rho}$ set equal to both ρ, creating fully associative flow, and zero, creating isochoric non-associative flow, as well as to an intermediate case where $\overline{\rho} = 0.150$ to improve the convergence behavior of the models.

It is interesting to note that when setting $\phi = 0^\circ$, resulting in $\rho = 0$, the Drucker–Prager yield condition of (4.9) reduces to the von Mises yield criterion. In effect, the elastoplastic lateral spreading model is constructed by considering the upper and lower solid layers to be Drucker–Prager materials and the liquefied middle layer as a low shear stiffness von Mises material. To provide a degree of simplicity in the model, the linear isotropic hardening and tension softening parameters are set to zero. This decision may create a material model which does not reflect the true behavior of a cohesionless soil, but it is considered sufficient for the purposes of this research.

4.5 Validation of Soil Models

As with all of the other aspects of this research, it is important to validate the elastoplastic soil models through simple tests before installing them into a larger model. The Drucker–Prager soil model is evaluated through a series of finite element simulations of geotechnical tests with a single element of elastoplastic soil. The chosen test are all commonly performed to evaluate the mechanical characteristics of soil samples, and allow for validation that the OpenSees implementation of the Drucker–Prager model is performing as expected.

The selected geotechnical tests are:

1. Confined compression (CC) test
2. Conventional triaxial compression (CTC) test
3. Simple shear (SS) test
4. Hydrostatic extension (HE) test.

With the exception of the hydrostatic extension test, all of the simple, single element, tests start from an initial hydrostatic stress state, $\sigma_1 = \sigma_2 = \sigma_3 = -p_o$, where p_o is an initial confining pressure. Each test is conducted for various initial confining pressures both with and without the inclusion of linear isotropic hardening. Unless otherwise indicated, the material parameters used in each test are those summarized in Table 4.2.

When dealing with three–dimensional stress states, plots of the various invariants of the stress and strain tensors are often the most effective means for visualizing the behavior of a particular material. If chosen carefully, such plots can display data in a more meaningful manner than traditional stress–strain plots. For each material test, four plots are chosen with the intent of fully characterizing the stress–strain response of the Drucker–Prager soil element. The chosen invariant axes include the norm of the deviatoric stress tensor, $\|\mathbf{s}\|$, the first invariant of the stress tensor, $I_1 = \text{tr}\boldsymbol{\sigma}$, the norm of the deviatoric strain tensor, $\|\mathbf{e}\|$, the trace of the strain tensor, $tr(\boldsymbol{\varepsilon})$, and the mean stress, $I_1/3$.

4.5.1 Confined Compression Test

In a confined compression test (here elided as the CC test, a convention which is followed for all of the single element tests described herein), the soil element is first brought to an initial state of hydrostatic stress. While holding the displacements fixed in the first and second principal stress directions, the displacement in the third principal direction is increased, creating an increase in the compressive stress in that direction. To achieve this in the context of the single element model, an entirely strain–controlled approach is adopted. The approach used to model this test is depicted in Figure 4.2.

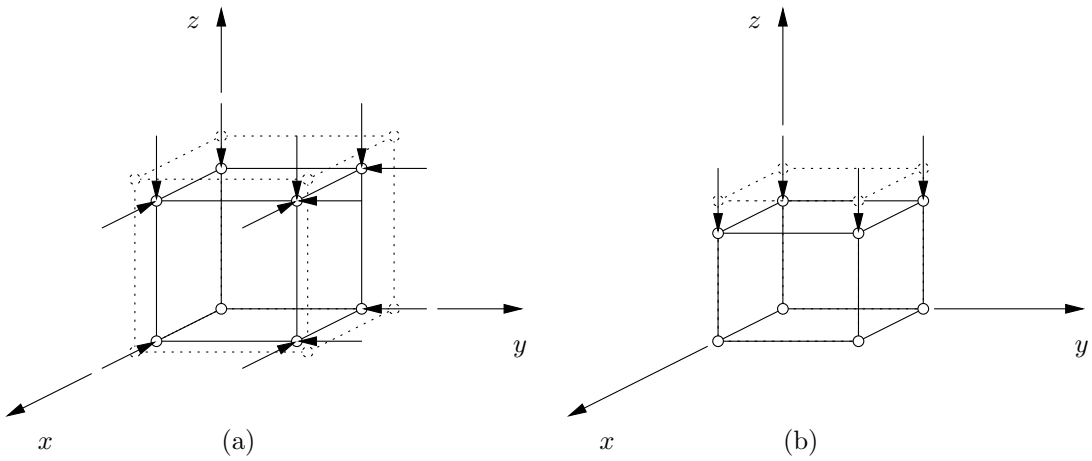

Figure 4.2: Schematic depiction of the CC test as performed in OpenSees. (a) During the application of the initial hydrostatic stress state, the free nodes are moved inwards. (b) In the confined compression phase, the top nodes are moved down while all of the other nodes are fixed against expansion.

As with the models in all of the soil tests, this model considers the soil element to be a unit cube. The nodes in the $x-y$, $y-z$, and $z-x$ planes are held fixed with respect to displacements normal to their faces. The nodes on the element faces opposite the fixed faces are moved inwards by equal increments to create the hydrostatic stress state. After the desired hydrostatic stress state has been reached, the nodes on the positive x– and y–faces are held fixed against x– and y–direction displacements, respectively, while the nodes on the positive z–face of the element are moved downwards. The stresses acting in the x– and y–directions do not stay constant, instead, the strains in those directions are held constant.

The stress path for the CC test is shown on the meridian planes in Figure 4.3 for three values of initial confining pressure ($p_o = 10$, $p_o = 20$, and $p_o = 40$ kPa). As expected, the normal stress increases along the I_1 axis during the hydrostatic loading phase, and then deviatoric stresses begin to develop during the confined compression phase. For the particular loading ratio used in the CC test, the soil element remains in the elastic range, never reaching the yield state, an event that would be evident by the stress path intersecting the line of the failure surface. Because the element remains entirely elastic during this test, no strain hardening cases are considered.

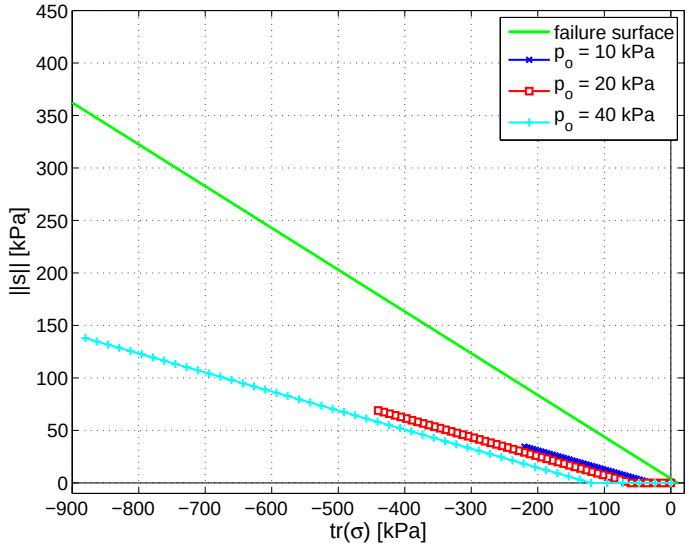

Figure 4.3: Stress paths for the confined compression (CC) test.

The material–response summary presented Figure 4.4 shows the stress–strain behavior of the soil element during the CC test on a series of four axes. Since the material remains

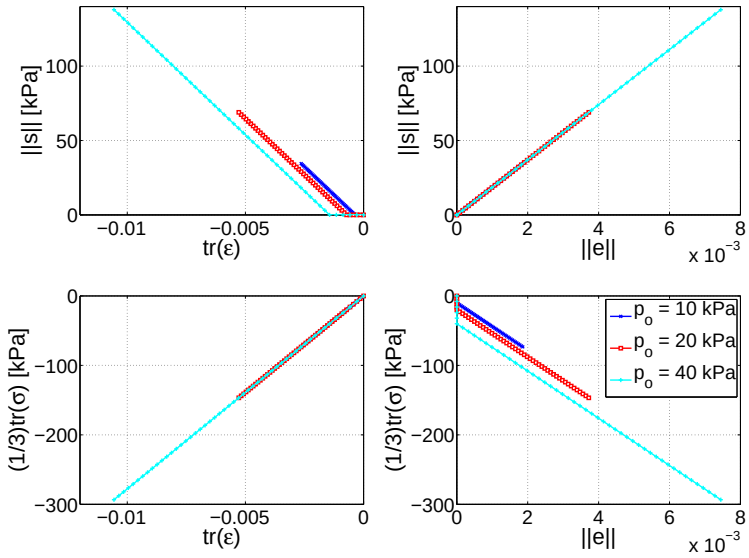

Figure 4.4: Stress–strain responses of Drucker–Prager soil element model subjected to confined compression (CC) stress path.

entirely elastic during this test, the slopes of the curves in all four plots remain constant. This verifies both the initial expectations for this test as well as the stress path shown in Figure 4.3. Additionally, the slopes for all three confining pressures are identical, suggesting that in the elastic range, the OpenSees Drucker–Prager implementation works equally well for any degree of initial confinement.

4.5.2 Conventional Triaxial Compression Test

The conventional triaxial compression (CTC) test is one of the most widely used test in soil mechanics. In this test, after the initial hydrostatic loading phase, two of the principal stresses are kept constant (i.e. $\sigma_1 = \sigma_2 = -p_o$), while the third principal stress, σ_3 is increased. This test differs from the confined compression test in that the first and second principal stresses do not change from their initial value at the the end of the hydrostatic phase, whereas the first and second principal stresses in the CC test increase in proportion to the applied stress increase in the third principal direction.

The CTC test is achieved in a single element model as depicted in Figure 4.5. This test uses mixed stress and strain control, as opposed to the pure strain control of the CC test,

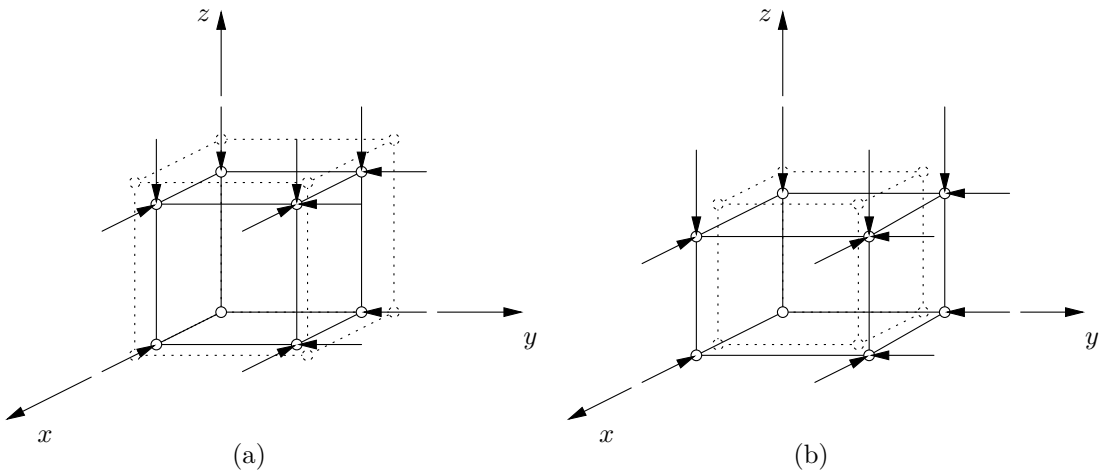

Figure 4.5: Schematic depiction of the CTC test as performed in OpenSees. (a) Loads are applied at the free nodes to create the initial hydrostatic stress state. (b) The z–direction loads are then increased while the others loads are held constant to produce the desired result.

however, the geometric boundary conditions are the same as those in the CC test model. The hydrostatic stresses are applied under stress control, by applying compressive loads on the free degrees–of–freedom. Once the desired hydrostatic state is achieved, the loads on the positive x– and y–faces are held fixed for the duration of the test, ensuring that the principal stresses in two directions remain constant, while the nodes on the positive z–face of the element are moved downwards under strain control to create the increase in the third principal stress. The nodes on the non–fixed faces of the element are left free to displace outward during this process.

Verification that the material model behaves in a predictable manner during this test can be obtained through a comparison of the predicted slope of the stress path resulting from the CTC test with the data returned from OpenSees. It can be shown that the slope of the CTC test stress path on a meridian ($I_1 - \|\mathbf{s}\|$) plane, is equal to $\sqrt{2/3}$. A line with this slope is plotted against the stress path returned from OpenSees for the $p_o = 10$ kPa case. As shown in Figure 4.6, the single element test slope is identical to the theoretical slope, thus providing further validation that the Drucker–Prager material model has been successfully implemented into OpenSees.

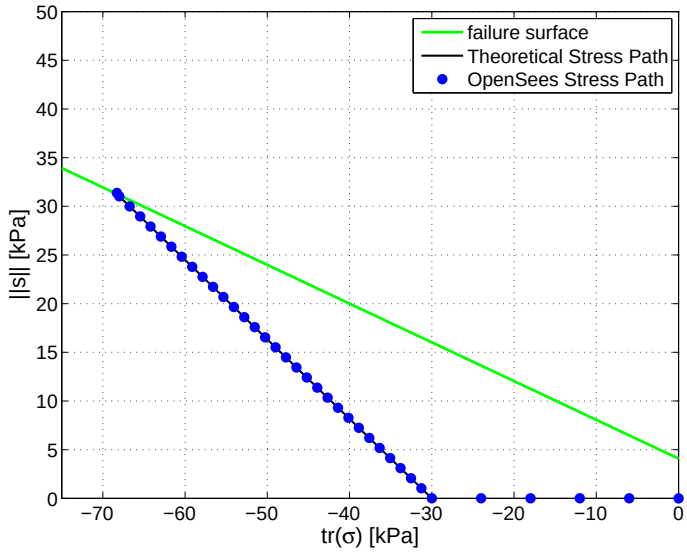

Figure 4.6: Comparison of slopes on the meridian plane for the OpenSees and theoretical CTC test stress paths.

The stress path corresponding to the CTC test for a soil element with no strain hardening is shown in the meridian plane in Figure 4.7 for three separate values of initial confining pressure. The same plot is shown in Figure 4.8 for a soil element including linear isotropic strain hardening. For the strain hardening cases, the hardening parameter K is set to $100,000$ kPa to enhance visualization. As opposed to the CC test, the CTC test brings the element to failure for all cases. For the three cases without strain hardening, once the deviatoric stress has increased to the point where the stress path intersects the failure surface, the material yields and the stresses no longer increase with increasing strain. This behavior is consistent with the expectations for a perfectly plastic material.

When linear isotropic hardening is included, the model exhibits behavior that is somewhat altered. Instead of displaying perfectly plastic behavior, the soil element hardens with increasing strain, allowing for the stresses to increase beyond the initial limiting values for the perfectly plastic cases. The inclusion of strain hardening effectively acts to expand the failure surface with increasing plastic strain. Again, the Drucker–Prager soil element behaves as expected, providing assurance that the OpenSees implementation is correct.

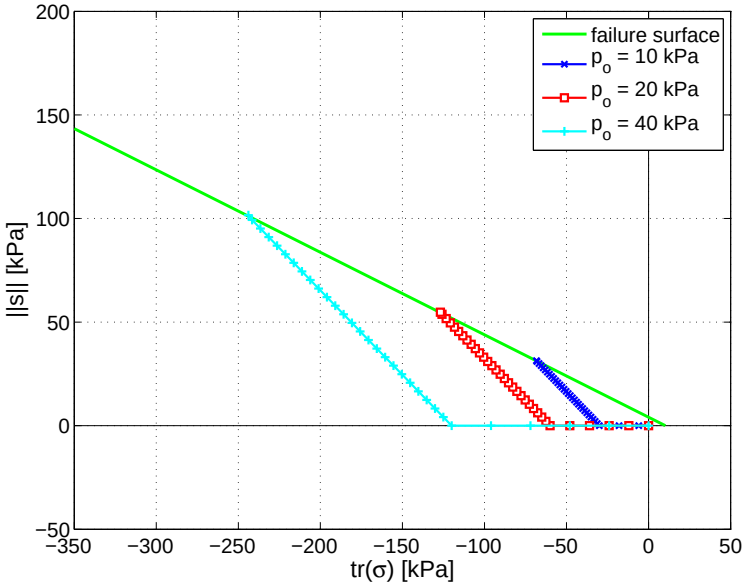

Figure 4.7: Stress paths for the conventional triaxial compression (CTC) test for the perfectly plastic case (no strain hardening).

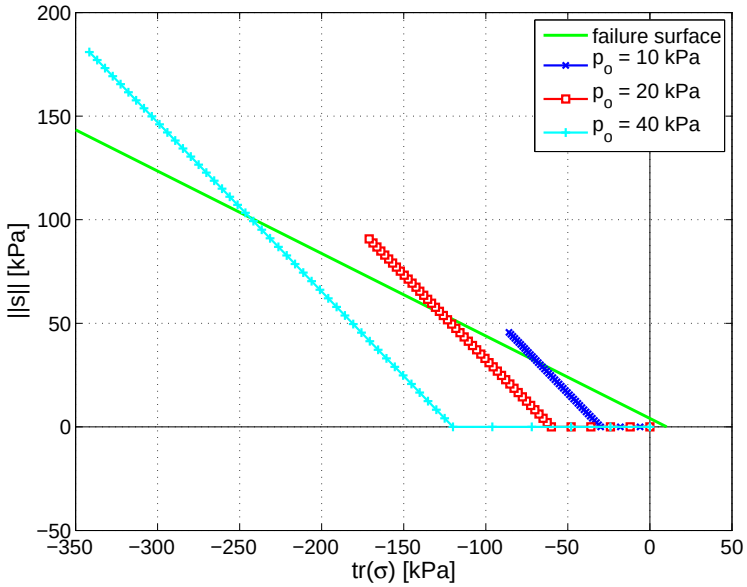

Figure 4.8: Stress paths for the conventional triaxial compression (CTC) test for the linear isotropic strain hardening case.

The stress and strain invariant plots of Figures 4.9 and 4.10 provide a more complete look at the plastic behavior of the soil element during the CTC test. The perfectly plastic behavior of the model for the cases without strain hardening is even more evident in Figure 4.9 than in Figure 4.7. After the elastic portion of the loading, the slopes of the curves all go to zero, indicating increases in shear and normal strain with no corresponding increases in shear or normal stress. For the cases with strain hardening, there is a change in slope at the end of the elastic range, however, here the slopes do not go to zero, instead they change according the the amount of strain hardening considered. The behavior displayed in these two figures validates that the OpenSees implementation of the Drucker–Prager model displays the intended post–yield behavior when the soil is brought to yield by an increase in normal stress.

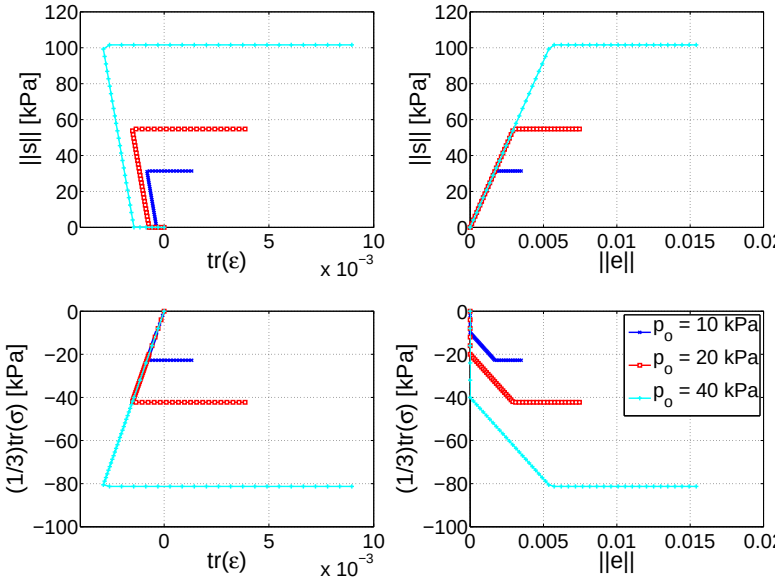

Figure 4.9: Stress–strain responses of a Drucker–Prager soil element model subjected to a conventional triaxial compression (CTC) stress path for the perfectly plastic case (no strain hardening).

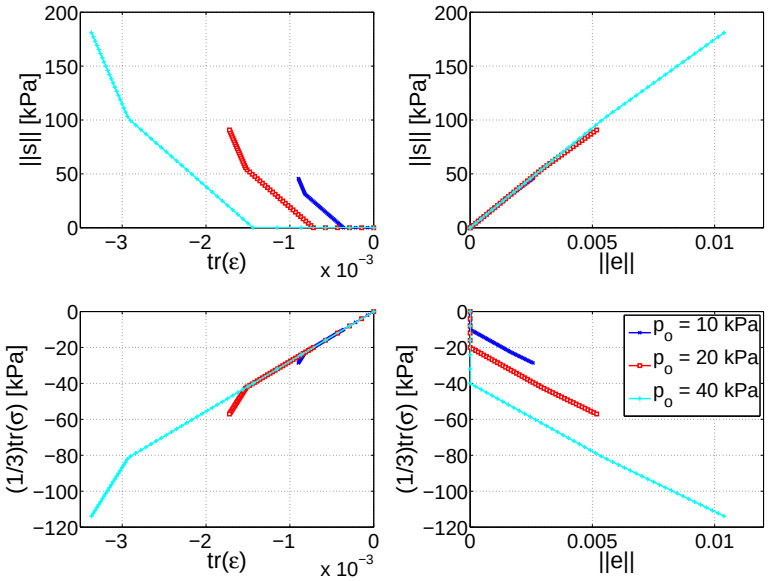

Figure 4.10: Stress–strain responses of the Drucker–Prager soil element model subjected to a conventional triaxial compression (CTC) stress path for the linear isotropic strain hardening case.

4.5.3 Simple Shear Test

In the simple shear (SS) test, as with the previously described CC and CTC tests, the soil element is first subject to hydrostatic stresses, slowly increased until $\sigma_1 = \sigma_2 = \sigma_3 = -p_o$. From this point, $\Delta I_1 = 0$, indicating that the stress path for this test lies entirely in the deviatoric plane through the initial hydrostatic stress state (Chen and Saleeb, 1994 [8]). In other words, the simple shear test brings the soil element to failure via the application of pure shear stresses.

In OpenSees, the SS stress path is implemented entirely under strain control. Figure 4.11 provides a visual representation of the single element SS test as analyzed by OpenSees. The initial hydrostatic state is induced in an identical manner to the previously described CC test. From this initial hydrostatic state, the nodes at the base of the element are held fixed while the upper nodes are displaced in the negative y–direction by equal increments. During this test, the upper nodes are not displaced in the x– or z–directions, resulting in an isochoric deformation. This type of deformation results in the desired state of pure shear stress (small strain only).

The simple shear test is run for three values of initial confining pressure, both with and

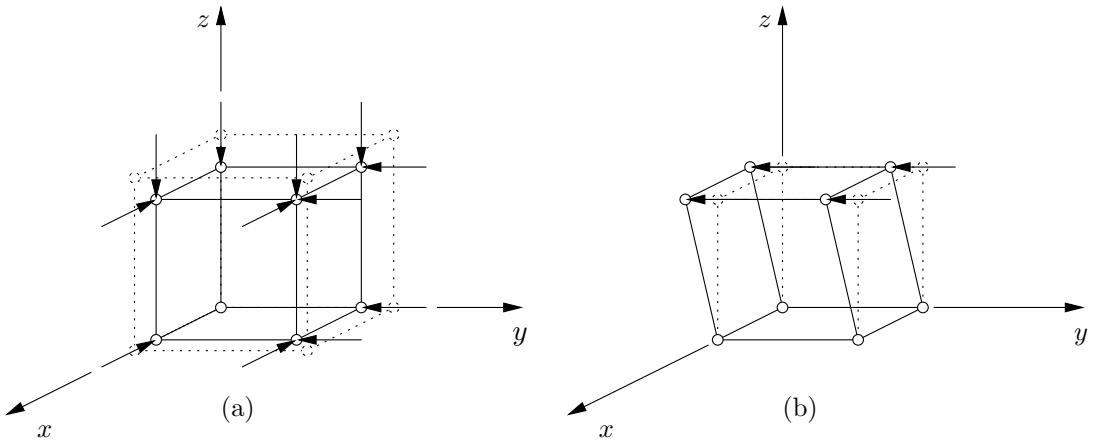

Figure 4.11: Schematic depiction of the SS test as performed in OpenSees. (a) During the application of the initial hydrostatic stress state, the free nodes are moved inwards. (b) To create a pure shear case, the top nodes are then moved laterally while the base nodes are held fixed.

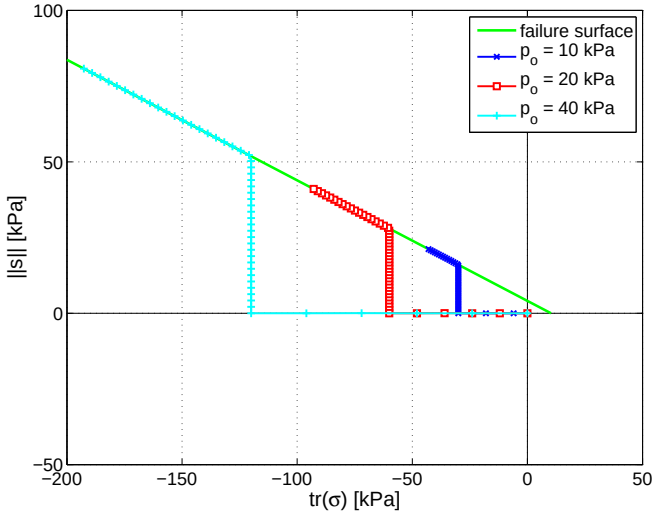

Figure 4.12: Stress paths for the simple shear (SS) test for the perfectly plastic case (no strain hardening).

without the inclusion of linear isotropic strain hardening. Figure 4.12 shows the stress paths for the three confining pressures on the meridian plane for the perfectly plastic cases, and Figure 4.13 shows the simulated stress–strain behavior during this test. In the elastic range,

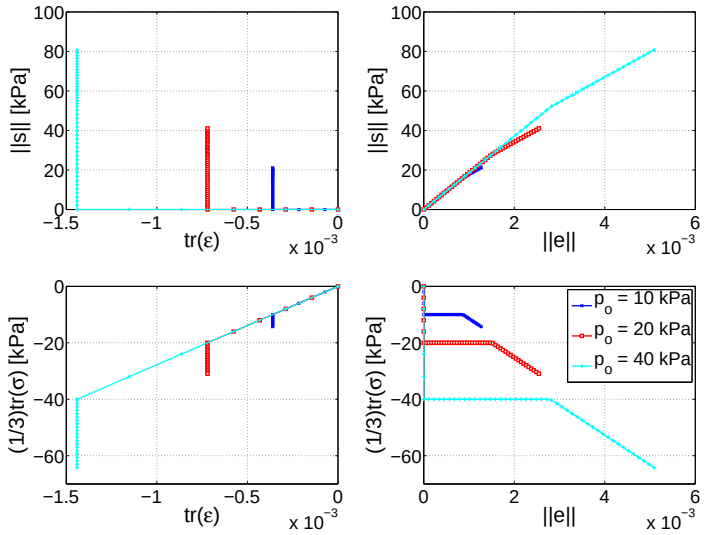

Figure 4.13: Stress–strain responses of the Drucker–Prager soil element model subjected to a simple shear (SS) stress path for the perfectly plastic case (no strain hardening).

the element only experiences an increase in deviatoric stress, the expected behavior. Once the soil element yields, the mean normal stress decreases (increased compression) and the deviatoric stress continues to increase with increasing deviatoric strain. However, there is no change in the total volumetric strain. The initial drop in volumetric strain, tr$\boldsymbol{\varepsilon}$, indicated in Figure 4.13 corresponds to the initial changes in hydrostatic pressure that take place during this test.

Figures 4.14 and 4.15 show the stress path and the stress–strain behavior, respectively, for the soil element which considers linear isotropic strain hardening. As with the CTC test, an unrealistically large value of $K = 100,000$ kPa is selected for the isotropic hardening coefficient for the sake of enhanced visualization. For these cases, the elastic behavior is unchanged; the stress path lies in the deviatoric plane from the initial hydrostatic state up until the initial yield point. Subsequent yielding under the inclusion of strain hardening allows for greater increases in deviatoric stress during the continued application of increasing deviatoric strains. This increase in deviatoric stresses corresponds to a less significant reduction in the mean normal stress as compared to the cases with no strain hardening. Additionally, the same failure surface expansion present in the CTC test results is observed.

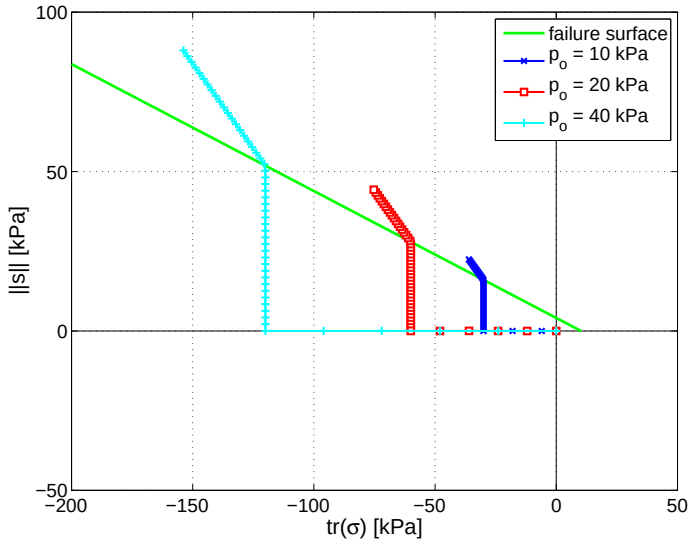

Figure 4.14: Stress paths for the simple shear (SS) test for the linear isotropic strain hardening case.

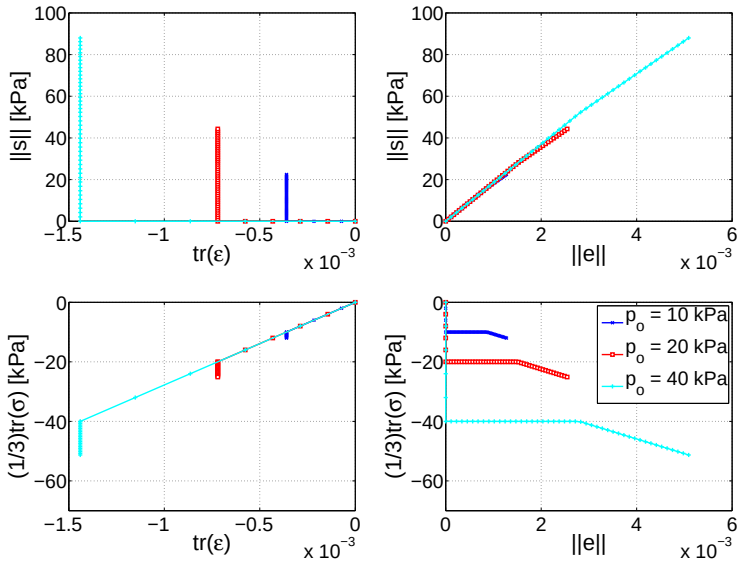

Figure 4.15: Stress–strain responses of the Drucker–Prager soil element model subjected to a simple shear (SS) stress path for the linear isotropic strain hardening case.

The results of the single element simple shear tests provide further validation that the Drucker–Prager material model reproduces the expected behaviors when subject to known stress/strain paths. When implemented in an element subject to pure shear, the material model is able to produce consistent results for all of the investigated cases.

4.5.4 Hydrostatic Extension Test

The final single element test performed in pursuit of validating the OpenSees implementation of the Drucker–Prager material model is a hydrostatic extension (HE) test. In this test, the soil element is subject to equally increasing principal stresses until failure is achieved. The resulting stress path follows the hydrostatic axis in the tensile direction, eventually reaching the tip of the cone depicted in Figure 4.1 (page 58).

To achieve the HE test in a single element model, the procedure is essentially the opposite of the hydrostatic compression phases of prior tests. From the same base model and boundary conditions, the free nodes are displaced outward in equal increments. This test is represented visually in Figure 4.16. The HE test is performed both to test the tensile behavior of the model and to evaluate the effectiveness of the tension–cutoff implementation.

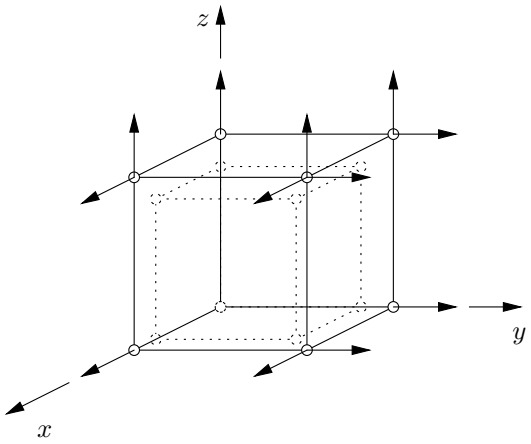

Figure 4.16: Schematic depiction of the HE test as performed in OpenSees. In this test, the free nodes are moved outwards in equal increments to create a case of hydrostatic tensile stress.

Due to the nature of this test, multiple confining pressures were not included in the results. However, the HE test is conducted for three values of the tension softening coefficient, δ. As shown in Figure 4.17, the intended stress path is returned by the model. Providing

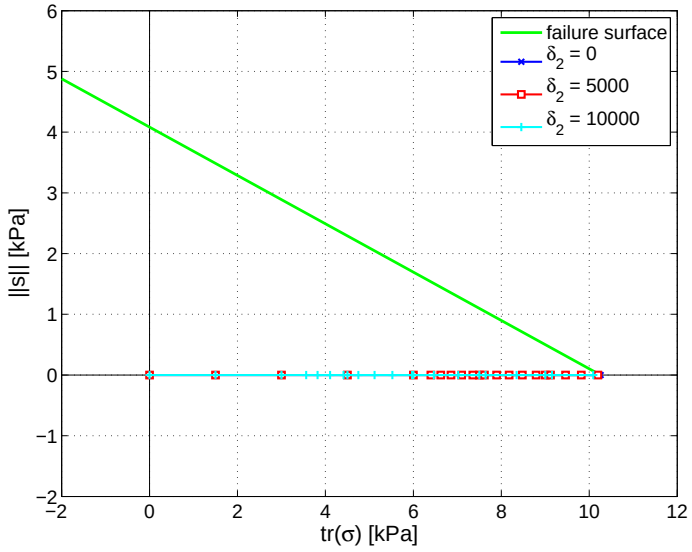

Figure 4.17: Stress paths for the hydrostatic extension (HE) test, shown on the meridian planes, for three values of the tension softening parameter, δ.

assurance that the Drucker–Prager material model can handle tensile stresses as well as compressive stresses. The stress and strain invariant plots of Figure 4.18 verify that the element develops no deviatoric strains nor stresses during the single element HE test. As is expected, only normal stresses and strains are experienced by the soil element. The effect of changes in the the magnitude of δ is evident in the lower left plot of Figure 4.18. When $\delta = 0$, the element displays perfectly plastic behavior after the tensile limit is reached, indicating that no softening occurs. The degree of softening increases with increasing values of δ, just as intended by the inclusion of the tension softening surface in the material model. All of the behavior displayed by the Drucker–Prager soil element in the HE test is consistent with expectations, thus providing further verification as to the correct implementation of the material model in OpenSees.

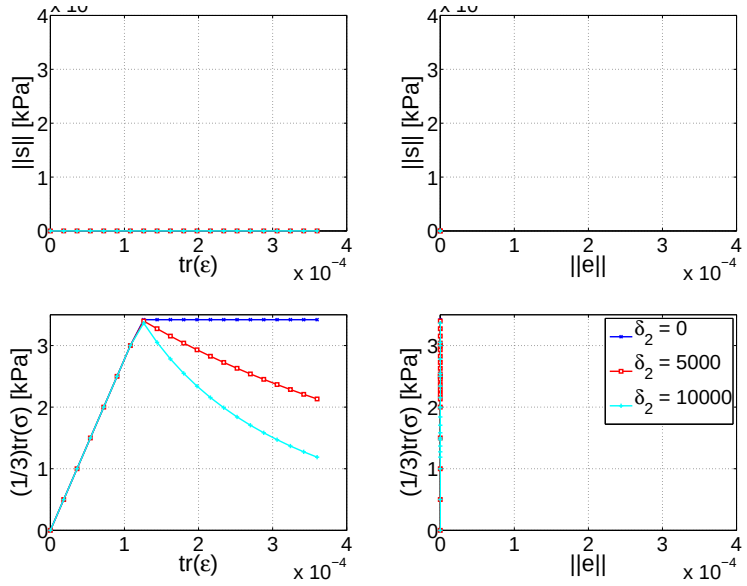

Figure 4.18: Stress–strain response of the Drucker–Prager soil element during the hydrostatic extension (HE) test for three values of the tension softening parameter, δ.

4.5.5 Multi–Element Plane–Strain Test

In the mechanical behavior tests described in Sections 4.5.1 through 4.5.4, the OpenSees implementation of the Drucker–Prager material model is tested with the use of a single

element. To assess the model in a somewhat broader context, a multi–element plane–strain test is conducted. A schematic of this test is shown in Figure 4.19. In this test, a distributed load is applied to a portion of the upper surface of a wall of soil material. The base of the model is held fixed against vertical displacements, the large planar surfaces of the model are held fixed against out–of–plane displacements (in the thickness direction) to create a plane–strain case. The symmetry condition alluded to in Figure 4.19 is applied by fixing displacements in the horizontal direction. The purpose of this plane–strain test is to evaluate the behavior of the Drucker–Prager material model in the context of a multi–element finite element model. Specifically, it is desirable to discern if the model shows a quadratic rate of asymptotic convergence, as is the expectation for this model.

The model used in the plane–strain test is three meters wide, three meters tall, and one meter thick. The soil elements are defined with the same parameters as the upper and lower soil layers in the lateral spreading model. These values are summarized in Table 4.2 (page 63). The finite element mesh used in this particular test has 576 elements (24–by–24–by–1), and all of the nodes are defined with three translational degrees of freedom. During the multi–element plane–strain test, a distributed load is applied over a one meter square. This load is increased linearly until the two nodes in the symmetry plane have undergone a 5 mm downward displacement.

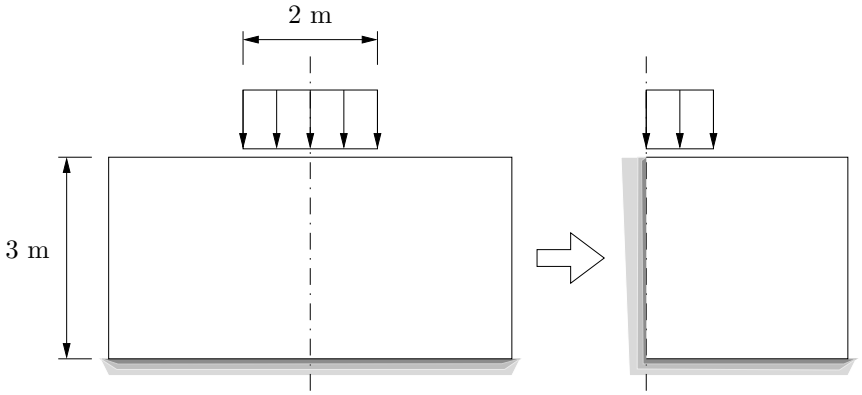

Figure 4.19: A representation of the load case modeled by the multi–element plane–strain test for the Drucker–Prager material model detailing the symmetry condition used.

The deformed shape of the mesh, magnified by a factor of ten, is shown in Figure 4.20 along with the distribution of the vertical stress component, σ_{yy}. As shown by this figure, the model is reacting in a manner consistent with initial expectations. Compressive stresses develop in the left hand portion of the model (the area beneath the load), while tensile stresses are generated in the right hand portion as those soil elements expand. The maximum compressive stress is depicted in blue in Figure 4.20. The absolute magnitudes of the compressive stress components decrease as the color progresses from blue towards red, while the maroon depicts the tensile stresses. Though the presented results are only for a relatively well–refined twenty–four element square mesh, this same test was conducted with differing numbers of elements. In all cases, the model displays predictable behavior as well as a quadratic rate of asymptotic convergence, further validating the OpenSees implementation of the Drucker–Prager material model described in Section 4.4.

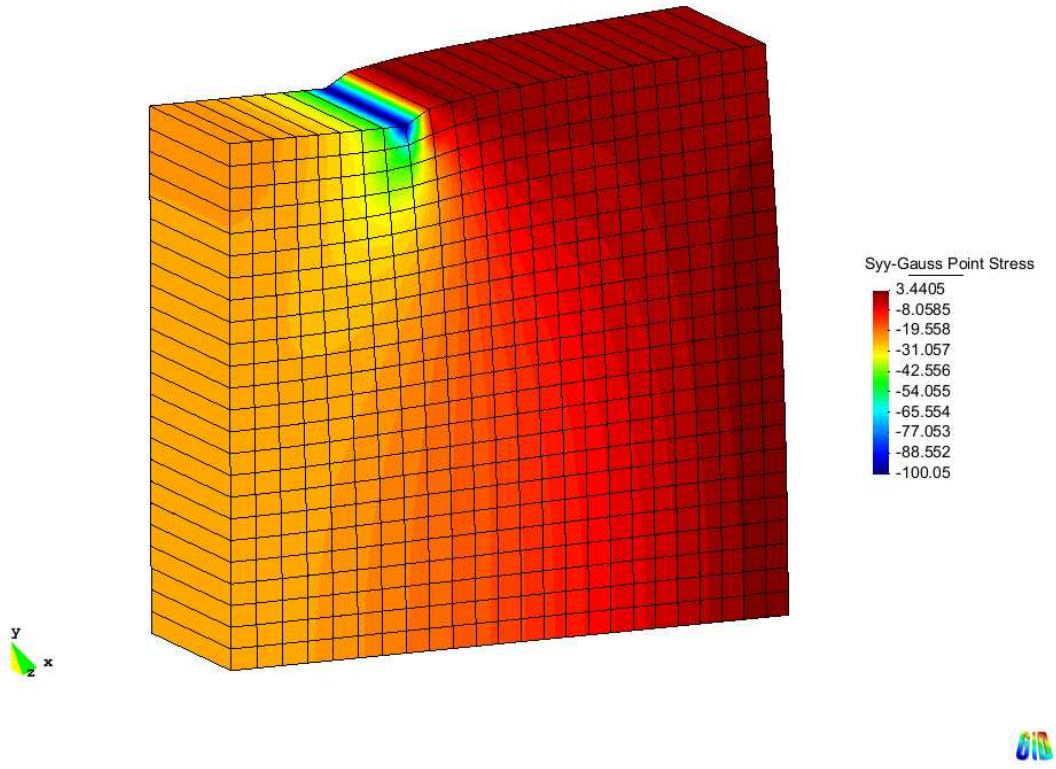

Figure 4.20: The deformed mesh for the plane–strain test along width the distribution of vertical stress in the soil elements (magnification factor = 10).

To further illustrate and verify the abilities of the Drucker–Prager material model, especially the various behaviors generated by the loading of the plane–strain model, the stress paths for several Gauss points along the top row of the mesh are plotted on the meridian plane in Figure 4.21. As shown, several elements are brought to yield in both tension and compression, while others remain in the elastic range during the test. Figure 4.21 provides further validation that the Drucker–Prager soil elements can be successfully implemented in a multi–element model, one which causes the elements to undergo a variety of stress paths.

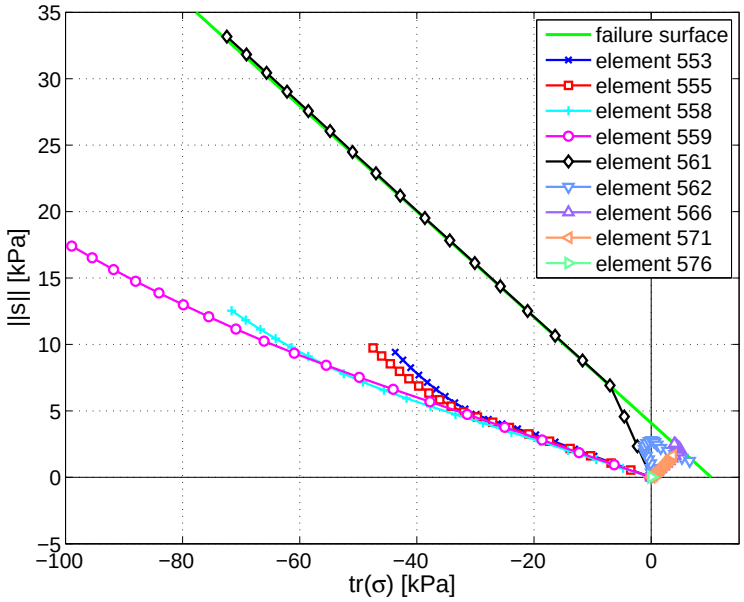

Figure 4.21: Stress paths for a selection of Gauss points along the top row of the plane–strain model.

Chapter 5

ANALYSIS AND EVALUATION OF SINGLE PILES IN LATERALLY SPREADING SOIL

5.1 Introduction

Piles embedded in laterally spreading cohesionless soils must be able to withstand large bending demands. The magnitude and location of the largest shear and moment demands are dependent upon many factors. Among these factors are the size and stiffness of the pile, the strength of the surrounding soil, the boundary and support conditions of the pile, the amount of lateral displacement that occurs, and the depth of the liquefied layer.

In this research, single piles in laterally spreading soil systems are analyzed by means of a three-dimensional finite element model (see Chapter 2). This model includes beam elements for the piles, solid elements for the soil, and beam-to-solid contact elements to define the interaction between the pile and the surrounding soil. Two separate pile head support conditions are considered in these simulations: (1) a fixed–head condition and, (2) a free–head condition. The fixed–head condition restricts the rotation of the pile head and is the most representative of an actual pile application, while the free–head cases allow the pile head to rotate freely and provide a means of comparison.

In all of the considered cases, the piles are subject to the imposed displacement profile discussed in Section 2.3 having a magnitude of one pile radius in the upper soil layer. This distance is sufficient to cause inelastic behavior in the elastoplastic pile and soil models, while remaining small enough to facilitate relatively short run–times in OpenSees. Run–time per case ranges from approximately 4 hours in linear elastic cases to 26 hours in elastoplastic cases, and varies for the three pile models. For all cases, the thickness of the liquefied layer is set at one pile diameter. The dimensional scheme discussed in Section 2.2 is utilized, resulting in a liquefied layer which is located ten pile diameters below the ground surface. Further information into the soil material parameters and element formulations is available

in Chapter 4. All of the specifics into the pile models are discussed in Chapter 3.

The behavior of a single pile in a laterally spreading soil system is evaluated through comparisons between the data returned from each of twenty-four cases run with the various pile, soil, and pile support condition combinations included in the study. The models are evaluated via the bending behavior of the piles, the stresses that develop in the soil, and the soil–pile interface forces developing in the contact elements, among other factors. The individual results of each modeling approach are examined and compared in order to provide further insight into the lateral spreading problem.

5.2 Summary of Considered Cases

Various combinations of pile and soil constitutive models are considered in this research. With respect to the piles, those combinations create two general sets of lateral spreading cases; those with elastic pile models and those with elastoplastic pile models. The pile models used in each set are discussed in detail in Chapter 3. Two soil constitutive models are used in combination with each set of pile models, an elastic soil model, and an elastoplastic soil model which employs a Drucker-Prager constitutive model. The details of each of these soil models are discussed in Sections 4.3 and 4.4, respectively. When combined with the variation in the pile head fixity, this set of parameter combinations yields a set of cases which can be divided into four main categories, designated as Series 1-4. The four test Series each consider the following six pile cases:

1. Free–head 2.5 m pile.

2. Free–head 1.3716 m pile.

3. Free–head 0.6096 m pile.

4. Fixed–head 2.5 m pile.

5. Fixed–head 1.3716 m pile.

6. Fixed–head 0.6096 m pile.

Table 5.1: Overview of the four considered test Series.

	Series 1	Series 2	Series 3	Series 4
Elastic Pile	X		X	
Elastic Soil	X	X		
Elastoplastic Pile		X		X
Elastoplastic Soil			X	X

This creates a total of twenty–four distinct analysis cases. Each test Series is differentiated by means of the type of pile and soil constitutive models that are employed in its respective set of six cases. The highlights of each Series are presented in the following discussion. A brief summary of the four test Series is presented in Table 5.1.

5.2.1 Series 1: Elastic Piles with Elastic Soil

Using linear elastic piles in the lateral spreading model allows for general behavioral mechanisms to be developed for the lateral spreading case. The elastic pile embedded in linear elastic soil models are the simplest cases that are evaluated using the three-dimensional lateral spreading model. These cases are computationally cheap when compared to the other cases (run–time per case approximately 4 hours), however, the data returned by these models is not, in itself, indicative of the type of behavior that would occur in an actual lateral spreading event. Instead of offering direct insights into pile behavior, the fully elastic cases provide a benchmark for comparison and evaluation of more computationally intensive models. As is the case for each of the four main categories of soil–pile combinations considered, six elastic pile in elastic soil cases are analyzed, one for each pile and boundary condition combination.

5.2.2 Series 2: Elastoplastic Piles with Elastic Soil

The use of fiber elements to create elastoplastic pile models allows for the examination of the interaction between the soil and the pile during a lateral spreading event in a more realistic

fashion than that which is returned by elastic pile models. When using elastoplastic piles, the piles are able to yield and develop plastic hinges under the influence of the imposed displacement profile. This changes the way in which the soil and pile interact in the model, often in dramatic fashion.

The series of cases which consider elastoplastic piles in elastic soil are included in this research as an intermediate set of cases through which comparisons can be drawn between the entirely linear elastic cases (Series 1) and the entirely elastoplastic series of cases (Series 4). Additionally, this series allows for the effects of plastic behavior in the piles to be examined in an isolated fashion.

5.2.3 Series 3: Elastic Piles with Elastoplastic Soil

In addition to the entirely linear elastic models, the same spectrum of cases are run for elastic piles embedded in elastoplastic soil elements. These six cases offer a direct means of evaluation for the effects of yielding in the soil on the behavior of the pile in the lateral spreading case. Leaving the pile elastic creates a situation in which the only differences between these cases and the entirely elastic cases must be due to the plastic behavior of the soil, allowing any mechanisms to be pinpointed.

Additionally, the elastic pile in elastoplastic soil series allows for the extraction of $p-y$ curves at various depths within the soil system, providing a means of comparison for the results of the three dimensional lateral spreading model with other, more commonly used models for the lateral analysis of piles. The $p-y$ curves are determined from the resulting contact forces applied to each pile node and the displacement of the pile relative to the soil at each of these positions. Further discussion on $p-y$ curves will be given in Chapter 6.

5.2.4 Series 4: Elastoplastic Piles in Elastoplastic Soil

The fully elastoplastic cases offer the most realistic glimpse into the behavior of the lateral spreading problem, though at the highest computational cost (run–times approximately 24–26 hours). This set of cases enables observations to be made into the behaviors that develop when both the piles and the soil yield and display plastic behavior. Additionally, it is of

interest to evaluate if the results found in the fully elastoplastic series can be successfully reproduced by using the $p-y$ method with elastoplastic pile models and the $p-y$ curves extracted from the elastic pile with elastoplastic soil series of cases.

5.3 General Behavior of Piles in Laterally Spreading Soil

The behavior of single piles embedded in laterally spreading soil systems is determined by the complex interaction of many factors. In order to evaluate the various mechanisms that contribute to the overall behavior of the pile, twenty-four cases with various combinations of parameters are considered and compared. Though no two piles will act in the exact same manner, there is a general pattern of behavior that is observed. The key results, those that are deemed most indicative of the pile behavior as a whole and therefore used as comparative measures, include the magnitudes of the maximum moment and shear force demands in the pile and the locations of these extreme values. Also of interest are the trends that develop in how the extreme moments in each layer evolve over time, and the way in which the lateral spreading soil deformation profile manifests itself as a load on the pile.

5.3.1 General Behavioral Mechanisms

Many insights into the behavior of the laterally spreading soil–pile system are obtained from the results of the twenty-four test cases. Though there is variation in the details between each case, a general pattern of behavior can be observed throughout the results. In all of the cases, the interaction between the soil and the pile, governed by their respective material properties, defines the resulting behavior of the system. As the upper layer of soil begins to displace laterally with respect to the immobile lower layer, the entire pile provides resistance to this motion as the upper portion is pushed along with the flow of soil. This behavior is illustrated in Figure 5.1, which shows the the distribution of horizontal normal stress (in the direction of motion) in the soil elements, as well as the deformed shape of the system, for the Series 1 free–head case for the 0.6096 m pile.

The entirely linear elastic case is selected to illustrate the lateral stress distribution in the soil because it allows truly large stresses to develop. The locations of the largest tensile and compressive lateral stress in the elastic soil elements identify where initial yielding is

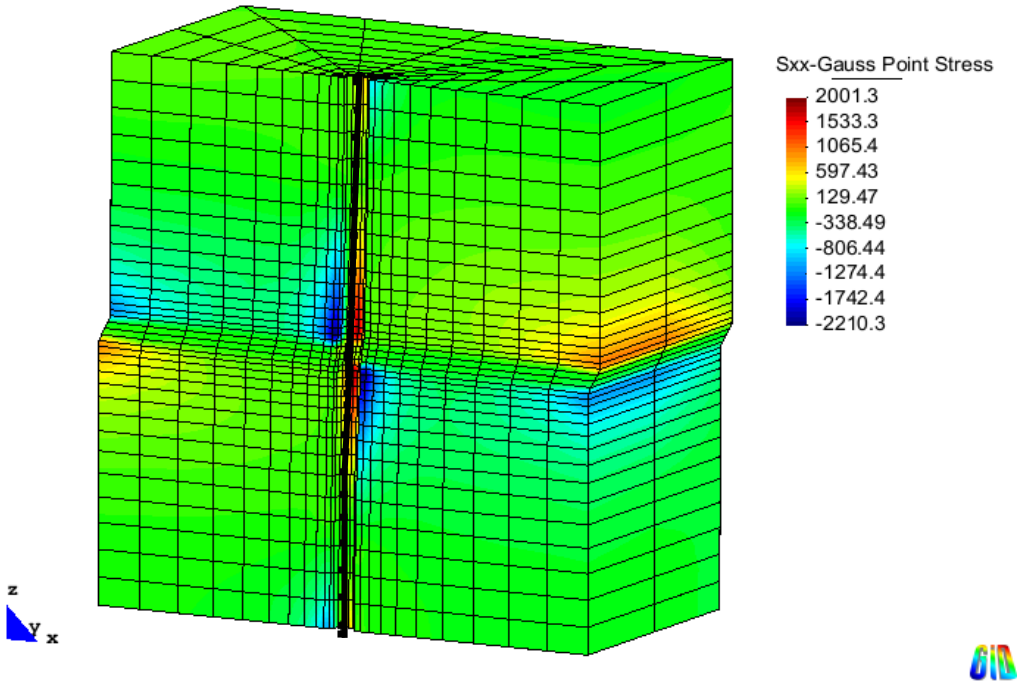

Figure 5.1: Deformed shape and distribution of lateral stress in soil elements for the Series 1 free–head case for the 0.6096 m pile. Magnitudes of horizontal (normal) stress are given in kPa.

likely to occur in the soil in both the elastoplastic soil models and in an actual soil system. Were the elements assigned elastoplastic behavior, the yielding that may occur would likely obscure the marked differences in stresses that are able to develop in the linear elastic case, leading to an image in which it would become difficult to differentiate between the stresses in adjacent locations.

From the lateral stresses developed in the linear elastic soil elements in the vicinity of the pile, it can be clearly seen that the imposed displacement profile puts the pile in bending. In the lower solid layer, the distribution of compressive stresses shows that the pile pushes back into the soil at its base while it is pushed into the soil at the interface with the liquefied soil layer. The opposite is observed in the upper soil layer, where the pile resists the ground motion at the interface with the liquefied layer and is pushed into the soil at the pile head.

Additionally, at each location of large compressive stress on the leading and trailing faces of the pile, there is a corresponding zone of tensile stress in the soil. These tensile regions signify where the soil elements are being pulled apart by either the passive or active passage of the pile through the soil. While the results of Figure 5.1 are for the 0.6096 m pile, this same pattern of lateral stress is present in all of the lateral spreading models.

In addition to the lateral stress near the pile, it is also of interest to observe the distribution of lateral stresses in the remainder of the soil system. The lateral stresses in the liquefied layer remain relatively small during the simulated lateral spreading event, however, the imposed ground motion causes large compressive and tensile stresses to develop in the solid soil layers at the boundaries of the model. These zones of increased stress are higher near the symmetry plane. Though these distributions are most certainly at least partially due to the boundary and loading conditions imposed upon the model, these results suggest that the pile is able to influence a far wider area than just its immediate vicinity during a lateral spreading event.

Figure 5.2 shows a series of plots which detail exactly how the lateral spreading ground motion affects the embedded pile. This figure presents results obtained from the same 0.6096 m pile case as the lateral stress distribution shown in Figure 5.1, the entirely linear elastic, free pile head case. This series of summary plots illustrates the general pattern of shear force and bending moment demands that develop in a pile during a lateral spreading event, as well as the deflected shape of the pile. All of the piles display distributions of bending demands which are similar in form to the general shapes presented here.

The maximum shear force demand occurs at the center of the liquefied layer (depicted as the shaded region in Figure 5.2), where the differential motions of the two solid layers are felt most strongly by the pile, and minimal resistance is provided by the liquefied soil. It can be expected that in any lateral spreading event, the largest shear force demand will occur at, or very near, this location. There are also extreme values of shear in each of the two solid layers, located approximately two-thirds of the total layer thickness away from the interface with the liquefied layer. The extreme shear demand in the lower layer is greater due to the increased effective stress in the soil with depth.

The locations of minimum moment occur at the center of the liquefied layer, where

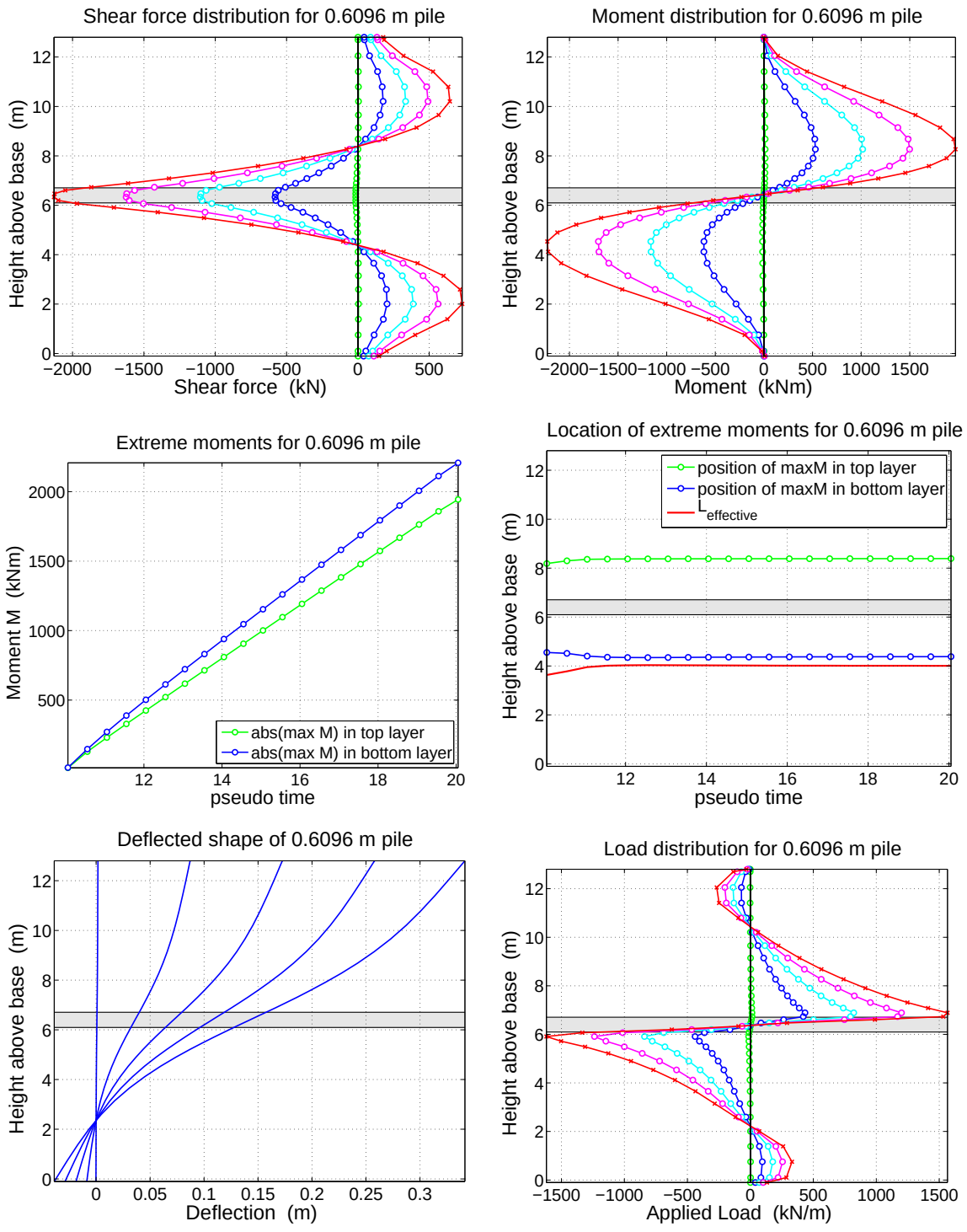

Figure 5.2: Pile summary plots for the 0.6096 m pile. Elastic pile and elastic soil, free–head case. The liquefied layer is the shaded region.

there is zero moment, and due to the boundary condition of this model, at each end of the pile, where the moment is also zero. The extreme moments in the pile correspond to the locations of zero shear force, with one falling in each of the solid soil layers. The absolute maximum moment occurs in the lower solid layer. As with the extreme shear force demand in that layer, the extreme moment demand here is larger than the extreme value in the upper layer due to the increased overburden pressure with depth. The locations of the extreme moments in each layer tend to stay relatively constant in this entirely linear elastic model. The distance between these locations defines an effective length, L_{eff}, for the pile, as shown in Figure 5.3. The effective length is a parameter signifying, in part, the influence of the liquefied layer on the pile. The effective length of pile is a convenient parameter to utilize in simplified analyses of the lateral spreading problem, as well as a useful parameter for comparing the results for the various pile sizes.

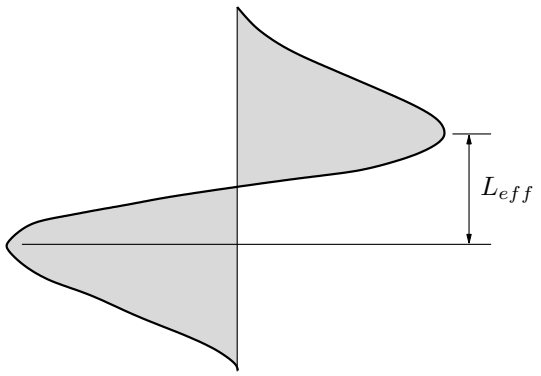

Figure 5.3: The effective length, L_{eff}, is the distance between the extreme moments in each solid soil layer, as shown in this moment diagram.

In addition to the plots related to the deformation and bending demands in the pile, Figure 5.2 also shows the distribution of load imposed upon the pile by the lateral flow of the upper soil layer. This plot of the load distribution on the pile is determined from the slope of the shear diagram using the familiar relation

$$\frac{dV}{dx} = -w(x) \tag{5.1}$$

in which $w(x)$ is the distributed load and V is the shear force. The plot of the load

distribution provides a insight into how the displacement of the surrounding soil manifests as load acting upon the pile and corresponds well to the distribution of lateral stress in the soil as shown in Figure 5.1. The magnitude and shape of this load profile varies from pile to pile and also shows a dependence on the constitutive models used to represent the pile and the soil, though the shape presented in Figure 5.2 is indicative of the general shape resulting from each case.

It is also observed that the liquefied layer of soil affects the behavior of the solid soil layers. The degree of this influence depends upon a few factors, including the stiffness of the pile and the constitutive model used for the soil. Additionally, the degree of influence of the liquefied layer on the soil near its boundaries is most significant in the vicinity of the pile, becoming less apparent as distance from the pile increases.

The cases with elastoplastic soils exhibited an increased amount of interaction between the solid and liquefied soil layers, with the stronger solid layers being pushed into the weaker liquefied layer by the pile. Figure 5.4 shows the pile pushing the solid (orange) soil layers into the liquefied (white) layer for the Series 4 case for the 0.6096 m pile. In this figure, the motion of the upper layer is to the right. As shown in Figure 5.4, the push–out of the solid soil occurs on either side of the pile in the areas which, as indicated by Figure 5.1, the pile is cutting into the soil. In addition to the push–out observed on the leading edges of the pile, there is significant gapping taking place on the trailing edges of the pile, leading to the evident mesh distortion.

The push–out behavior displayed during the lateral spreading motion lessens the amount of lateral resistance that can be provided by the soil in the area surrounding the liquefied layer. The solid soil can be pushed into the adjacent weaker layer more easily than it can be pushed into the adjacent solid soil elements or flow around the pile, effectively reducing the strength of the soil surrounding the liquefied layer. This reduction in strength can significantly alter the behavior of the pile, causing increased curvature demands and increasing the potential for the formation of plastic hinges. Additionally, this reduction in soil strength results in a smaller effective length for the pile, which, as shown in Section 5.5.3 results in an increased moment and curvature demand on the pile and corresponding increase in the potential for pile failure due to the lateral spreading event.

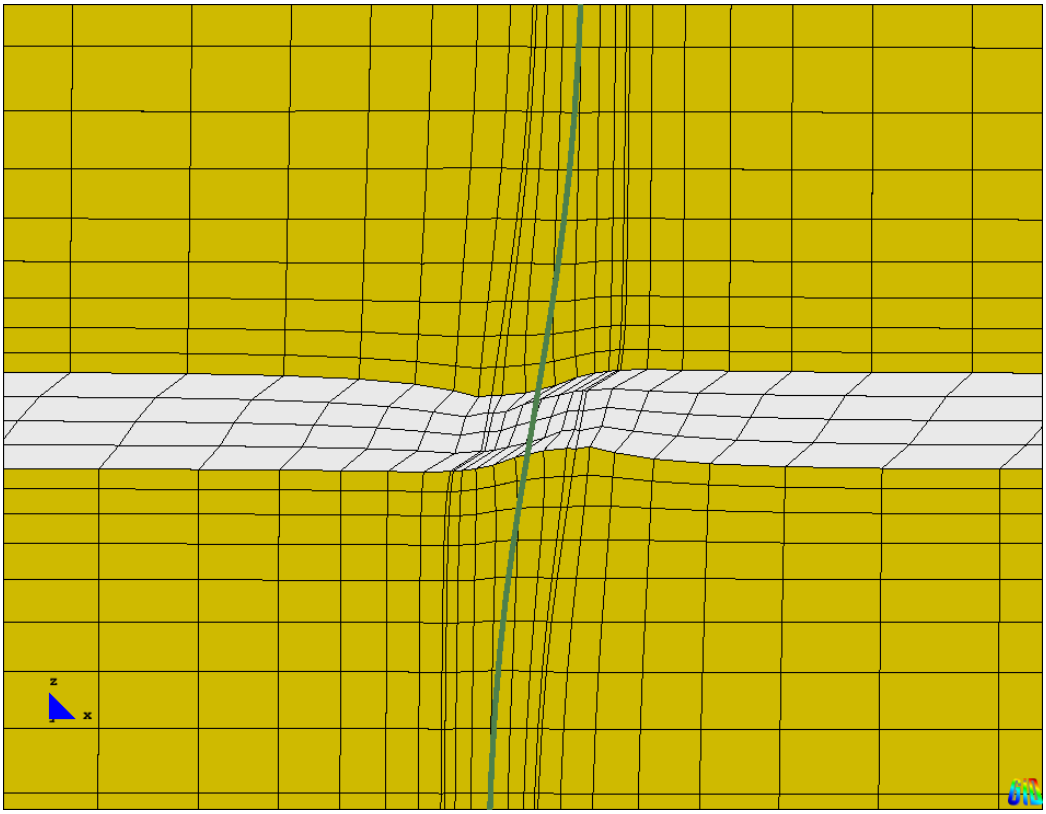

Figure 5.4: Soil deformation pattern in the vicinity of the 0.6096 m pile in the Series 4 case highlighting the push–out of the solid layers into the liquefied layer.

5.4 Summary of Results from Lateral Spreading Simulations

A small parametric study consisting of twenty-four distinct cases is conducted using the three-dimensional lateral spreading model with the pile and soil elements discussed in Chapters 3 and 4. There are three pile designs included in the study, each with elastic and elastoplastic constitutive formulations. These piles are given two separate boundary conditions: a fixed pile head condition and a free pile head condition. As for the soil, there are two constitutive models incorporated into the study, one linear elastic and the other an elastoplastic Drucker-Prager model. In all of the simulations the liquefied layer is assigned a thickness of one pile diameter and this layer is centered between two ten-pile-diameter thick solid soil layers.

Table 5.2: Summary of lateral spreading cases for the 2.5 m pile at $\Delta = 1.25$ m.

Pile-Soil Type	$\max V$ (kN)	$\max M$ (kNm)	$\max \phi$ (m^{-1})	$\max U$ (m)	L_{eff} (m)
Series 1: Free	46100	235500	0.0012	1.47	17.62
Series 2: Free	40600	186600	0.0021	1.43	16.19
Series 3: Free	54000	300500	0.0015	1.57	16.14
Series 4: Free	48800	227200	0.0036	1.51	15.11
Series 1: Fixed	53500	389500	0.0020	1.27	35.51
Series 2: Fixed	42600	195500	0.0023	1.30	18.32
Series 3: Fixed	63200	393500	0.0020	1.30	18.77
Series 4: Fixed	50900	230100	0.0039	1.33	15.96

The results of all twenty-four lateral spreading cases are summarized in Tables 5.2, 5.3, and 5.4 for the 2.5 m, 1.3716 m, and 0.626 m piles, respectively. These tables list the maximum values of shear force, $\max V$, moment, $\max M$, curvature, $\max \phi$, and displacement, $\max U$, for the pile as well as the effective length, L_{eff}. The data in these tables is separated based upon the particular parameters and constitutive models used in each of four Series, as well as by the fixity of the pile head in each simulation. The specifics of each of the four Series are detailed in Section 5.2.

From the results presented in Tables 5.2, 5.3, and 5.4, a few behavioral trends are observed. The stiffness of the pile, or more importantly the ratio of the pile stiffness to the lateral stiffness of the soil, plays a significant role in defining the interaction between the piles and the soil. This is manifested not only in the observation that increased pile capacity leads to increased bending demands, but also in the way in which the dependent variables from each Series relate to those from the other Series for each respective pile. The fixity of the pile head also affects the resultant behavior of the soil–pile system during the lateral spreading event, though certain trends are consistent in both the free–head and fixed–head cases. The observations and analyses related to these various factors are discussed in further detail in the subsequent sections of this chapter.

Table 5.3: Summary of lateral spreading cases for the 1.3716 m pile at $\Delta = 0.6858$ m.

Pile-Soil Type	$\max V$ (kN)	$\max M$ (kNm)	$\max \phi$ (m^{-1})	$\max U$ (m)	L_{eff} (m)
Series 1: Free	10600	24300	0.0049	0.76	8.12
Series 2: Free	5070	6460	0.0191	0.73	5.17
Series 3: Free	12000	30600	0.0061	0.80	7.54
Series 4: Free	4970	6575	0.1046	0.69	4.74
Series 1: Fixed	10800	24900	0.0050	0.71	8.47
Series 2: Fixed	5076	6467	0.0190	0.71	5.16
Series 3: Fixed	12500	31000	0.0062	0.73	7.65
Series 4: Fixed	4969	6574	0.1045	0.69	4.74

In addition to the pile–to–soil stiffness ratio and the pile head fixity, it is observed that the degree of plasticity incorporated into the models also plays a significant role in the resultant behavior of the soil–pile system. Comparison between the Series 1 and 2 cases gives a feeling for what happens when the piles yield. Similarly, comparison between the Series 1 and 3 data allows the effects of soil plasticity to be analyzed. The fully elastoplastic

Table 5.4: Summary of lateral spreading cases for the 0.6096 m pile at $\Delta = 0.3048$ m.

Pile-Soil Type	$\max V$ (kN)	$\max M$ (kNm)	$\max \phi$ (m^{-1})	$\max U$ (m)	L_{eff} (m)
Series 1: Free	2130	2228	0.0095	0.34	3.63
Series 2: Free	1200	804	0.0248	0.32	2.66
Series 3: Free	2027	2569	0.0109	0.38	3.62
Series 4: Free	1258	981	0.0443	0.31	2.86
Series 1: Fixed	2196	2293	0.0097	0.32	3.83
Series 2: Fixed	1198	805	0.0249	0.31	2.65
Series 3: Fixed	2200	2592	0.0110	0.33	3.74
Series 4: Fixed	1258	981	0.0445	0.31	2.86

cases of Series 4 offer observations into the behavior of the soil–pile system when elements in each medium display plastic behavior. The discussion provided in Section 5.5 details the observations made with respect to the constitutive models used in each case and how they affect the behavior of the system during the simulated lateral spreading event.

5.4.1 The Effects of Pile Stiffness on the Soil-Pile System

There are three pile sizes considered in this research, a 2.5 m diameter pile, a 1.3716 m diameter pile, and a 0.626 m diameter pile. As the size of the pile increases, so does the bending stiffness of the pile. The pile's bending stiffness is an important factor in defining how a pile reacts to a lateral spreading event. More important, perhaps, is the ratio of the pile's bending stiffness to the lateral stiffness provided by the soil. For large pile–to–soil stiffness ratios, the behavior of the soil–pile system during a lateral spreading event is governed primarily by the pile. Conversely, as this ratio becomes smaller, the influence of the soil becomes more apparent in the overall behavior of the system. The piles can no longer cut easily into the soil, instead the soil is able to resist the piles, increasing the curvature demand and altering the locations of the maximum moments.

The load distribution plots of Figure 5.5, which show the loading applied to the pile by the imposed lateral spreading displacement for the Series 1 free pile head cases for the 0.626 m and 2.5 m piles, typify the differences between small and large pile–to–soil stiffness ratios. It is important to note that the load distributions shown in Figure 5.5 are the loads that are felt by the piles over their respective lengths. These loads are the result of both the soil pushing against the pile in the upper layer and the pile pushing against the soil in the lower layer. Were the pile–to–soil stiffness ratios for each model set to be equal, the resulting load distributions would be identical despite the increased size of the larger pile.

For the 0.6096 m pile, which has a relatively small stiffness ratio, the magnitude of the load applied by the surrounding soil is much smaller than it is for the 2.5 m pile. This indicates that the stiffer 2.5 m pile is cutting further into the soil, activating more resistance from the surrounding soil elements. This is confirmed by the displaced shapes of each pile provided in Figure 5.6, which shows the resultant deflected shapes for the two piles for both

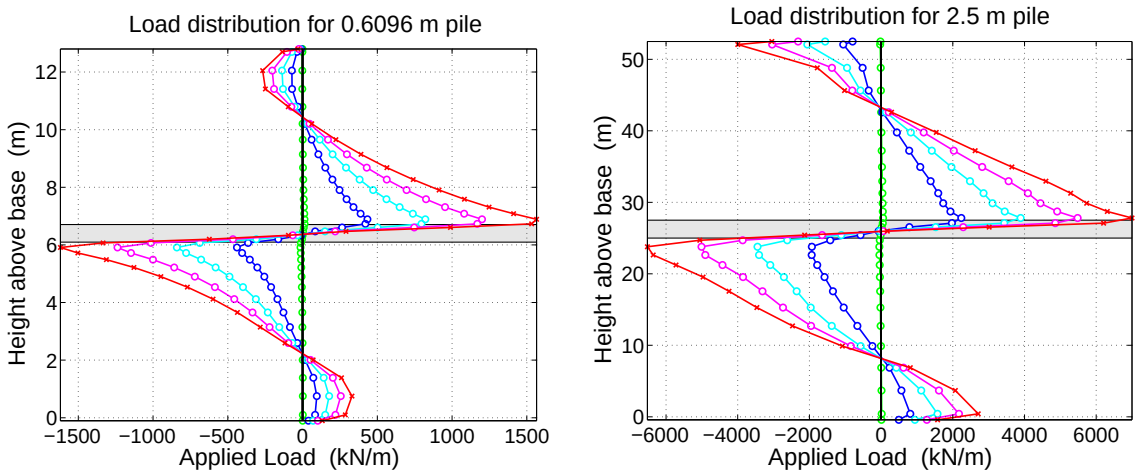

Figure 5.5: Load distributions resulting from the lateral spreading ground motion for the free–head Series 1 cases for the 0.626 m and 2.5 m piles, respectively. The red lines represent the final time step in the analysis.

the free–head Series 1 and Series 2 (elastoplastic pile) cases. In the entirely linear elastic Series 1 case shown in Figure 5.6(b), the 2.5 m pile remains almost straight during the deformation due to its high stiffness ratio.

The corresponding case for the 0.6096 m pile shown in Figure 5.6(a) displays visible curvature, indicating that the soil imposes larger curvature and bending demands on the pile with the smaller pile–to–soil stiffness ratio. The elastoplastic pile in elastic soil Series 2 cases of Figures 5.6(c) and 5.6(d) accentuate this observation. Even with elastoplastic pile elements creating the potential for plastic hinge formation, the displaced shape of the stiffer pile remains essentially straight and is much further from the imposed displacement profile than the softer pile, providing verification that this trend is not isolated to the entirely elastic cases.

The effects of the pile–to–soil stiffness ratio can also be seen in the locations of the maximum moments for each of the piles. As depicted in Figure 5.2 for the 0.6096 m pile, the maximum moments occur somewhat beyond the extents of the liquefied layer. The ratio of the effective length of the pile, which is the distance between the maximum moments, to pile diameter decreases as the stiffness ratio decreases. This normalized comparison

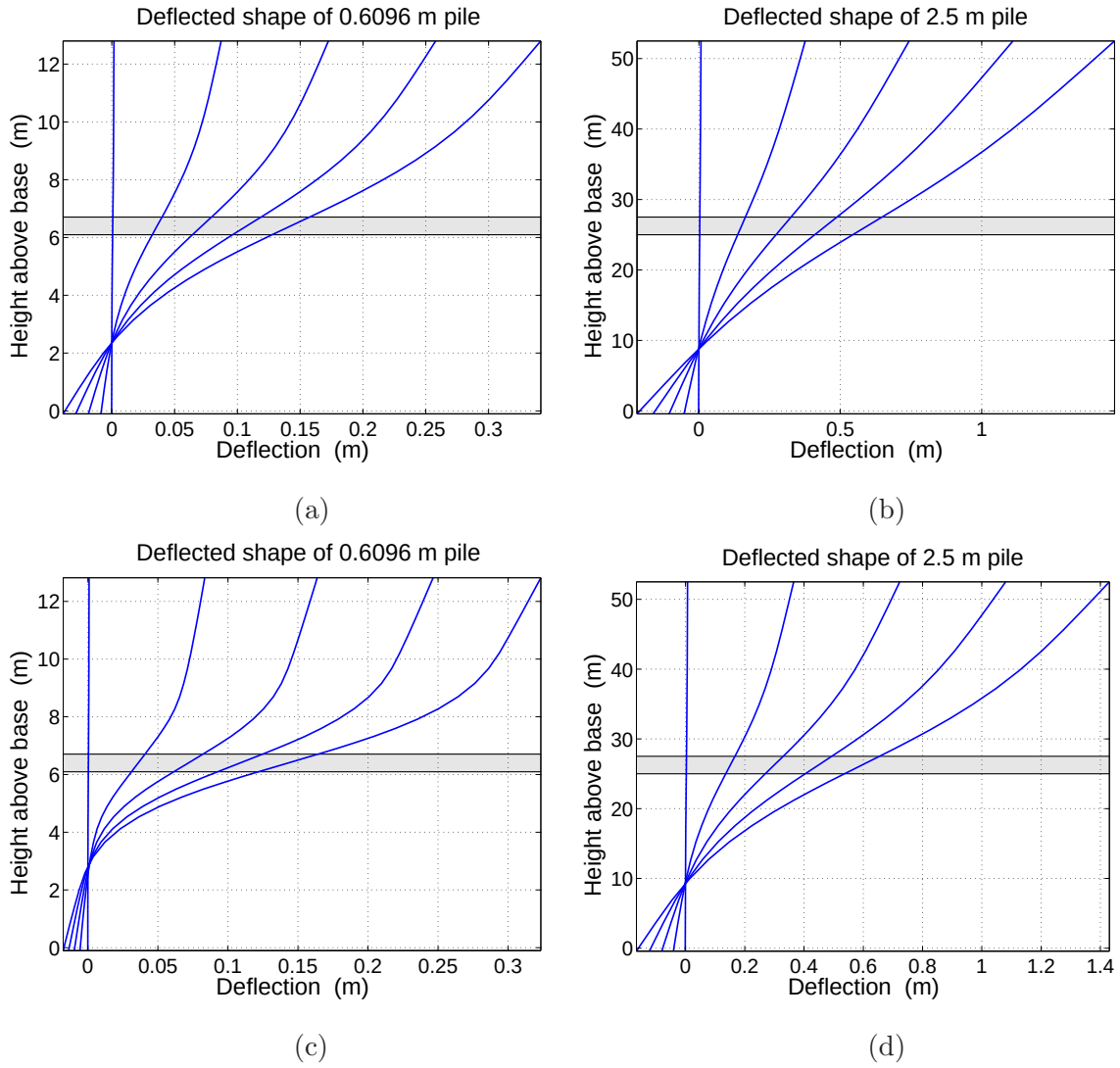

Figure 5.6: Deflected shapes of the free–head Series 1 cases for the 0.626 m and 2.5 m piles, (a) and (b), as well as the free–head Series 2 cases for the same piles, (c) and (d). The evolution of the deflected shapes with increasing soil displacement are shown.

indicates that the maximum moments become closer together as the pile–to–soil stiffness ratio decreases, thus creating a larger curvature demand and a proportionally larger moment and shear demand in the pile.

The larger the ratio of a pile's bending stiffness to the lateral stiffness of the soil in which it is embedded, the more the pile controls the overall behavior of the laterally spreading

soil–pile system. Larger, stiffer, piles are better able to cut into the soil during the lateral spreading event. As the pile pushes further into the soil, this leads to an increased potential for yielding in the soil. Additionally, the larger the stiffness ratio becomes, the larger the potential for push–out of the solid soils into weaker adjacent layers becomes.

This push–out can occur at the interface with the liquefied layer, similarly to what is displayed in Figure 5.4, and as shown in Figure 5.7, the soil can be pushed out above the ground surface. Figure 5.7 shows the ground surface for the Series 4 free–head case for the 2.5 m pile with a magnification factor of one. Similar push–out behavior is not present at the ground surface for either of the two softer piles, while the push–out into the liquefied layer is present for all three piles, the degree of push–out increases with increasing stiffness ratio. As more solid soil is pushed into the adjacent layers, the soil becomes less able to resist the motion of the pile in those areas, increasing the pile deflections and the potential for failure of the pile head connection during a lateral spreading event.

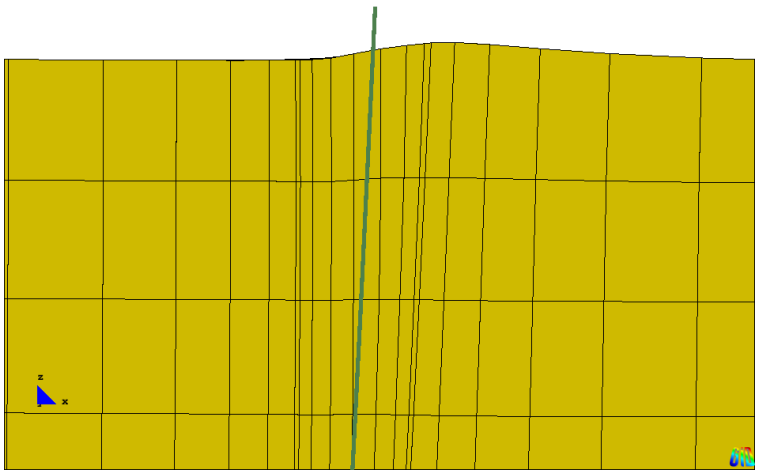

Figure 5.7: The push–out of soil elements at the ground surface for the 2.5 m pile, Series 4 free–head model (magnification factor = 1).

5.4.2 The Effects of Pile Head Fixity

The parametric study conducted to evaluate the lateral spreading problem includes two pile head boundary conditions. The fixed–head condition simulates a rigid pile cap or other structure affixed to the top of the pile, preventing the pile head from rotating. The free–head cases represent the opposite end of the spectrum, piles which are not subject to significant rotational resistance at the pile head connection. In actual applications, the support or connection at the pile head will likely fall somewhere between these two extremes, though the condition is often closer to the fixed–head piles than not. In all simulations the pile is left free to rotate at its base, approximating the condition found at the bottom of actual pile foundations.

For all three piles, the inclusion of a fixed pile head into the lateral spreading model results in maximum moment and shear force demands that are greater than, or approximately equal to, the demands resulting from the free–head cases. The magnitude of the difference between these extreme values is related to the pile–to–soil stiffness ratio. For the 2.5 m pile, which has a large stiffness ratio, the relative difference between the maximum demands for the fixed–head and free–head piles are significantly larger for all analysis Series. For the other two piles, which have relatively smaller pile–to–soil stiffness ratios, the differences are less significant. Another effect of the fixed–head condition is the tendency for the extreme moment in the upper layer to increase as compared to the value resulting from the free–head cases. The addition of in–plane rotational fixity at the pile head increases the amount of curvature in the pile in this layer, thus increasing the magnitude of the resulting extreme moment.

When the stiffness ratio is large, the free–head cases show that the pile tends to deform only slightly, able to essentially remain straight during the lateral spreading event. For the pile to be fixed against rotation at the pile head, a significant curvature demand must be imposed near the top of the pile. This increased curvature demand results in an increased maximum moment. Additionally, for larger stiffness ratios, the inclusion of a fixed pile head not only increases the extreme moment in the upper solid layer of soil, it shifts the absolute maximum moment from the lower soil layer, where it was located in the free–head cases, to

the upper soil layer. This is illustrated in the moment distribution for the 2.5 m pile Series 1 case shown in Figure 5.8. A corresponding shift is not present for smaller stiffness ratios, as shown in the moment distribution for the 1.3716 m pile Series 1 case of Figure 5.8, where the soil in the lower solid layer imposes a larger curvature demand on the pile than does the fixed–head boundary.

The maximum moment in the upper layer is significantly larger than that in the lower layer for the 2.5 m pile, where for the 1.3716 m pile, the extreme moment in the lower layer is slightly larger than that in the upper layer. The deflected shapes of each pile explain this

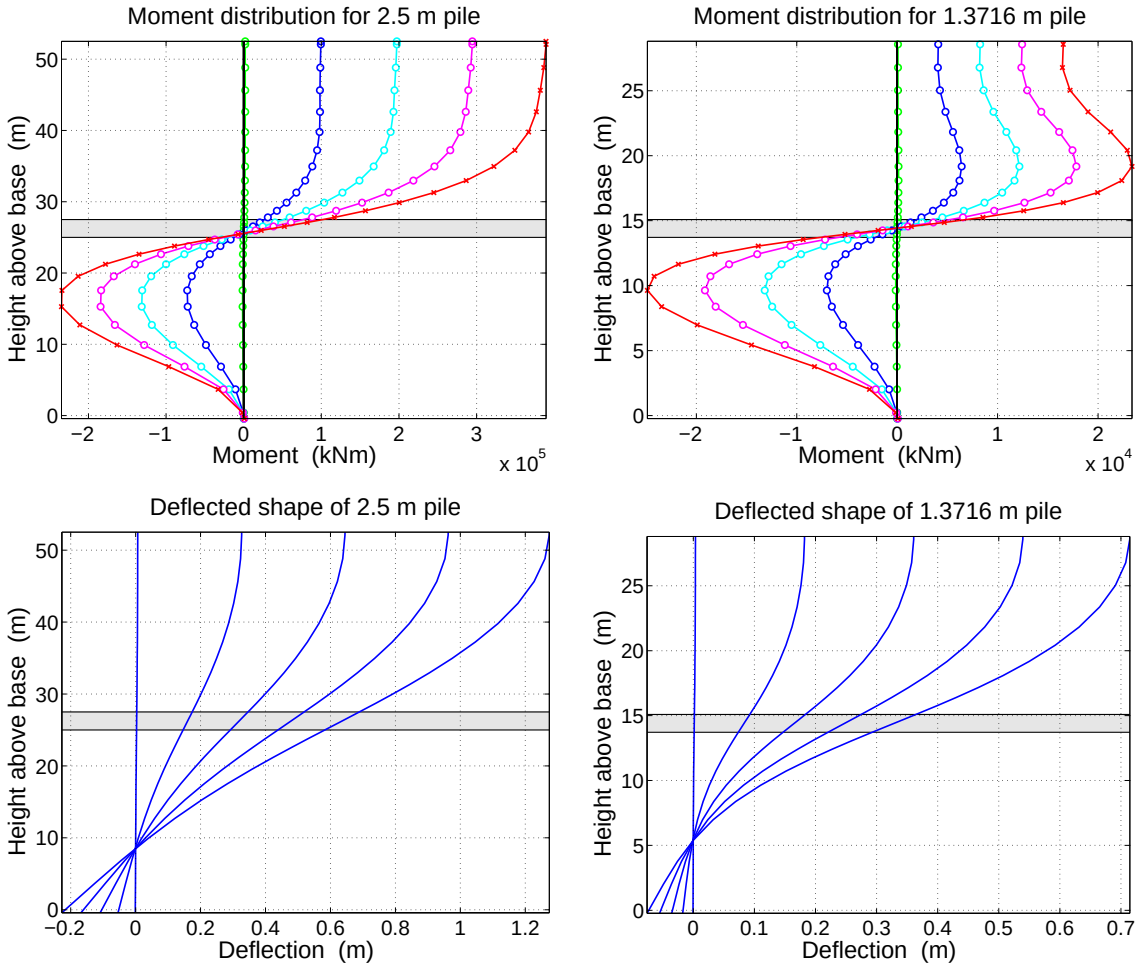

Figure 5.8: Comparison of moment distribution and deflected shapes for the fixed–head Series 1 cases for the 2.5 m and 1.3716 m piles.

difference. Notice how the lower half of the 2.5 m pile remains almost perfectly straight throughout the lateral spreading deformation while there is visible curvature at the top of the pile due to the pile head fixity. For the softer pile, there is visible curvature occurring in both the upper and lower portions of the pile and the bending demand in the upper portion is due to a combination of the pile head condition and the imposed soil deformation.

The tendency for the maximum demands developing with a pile head fixed against rotations to be greater than or equal to those generated from a free–head condition shows that the behavior of the pile is influenced greatly on the type of boundary condition assumed, especially for stiff piles. In design applications, it would be conservative to assume a fixed-type pile head condition if there is any indication that the pile may be less apt to rotate at that location. Considerations to this end become increasingly important for cases with large pile–to–soil stiffness ratios.

Another interesting observation to be made with regards to the pile head fixity is the location of the extreme moments for the fixed–head cases. With the exception of the Series 1 case for the 2.5 m pile shown in Figure 5.8, the extreme moment in the upper soil layer is not located at the pile head. The magnitude of the moment at the pile head is not zero in these cases, but it is not the largest value in the upper layer. Instead, the extreme moment is located further down in the layer, near the boundary of the liquefied layer, in a similar location as with the free–head cases. In the single case in which the extreme upper moment is located at the pile head, the combination of the large pile–to–soil stiffness ratio and fact that the elastic soil is able to continuously pick-up load results in the boundary condition, rather than the lateral layer motion, imposing the largest curvature demand on the pile. In all of the other cases, the fixity at the pile head causes the extreme moment in the upper layer to move slightly upward, while affecting little or no change in the location in the extreme moment in the lower layer.

5.5 The Effects of Plasticity on the Laterally Spreading System

Including plasticity in the constitutive models for either the piles or the soil creates a limit on the amount of stress that can build up in either component of the lateral spreading system. When the pile yields, plastic hinges develop, exacerbating the affects of the lateral

spreading deformation on the pile. Similarly, when the soil surrounding the pile yields, no further resistance is offered against the passage of the pile, leading to increased bending demands. The effects of plasticity in both the pile and soil elements are explored in the following sections of this thesis.

5.5.1 The Effects of Pile Plasticity

When the pile models are assigned elastoplastic behavior, as in analysis Series 2 and 4, certain new trends develop in the behavior of the laterally spreading soil–pile system. In general, the cases run with elastoplastic pile models display smaller extreme moment and shear demands than their elastic-pile counterparts. Additionally, the locations of the extreme moments in each of the solid soil layers become closer to the boundary of the liquefied layer, leading to a significant reduction in the effective length of the pile. These general trends are present for all three piles and for both boundary conditions.

The decrease in the maximum moment and shear force magnitudes is attributed to the inelastic behavior in the piles. The bending stresses in the piles due to the lateral spreading ground motion are significant enough to cause the piles to leave their respective elastic ranges, leading to a reduced pile–to–soil stiffness over time. The reduction in this ratio indicates that more of the stress generated by the imposed displacement profile is carried by the soil elements. The lower stiffness ratio also indicates that the soil controls more of the behavior of the entire system, resulting in piles which experience far more deformation than in the elastic-pile cases.

In the elastoplastic pile cases, the piles not only experience more deformation than in the elastic pile cases, this deformation is concentrated over a smaller length of the pile. Essentially, the lateral spreading ground deformation causes two plastic hinges to develop in the pile. This is illustrated in Figures 5.6(a) and 5.6(c), which show the deflected shapes for the free–head 0.6096 m pile cases for Series 1 and 2, respectively. Compared to the entirely linear elastic case, where the deformation is spread out over most of the pile, the deflected shape of the the Series 2 case shows that the curvature demand is focused in two areas, one in each solid soil layer. The tendency for the pile to become inelastic allows

the soil to control the system, leading to a deformed shape that is closer to the imposed displacement profile.

5.5.2 The Effects of Soil Plasticity on the Pile

To evaluate the effects of considering plastic behavior in the soil on the behavior of the pile, the results of Series 1 and 3 are compared. Series 1 considers both the pile and soil to be elastic, while Series 3 considers the pile to be elastic and the soil to be elastoplastic. For each pile and boundary condition combination, any differences between the results of Series 1 and 3 can be assumed to be attributable to the plastic behavior of the soil elements.

To illustrate the differences between these two cases, the 0.6096 m pile is used. This pile has the lowest pile–to–soil stiffness ratio of the three piles and therefore shows the effects of plastic soil in the most dramatic visual fashion, though the observations made for this pile are consistent across all three pile sizes. The results of the Series 1 and 3 cases for the 0.6096 m pile are displayed in Figures 5.2 (page 88) and 5.9, respectively, and are actually fairly similar. The general shape of the shear, moment, and load diagrams are unchanged across the two cases, though the results of the soil going plastic are evident in the more rounded shape of the load distribution. Additionally, the effects of yielding in the soil can be seen in the evolution of the extreme moments in each layer. In the Series 1 case, the moments grow in an almost linear fashion, while in the Series 3 case there is visible nonlinearity in the moment history.

The main difference between the two cases is the increase in maximum moment observed in the case with elastoplastic soil elements. The maximum moment in the entirely elastic case for the 0.6096 m pile is 2228 kNm. In the elastic pile with elastoplastic soil case, the maximum moment increases to 2569.3 kNm. The locations of the extreme moments in each layer also differ between the Series 1 and 3 cases, with a larger effective length present for the elastic soil than that returned for the elastoplastic soil.

This increase in maximum moment for the elastoplastic soil is not relegated to the free–head, 0.6096 m pile cases presented in Figures 5.2 (page 88) and 5.9. Similar increases in $\max M$ between the Series 1 and 3 results are also evident for both the 2.5 m and

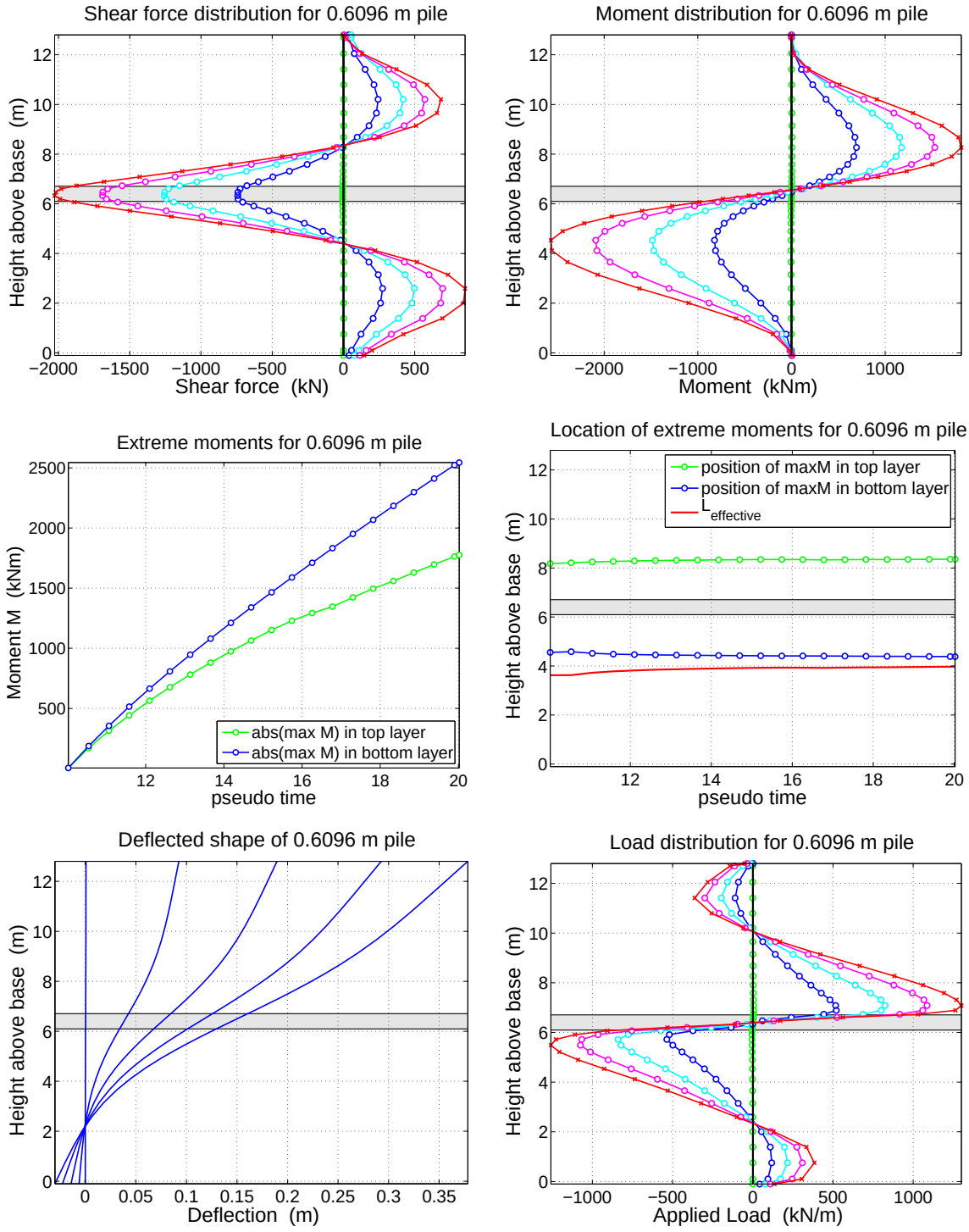

Figure 5.9: Pile summary plots for the 0.6096 m pile. Elastic pile and elastoplastic soil, free–head case. The liquefied layer is the shaded region.

1.3716 m piles. Interestingly, as the pile–to–soil stiffness ratio becomes larger, the increase in maximum moment becomes more significant. For the larger pile–to–soil stiffnesses, the pile has an increased capacity for stress as compared to the soil, suggesting the presence of a stress transfer from the soil to the pile in the elastoplastic soil cases.

The same type of increase in maximum moment occurs regardless of the pile head fixity, and is also evident between the Series 2 and 4 cases where the piles are elastoplastic, though the corresponding decrease in in L_{eff} is not observed between for the elastoplastic pile cases for the 0.6096 m pile.

The fact that the maximum moment increases while the effective length decreases in the elastoplastic soil seems illogical. It intuitively seems that as the effective length increases or decreases, the maximum moment would similarly increase or decrease. The data, however, suggests otherwise. It is hypothesized that this increase in maximum moment is attributable to the increased bending stress that the pile must carry when the soil yields. To aid in explaining this observation, two simple beam models are created and analyzed in order to prove that the seemingly counterintuitive increase in moment for the Series 3 cases over the Series 1 cases is correct.

5.5.3 Simple Verification Models for Pile Behavior in Elastoplastic Soil

As discussed during the evaluation of the results from the pile comparison study, there is a difference in the maximum bending moment returned for each pile depending upon the soil constitutive model employed. When the soil displays elastoplastic behavior, there is an increase in the maximum moment from when the soil is considered to be entirely elastic. Oddly, the effective length of the piles in the elastic soil cases is larger than in the elastoplastic soil cases, which would seem to correspond to an increase in maximum moment. In order to verify that the somewhat counterintuitive behavior displayed in the 3D lateral spreading model is correct, as well as to gain a better understanding of the problem in general, two simple beam models are created.

In a traditional simplified analysis of a pile during a lateral spreading event, the pile is modeled as a fixed-fixed beam of length L_{eff} undergoing a set end displacement. In this

model, the length of the beam is set equal to the effective length of the pile, commonly estimated as the thickness of the liquefied layer combined with a prescribed embedment length on either side of the liquefied layer. Using this approach, which is sometimes favored by structural designers, the maximum moment occurring at either end of the pile is estimated as

$$\max M = \frac{6EI\Delta}{L_{eff}^2} \tag{5.2}$$

where EI is the bending stiffness of the pile, L_{eff} is the effective length of the pile, and Δ is the displacement at the end of the beam. If this model is correct, than it would be expected that an increase in L_{eff} would correspond to a decrease in the maximum moment. The two simple beam models discussed in this section attempt to model the lateral spreading problem in a more accurate manner in order to verify that the results observed in opposition to the simple fixed-fixed model are sensible.

The two simple models developed for this purpose are shown in schematic form in Figure 5.10. Each model is fixed at one end and has a slider capable of resisting rotations but not displacements at the opposite end. Each model is subject to a unique load distribution, $w(x)$, attempting to mime the lateral spreading case with varying degrees of complexity.

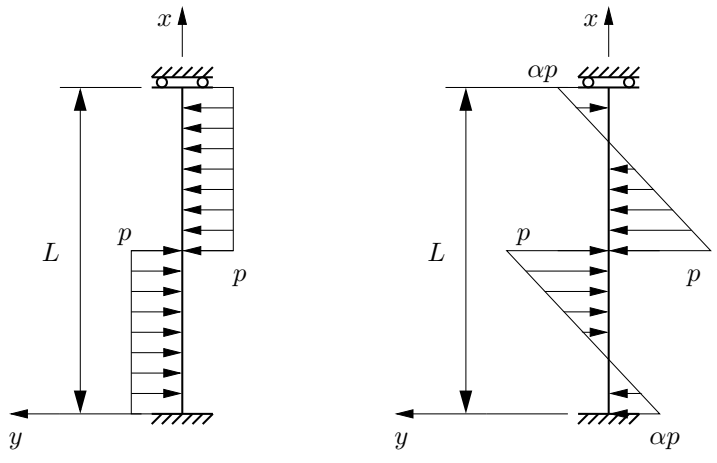

Figure 5.10: The two simple beam models used for verification of results. (a) The first simple model. (b) The second simple model.

These models provide a more reasonable approximation of the type of loading that a pile embedded in laterally spreading soil would experience, while remaining simple enough to solve by hand. It is of interest to determine the relationship between the magnitude of the applied loading, represented by p in the models, and both the effective length of the beams and the maximum moment in the beams for a given constant end displacement.

The First Simple Model

The first simple model is depicted in Figure 5.10(a). This model is similar to the fixed-fixed model discussed previously in that it models a beam having a length equal to the effective length of the pile. This means that the maximum moments are located at the ends of the beam, while the shear force at those locations is zero. The shear force will have a maximum at mid–span, while the moment at the middle of the beam should be zero. This model effectively represents the region of the pile located between the maximum moments, and does not consider the regions of the pile that are outside of this central region.

The loading assigned to the first simple beam model is a constant distributed load which changes sign at mid–span. Due to the discontinuity in the loading, the applied load must be represented as two separate equations, one for each half of the beam, necessitating that the beam be solved in two sections. For this model, the governing differential equation of bending can be written as

$$EI\frac{d^4v}{dx^4} = \begin{cases} -w_1(x) = -p & \text{for } 0 < x < \dfrac{L}{2} \\ -w_2(x) = p & \text{for } \dfrac{L}{2} < x < L \end{cases} \tag{5.3}$$

These expressions can then be solved in order to obtain the displacement of the beam under the prescribed load case. The following expressions result from integrating (5.3).

$$EIv_1(x) = -\frac{p}{24}x^4 + \frac{c_1}{6}x^3 + \frac{c_2}{2}x^2 + \frac{c_3}{2}x + c_4 \tag{5.4a}$$

$$EIv_2(x) = \frac{p}{24}x^4 + \frac{c_5}{6}x^3 + \frac{c_6}{2}x^2 + \frac{c_7}{2}x + c_8 \tag{5.4b}$$

In order to solve for the eight unknown constants, four boundary conditions and four compatibility conditions must be enforced. These boundary conditions are

$$v_1(x=0) = 0 \tag{5.5a}$$

$$\left.\frac{dv_1}{dx}\right|_{x=0} = 0 \tag{5.5b}$$

$$\left.\frac{dv_2}{dx}\right|_{x=L} = 0 \tag{5.5c}$$

$$V_L = EI\left.\frac{d^3v_2}{dx^3}\right|_{x=L} = 0 \tag{5.5d}$$

The compatibility conditions, which describe the relationship between the two halves of the beam at the point where they meet, can be expressed as

$$v_1\left(x=\frac{L}{2}\right) = v_2\left(x=\frac{L}{2}\right) \tag{5.6a}$$

$$\left.\frac{dv_1}{dx}\right|_{x=\frac{L}{2}} = \left.\frac{dv_2}{dx}\right|_{x=\frac{L}{2}} \tag{5.6b}$$

$$M_{1,L/2} = EI\left.\frac{d^2v_1}{dx^2}\right|_{x=\frac{L}{2}} = EI\left.\frac{d^2v_2}{dx^2}\right|_{x=\frac{L}{2}} = M_{2,L/2} \tag{5.6c}$$

$$V_{1,L/2} = EI\left.\frac{d^3v_1}{dx^3}\right|_{x=\frac{L}{2}} = EI\left.\frac{d^3v_2}{dx^3}\right|_{x=\frac{L}{2}} = V_{2,L/2} \tag{5.6d}$$

Applying the boundary and compatibility conditions of (5.5) and (5.6), the unknown constants in (5.4) can be determined. This results in the following expression for the displacement in the beam for the first simple model

$$v_1(x) = \frac{pL^4}{48EI}\left[3\left(\frac{x}{L}\right)^2 - 2\left(\frac{x}{L}\right)^4\right] \tag{5.7a}$$

$$v_2(x) = \frac{pL^4}{192EI}\left[8\left(\frac{x}{L}\right)^4 - 32\left(\frac{x}{L}\right)^3 + 36\left(\frac{x}{L}\right)^2 - 8\left(\frac{x}{L}\right) + 1\right] \tag{5.7b}$$

The displaced shape for the first simple model described by (5.7), along with the corresponding expressions for the moment and shear in the beam are plotted in Figure 5.11

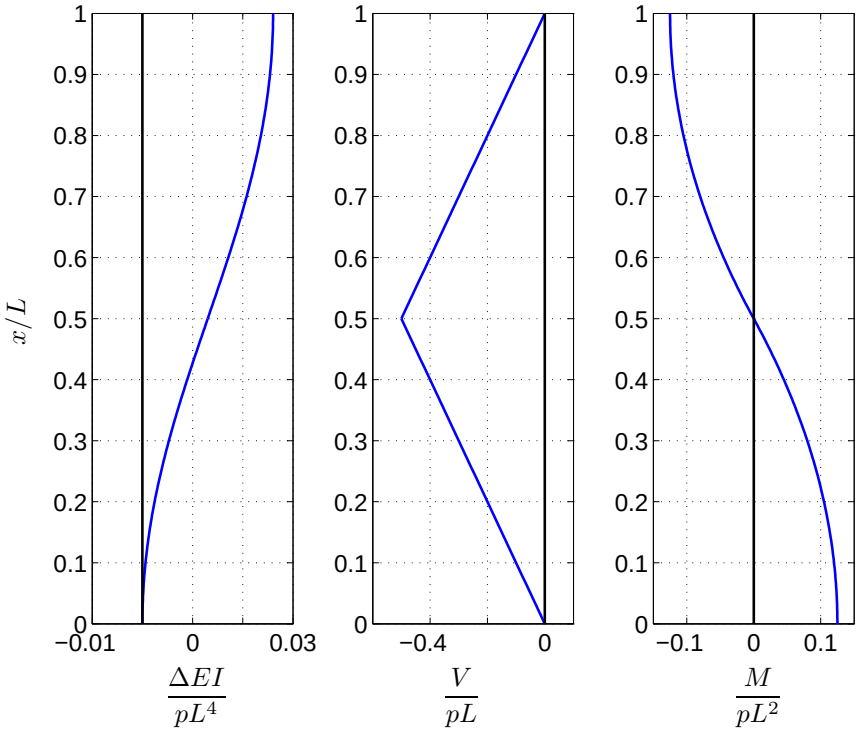

Figure 5.11: Displaced shape, shear diagram, and moment diagram for the first simple model.

using the shown dimensionless parameters. As shown, the maximum moments in the beam occur at the boundaries of the model and the maximum shear force occurs in the middle. This coincides with the intention of the first simple model to represent only the effective length, L_{eff}, of the pile subjected to the lateral spreading load case.

The maximum displacement, as shown in Figure 5.11, occurs at the position $x = L$. Substituting this into (5.7b) defines the end displacement, Δ, as

$$\Delta = v_2(L) = \frac{5pL^4}{192EI} \tag{5.8}$$

where p is the magnitude of the applied load, EI is the beam stiffness, and L is the beam length. Recalling that for this simple model, the length of the beam is equal to the effective length, L_{eff}, for the lateral spreading load case, (5.8) can be rearranged in order to obtain an expression for the effective length of the beam in terms of Δ, p, and EI.

$$L_{eff} = \left(\frac{192EI\Delta}{5p}\right)^{0.25} \tag{5.9}$$

The maximum moment in the beam can be determined in a similar manner. Evaluating the moment equation at $x = L$ gives an expression for the absolute value of the maximum moment in the beam of the form

$$\max M = \frac{pL^2}{8} \tag{5.10}$$

The expressions developed in (5.9) and (5.10) can be used to explore the relationships between the effective length and maximum moment of the beam with the magnitude of the applied load.

The Second Simple Model

The second simple model expands the relatively basic concept behind the first model to include a beam that represents the entire length of the pile in the lateral spreading model and a distributed loading that varies in magnitude with position. In a way, this model is a rough approximation of the load distribution resulting from the imposed displacement profile of the 3D lateral spreading model in the cases where the piles are entirely elastic. Notice the similarity of this assumed distribution to that returned from the elastic 2.5 m pile in elastic soil shown in Figure 5.5.

The second simple beam model is schematically depicted in Figure 5.10(b). As with the first model, the base of the beam is fixed while the opposing end of the beam is assigned a slider. In the second simple beam model, the maximum moment will not occur at the ends of the beam, instead, the moment should be zero at the ends. The maximum moment will occur at some location between the mid–span and end of the beam, with the exact location depending upon the assigned beam and load parameters. The shear force in the beam should still be zero at the ends and have a maximum in the center of the beam.

The distributed load acting upon the beam varies linearly with position, increasing in the lower section of the beam from a somewhat arbitrary value of -αp at the base to a value of p at mid–span. This loading pattern is then mirrored in the second half of the beam, with the load increasing linearly from a value of -p at the center to αp at the top. To increase the generality of this model, the coefficient α is used to represent a constant loading factor such that $0 < \alpha < 1$. For most of the post-processing associated with this model, $\alpha = 0.5$.

As with the first simple model, there is a discontinuity in the loading at mid–span. For this reason, in a manner similar as that shown before, the beam must be represented by two sets of equations, each existing only over its respective half of the beam. For the second simple model the governing differential equation of bending can be written as

$$EI\frac{d^4v}{dx^4} = \begin{cases} -w_1(x) = -2p(1+\alpha)\dfrac{x}{L} + \alpha x & \text{for } 0 < x < \dfrac{L}{2} \\ -w_2(x) = -2p(1+\alpha)\dfrac{x}{L} + p(2+\alpha) & \text{for } \dfrac{L}{2} < x < L \end{cases} \tag{5.11}$$

Integrating these expressions to obtain the displacement of the beam results in

$$EIv_1(x) = -\frac{p}{60L}(1+\alpha)x^5 + \frac{p}{24}\alpha x^4 + \frac{c_1}{6}x^3 + \frac{c_2}{2}x^2 + \frac{c_3}{2}x + c_4 \tag{5.12a}$$

$$EIv_2(x) = -\frac{p}{60L}(1+\alpha)x^5 + \frac{p}{24}(2+\alpha)x^4 + \frac{c_5}{6}x^3 + \frac{c_6}{2}x^2 + \frac{c_7}{2}x + c_8 \tag{5.12b}$$

For the second simple model, the boundary and compatibility conditions are unchanged from the first simple model, a fact that can be verified through examination of Figure 5.10. Therefore, (5.5) and (5.6) are applied to determine the unknown constants of (5.12), resulting in the following expressions for the displaced shape of the beam

$$v_1(x) = \frac{pL^4}{240EI}\left[-4(1+\alpha)\left(\frac{x}{L}\right)^5 + 10\alpha\left(\frac{x}{L}\right)^4 + 5(1-2\alpha)\left(\frac{x}{L}\right)^2 \right] \tag{5.13a}$$

$$v_2(x) = \frac{pL^4}{960EI}\left[-16(1+\alpha)\left(\frac{x}{L}\right)^5 + 40(2+\alpha)\left(\frac{x}{L}\right)^4 - 160\left(\frac{x}{L}\right)^3 + 20(7-2\alpha)\left(\frac{x}{L}\right)^2 - 40\left(\frac{x}{L}\right) + 5 \right] \tag{5.13b}$$

The displaced shape and distributions of shear force and bending moment in the second model are shown in Figure 5.12 using the shown dimensionless parameters. The coefficient α is assigned a value of one–half. These plots verify that the second simple model accomplishes its goal of approximating the loading applied to a pile in the lateral spreading model. The shear force is zero at each end with a maximum in the center of the beam, and the moment has maximums where the shear is zero, occurring at a location between the center and

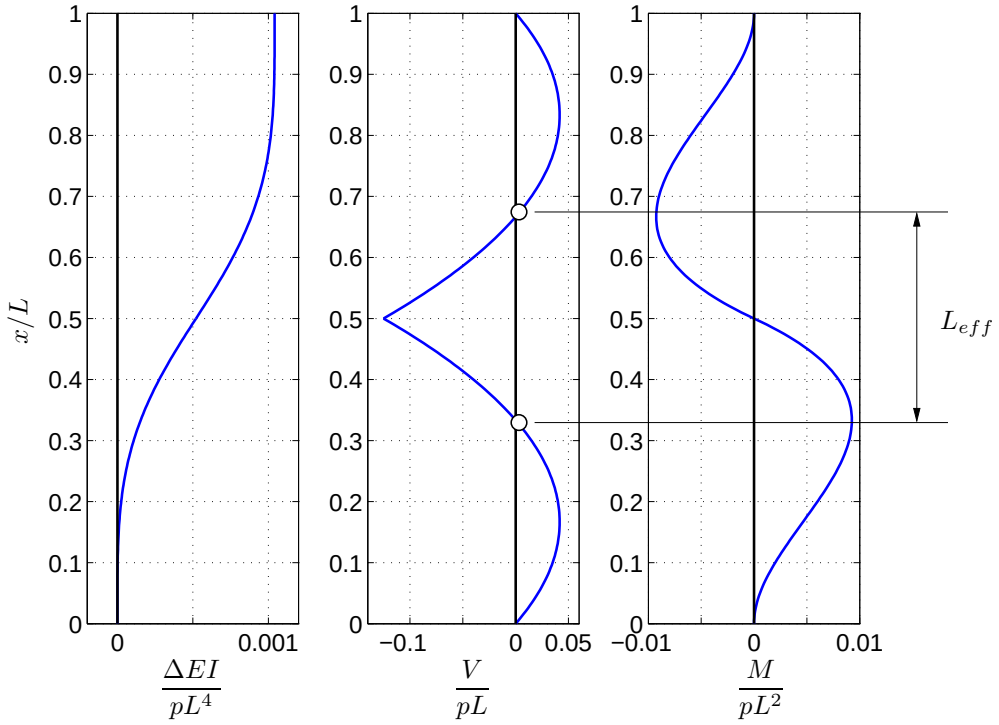

Figure 5.12: Displaced shape, shear diagram, and moment diagram for the second simple model.

the end of the beam. The distributions of both moment and shear for this model are fairly similar to those developed in the lateral spreading model The results from the simple models are more uniform due to the prescribed load distribution, but they share the same general shape as their more complex counterparts.

An expression for the end displacement, Δ, occurring at the position $x = L$ (the top of the beam), is determined from (5.13b) as

$$\Delta = \frac{(9 - 16\alpha)pL^4}{960EI} \tag{5.14}$$

To determine the effective length for the second simple model, the location of the maximum moment is computed in each segment of the beam. This is accomplished by determining

the locations in which the shear force is zero. These locations are

$$\xi_1 = \frac{\alpha}{1+\alpha} \qquad \text{for } 0 < \xi_1 < \frac{1}{2} \tag{5.15a}$$

$$\xi_2 = \frac{1}{1+\alpha} \qquad \text{for } \frac{1}{2} < \xi_1 < 1 \tag{5.15b}$$

The effective length of the beam is found as

$$\frac{L_{eff}}{L} = \min\left\{1, \min\left\{\xi_2, \frac{1}{2}\right\}\right\} - \max\left\{0, \min\left\{\xi_1, \frac{1}{2}\right\}\right\} \tag{5.16}$$

which defines the effective length for any value of the coefficient α. The maximum moment in the beam is determined by evaluating the moment equation at the previously obtained locations of maximum moment. For values of α which satisfy the conditions of (5.15), the maximum moment in the beam can be expressed as

$$\max M = \frac{pL^2\alpha^3}{6(1+\alpha)^2} + \frac{pL^2}{24}(1-2\alpha) \tag{5.17}$$

Observations and Conclusions

When elastoplastic soil elements are used in the lateral spreading model, there is a limit to the amount of resistance the soil will provide. In the areas where yielding occurs, such as near the liquefied layer, the load on the pile increases as the contact zone between the soil and pile increases in length. In the simple models, this behavior could be represented as an increase in the magnitude of p. In order to gain insight from the two simple models, plots of p versus the effective length of the beam and p versus the maximum moment in the beam are made for each simple beam model for a constant end displacement, Δ.

The plots of Figure 5.13 show the variation in the key bending parameters, effective length, L_{eff}, and maximum moment, $\max M$, with the magnitude of the applied loading, p, for a constant end displacement of $\Delta = 1$. In all of the plots of Figure 5.13, dimensionless analysis is used to allow the curves to be shown in a normalized manner. For both of the simple beam models, these plots show that the somewhat counterintuitive results of the three-dimensional lateral spreading model are reasonable. For increasing values of p the effective length of each model decreases while the maximum moment in the models

increases. This is the same behavior observed for all three elastic pile models in the 3D lateral spreading simulations, attainable from models easily solved by hand.

It has been shown that the two simple beam models are able to approximate the behavior of the piles in the three–dimensional lateral spreading model. Both Figures 5.11 and 5.12 show moment and shear diagrams that are reasonably similar to the moment and shear diagrams resulting from the lateral spreading model. With this reassurance, it is concluded that the behavior of these models is representative of the behavior of the piles due to the imposed displacement profile. The observed tendency for increasing maximum moment and

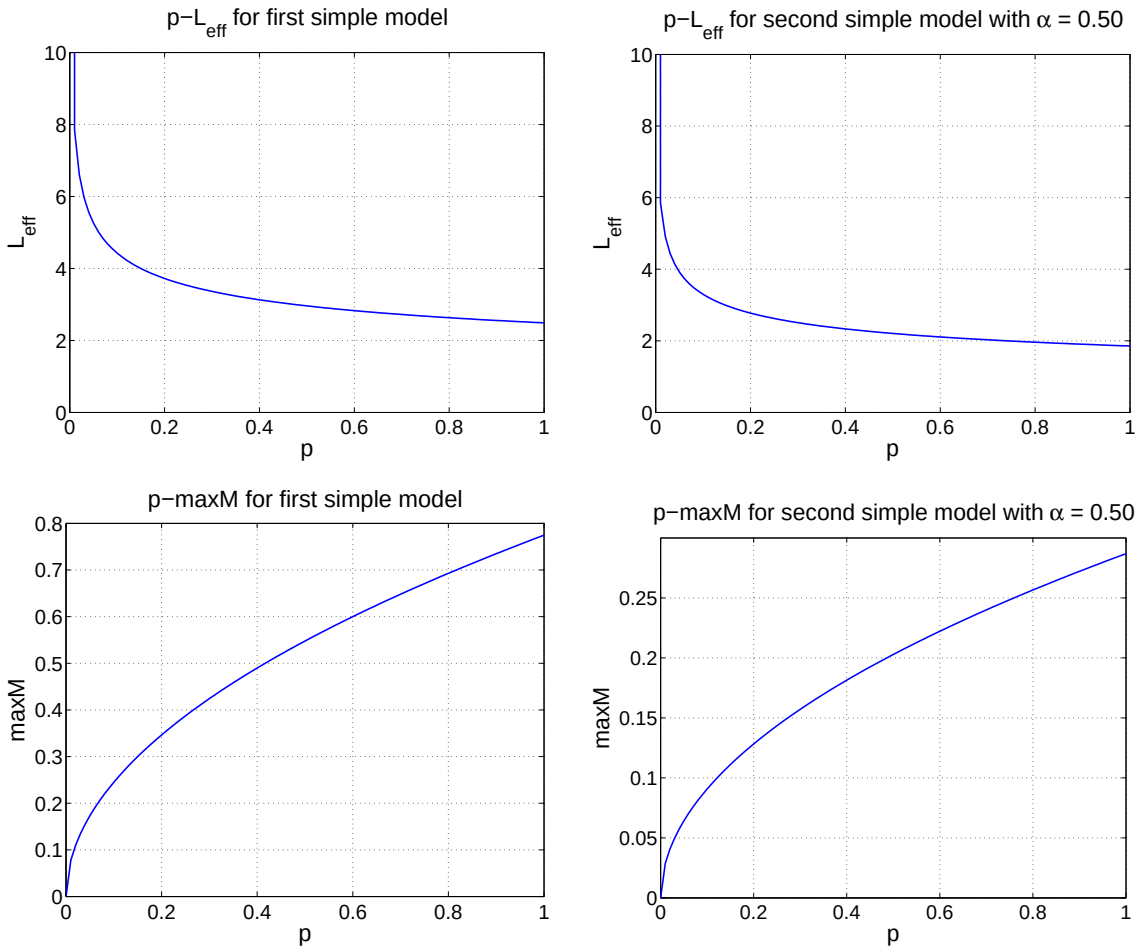

Figure 5.13: Normalized relationships between L_{eff}, $\max M$, and p for the two simple models.

decreasing effective length for increasing magnitudes of the applied load distribution in the simple models verifies that the lateral spreading results are reasonable while also offering a mechanism for this behavior.

5.6 Summary

During a lateral spreading event, an embedded pile foundation fundamentally alters the deformation of the soil system while simultaneously undergoing deformation of its own. Many factors contribute to the resultant behavior of the pile and the surrounding soil, among them the bending stiffness of the pile as compared to the lateral stiffness of the soil, the ultimate strength of both the pile and the soil, as well as the degree of fixity at the extents of the pile.

When the soil–pile system is modeled as entirely linear elastic, fundamental behavioral mechanisms can be observed in the system. As the lateral movement of the upper soil layer progresses, the pile embedded in the soil is pushed in the direction of flow. Depending upon the magnitude of the ratio of the pile's bending stiffness to the lateral stiffness of the soil, the pile also offers resistance to the lateral flow of soil, with greater resistance provided by those piles with the largest stiffness ratios. The bending demands which are generated in the piles follow consistent patterns for all pile sizes with the maximum shear force demand developing at the center of the liquefied layer due to the change in sign of the applied loading, and the maximum moment demands falling somewhat outside the boundaries of the liquefied layer, with one extreme value in each of the two solid soil layers. The distance between the maximum moments defines the effective length of the pile, L_{eff}, a parameter which provides an indication of the severity of the bending demand.

By altering the soil constitutive model to consider plastic behavior, the amount of load that the pile must carry increases, leading to increased bending demands when compared to the linear elastic models. This phenomenon has been verified through the use of simple beam models; confirming the presence of this somewhat unexpected mechanism for increased pile demands. In addition to changing the relationship between the pile and the soil, considering elastoplastic soil behavior allows for the observation of the ways in which the weaker liquefied layer affects the surrounding solid soil layers. As the pile is pushed into the soil, the solid

soil near the boundary of the liquefied layer is able to be pushed into the adjacent liquefied layer, thus effectively reducing the lateral resistance of the soil in the regions near the liquefied layer. This final aspect of the behavior observed in the system is explored further in Chapter 7 of this thesis.

Chapter 6

EXTRACTION OF REPRESENTATIVE FORCE DENSITY–DISPLACEMENT CURVES FROM LATERALLY–LOADED PILE MODELS

In current geotechnical engineering practice, the $p-y$ method (McClelland and Focht, 1958 [18], Matlock and Reese, 1960 [16], and Reese et al., 1974 [22]) is commonly used in the design process for pile foundations subject to lateral loads. Fairly extensive research has been performed in pursuit of furthering the capabilities of this design paradigm, allowing $p-y$ curves to be used in almost any design context. To evaluate the problem of a pile embedded in a laterally spreading soil system in the context of the $p-y$ method, it is necessary to establish a reliable procedure for extracting representative $p-y$ curves from the finite element models. The extraction process and some of the valuable insights gained during its development are discussed in the following sections of this chapter.

For cohesionless soils, the method of Reese et al. (1974) [22], which is summarized well, along with all other aspects of the $p-y$ method, in Reese and Van Impe, 2001 [23], is the most common procedure used to define sensible $p-y$ curves for a given soil and pile combination. The procedure of Reese et al. (1974) [22] has been incorporated into the computer program LPile, used to analyze piles under lateral loading, as well as adopted by the American Petroleum Institute (API), in a slightly modified form, as the recommended procedure for establishing curves for use in analyzing offshore piles under lateral loads (API, 1987 [2]). In the procedure developed by Reese et al. (1974) [22], $p-y$ curves are established based upon characteristics of the soil and pile, such as the angle of internal friction, pile diameter, and soil unit weight. The curves vary with depth, reflecting the effects of increased confinement on the soil response.

Two characteristics which can be used to define the $p-y$ curves resulting from these conventional methods are the initial stiffness and the ultimate lateral resistance. The initial stiffness of a given curve provides an indication of the amount of resistance the soil is able

to provide for small pile displacements, while the ultimate lateral resistance signifies the largest amount of resistance the soil is capable of providing against the passage of the pile. In this research, these two parameters are employed as a comparative means for evaluating conventional $p-y$ curves and $p-y$ curves extracted from three–dimensional finite element models. Using these two parameters, the essentials of the soil response represented by each curve can be quantified and compared.

This chapter discusses the extraction methods used and presents the results of parameter studies conducted to evaluate factors which may affects these curves. Further evaluation of the extracted curves, and comparisons with conventional analysis methods are presented in Chapter 7.

6.1 Extraction of $p-y$ Curves from Finite Element Models

In designing the three–dimensional finite element models used in this research, it was important to devise a simple way to extract force and displacement data from the pile at various depths within the soil. Due to the contact elements employed in the model, both sets of data are readily attainable. The beam–solid contact elements discussed in Section 2.4 are utilized to obtain the force vectors exerted on the pile by the surrounding soil at each pile node for a series of discrete points in pseudo time. These force vectors, which are passed to the beam elements as part of the normal function of the contact elements, contains the resultant forces acting at each pile node in the directions of three cartesian axes. By recording this vector, the resultant force components acting in the direction of loading are defined at each of the pile nodes.

These forces reflect the results of integrating the stresses acting around the perimeter of the pile. Due to the symmetry conditions utilized in the models the magnitudes of these force components reflect only one–half of the full pile. To obtain results consistent with the full diameter of the piles, the force components returned by the beam–to–solid contact elements are multiplied by a factor of two. The data returned by the contact elements are the pure force resultants of the stress distributions acting around the exterior of the pile. This data must be normalized by the lengths of the pile elements in order to obtain results which are independent of the mesh used in the model. Additionally, in the literature, force density

(units of force/length) is commonly used to represent the resistance in the development of $p-y$ curves. The normalization is performed by dividing the forces by the tributary length of pile over which it acts. For each respective pile node, the tributary length is defined as half the distance to the adjacent pile nodes in either direction, as depicted in Figure 6.1. For the nodes on the ends of the pile, the tributary length is half the distance to the sole adjacent node.

To obtain the displacement portion of the $p-y$ curves, the displacements of the pile nodes are recorded at the same points. In the case of the lateral spreading soil–pile models, the displacement values recorded directly from the pile are not a measure of the distance that the pile is pushed into the surrounding soil, but a measure of the actual displacement experienced by the pile. The desired displacement for generation of a $p-y$ curve representative of the soil response at a particular location is the differential displacement between the pile and the soil. To obtain the displacement of the pile relative to the surrounding soil at each pile node, the imposed far–field soil displacement profile discussed in Section 2.3 is subtracted from the pile displacement profile recorded by the model. This procedure is represented schematically in Figure 6.2. As shown, the relative displacements are much smaller than the total displacements recorded by OpenSees. For the alternative pile kinematic models discussed in Section 6.1.1 this procedure is not required as the recorded pile displacements are the relative displacements between the pile and the surrounding soil.

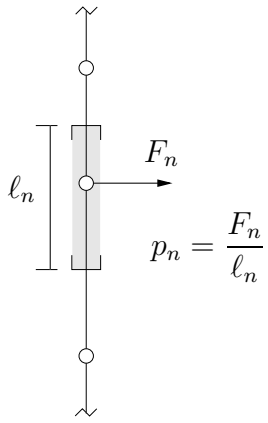

Figure 6.1: Schematic depicting the tributary length, ℓ_n, for node n.

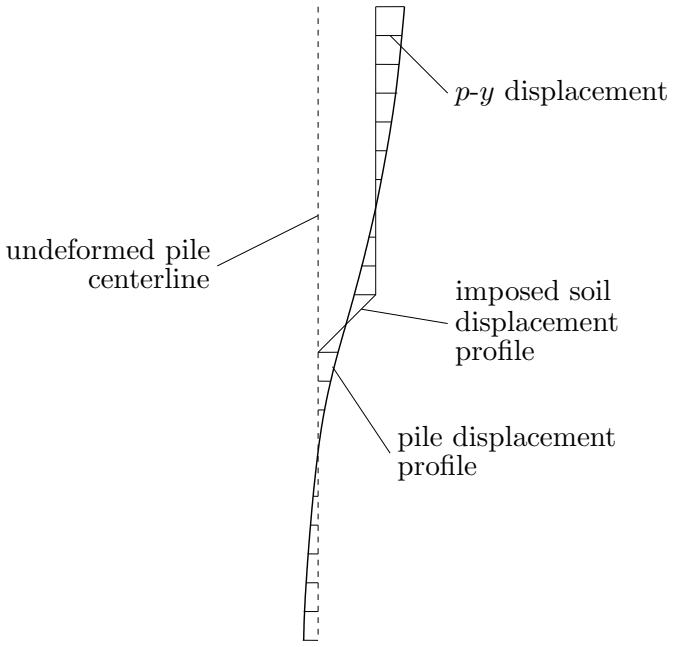

Figure 6.2: Determination of displacements suitable for use in $p-y$ curves for the lateral spreading case.

Evaluation and comparison of the $p-y$ curves resulting from the FEA are conducted using several means. Because the data returned from the finite element model represents values of force and displacement at discrete points in time, it is important that continuous curves be fit to the data. These curves can then be used to determine the characteristic parameters for each $p-y$ curve; the initial tangent, k_T, and the ultimate lateral resistance, p_u. The curve–fitting procedures used to this end are discussed in Section 6.1.2.

In addition to fitting smooth mathematical functions to the data, a lateral resistance ratio, LRR, introduced by Yang and Jeremic (2005) [27], is used as a further comparative means. The lateral resistance ratio describes the amount of resistance provided at a specific level of displacement for a given analysis case relative to the same level of displacement in a reference case. In this research, the lateral resistance ratio is evaluated at displacements of $y = 0.5\%D$, $y = 1.0\%D$, $y = 2.0\%D$, and $y = 4.0\%D$, where D is the pile diameter. The LRR is used to evaluate the effects of a liquefied layer on the mobilized resistance in the soil for each of the three cases as well as a means of comparing the cases to each other.

6.1.1 Considered Kinematic Cases

To evaluate the applicability of conventional $p-y$ curves to the laterally spreading soil problem, representative force–displacement curves are extracted from three–dimensional finite element models of laterally loaded piles. Three separate pile deformation patterns are considered in order to provide a means to evaluate the effects of varying pile kinematics on the $p-y$ curves resulting from the FEA. These cases include the lateral spreading case which is the primary focus of this thesis, a top pushover case, Figure 6.3(a), intended to simulate the type of test used to empirically derive $p-y$ curves for piles, and a rigid pile case, Figure 6.3(b), in which the entire length of the pile is pushed a uniform distance into the soil. These two additional kinematic cases are modeled using the same finite element mesh used in the previously discussed lateral spreading simulations.

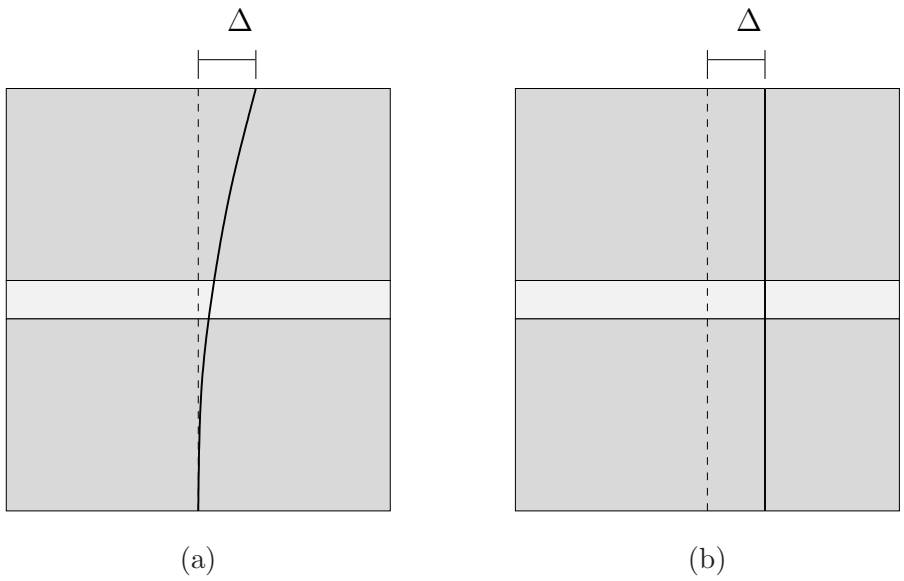

Figure 6.3: The two additional pile-soil deformation patterns examined in $p-y$ curve analysis. (a) Top pushover case. (b) Rigid pile case.

In the top pushover cases, the top node of the pile is pushed laterally while all other nodes are left unloaded. The magnitude of the pile's displacement naturally decreases with depth, remaining essentially zero at the base of the pile. As is the case in full–scale pile tests, this decrease in displacement with depth leads to $p-y$ curves that may not fully capture the

soil response for deeper soil layers. However, this kinematic mode provides a direct means of comparison with existing empirical methods. The top pushover models utilize the same boundary conditions as the free–head lateral spreading cases discussed in Chapter 3.

The rigid pile cases are included in order to gain a consistent level of displacement at all depths, and thus, provide useful pressure–displacement information for the entire length of the pile in each model. In the rigid pile case, each pile node is translated laterally into the soil by an equal amount, creating a uniform displacement profile with depth. In this case, the pile nodes are held fixed against all rotations, creating a truly rigid pile which does not deform during the simulation. With this lone exception, the boundary conditions in the rigid pile models match those in the other cases. All of the simulations conducted with intentions of extracting $p-y$ curve data are performed with linear elastic pile models and elastoplastic soil constitutive models using the formulations discussed in Sections 3.5 and 4.4, respectively. All three of the template pile designs are considered in this study.

6.1.2 Curve-fitting Strategies

The $p-y$ data returned from the OpenSees simulations for each of the pile nodes is a set of discrete points representing the force, normalized by element length, applied to the pile at specific values of displacement. In order to manipulate and analyze this data mathematically, curves must be fit to the data points in order to obtain smooth and continuous functions which describe the force–displacement relationship at each pile node. A least squares curve–fitting strategy is employed to this end for two separate functional forms, a polynomial function and a hyperbolic tangent function. Each functional form is intended to serve an independent purpose. Because the forces and displacements recorded from each of the three considered cases may be positive or negative, depending upon the specific deformation pattern in each case, the absolute values of the forces and displacements are used for curve–fitting purposes.

Polynomial Function Least Squares Fit

The polynomial functions used in this research are utilized primarily to estimate the initial tangent for the $p-y$ curves obtained from the 3D OpenSees simulations. Often, these polynomial curves are fit to only the first several points of the data set, ensuring that the initial tangent is accurately captured. These functions do not provide a measure of the ultimate lateral resistance provided by each $p-y$ curve, thus necessitating the use of the hyperbolic tangent function described in the following section.

Two polynomial functions are used for the purpose of curve–fitting. For the majority of the cases a third–order function is used, though in certain cases fifth–order functions are used to provide a better fit for the data. Fitting a cubic function to the data is an imperfect fit, however, the top pushover and lateral spreading cases have nodes with very small displacements which lead to nearly singular matrices in the fitting algorithm. For the rigid pile cases, each pile node is translated a specified uniform distance into the adjacent soil layers, ensuring that the displacement values at each node are large enough for the fifth-order polynomial fit.

The cubic polynomials used for curve-fitting have the form shown in (6.1a), while the fifth-order functions see the inclusion of an additional term as shown in (6.1b).

$$p(y) = a_1 y + a_3 y^3 \tag{6.1a}$$

$$p(y) = a_1 y + a_3 y^3 + a_5 y^5 \tag{6.1b}$$

The curve parameters a_1, a_3, and a_5 are constants defining the $p-y$ curves at each pile node. The first curve parameter, a_1, is the initial slope of the curve. Taken in the context of a $p-y$ curve, this parameter provides a good representation of the initial stiffness at each pile node.

The least squares fit procedure seeks to minimize the error function, $\mathcal{E}$, defined as

$$\mathcal{E}(a_i) = \sum_k \frac{1}{2} \left[p_k - p(y_k) \right]^2 \tag{6.2}$$

where p_k and y_k are the values of force density and displacement, respectively, returned from the model at a given node for the kth timestep, and $p(y_k)$ is the chosen curve-fitting

function, i.e. (6.1a) or (6.1b), evaluated at each of the values of y_k. For the cubic polynomial, the error function can be expressed as

$$\mathcal{E} = \sum_k \frac{1}{2} \left[p_k - a_1 y_k - a_3 y_k^3 \right]^2 \tag{6.3}$$

This resulting error function is minimized by computing the derivatives of (6.3) with respect to both a_1 and a_3, setting these to zero, and solving for the unknown constants. The resulting equations have the form

$$\frac{\partial \mathcal{E}}{\partial a_1} = 0 = \sum_k \left(-p_k + a_1 y_k + a_3 y_k \right) y_k$$

$$\Longrightarrow a_1 \sum_k y_k^2 + a_3 \sum_k y_k^4 = \sum_k p_k y_k \tag{6.4a}$$

$$\frac{\partial \mathcal{E}}{\partial a_3} = 0 = \sum_k \left(-p_k + a_1 y_k + a_3 y_k \right) y_k^3$$

$$\Longrightarrow a_1 \sum_k y_k^4 + a_3 \sum_k y_k^6 = \sum_k p_k y_k^3 \tag{6.4b}$$

from which the unknown constants a_1 and a_3 can be determined using

$$\left\{ \begin{array}{c} a_1 \\ a_3 \end{array} \right\} = \left[\begin{array}{cc} \sum y_k^2 & \sum y_k^4 \\ \sum y_k^4 & \sum y_k^6 \end{array} \right]^{-1} \left\{ \begin{array}{c} \sum p_k y_k \\ \sum p_k y_k^3 \end{array} \right\} \tag{6.5}$$

The use of the fifth–order function introduces an additional curve constant, a_5, and alters the error function and its derivatives, resulting in a system of equations which can be solved with

$$\left\{ \begin{array}{c} a_1 \\ a_3 \\ a_5 \end{array} \right\} = \left[\begin{array}{ccc} \sum y_k^2 & \sum y_k^4 & \sum y_k^6 \\ & \sum y_k^6 & \sum y_k^8 \\ symm. & & \sum y_k^{10} \end{array} \right]^{-1} \left\{ \begin{array}{c} \sum p_k y_k \\ \sum p_k y_k^3 \\ \sum p_k y_k^5 \end{array} \right\} \tag{6.6}$$

The fifth-order curves provide a better fit for most of the data, however, for the top pushover and lateral spreading cases, there are pile nodes at which the displacement is sufficiently small as to create matrices which are singular to working precision, rendering the curves generated at these points useless for further analysis. This tendency is more prevalent in the fifth–order curve–fitting procedure of (6.6) where the exponents are far larger than in (6.5),

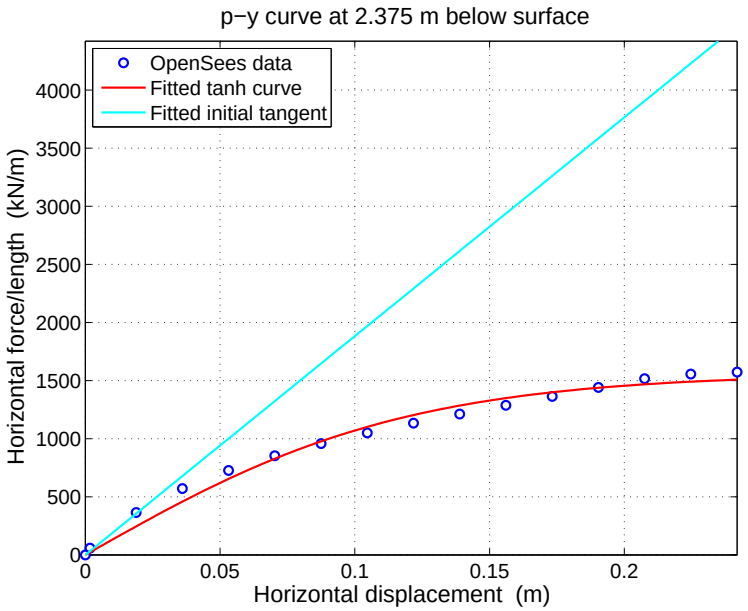

Figure 6.4: Extracted $p-y$ curve for the 1.3716 m pile at a depth of 2.375 m below the ground surface.

and it is the main impetus for the use of the two functions. The fifth–order curves are only employed when examining the values for the rigid pile cases, or in the comparison of two separate rigid pile cases. In all other cases, or in comparisons of the rigid pile data to other cases, the third–order functions are used. These functions provide adequate fits for the data, especially in the context of this research. An example of the $p-y$ data extracted from one of the OpenSees simulations and its associated fitted initial tangent obtained from the polynomial function can be seen in Figure 6.4.

Hyperbolic Tangent Function Least Squares Fit

A hyperbolic tangent function is chosen as a curve–fitting solution which allows for the estimation of both the ultimate lateral resistance and the initial stiffness represented in the extracted $p-y$ curves. While many functional forms are able to represent asymptotic behavior of the type generally exhibited by $p-y$ curves, the hyperbolic tangent function is chosen for two inherent advantages. The American Petroleum Institute (API) (1987) [2]

recommendations for the design of offshore piles utilize a hyperbolic tangent function to define the shape of the $p-y$ curves for cohesionless soils. The procedure adopted by the API is based upon the original work of Reese et al. (1974) [22], however where Reese et al. specified curves which have both linear and parabolic sections, the API curves are represented as one continuous function having a matching initial slope and asympote. Fitting this functional form to the FEA data allows for direct comparison to the conventional API $p-y$ curves. Additionally, the specific function chosen provides a direct means with which to transfer the data extracted from the 3D simulations to curves suitable for use in $p-y$ spring elements in subsequent OpenSees simulations, through the use of existing $p-y$ spring elements implemented in OpenSees which are able to approximate the shape of the API curves when used in static loading.

The chosen hyperbolic tangent function has the form

$$p(y) = p_u \tanh\left(\frac{kz}{p_u}\, y\right) \tag{6.7}$$

in which the parameter p_u is the ultimate resistance provided by each curve with units of force/length, z is the depth, and the parameter k, with units of force/length^3, is indicative of the curvature of the function. A measure of the initial stiffness of a hyperbolic tangent function can be found by evaluating the first derivative of (6.7) at $y = 0$, resulting in the initial slope of the exponential function, $k_t = kz$. When compared to the values of $k_T = a_1$ obtained from the fitted polynomial functions, the initial stiffness of the hyperbolic tangent functions are somewhat lower. This is illustrated in Figure 6.4. As indicated, the stiffness obtained from the polynomial curve–fit is much more representative of the initial stiffness of the curve. The results presented in this figure are representative of the extracted curves as a whole, and for this reason, the polynomial initial tangents of $k_T = a_1$ are used for all work related to initial curve stiffness.

A least squares fitting procedure is used to determine the constants p_u and k for the $p-y$ data at each pile node. For the hyperbolic tangent function of (6.7), the residual, r_j, at each pile node can be expressed as the difference between the value returned from the simulation and that estimated by the curve–fitting function.

$$r_j = p_j - p_u \tanh\left(\frac{kz}{p_u}\, y_j\right) \tag{6.8}$$

The best fit for the data is achieved when the error is at a minimum. For this problem, the error function is obtained as

$$\mathcal{E}(p_u, k) = \sum_j \frac{1}{2} r_j^2 = \sum_j \left[p_j - p_u \tanh\left(\frac{kz}{p_u}\, y_j\right)\right]^2 \tag{6.9}$$

The error is at a minimum when its gradient is zero. Because there are two parameters, it is expedient to perform the solution in vector form by defining the vector $\boldsymbol{\lambda}$ with two components $\lambda_1 = p_u$ and $\lambda_2 = k$. The gradient equations can thus be written in terms of this vector, $\boldsymbol{\lambda}$, as

$$\frac{\partial \mathcal{E}}{\partial \lambda_i} = \sum_j r_j \frac{\partial r_j}{\partial \lambda_i} = 0 \tag{6.10}$$

The necessary derivatives of the residual with respect to the two parameters λ_1 and λ_2 can be expressed as

$$\frac{\partial r_j}{\partial \lambda_1} = \frac{\partial r_j}{\partial p_u} = \frac{kz}{p_u}\, y_j \operatorname{sech}^2\left(\frac{kz}{p_u}\, y_j\right) - \tanh^2\left(\frac{kz}{p_u}\, y_j\right) = 0 \tag{6.11a}$$

$$\frac{\partial r_j}{\partial \lambda_2} = \frac{\partial r_j}{\partial k} = -z y_j \operatorname{sech}^2\left(\frac{kz}{p_u}\, y_j\right) = 0 \tag{6.11b}$$

Due to the nonlinear nature of (6.11a) and (6.11b), to obtain values for the unknown parameters, p_u and k, an iterative procedure must be employed. For a known (estimate) value of $\boldsymbol{\lambda}^\ell$ in the current iteration, a Taylor series expansion is used to estimate the value of $p(y)$ in the next iteration as

$$p(y_j, \boldsymbol{\lambda}) \approx p(y_j, \boldsymbol{\lambda}^\ell) + \sum_i J_{ji} \Delta\lambda_i \tag{6.12}$$

in which $\boldsymbol{\lambda}^\ell$ contains the values of λ_1 and λ_2 in the current iteration, $\Delta\boldsymbol{\lambda} = (\Delta\lambda_1, \Delta\lambda_2)^T$ is the change in $\boldsymbol{\lambda}$ between iterations, and the Jacobian, $\mathbf{J}$, has components

$$J_{ij} = -\frac{\partial r_i}{\partial \lambda_j} \tag{6.13}$$

Plugging the result of (6.12) into the residual gives

$$\begin{aligned} r_j &= y_j - p(y_j, \boldsymbol{\lambda}^\ell) - \mathbf{J} \cdot \Delta\boldsymbol{\lambda} \\ &= \Delta y_j - \mathbf{J} \cdot \Delta\boldsymbol{\lambda} \end{aligned} \tag{6.14}$$

Applying this result to the minimization problem (6.10) leads to

$$\mathbf{J}^T\mathbf{J}\Delta\boldsymbol{\lambda} = \mathbf{J}^T\Delta\mathbf{y} \tag{6.15}$$

from which appropriate values for the components of $\boldsymbol{\lambda}$, the parameters p_u and k, can be determined by iterating with a Newton–Raphson–like procedure until the specified convergence criterion is met. For the presented results, the process continues to iterate until

$$\left|\frac{\Delta\lambda_j}{\lambda_j}\right| < 0.001 \tag{6.16}$$

For the more regularly–shaped curves obtained from the finite element models, the hyperbolic tangent function provides a good fit to the data. A typical example of a fitted curve is shown in Figure 6.4 (page 125). As shown, the hyperbolic tangent curve tends to underpredict the initial stiffness of the data, leading to the use of the polynomial functions to obtain an accurate representation of the initial stiffness, k_T. An additional item of note is also illustrated in Figure 6.4. At the depth that this particular curve represents, it appears that the soil did not quite reach its ultimate lateral resistance, therefore, the value of p_u obtained from the curve–fitting procedure is an extrapolation. This phenomenon occurs with increasing frequency as the depth below the ground surface increases. Further discussion on the extrapolated values of p_u will be provided in subsequent sections.

6.2 Effects of Pile Kinematics on $p-y$ Curve Data

The pile kinematics in these simulations play an important role in defining the success rate for $p-y$ curve extraction from the finite element model. It is observed that in addition to the known effects of differential soil layer strength on the $p-y$ curves for a given case, there is also a tangible effect which can only be attributed to the kinematics of the piles. In these cases, the generated curves differ in quality and consistency based upon the magnitude of the displacement at their respective nodes and how these displacements evolve over the duration of the deformation. Due to this effect, there are regions in which the curves resulting from the different kinematic cases are comparable to each other and regions in which they differ substantially.

Table 6.1: Overview of the four considered kinematic comparison cases.

	Rigid	Top Pushover	Lateral Spread
Homogenous Soil	X	X	
Layered (Liquefied) Soil	X		X

The rigid pile cases, in which the piles undergo uniform displacements at all depths are used as benchmarks for this study. These cases eliminate the deformation of the pile as an influencing factor and are able to record the response of the soil to the passage of the pile consistently with depth. The $p-y$ curves resulting from the rigid pile cases are similar in shape to those used in practice. This similarity is not always observed for the lateral spreading and top pushover cases, where differential pile displacements occur with depth. The curves resulting from these two cases are generally comparable to those resulting from the rigid pile case, however, in certain locations, dependent upon the deformation pattern of the pile, the curves deviate from the benchmarks. This observation underscores a potential flaw in the assumption that representative $p-y$ curves can be extracted from the 3D finite element model without exception and identifies the need for a more careful approach to $p-y$ curve extraction.

Table 6.1 provides a brief overview of the four kinematic comparison cases considered for each pile. There are two rigid pile cases, one top pushover case, and one lateral spreading case for each pile. The results of each of the two variable kinematic cases, the top pushover and lateral spreading cases, are compared to a rigid pile in a corresponding soil profile by means of two measures. The initial stiffness of each case, the parameter $k_T = a_1$ obtained from the procedure of Section 6.1.2, is compared as a ratio of the variable kinematic case to the rigid pile case. The k_T ratio provides insight into the variation in the initial stiffness recorded by each case with depth. Because there are locations at which the displacements are very small and little soil resistance is mobilized, ultimate lateral resistances are not compared in this study.

To provide an additional comparative means, the lateral resistance ratio, LRR, intro-

duced by Yang and Jeremic (2005) [27], is employed. The LRR is the ratio between the resistance in the variable kinematic cases to that in the rigid pile cases at a specific level of displacement. An example of how the LRR works is illustrated in Figure 6.5. Four displacement increments are investigated in this study in an effort to gauge how the relationships between the curves may vary over time. The LRR is computed at displacements equal to 0.5%, 1%, 2%, and 4% of the pile diameter in each respective case. The evolution of the differential displacement between the pile and the soil is also included in the summarizing figures in order to provide a context for the deformation pattern with depth. The depth and displacement scales are normalized by pile diameter in order to encourage comparison between the results of the three piles.

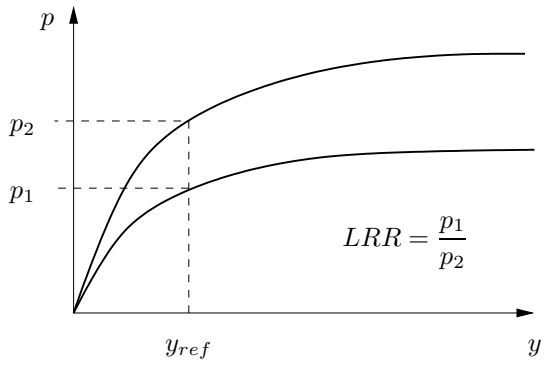

Figure 6.5: The lateral resistance ratio, LRR, is the ratio of the soil resistance values computed in two reference $p-y$ curves at a prescribed value of displacement.

The top pushover case and a rigid pile case are run in identical, entirely homogeneous, soil systems, so as to eliminate any additional effects due to the presence of a liquefied layer, and the results of these two simulations are compared in Figures 6.6, 6.7, and 6.8. The lateral spreading case and one of the rigid pile cases are run using the three–layer liquefied soil model of Figure 2.1. Both models utilize the same soil profile in order to provide meaningful comparisons between the two. The lateral spreading cases do not make sense in the context of an entirely homogeneous soil, and the presence of the liquefied layer affects each case in a similar manner. The results of these simulations are compared in Figures 6.9, 6.10, and 6.11.

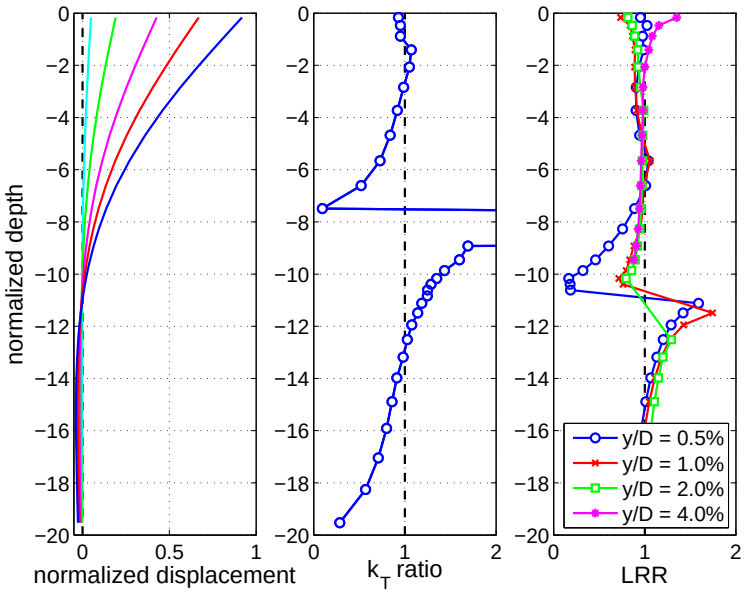

Figure 6.6: Pile kinematic comparison for the 2.5 m pile. The top pushover case is compared to the rigid pile case. Both piles are embedded in homogenous soils.

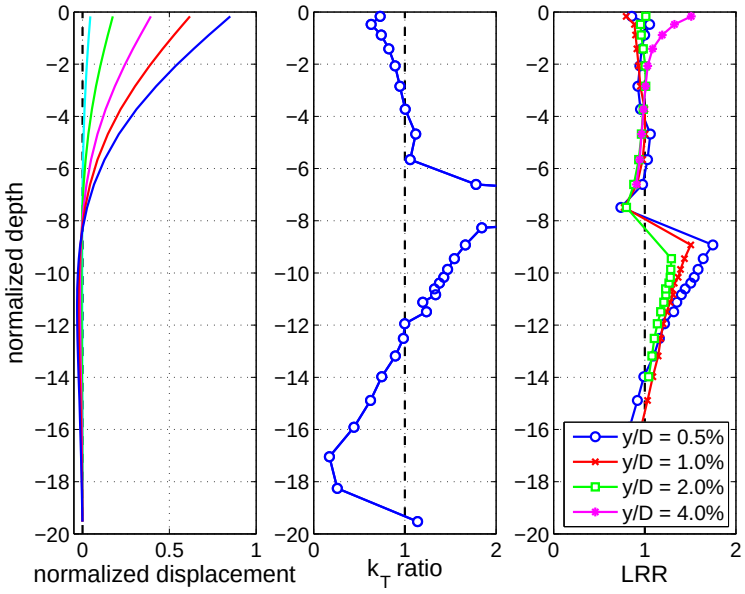

Figure 6.7: Pile kinematic comparison for the 1.3716 m pile. The top pushover case is compared to the rigid pile case. Both piles are embedded in homogenous soils.

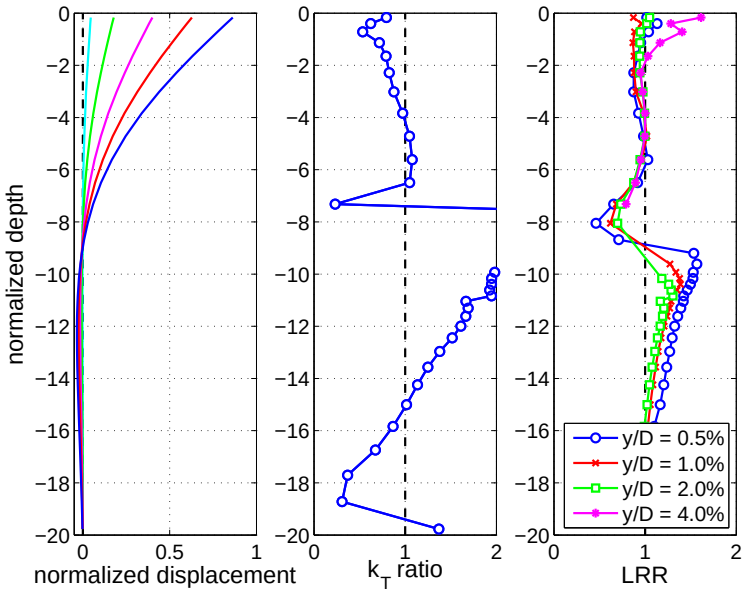

Figure 6.8: Pile kinematic comparison for the 0.6096 m pile. The top pushover case is compared to the rigid pile case. Both piles are embedded in homogenous soils.

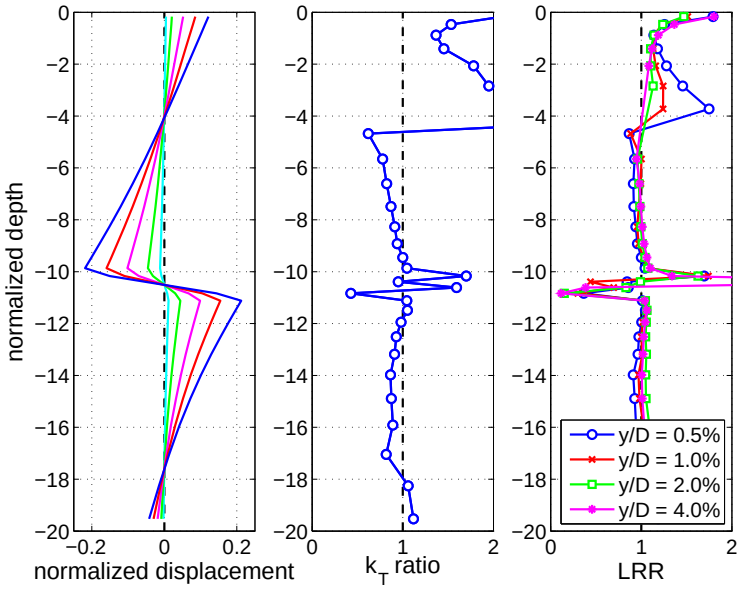

Figure 6.9: Pile kinematic comparison for the 2.5 m pile. The lateral spreading case is compared to the rigid pile case. Both piles are embedded in a three–layer liquefied soil system.

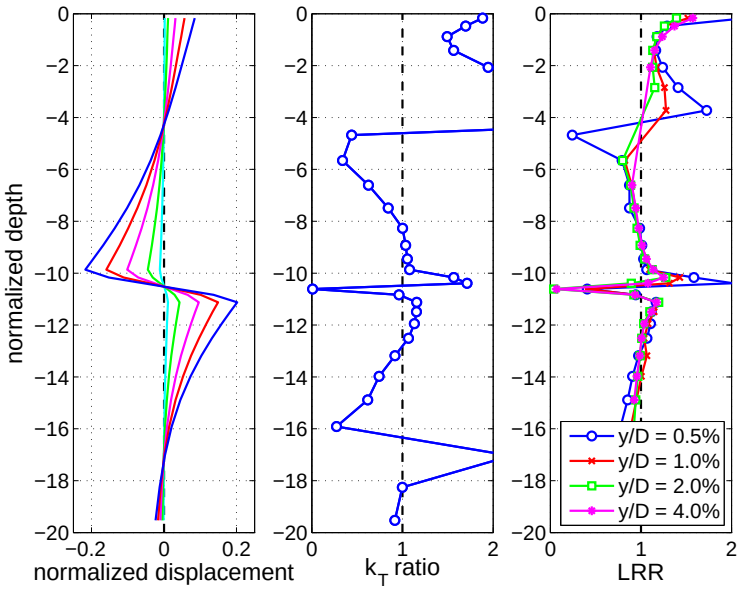

Figure 6.10: Pile kinematic comparison for the 1.3716 m pile. The lateral spreading case is compared to the rigid pile case. Both piles are embedded in a three–layer liquefied soil system.

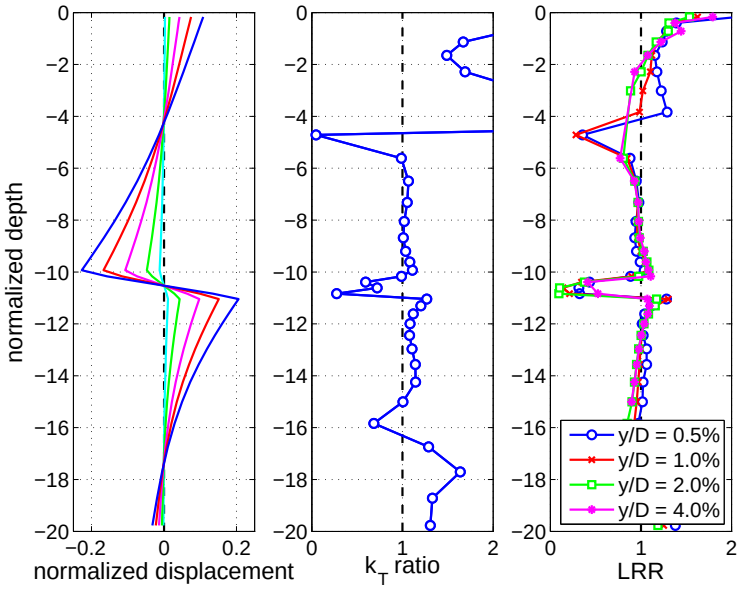

Figure 6.11: Pile kinematic comparison for the 0.6096 m pile. The lateral spreading case is compared to the rigid pile case. Both piles are embedded in a three–layer liquefied soil system.

In the k_T ratio and LRR plots, a value of one indicates that the $p-y$ curves extracted from the two kinematic cases are similar with respect to either their initial stiffnesses or their resistances at a particular displacement. If the kinematics of the piles did not affect the extracted $p-y$ curves, both the initial stiffness ratio and LRR for all compared cases would be one over the entire length of the piles. As shown in the figures on the preceding pages, both ratios vary with depth and are only at or near unity for limited portions of the length of the pile. This suggests that the kinematics of the pile do indeed affect the quality of the extracted curves and any subsequent observations of the soil's response made using these curves.

Aside from the top few diameters of the top pushover comparisons, which are affected by interaction with the free surface, the initial stiffness and lateral resistance ratios show that the curves resulting from the two kinematic cases are generally similar in the areas where the differential displacements between the soil and piles are large. Figures 6.12 and 6.13, showing the extracted curves for both cases for the 0.6096 m pile, further demonstrate this observation. In general, for the shown curves, the larger the displacement is at a particular depth, the more similar the two curves tend to be. In the areas where the displacements are relatively small, both the plotted ratios and curves show deviations between the curves generated from each case.

There are a few general trends observed due the effects of pile kinematics on the extracted $p-y$ curves. In some instances, such as at a normalized depth of approximately 9 for the 1.3716 m pile top pushover case shown in Figure 6.7, the curves are initially very different from the rigid pile curves, however, as the displacements increase, the curves become more similar to the rigid pile curves. This can be observed in the tendency of the LRR to decrease between successive displacement increments. At other locations, the opposite holds; the curves generated from one of the variable kinematic cases are initially very similar to the rigid pile curves and then become less similar as the displacements increase. An example of this behavior occurs in the middle of the 2.5 m pile lateral spreading case shown in Figure 6.9. At this location, the LRR increases from increment to increment. Both of these trends can also be observed when looking at comparisons between the actual $p-y$ curves extracted from the simulations. A selection of extracted $p-y$ curves for the 0.6096 m pile

is shown in Figures 6.12 and 6.13. These plots also demonstrate the inadequacy of the top pushover and lateral spreading cases in the activation of the ultimate resistance of the soil, leading to the conclusion that a reasonable estimate of p_u is not possible for these cases, and that the rigid pile cases should be used exclusively for the determination of the parameter, p_u.

An additional effect of the pile kinematics can be observed in the plotted $p-y$ curves shown in Figures 6.12 and 6.13. At a depth of 5.61 m in the top pushover case and 2.88 m in the lateral spreading case, the curves are initially dissimilar and remain so at all levels of displacement. This suggests that in these cases, the pile kinematics are completely controlling the recorded responses. At these depths, it can be observed from the displaced shape plots in Figures 6.8 and 6.11 that the pile displacements are changing in sign. It is hypothesized that at such locations, due to the oscillatory deflective tendency of a beam on an elastic foundation, a pile node in this location begins to deflect in one direction while the imposed deformations are small and the pile increasingly develops a gap from the surface down. As the magnitude of the imposed deformations increases, the node is pulled in the opposite direction. This tendency for the pile to change direction can be observed in the plots of normalized differential displacement available for each considered case in Figures 6.6 through 6.11.

This discussion shows that there are discrepancies between the $p-y$ curves generated for various pile kinematics. In all of the comparisons, both of the considered cases are embedded in identical soil profiles, eliminating the possibility for variable soil conditions to affect the results. Additionally, the top pushover cases are run using entirely homogenous soil systems, removing the liquefied layer completely from consideration. This tendency for differing results based upon pile kinematics occurs for all of the three considered pile designs. A closer look at the results for all three piles, shown in Figures 6.6 through 6.11, shows that the areas of greatest divergence in the two sets of curves tend to occur near the areas where the pile displacement changes sign. The depth at which these transitions occur is not the same for each pile, therefore, it is reasonable to rule out any depth or meshing effects. For all cases, the only difference between the two compared models is the pile kinematics. The effects of varying the pile kinematics are most evident when the differential displacements

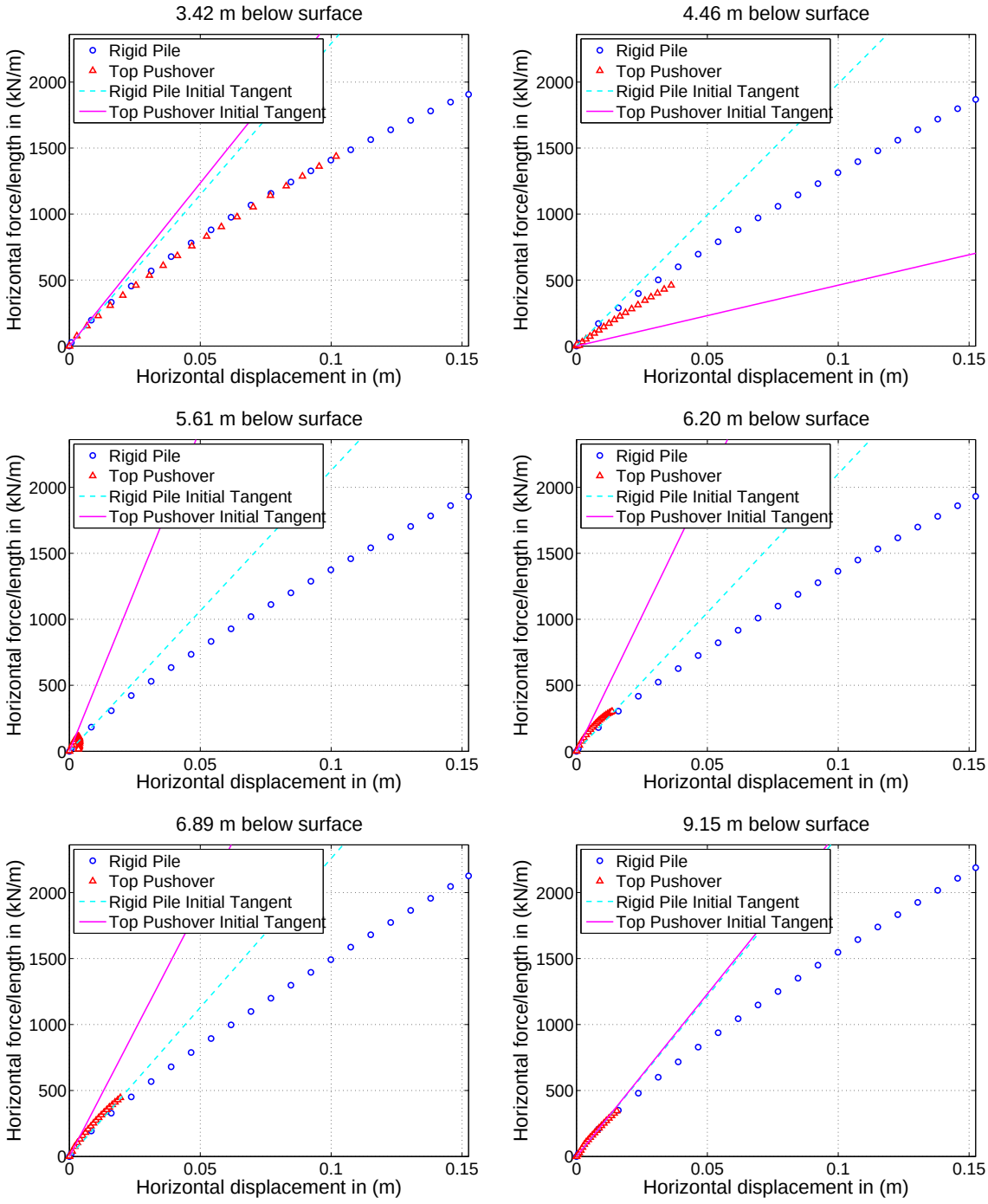

Figure 6.12: Extracted $p-y$ curves from the top pushover and rigid pile cases in homogenous soil for the 0.6096 m pile. The fitted initial tangents are shown for each case.

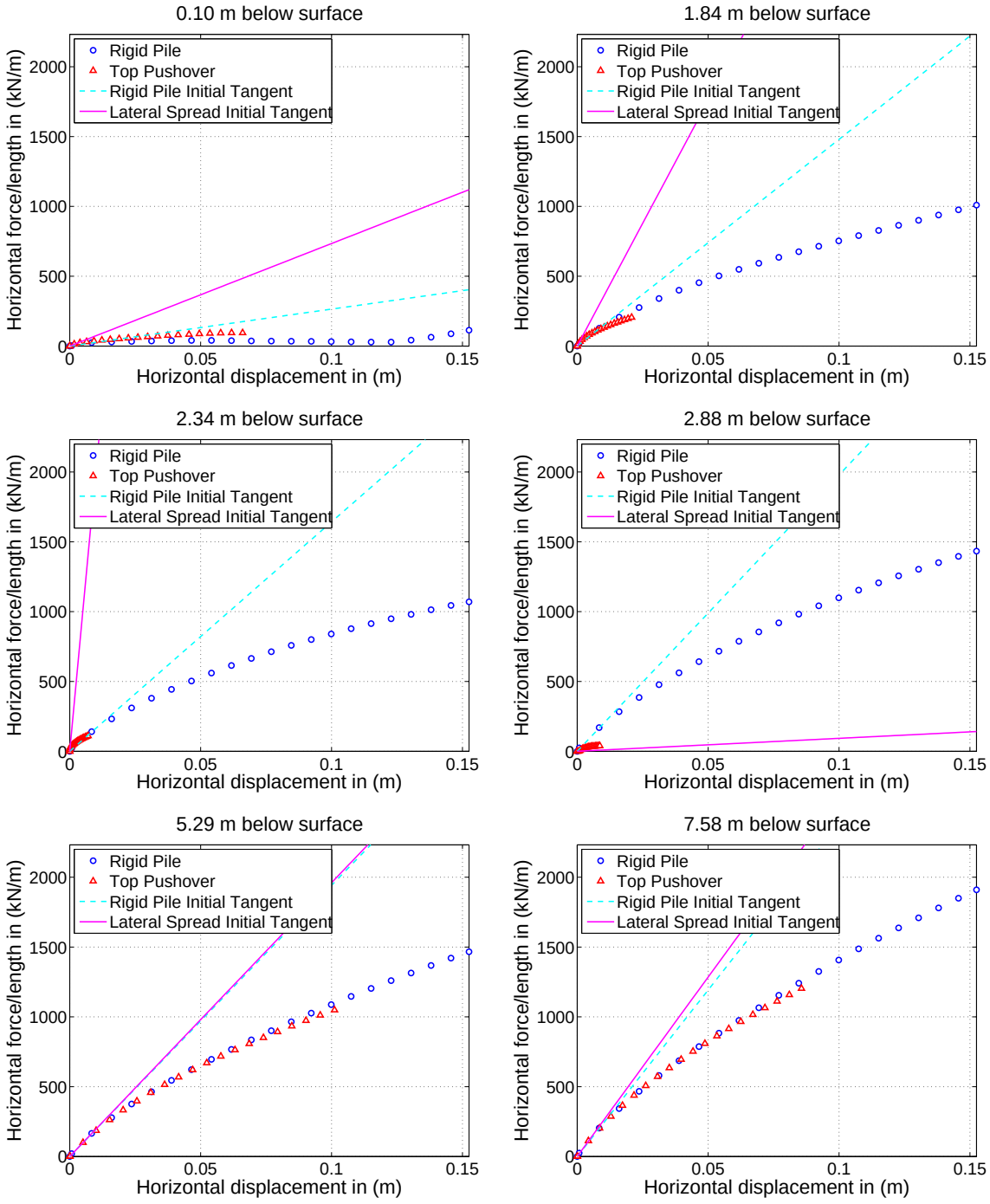

Figure 6.13: Extracted $p-y$ curves from the lateral spreading and rigid pile cases in non-homogenous soil for the 0.6096 m pile. The fitted initial tangents are shown for each case.

between the pile and the soil are small. An explanation for this observation is offered by way of the Betti–Rayleigh theorem of reciprocal work (Megson, 2005 [19]).

6.2.1 Betti–Rayleigh Theorem of Reciprocal Work

The Betti–Rayleigh theorem of reciprocal work is a principle which relates the work done by two separate load cases acting on a linear elastic body. Consider the elastic body of Figure 6.14 which depicts two separate load cases, **P** and **Q**, acting on the same points of the body, and their respective displacements, **u** and **v**.

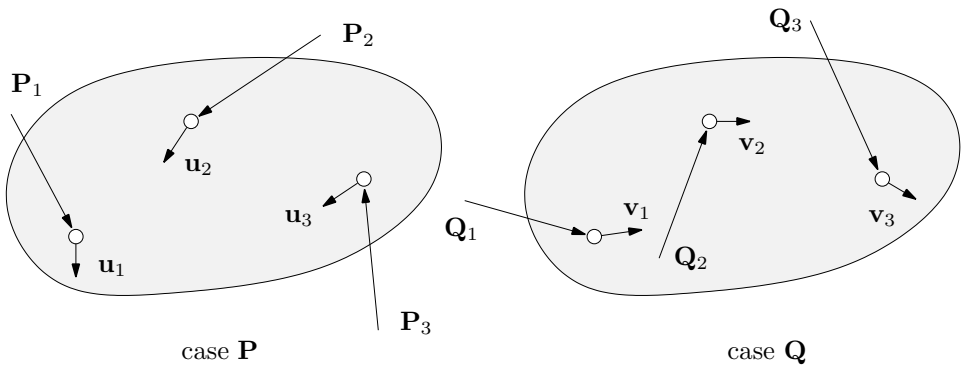

Figure 6.14: Two separate load cases, **P** and **Q**, with respective displacements, **u** and **v**, applied to the same points on a general elastic body.

The reciprocal theorem states that the work done by loads $\mathbf{P}_i$ when moving through the displacements produced by loads $\mathbf{Q}_j$ is equal to the work done by loads $\mathbf{Q}_j$ when moving through the displacements produced by loads $\mathbf{P}_i$ (Megson, 2005 [19]). The Betti–Rayleigh theorem can be expressed using the dot product as

$$\sum_i \mathbf{P}_i \cdot \mathbf{v}_i = \sum_j \mathbf{Q}_j \cdot \mathbf{u}_j \tag{6.17}$$

6.2.2 Application of the Betti–Rayleigh Theorem

To apply this theorem to the problem of a laterally loaded pile, it is convenient to designate load case **P** as the nodal forces applied to a pile having n nodes as its passage is resisted by the surrounding soil, indicating that **u** is the corresponding vector of nodal displacements.

These are the terms which are related to each other to generate the $p-y$ curves at each pile node. If load case **Q** is a unit load applied at an arbitrary node, j, on the pile, then **v** represents the corresponding nodal displacements for this load and (6.17) can be written as

$$P_1 v_1 + P_2 v_2 + \ldots P_n v_n = u_j \tag{6.18}$$

from which a full set of equations can be written, in matrix form, as

$$[\mathbf{A}]\{\mathbf{P}\} = \{\mathbf{u}\} \tag{6.19}$$

in which **P** carries the lateral pile forces, **u** contains the lateral pile displacements, and the components A_{ij} are the displacements at each node i produced by a unit load at node j. Solving (6.19) for the nodal forces results in

$$\{\mathbf{P}\} = [\mathbf{A}]^{-1}\{\mathbf{u}\} \tag{6.20}$$

which can be evaluated for the force, P_j acting at an arbitrary node j as

$$P_j = A_{j1}^{-1} u_1 + A_{j2}^{-1} u_2 + \ldots A_{jn}^{-1} u_n \tag{6.21}$$

where A_{ji}^{-1} represents the components of $[\mathbf{A}]^{-1}$.

A conclusion about the effects of pile kinematics on the $p-y$ curve extraction procedure can be drawn from (6.21) by considering what happens when the displacement at node j is varied in each kinematic case. In the top pushover and lateral spreading cases, if u_j is large, the force acting at node j is largely dependent upon u_j as the contribution by the term $A_{jj}^{-1} u_j$ in (6.21) is dominant

$$P_j = A_{j1}^{-1} u_1 + A_{j2}^{-1} u_2 + \ldots A_{jn}^{-1} u_n \approx A_{jj}^{-1} u_j \tag{6.22}$$

In this case, the assumption that there is a one–to–one relationship between the force and displacement at a node is relatively good, though it is still an approximation. The regions of Figures 6.6 through 6.11 in which the a_1 and lateral resistance ratios are nearly unity coincide with the areas in which the displacements are large, supporting this explanation.

In contrast, in the regions where the displacements of the pile are small, great divergence between the $p-y$ curves returned by the rigid and top pushover cases is observed.

If u_j is small, then the contributions to the force acting at node j by the other terms in (6.21) are no longer insignificant, meaning that at such a point, the assumption of a local force–displacement relationship is relatively poor. This effect is exacerbated when the displacement at a particular node is small compared to adjacent nodes at which the coefficients of [**A**] are relatively large. An example of this is most clearly made by looking at the middle sections of the lateral spreading cases. The nodes which are very near the center of the imposed displacement profile do not tend to move much during the entire process. The nodes just outside of this middle region undergo considerably larger displacements into the surrounding soil, thus affecting the results for the nodes in the middle region.

6.2.3 Proposed Solution to the Problem of Pile Kinematics

The $p-y$ curves extracted from the three–dimensional finite element models cannot be separated from the kinematics of the pile. In the top pushover and lateral spreading cases, the variable magnitude of the displacements with depth causes nodal forces to develop which are inconsistently related to the nodal displacements. A method of $p-y$ curve extraction which is potentially able to work around this kinematic issue is the use of the rigid pile cases to generate the curves for each pile.

In the rigid pile cases a uniform displacement profile is applied over the length of the pile, thus, the displacements at each node are identical. This aspect of the rigid case indicates that the coefficients of [**A**] are the determining factor in the force applied at a given node. In a manner similar to that of the nodes experiencing large displacements in the variable kinematic cases, this creates a situation in which the assumption of a direct relationship between the forces and displacements at the individual nodes is relatively good, as [**A**] is diagonal dominant.

It is hypothesized that the soil response resulting from a given laterally–loaded pile is independent of the pile kinematics, though the $p-y$ curves extracted are not. Additionally, it is hypothesized that the curves generated from the rigid pile cases using the three-dimensional model can adequately describe the soil response, via $p-y$ curves, for any soil–pile combination. To test the validity of these hypotheses, the set of $p-y$ curves

generated using the rigid pile case for each pile are applied as soil resistance springs in one–dimensional models of the piles. The 1D cases are created using $p-y$ curves representing homogenous soil as well as those reduced due to the presence of the liquefied layer. These 1D models are then subject to the top pushover and lateral spreading cases to verify if the resulting pile shear and moment distributions are consistent with those returned by the corresponding three–dimensional cases. This process is discussed further in Chapter 7.

6.3 Effects of Mesh Size on $p-y$ Curve Data

In all finite element analyses, the level of mesh refinement present in the model has bearing on the results which are returned. In general, the more refined a mesh becomes, the better the model is able to simulate the intended scenario. As a mesh becomes more fine, the number of nodes, elements, and degrees–of–freedom in the model must increase. Along with these increases comes an increased computational demand associated with running the model. The size of the global stiffness matrix is dependent upon the square of the number of degrees–of–freedom in the model, and this corresponds with the storage demand related to the problem. The solution effort for solving the global system of equations is related to the the number of degrees–of–freedom and the bandwidth of the stiffness matrix. For a three–dimensional problem with a fully populated stiffness matrix, increasing the number of nodes in the model by two results in approximate increases in the storage and solution demands of 60 and 500 times, respectively. The drastic computational cost which is associated with increased mesh refinement must be accounted for when creating and running large 3D models.

The models used in this research attempt to limit the number of degrees–of–freedom through the use of symmetry, however, there are still thousands of nodes and associated degrees–of–freedom in the models. Relatively small increases in the number of elements through mesh refinement can significantly affect the computational effort. Exacerbating the cost further, the formulation used for the beam–to–solid contact elements generally leads to large bandwidths in the global stiffness matrices, and a corresponding increase in the necessary solution time. The inclusion of plasticity in the constitutive models necessitates smaller time steps, also increasing the computational effort involved in running the model.

Due to these limiting factors, the meshes involved in the models are necessarily coarse. In an attempt to take advantage of the benefits associated with a refined mesh without greatly increasing the computational time and effort, selective mesh refinement is used in the finite element models.

6.3.1 Selective Mesh Refinement

When a pile is pushed through a soil profile with a liquefied layer, it is important to capture the interaction between the pile and the soil near the solid–to–liquefied layer interface with a relatively high degree of resolution. For this case, the regions near the top and bottom of the pile are comparatively less important. The models are built to take advantage of the relative levels of importance assigned to the various sections along the length of the pile through the use of selective refinement. The vertical size of the soil and pile elements is somewhat large at the top and bottom of the mesh. These large elements gradually transition into smaller elements from either side of the liquefied layer, with the smallest elements existing in the middle of that layer. Similarly, the horizontal size of the soil elements is large at the boundaries of the mesh and becomes smaller as the radial distance to the center of the pile decreases. This pattern of selective refinement is illustrated in Figure 2.1 (page 11). Effectively, the models have been developed such that the mesh is refined in the areas of importance and left unrefined in the other areas.

6.3.2 Effects of Selective Refinement on the $p-y$ Parameters

Examining the results for each of the kinematic cases discussed in Section 6.1.1, it is observed that there are fluctuations in the plots of initial stiffness and ultimate lateral resistance with depth in the location of the liquefied layer. This behavior is present in all cases and for all piles, even those in which the soil profile is entirely homogenous. The summary plots of the previous section involve the ratios of two cases run using the same selectively refined mesh and therefore do not display similar fluctuations. While these ratios are valuable evaluation tools, the actual values of the curve parameters must also be verified as sensible, otherwise any conclusions drawn from the ratios are meaningless. In order to gain confidence in the

extracted $p-y$ parameter distributions, the cause of the fluctuations must be discerned.

It is hypothesized that the selective mesh refinement scheme is responsible for altering the results. The areas of inconstancy in the parameter distributions correspond not only to the location of the liquefied layer, but to the areas of differential mesh refinement as well. Because the failure of a cohesionless soil is governed by shear, it seems sensible to assume that the size of the elements will affect the perceived stiffness that the elements display towards this failure mechanism. For example, in the wedge–type soil failure mechanism that is common at shallower depths, all of the gauss points which are aligned with the failure surface must have reached yield in their associated constitutive models for the model to display the global behavior. Changing the vertical size of the elements changes the spacing of the gauss points and may alter the number of gauss points which must experience local failure in order for the global failure to occur, thus, altering the response of the soil as a whole, and subsequently, the extracted $p-y$ curves.

In order to test the hypothesis that the selective mesh refinement is responsible for the observed fluctuations in the soil response extracted from the models, a uniform mesh is generated for each of the piles. This uniform mesh has the same outer dimensions and layout as the selectively refined meshes, however, the soil and pile elements are all uniformly sized in the vertical direction. Two rigid pile cases are run using this uniform model, one in a homogenous soil profile, and the other in a three–layer soil profile with a liquefied center layer. Figure 6.15 shows the distributions of initial stiffness and ultimate resistance, respectively, over the length of the 1.3716 m pile for the rigid pile case in homogenous soil using the uniform and selectively refined meshes. As shown, both the stiffness and resistance values fluctuate in the center of the pile for the selectively refined case. The uniform case does not display similar behavior. Instead, the distributions resulting from the uniform mesh are smooth over the entire length of the pile. These results support the hypothesis.

A solution is proposed to smoothen the soil response in the selectively refined cases by using the results of the uniform mesh cases. This solution is proposed in lieu of running all previously analyzed cases a second time, using a uniform mesh, in order to obtain smooth soil response while simultaneously losing the valuable mesh resolution at the liquefied interface. Instead of that laborious pursuit, the selectively refined results are smoothened through

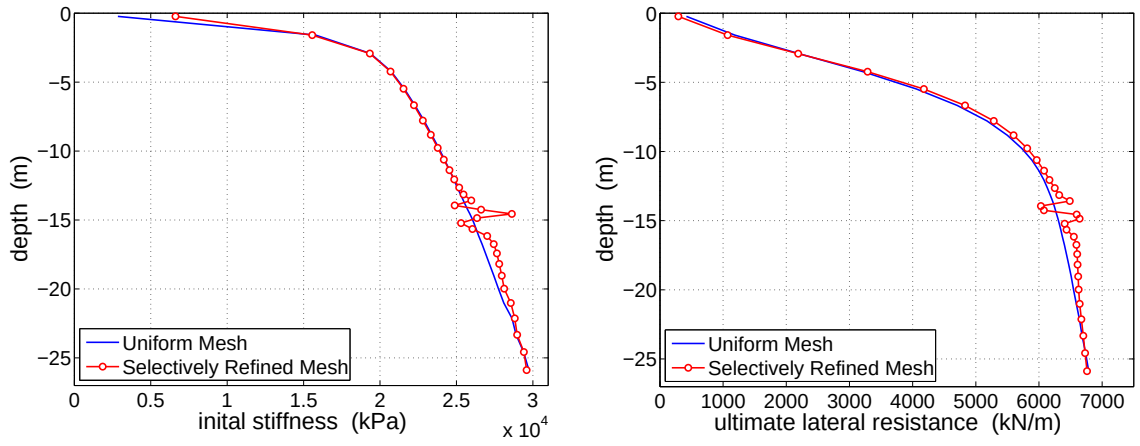

Figure 6.15: Distributions of initial stiffness and ultimate lateral resistance with depth for the 1.3716 m rigid pile case in an entirely homogenous soil profile.

multiplication with the ratios of uniform results with the refined results for the rigid pile in homogenous soil case for each pile. In addition to saving weeks of effort, this proposed solution also allows for further verification of the hypothesis that the selectively refined mesh scheme is the cause of the fluctuations in soil response.

Figure 6.16 shows both the original and smoothened distributions of initial stiffness and ultimate lateral resistance for several kinematic cases. For the ultimate resistance, only the rigid pile case is considered due to the inability of the alternate kinematic cases to fully activate the soil response at all depths. The ratios obtained using the rigid pile cases in homogenous soil profiles are able to remove the fluctuations in the parameter distributions for each of the alternative pile kinematic cases. Though the stiffnesses are suspect, for reasons related to the pile kinematics and discussed in Section 6.2, the plot shown in Figure 6.16(c) illustrates well the effect of the smoothening procedure. The presented case is a top pushover in an entirely homogenous soil profile, and like the rigid pile case discussed previously, there are fluctuations in the data set in the area where the mesh is more refined. It is important to note that though these effects may appear as if there is a separate soil layer in this location, that is simply not the case. Through multiplying the initial stiffness distribution from this top pushover case by the ratio of the uniform results to the selectively

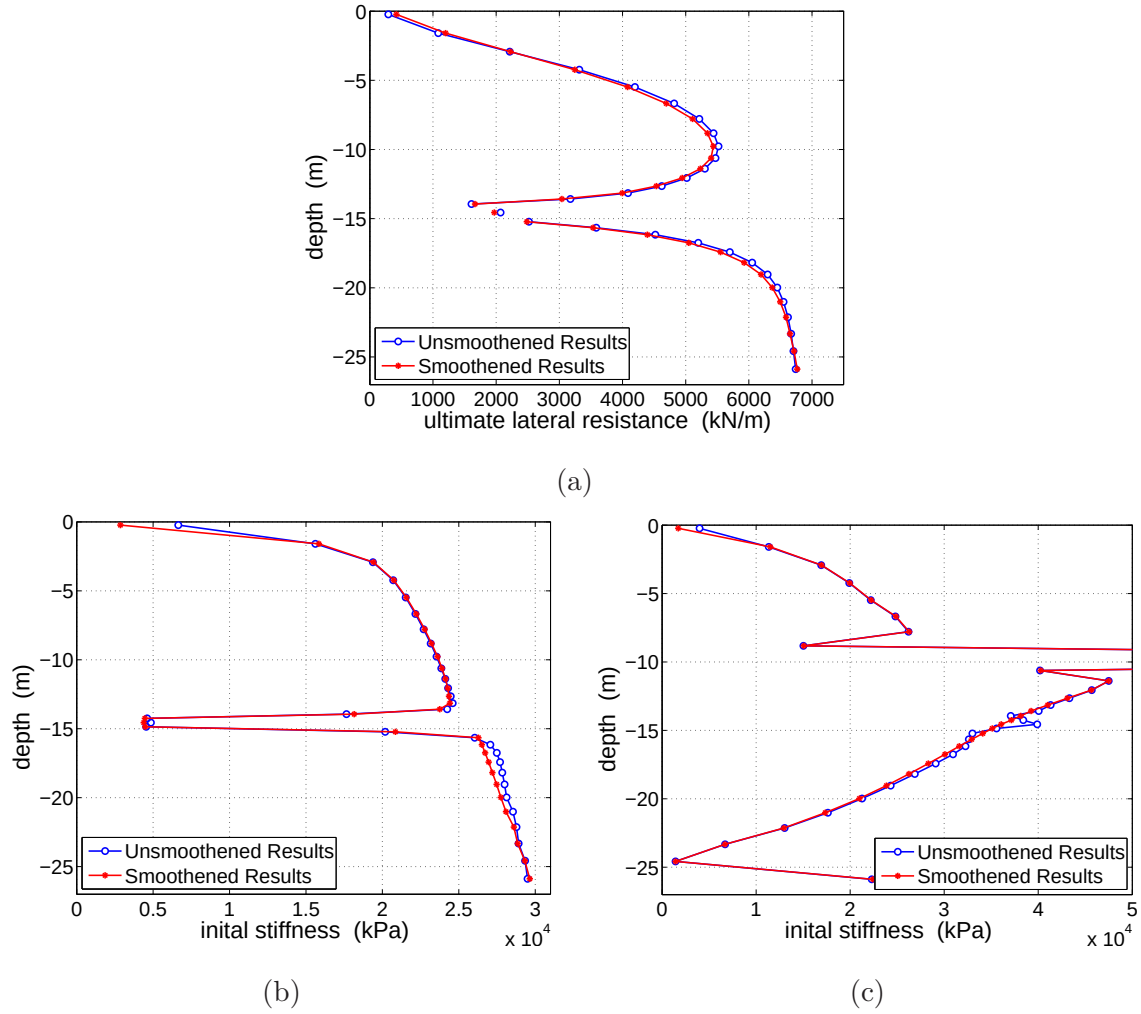

Figure 6.16: Examples of applying the smoothening process to the distributions of $p-y$ curve parameters for the 1.317 m pile. (a) Distribution of p_u from rigid pile in liquefied soil profile. (b) Distribution of a_1 from rigid pile in liquefied soil profile. (c) Distribution of a_1 from top pushover in homogenous soil profile.

refined results for the rigid pile case, the inconsistencies in the results are removed, creating a smooth distribution through the depths encompassed by the increased mesh resolution.

The results of Figure 6.16 demonstrate the effectiveness of the smoothening procedure of multiplying the soil parameters by a ratio obtained through comparison with a uniformly–meshed model. This result further verifies the validity of the hypothesis with respect to the selective mesh refinement. Additionally, considerable effort is saved through the use of

this procedure, allowing for the results of all previously run cases to be modified to account for the known effects of the selective mesh refinement incorporated into the models. The benefits of an increased level of resolution in the regions in and around the liquefied layer can still be reaped, now with an improved confidence that the results are valid. It has been shown that the use of a selectively refined mesh can affect the results of a three–dimensional finite element simulation, but through careful diagnosis and recognition, these effects can be nullified in a relatively cheap and simple manner.

6.4 Boundary Effects on Soil Response

The finite element models generated for the studies performed in this research are intended to include sufficient lateral extents such that the behavior of the pile is relatively unaffected by the fixed boundaries on the outside surfaces of the mesh. In order to gauge the significance of the fixed boundaries on the soil response recorded in the models, a new mesh is generated having increased lateral extents. This extended mesh is shown in Figure 6.17. The extended mesh uses the standard mesh used in all other aspects of this research as a foundation, however, in this alternate model, the soil elements extend for an additional ten pile diameters in the direction of loading. By increasing the amount of soil between the pile and the fixed boundary, it is expected that the effects of the boundary on the lateral response of the soil profile can be discerned. In line with the findings discussed in Section 6.2, all of the analyses discussed herein involve the rigid pile kinematic case.

The distributions of the relevant $p-y$ curve parameters of initial stiffness and ultimate lateral resistance are plotted in Figure 6.18. As could be expected, the initial stiffnesses returned from the two meshes are very similar. The proximity of the boundary should not significantly affect the response of the soil at such low levels of pile displacement. The differences between the two distributions are easily attributable to minor variations in the meshing around the pile between the two models. The ultimate lateral resistance, however, displays a reduction in magnitude for the extended mesh case as compared to the standard mesh case. This result confirms the suspicion that the fixed boundary is able to affect the results of the laterally–loaded pile models, at least with regards to the ultimate resistance provided by the soil elements.

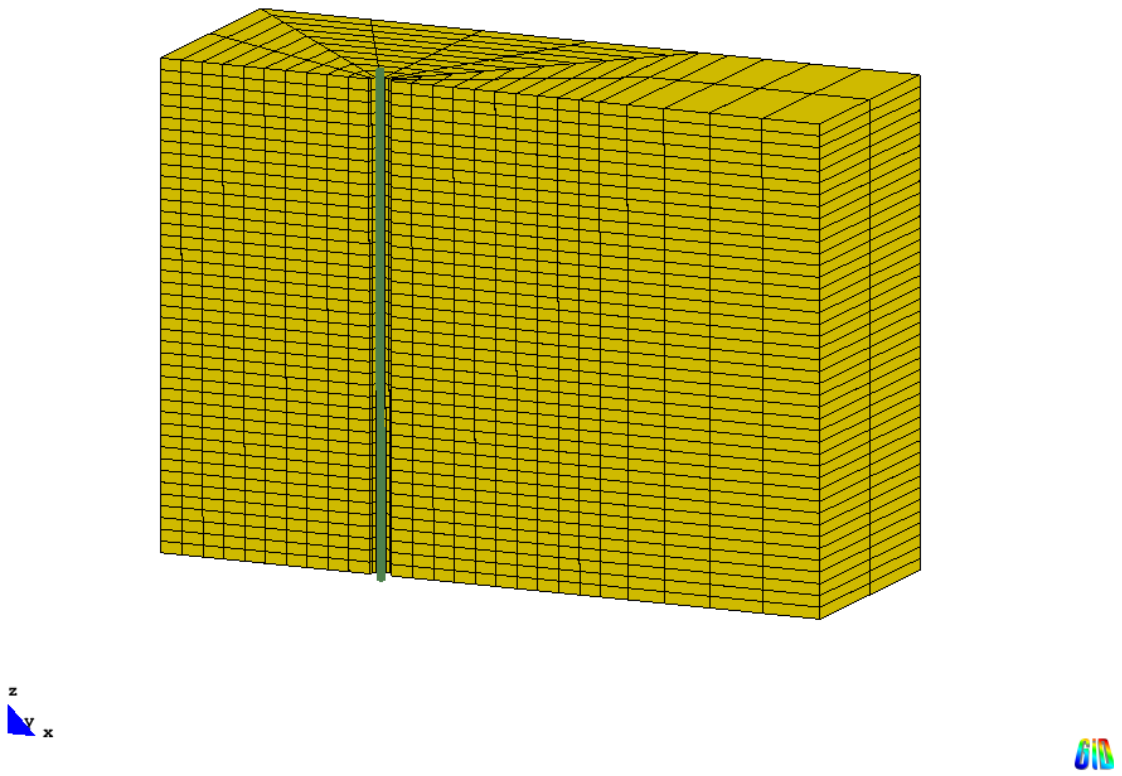

Figure 6.17: Laterally–extended mesh for 0.6096 m pile design.

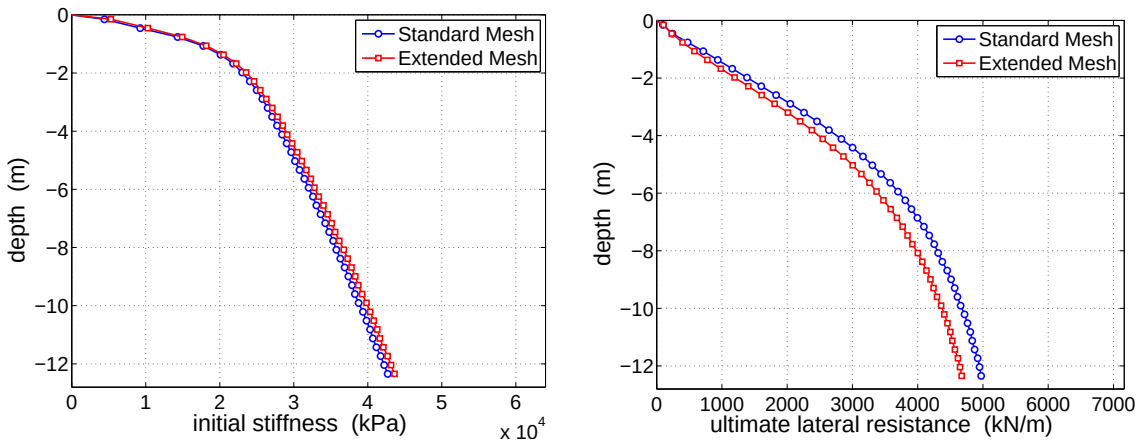

Figure 6.18: Comparison of $p-y$ curve parameter distributions for extended and standard meshes for the 0.6096 m pile.

The value of p_u returned by the models reflects the maximum load which the pile can exert on the soil before failure. This parameter is directly related to failure of the soil surrounding the pile. The Drucker–Prager plasticity model has a pressure–dependent yield surface, indicating that as the confining pressure on a particular element increases, there is a corresponding increase in the yield capacity for that element. This indicates that p_u should increase with either increasing depth or with increasing confining stress. As the pile is pushed into the soil profile, the soil elements must deform to accommodate its passage. At shallow depths, the overburden stress is relatively small, thus, as the pile is pushed laterally, the soil elements are pushed outwards and upwards by its passage. The distribution of this soil heave extends well in front of the pile, and to the side as well, as illustrated in Figure 6.19 which shows the distribution of vertical displacement in the soil in a plan view.

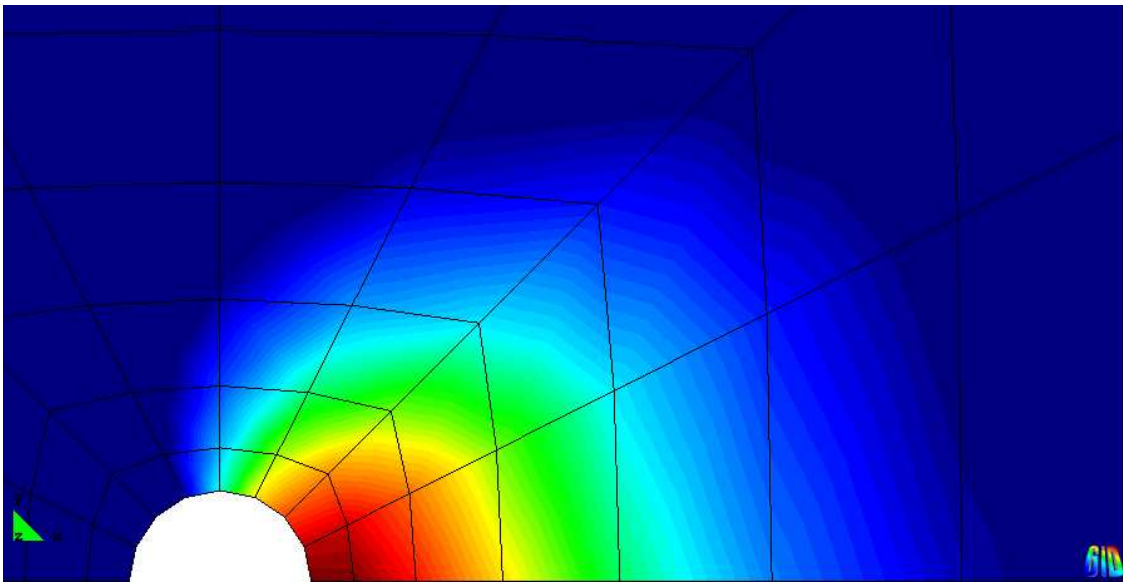

Figure 6.19: Plan view detailing the distribution of vertical displacement (i.e. soil heave) in the soil elements due to the passage of the pile. The dark red areas indicate the greatest magnitude of vertical displacement, while the darker blue areas represent zero displacement.

At increased depth, the overburden pressure in the soil elements becomes larger due to both the self weight of the soil and the active pressure provided by the overlaying elements expanding upwards. The zone in which the soil elements are pushed upwards and outwards by the passage of the pile therefore reduces in areal extent with increasing depth, naturally forming a wedge–like shape of moving soil in front of the pile. This type of wedge failure can clearly be seen in Figure 6.20 which shows the distribution of positive vertical displacements in the extended mesh model. The formation of the wedge affects the deeper soil elements by actively increasing the confining pressure as it expands.

In the case of the standard mesh, shown in Figure 6.21, the proximity of the fixed boundary prevents the formation of a full wedge by limiting the forward movement of the soil elements. The boundary also allows for larger compressive lateral stresses to develop. The overburden pressure can be overcome more easily at deeper locations, leading to the increased magnitude in vertical displacements and the increased extents of this upwardly–moving zone displayed in Figure 6.21. This increase in both the volume of soil which is moved upwards and the magnitude of the displacement leads to an increase in the confining pressure at lower depths, especially as compared to the results obtained from the laterally–extended mesh. The stress increase can be observed in Figures 6.22 and 6.23 which show the distributions of the first invariant of stress, $I_1 = \sigma_1 + \sigma_2 + \sigma_3$, in the two models. As shown, the first stress invariant is significantly larger in compression in the standard mesh than in the extended mesh due to the build–up caused by the proximity of the pile to the fixed boundary. The observed increase in the ultimate lateral resistance of the soil elements in the standard mesh over that displayed by the extended mesh shown in Figure 6.18 is attributable to the increased confining stresses which exist in that model.

The increase in the estimated values of p_u associated with the use of the standard mesh is apparent, but is not necessarily significant. In the current simulations, the pile is not pushed sufficiently far into the soil as to fully activate the ultimate resistance of the soil at depth. Due to this shortcoming, the obtained values of p_u in these locations are extrapolated by the curve–fitting procedure and may not represent the true capacity of the soil. This observation, along with alternative plasticity formulations which alleviate the boundary effects, is analyzed and discussed in Chapter 7.

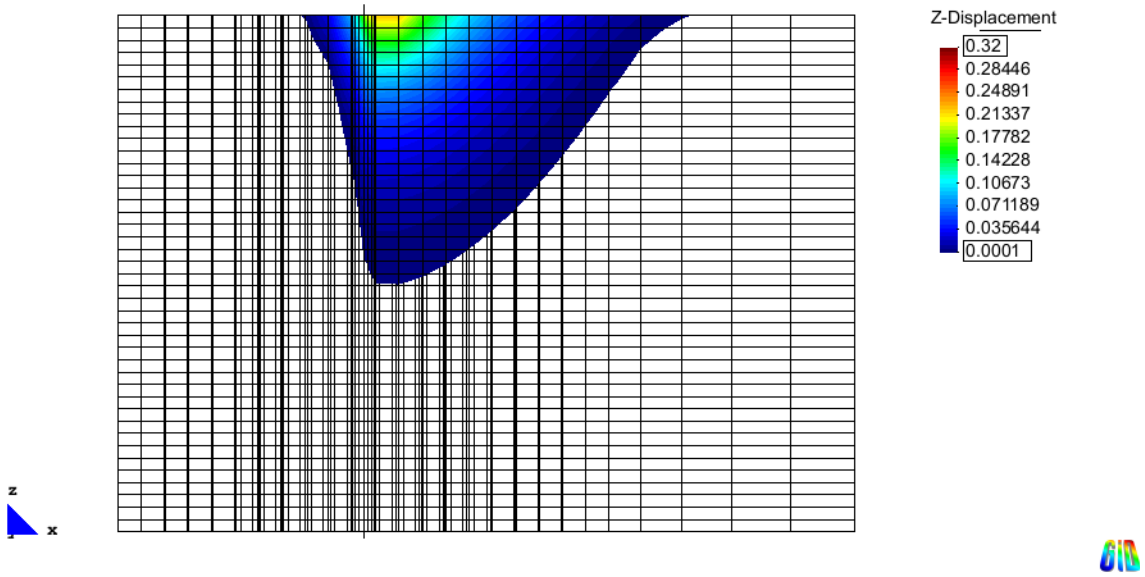

Figure 6.20: Contour plot of vertical soil displacements for the rigid pile case in the laterally–extended mesh. Only upward displacements are considered.

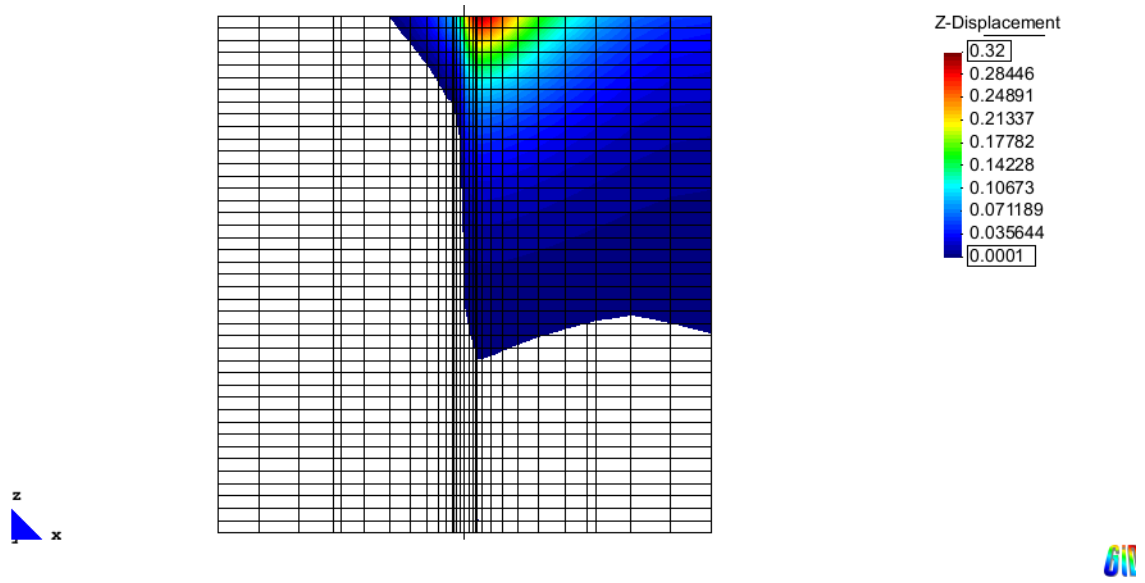

Figure 6.21: Contour plot of vertical soil displacements for the rigid pile case in the standard mesh. Only upward displacements are considered.

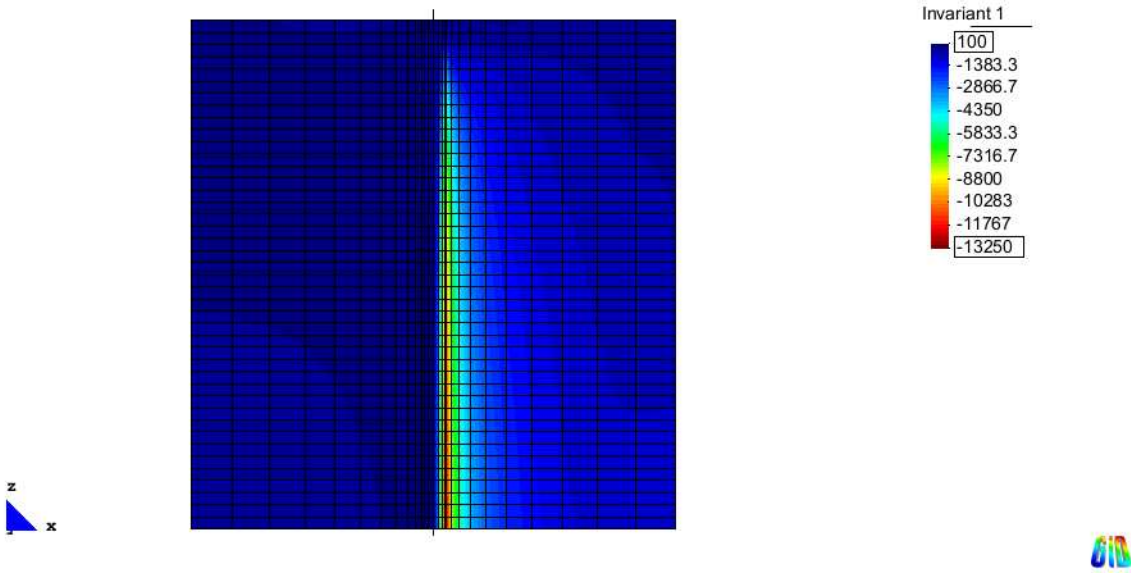

Figure 6.22: Distribution of the first invariant of stress, $I_1 = \sigma_1 + \sigma_2 + \sigma_3$, in the standard mesh for the 0.6096 m pile.

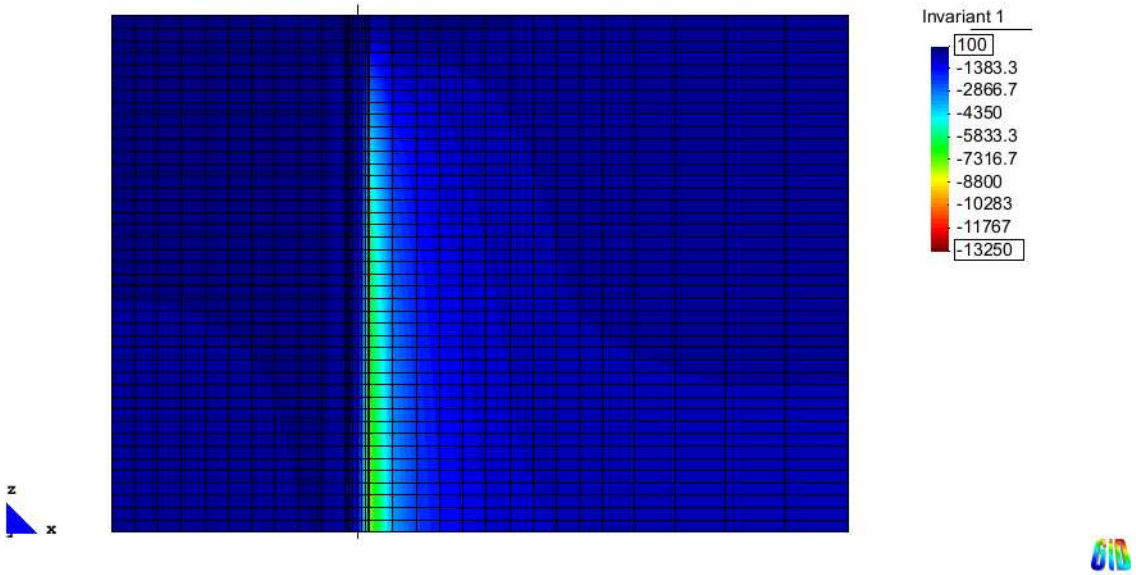

Figure 6.23: Distribution of the first invariant of stress, $I_1 = \sigma_1 + \sigma_2 + \sigma_3$, in the extended mesh for the 0.6096 m pile.

6.5 Summary

It is of interest to evaluate the results obtained using three–dimensional finite element models of piles embedded in laterally spreading soils in the context of the commonly used $p-y$ method. In order to accomplish this goal, a method in which to extract reliable and sensible $p-y$ curves was developed. Through identifying the key curve parameters of initial stiffness and ultimate lateral resistance, a least squares fitting technique is used to obtain smooth functions which describe both the key parameters and the curves themselves. During the initial analysis of certain extracted curves, it is hypothesized that the pile kinematics are influencing the extracted $p-y$ curves. Three distinct kinematic cases are developed and analyzed to test this hypothesis: a rigid pile case, a top pushover case, and the previously analyzed lateral spreading case. Comparing the results of each case by way of the identified key curve parameters, it is determined that the kinematics of the pile do indeed affect the extracted $p-y$ curves. The kinematic effects on the $p-y$ curves include insufficient activation of soil response and inconsistent stiffness both initially and over the course of the loading process. To work around the kinematic problem, the rigid pile cases, which eliminate the pile kinematics from the model, are used to extract all subsequent $p-y$ curves.

It is also observed that variations in the size of the mesh along the length of the pile cause the soil response to be inconsistently represented in the results. A uniformly–meshed model is generated and the ratios of the initial stiffness and lateral resistance in this new model to corresponding results obtained from the original, selectively refined, models are used in order to smoothen the past results. When analyzing the ratios of two cases formed using the same mesh, these effects are unimportant, however, in order to view the parameter distributions with their actual values or to compare results from a dissimilar mesh, the smoothening process must be employed.

During the process of extracting and initially analyzing representative $p-y$ curves from the finite element models, the effects of the fixed boundaries on the recorded soil response are also explored. It is determined that the initial stiffness of the curves is unaffected by the proximity of the boundary to the center of the pile, however, the ultimate lateral resistance of the curves is reduced by up to 10% when the lateral extents of the model are increased.

This reduction is related to the ability of the extended soil mesh to allow a full soil failure wedge to develop as well as the increased capacity for the soil to compress before the pile begins to feel the boundary. This study indicates that the presence of the fixed boundary is able to affect the distribution of lateral resistance in the soil, though only to a certain degree. The significance of this observation is discussed further in Chapter 7.

Chapter 7

EVALUATION OF REPRESENTATIVE SOIL RESPONSE CURVES EXTRACTED FROM FINITE ELEMENT MODELS

7.1 Introduction

Representative $p-y$ curves describing the soil response to three laterally–loaded piles are obtained from three–dimensional finite element analyses. A series of comparative studies are conducted in order to evaluate these curves and the recorded soil responses. The effect of a liquefied layer on the response of the adjacent solid soil layers is evaluated through comparisons between the results of models run both with and without a liquefied layer. Through the use of the application of increasing overburden pressure to the surface of the models, the weakening effects of the liquefied layer at different depths are also investigated.

The use of conventional analysis methods in the context of the lateral spreading deformation case is evaluated using the extracted soil responses from the 3D models. Comparisons are made between the distributions of the previously identified key curve parameters of initial stiffness and ultimate lateral resistance, p_u, over the length of the pile, and the extracted curves themselves are compared to $p-y$ curves as defined by conventional methods. Lateral spreading models are created and analyzed in one–dimension using beam elements and nonlinear force density–displacement springs to represent the soil. Both FEA–extracted and conventionally–derived $p-y$ curves are used to define the soil response springs in these models and the resulting pile bending responses are compared to each other and to the results obtained from 3D lateral spreading simulations.

Several new models are created in order to verify and expand upon observations made from the existing finite element models. Examination of the results from the finite element simulations indicate that increased mesh resolution is required to capture the appropriate soil response at near–surface depths. A solution is provided through the generation of a series of new meshes which only consider the soil and pile up to a depth of ten meters.

The decrease in depth allows for increased mesh refinement over the standard models with no corresponding increase in computational demand. Additionally, evaluation of the existing models indicates that the magnitudes of p_u returned from the models at depth are significantly less than those predicted using conventional means. Plane strain models are generated and analyzed in order to investigate this observation.

7.2 The Ultimate Lateral Resistance of Cohesionless Soil

The problem of a pile moving through soil is highly three–dimensional as well as nonlinear, making the task of determining a suitable distribution for the ultimate lateral resistance of a cohesionless soil a difficult one. The complexity of the problem is such that, over the past fifty years, there have been multiple proposed methods for defining a suitable distribution of ultimate lateral resistance provided by a particular cohesionless soil against the lateral motion of a pile. The methods often utilize approximate analyses and semiempirical strategies in order to determine the ultimate lateral resistance. Perhaps due to the inherent simplifications necessary to reach these proposed solutions, the results obtained from the various methods display significant variation.

In general, each method is a function of the angle of internal friction of the soil as well as the diameter of the pile, the unit weight of the soil, and the depth below the ground surface. These are all constant values for a particular problem, indicating that the resulting ultimate resistance values from the various methods should be similar, however, in practice, the various methods produce resistances which display significant variation for matching input parameters, especially at depth. Figure 7.1 shows the distributions of ultimate resistance estimated by several considered methods for a 0.5 m diameter pile in soil having a unit weight, $\gamma = 20$ kN/m^3, and a friction angle, $\phi = 35^\circ$. As shown, the methods match up fairly well at shallow depths, however, as depth increases, the predicted ultimate resistances begin to diverge significantly.

It is important to note that these methods were developed based primarily upon piles loaded at the top. In this case, overestimation of the ultimate lateral resistance, p_u, at increased depths is relatively harmless. The majority of the deformation takes place at shallow depths, and unless the pile is extremely stiff, there is not much deflection at increased

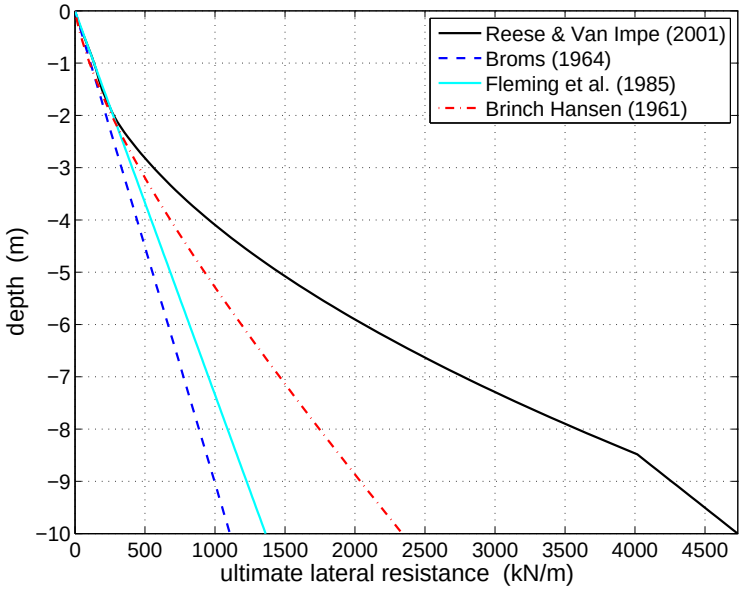

Figure 7.1: Distributions of ultimate lateral resistance for a 0.5 m diameter pile as specified by four predictive methods. The soil is assigned a unit weight of $\gamma = 20$ kN/m^3 and a friction angle of $\phi = 35°$.

depths, thus, the ultimate resistance is not activated. In the case of lateral spreading, however, large pile deformations do occur at advanced depths, and the predicted values of p_u at these depths become increasingly important. A selection of the proposed methods are summarized briefly in the following section.

7.2.1 A Brief Summary of the Considered Predictive Methods

Four proposed methods found in the literature for predicting the distribution of the ultimate lateral resistance of a cohesionless soil are used to evaluate the relevance of the extracted distributions of that same parameter from three–dimensional finite element models. These four methods vary in complexity and also vary greatly in their results. A summary of the essentials of each of these considered methods follows.

Broms' Method

Broms (1964) [6] proposed a method based upon the passive earth pressure coefficient, as calculated by the Rankine earth pressure theory, K_p, which can be computed as

$$K_p = \tan^2\left(45^\circ + \frac{\phi}{2}\right) \tag{7.1}$$

Working under the assumptions that the active earth pressure acting on the back of the pile can be neglected and that the shape of the pile has little effect on the mobilized soil resistance, Broms proposed the following expression for the prediction of the ultimate lateral resistance, p_u, in units of force per unit length of pile

$$p_u = 3K_p\gamma zB \tag{7.2}$$

in which z is the depth, γ is the soil unit weight, and B is the pile diameter. Broms defined the distribution of passive pressure on the front of the pile to be equal to three times the Rankine earth pressure coefficient based upon correlations with limited empirical evidence, indicating that this tends to underestimate the magnitude of p_u which in turn leads to conservative results when applied to a pile. This method creates a distribution of lateral resistance which varies linearly with depth, making no distinctions for depth–appropriate failure mechanisms such as wedge failure at near–surface depths or flow–around failure at deeper depths. As shown in Figure 7.1, Broms' method estimates the lowest values of p_u with depth of all the considered procedures.

Method of Fleming et al.

Using a similar line of thought to that of Broms, Fleming et al. (1985) [10] propose a distribution of p_u which is proportional to the square of the Rankine passive earth pressure coefficient and is described by the expression

$$p_u = K_p^2\gamma zB \tag{7.3}$$

The method of Fleming et al. also results in a linear distribution of p_u with depth with no contingency for depth–appropriate failures. Compared to the method of Broms (1964) [6],

which tends to underestimate the magnitude of p_u, the values of p_u calculated using (7.3) compare more favorably with empirical results. When the angle of internal friction $\phi = 30°$, the results of (7.2) and (7.3) are identical. For most sands encountered in the field, $\phi > 30°$. Therefore, in the majority of cases, the method of Fleming et al. produces larger values of p_u with depth than the method proposed by Broms.

Method of Reese and Van Impe

Reese and Van Impe (2001) [23] present a method of estimating the ultimate lateral resistance for a cohesionless soil which, unlike the methods described by (7.2) and (7.3), accounts for two distinct depth–specific soil failure mechanisms. The ultimate resistance distribution discussed by Reese and Van Impe utilizes two expressions

$$p_u = \overline{A}\gamma z \left[\frac{K_o z \tan\phi \sin\theta}{\tan(\beta-\phi)\cos\alpha} + \frac{\tan\beta}{\tan(\beta-\phi)}(B + z\tan\beta\tan\alpha) + K_o z \tan\beta(\tan\phi\sin\beta - \tan\alpha) - K_a B \right] \tag{7.4a}$$

$$p_u = \overline{A}\gamma z B \left[K_a(\tan^8\beta - 1) + K_o \tan\phi \tan^4\beta \right] \tag{7.4b}$$

of which the lesser result is taken as p_u for a particular depth. The coefficient, $\overline{A}$ is determined from the ratio of depth, z, to pile diameter, B. Reese and Van Impe recommend using $K_o = 0.4$ and define the other terms of (7.4a) and (7.4b) as

$$\alpha = \frac{\phi}{2} \tag{7.5a}$$

$$\beta = \frac{\pi}{4} + \alpha \tag{7.5b}$$

$$K_a = \tan^2\left(\frac{\pi}{4} - \alpha\right) \tag{7.5c}$$

At near surface depths, (7.4a) accounts for a wedge–type failure of the soil. The wedge–type failure mechanism controls the ultimate lateral resistance resulting from this method from the ground surface until a certain depth at which the curve defined by (7.4a) intersects that defined by (7.4b). At this intersection point, which generally occurs well below the

ground surface, the failure mechanism changes from the wedge failure to a plane strain failure mode in which the soil must flow around the pile. The depth at which this transition occurs is dependent upon both the diameter of the pile and the friction angle of the soil. As the magnitudes of these values increase, the depth of the intersection between the wedge and plane strain failure curves also increases. In Figure 7.1, the intersection of (7.4a) and (7.4b) is clearly visible, occurring at a depth of approximately 8.5 m.

The method used by Reese and Van Impe returns the largest values of p_u with depth of any of the four considered methods for establishing the distribution of ultimate lateral resistance in a cohesionless soil. Reese and Van Impe provide an expansive summary of the $p-y$ analysis method, and for cohesionless soils, present the work of Reese et al. (1974) [22]. The $p-y$ curves commonly used in practice for laterally loaded cohesionless soil are based upon this work, including those used in the computer program LPile (`www.ensoftinc.com`) and those recommended by the American Petroleum Institute (API) (1985) [2].

Brinch Hansen's Method

The method of Brinch Hansen (1961) [5] provides a means of estimating the ultimate lateral resistance for a general frictional soil with cohesion ($c-\phi$ soil), where c is the cohesion and ϕ is the angle of internal friction. Brinch Hansen proposes a distribution of ultimate lateral resistance of the form

$$p_u = \left(\gamma z K_q^D + c K_c^D\right) B \tag{7.6}$$

The coefficients K_q^D and K_c^D are determined using a methodology developed by Brinch Hansen, who, similarly to Reese and Van Impe (2001) [23], approached the problem of defining the distribution of lateral soil resistance with consideration towards appropriate soil failure mechanisms with depth. This is accomplished by defining limiting values of p_u at the ground surface and at great depth. Using these limiting values, the ultimate lateral resistance at any arbitrary depth is determined through interpolation.

For a cohesionless soil, the second term of (7.6) becomes zero, and the coefficient K_q^D must be determined based upon two extreme cases. The limiting value of K_q^D existing at the surface ($z = 0$) is designated as K_q^o and is defined as the difference between the passive

and active coefficients corresponding to the lateral translation of a rough wall, resulting in the expression

$$K_q^o = \exp\left[\left(\frac{\pi}{2}+\phi\right)\tan\phi\right]\cos\phi\tan\left(\frac{\pi}{4}+\frac{\phi}{2}\right) \tag{7.7a}$$

$$-\exp\left[-\left(\frac{\pi}{2}-\phi\right)\tan\phi\right]\cos\phi\tan\left(\frac{\pi}{4}-\frac{\phi}{2}\right) \tag{7.7b}$$

The limiting value at great depth, K_q^∞, is based upon the analysis of a deep strip foundation conducted using a similar plane strain soil failure mechanism as that used by Reese and Van Impe (2001) [23]. This analysis results in the following expression which defines the largest possible value of K_q^D, occurring at depth $z = \infty$.

$$K_q^\infty = N_c\, d_c^\infty K_o \tan\phi \tag{7.8}$$

The terms N_c, d_c^∞, and K_o in (7.8) are defined as

$$N_c = \left[\exp(\pi\tan\phi)\tan^2\left(\frac{\pi}{4}+\frac{\phi}{2}\right)-1\right]\cot\phi \tag{7.9a}$$

$$d_c^\infty = 1.58 + 4.09\tan^4\phi \tag{7.9b}$$

$$K_o = 1-\sin\phi \tag{7.9c}$$

Using these limiting values, Brinch Hansen proposes that the coefficient corresponding to any arbitrary depth be computed using

$$K_q^D = \frac{K_q^o + K_q^\infty a_q \dfrac{z}{B}}{1 + a_q \dfrac{z}{B}} \tag{7.10}$$

in which the term a_q is determined as

$$a_q = \frac{K_q^o}{K_q^\infty - K_q^o}\cdot\frac{K_o\sin\phi}{\sin\left(\frac{\pi}{4}-\frac{\phi}{2}\right)} \tag{7.11}$$

The method of Brinch Hansen estimates values for p_u which fall intermediately between the linear methods proposed by Broms (1964) [6] and Fleming et al. (1992) [10] and that of Reese and Van Impe (2001) [23].

7.3 The Initial Stiffness of $p-y$ curves for Cohesionless Soil

The method for developing $p-y$ curves for cohesionless soils presented by Reese and Van Impe (2001) [23] recommends that the initial portion of the curves be established by the following relation

$$p = k_{py} z y \tag{7.12}$$

in which k_{py} is the coefficient of subgrade reaction with units of force/length^3 and z is the depth below the ground surface. The proposed relation of (7.12) suggests that the initial stiffness of the curves is equal to $k_{py}z$, indicating that the initial tangent to the curves increases linearly with depth. It is suggested that the assumption of a linearly increasing initial stiffness takes some account of soil yield, as values near the surface are likely to be small and will increase with depth due to increased soil strength. Reese and Van Impe recommend a series of representative values for k_{py} based upon relative density for both submerged sands and those above the groundwater table.

The American Petroleum Institute (API) (1987) [2] recommends the following hyperbolic tangent function to describe the shape of $p-y$ curves for cohesionless soils

$$p = A\, p_u \tanh\left(\frac{kz}{A\, p_u} y\right) \tag{7.13}$$

in which the coefficient A accounts for the type of loading (i.e. cyclic or static) and is based upon empirical correlations. Evaluating the derivative of (7.13) with respect to y and evaluating this result at $y = 0$ leads to a definition of the initial stiffness of the curves as kz, which corresponds to that defined by the method of Reese and Van Impe (2001) [23]. The API recommends values of the parameter k which are also representative of sands both above and below the water table. Figure 7.2 shows the representative coefficient of subgrade reaction values for each case as functions of relative density and internal friction angle. The API methodology is originally based upon the work of Reese et al. (1974) [22], therefore, the k values presented in Figure 7.2 match the representative values for k_{py} recommended by Reese and Van Impe (2001) [23].

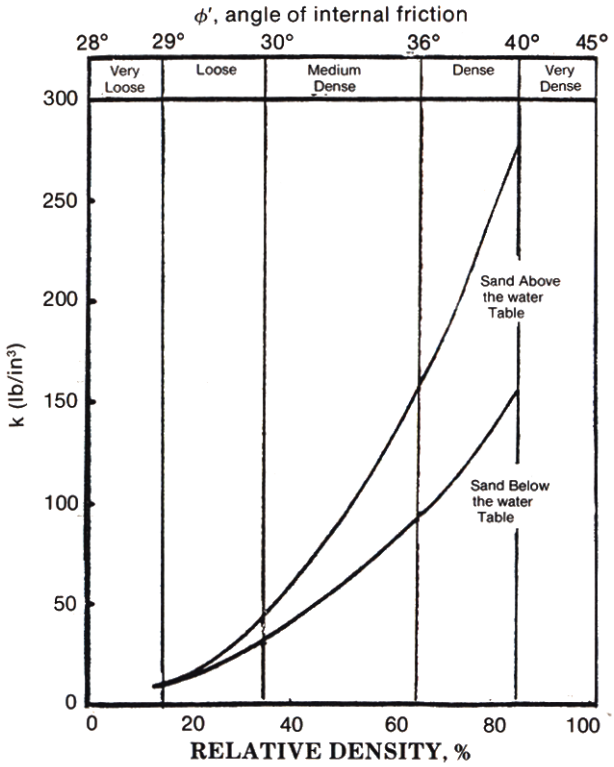

Figure 7.2: Recommended coefficient of subgrade reaction as a function of relative density and internal friction angle after API (1987) [2]. The conversion from units of lb/in^3 is obtained through multiplication with a factor of 271.45 to obtain units of kN/m^3.

7.4 Evaluation Soil Response Extracted from 3D Finite Element Models

Using the procedure discussed in Chapter 6, distributions of initial stiffness and ultimate lateral resistance which are characteristic of the soil response in the finite element models, are obtained for each of the three template pile designs. The distributions resulting from the finite element models with several commonly referenced methods for establishing the distributions of these two parameters along the length of the piles are compared. Through this comparison, the validity of the extracted parameter distributions is examined and the relative merits of the considered predictive methods are discussed. Because the methods discussed in Sections 7.2 and 7.3 have no inherent ability for the inclusion of a liquefied

layer, all of the comparisons of this section are made for a homogenous soil profile. The numerical simulations are conducted using elastic pile elements and the the Drucker–Prager soil constitutive model and associated parameters discussed in Chapter 4.

Figure 7.3 shows the extracted p_u distributions for the three piles at left and the extracted initial stiffness distributions for the same piles at right. Plotted with these extracted distributions are reference distributions for the considered predictive methods discussed in Sections 7.2 and 7.3, respectively. The estimated distributions of p_u are determined using the appropriate pile diameter and depths for each case as well as a soil unit weight of $\gamma = 17$ kN/m^3 and internal friction angle of $\phi = 36^\circ$, values which correspond to the input values used to define the soil constitutive model in the finite element analyses. The linear distributions of initial stiffness with depth for each pile are based upon (7.12). The values of k_{py} shown in each plot are selected such that they match the initial slope of each pile's initial stiffness distribution. The magnitudes of these shown values of k_{py} are summarized in Table 7.1.

7.4.1 Initial Stiffness Distributions

The extracted initial stiffnesses show an expected increase with increasing depth, however, the rate at which the stiffnesses increase is not constant over the length of the pile. The distributions of initial soil stiffness extracted from the finite element models display two distinct linearly–increasing zones. The stiffnesses at shallow depths are significantly less than those at depth, though the rate of increase in this near–surface zone is greater. As depth increases beyond this initial zone, the rate at which the stiffnesses increase begins to lessen, eventually reaching a constant level marked by the second zone of linear increase. The distributions of initial stiffness extracted from the FEA vary significantly from the linear variation suggested by Reese and Van Impe (2001) [23].

As discussed in Section 7.3, the linear distribution of initial stiffness assumed in the method of Reese and Van Impe is defined as the product of the coefficient of subgrade reaction, k_{py} with the depth below the ground surface, z. The results obtained from the FEA suggest that the soil response is represented by two values of k_{py}, one for shallow

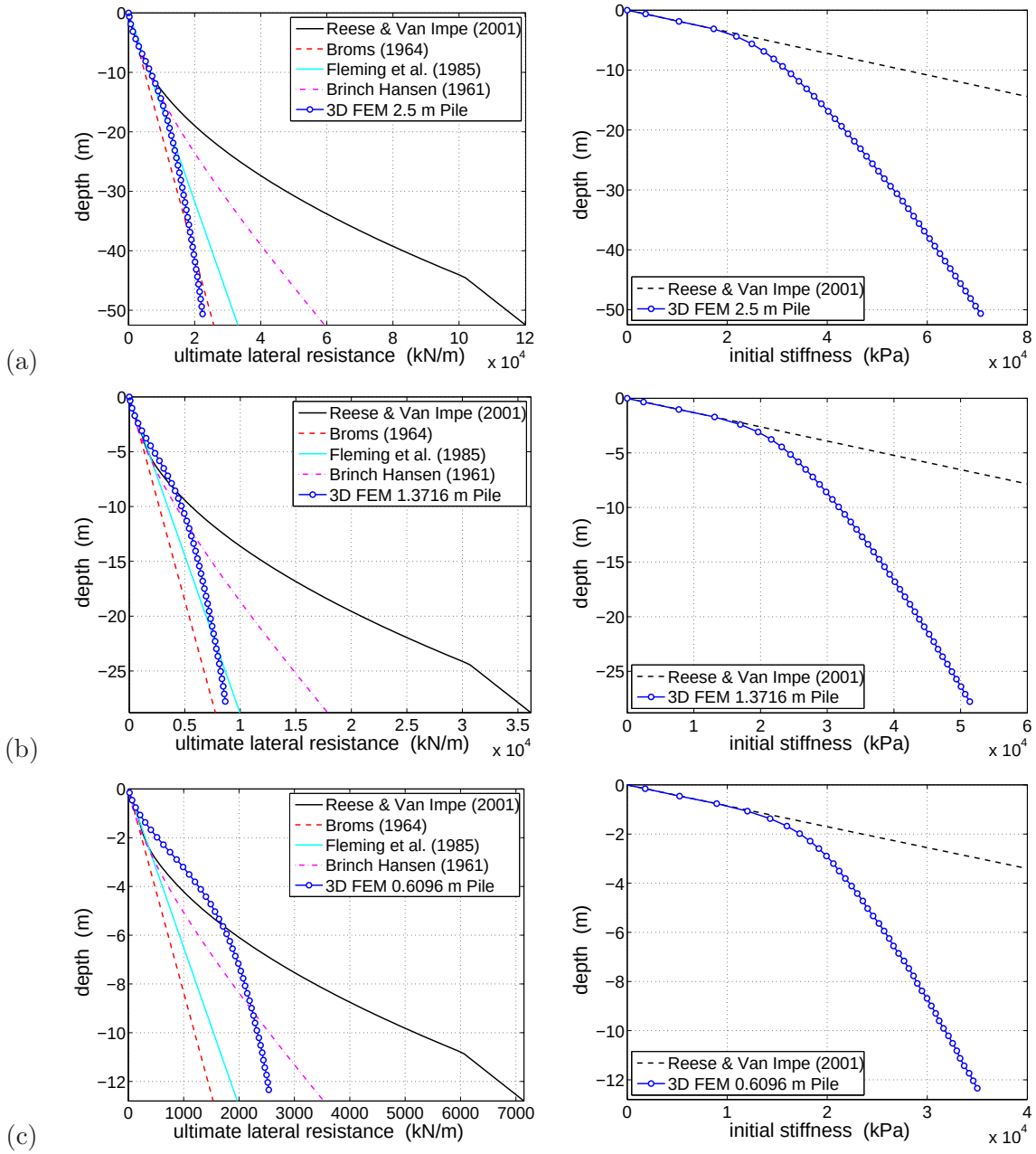

Figure 7.3: Distributions of ultimate lateral resistance and initial stiffness for each of the three template pile designs as compared to commonly referenced distributions. (a) 2.5 m pile; (b) 1.3716 m pile; (c) 0.6096 m pile.

Table 7.1: Coefficients of subgrade reaction which match the initial portion of the FEA initial stiffness distributions for each pile design using the full–length mesh.

	0.6096 m Pile	1.3716 m Pile	2.5 m Pile
k_{py} (kN/m^3)	11750	7650	5550

depths and one for increased depths. At shallow depths, the values of k_{py} represented in the extracted distributions, summarized in Table 7.1 and plotted in Figure 7.3, are similar in magnitude to the values of k_{py} estimated using Figure 7.2 for a loose to medium dense sand, which is in agreement with soil parameters assigned to the constitutive model. The value of k_{py} suggested at increased depths has a magnitude of approximately 1000 kN/m^3 which is less than half of the lowest value of k_{py} recommended in Figure 7.2. It is clear that there are at least two mechanisms contributing to the extracted distributions of initial stiffness with depth. It is also apparent that the linear variation of stiffness with depth recommended by Reese and Van Impe is only applicable to one of these two mechanisms.

The two zones of differing response observed in the distributions of initial stiffness extracted from the 3D models are related to two separate soil constitutive responses. Near the ground surface, the absence of significant overburden pressure leads to the nearly immediate yield of the soil due to the shear stresses generated by the passage of the pile. Thus, the elastoplastic tangent, and not the purely elastic tangent, is reflected in the initial stiffnesses returned near the ground surface. At deeper locations, the overburden pressure is enough to increase shear strength significantly, resulting in an increased elastic regime for those elements and initial stiffnesses which are indicative of the elastic tangent.

The tendency for early yield at shallow depth is illustrated in Figure 7.4 which shows the distribution of the norm of the deviatoric plastic strain, $||\mathbf{e}^p||$, a good indicator for yielding in the soil elements, for the finite element mesh related to the 0.6096 m pile. The distribution of $||\mathbf{e}^p||$ shown in Figure 7.4 represents the state of the soil in the early stages of loading (second increment in the total displacement of the pile). At this very low level of deformation, Figure 7.4 shows that the near surface soil elements are already yielding and that this zone of yielding is largest at the surface and shrinks with depth. These results

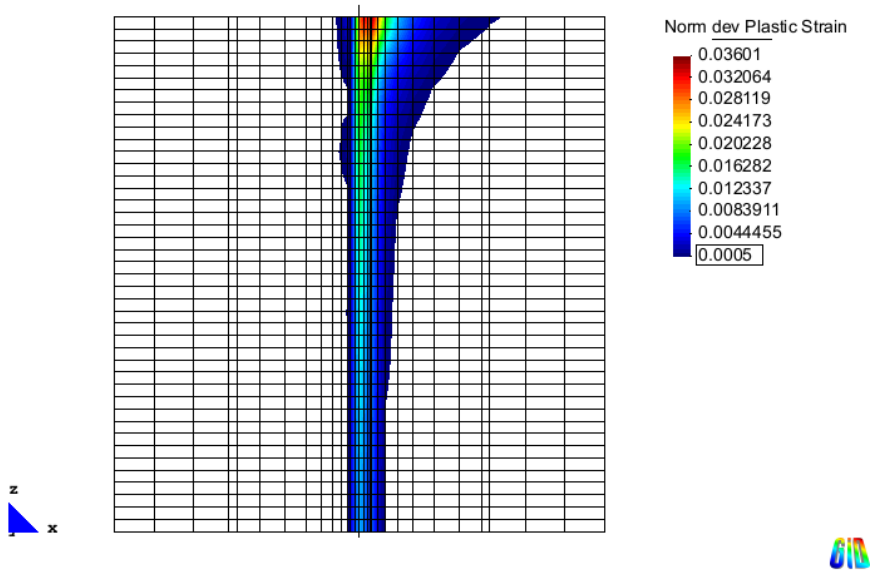

Figure 7.4: Distribution in the norm of the deviatoric plastic strain, $||\mathbf{e}^p||$, for the 0.6906 m pile in the second displacement increment.

suggest that the soil has yielded up to a depth of approximately 1.2–1.5 m below the ground surface, which corresponds well with the results shown in Figure 7.3 at which the initial stiffness rate changes for the 0.6096 m pile.

In order to explore this idea further, the existing models for each pile are run using linear elastic soil behavior for identical pile displacements. The results of these linear elastic simulations are plotted alongside the elastoplastic results for each pile in Figure 7.5. The elastic distributions increase linearly with depth, and do not start at zero. These elastic stiffnesses represent the largest possible values for the initial stiffnesses resulting from the the elastoplastic models. Once increasing overburden pressure has expanded the elastic regime sufficiently, the initial stiffness of the elastoplastic models should be entirely elastic. Above this point, the elastoplastic tangent is reflected in varying degrees in the elastoplastic initial stiffnesses, with increasing effects of yielding towards the surface.

At shallow depths, the initial stiffness is less than the elastic stiffnesses at the same depth. The initial stiffness then increases with depth, first approaching, and then reaching the elastic stiffness. The depth at which the elastoplastic stiffness becomes equal to the

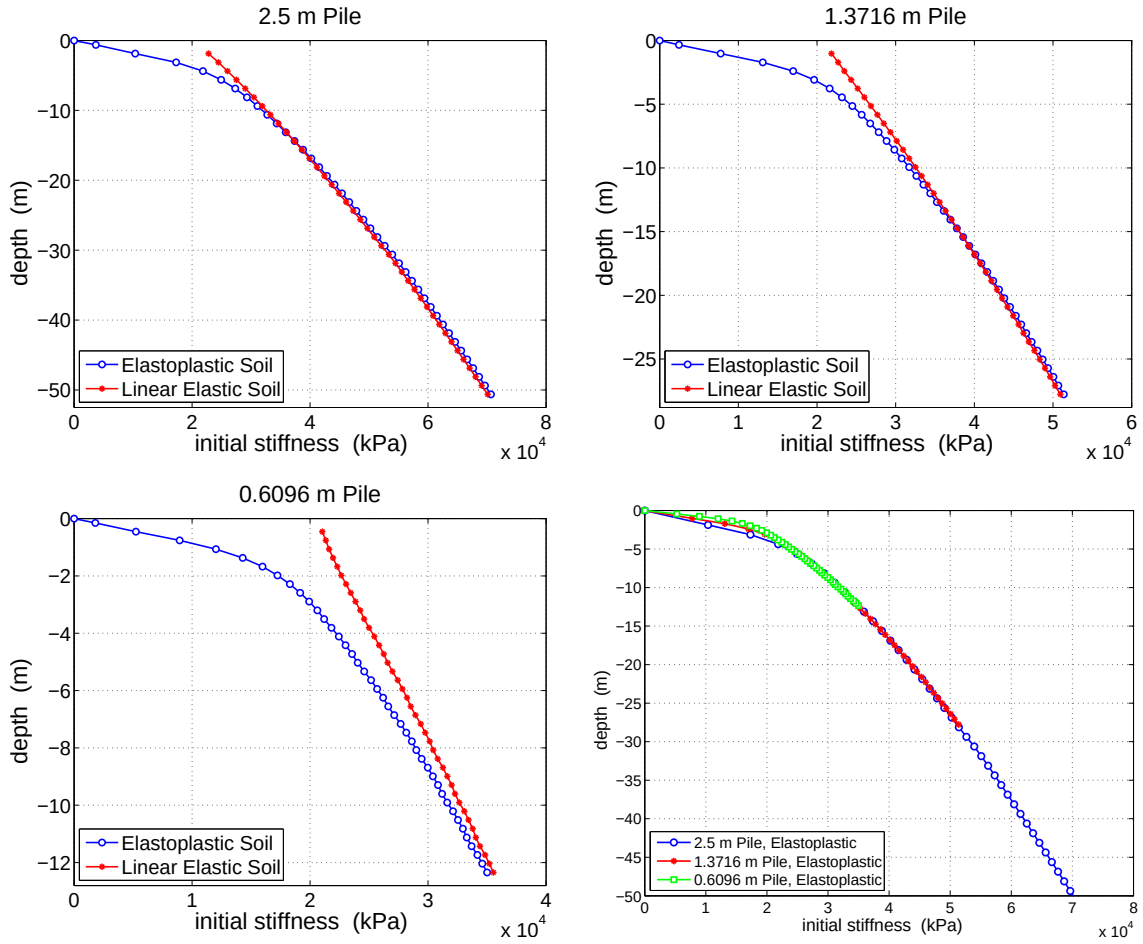

Figure 7.5: Comparison of the initial stiffness returned by models have linear elastic and elastoplastic soil elements for each of the three pile designs. The elastoplastic stiffnesses for each pile are compared in the lower right plot.

elastic stiffness should be similar for each pile, as the overburden pressure is the deciding factor. As shown in Figure 7.5, this depth is indeed similar for the three pile designs, occurring at approximately 10 m below the surface.

For circular piles, the elastic stiffness of the soil should not depend upon the diameter of the piles. This is confirmed in the lower–right plot of Figure 7.5 which shows the elastoplastic results for each pile plotted together, showing that the elastic regions of each curve are the same. This similarity should not apply to the near–surface depths. The failure of the soil is dependent upon the size of the pile, therefore, the near–surface stiffnesses, which reflect the

yield of the soil, should not be the same for each pile. As diameter increases, the size of the zone of plasticity on the leading face of the pile should similarly increase. For the 2.5 m pile, more of the soil elements near the surface are yielding than for the smaller piles, therefore, the initial stiffness returned for this larger pile is generally lower than those corresponding to the smaller piles near the surface. This is reflected in the extracted curves shown in Figure 7.5 and in the near–surface k_{py} values summarized in Table 7.1. The stiffness at a given depth increases with decreasing pile diameter in this plastic zone.

The observation that the initial stiffnesses extracted from the models for each of the three piles are similar at depth but differ near the ground surface leads to the desire to obtain a higher degree of resolution on the near–surface areas. To accomplish this end, a series of 10 m deep meshes are generated, one for each pile design, and analyzed using the same pile deformations. These results offer a means of validating the observations discussed in this section, as well as a closer look at the near–surface effects. These models and their extracted results are discussed in Section 7.5.

7.4.2 Ultimate Lateral Resistance Results

As previously discussed, there is good agreement between the four predictive methods for ultimate resistance at near–surface depths, however, as the depth below the ground surface increases, there are significant differences between the proposed methods. There is also a strong correlation between the FEA results and the predicted distributions at shallow depths, as shown in Figure 7.3. The length over which the FEA results are similar varies for each of the piles, and appears to be proportional to the pile diameter. At increased depths, there is no strong correlation between the results of the 3D models and any of the estimated ultimate resistance distributions, however, the FEA distributions are of the same approximate magnitude as the smaller estimated distributions.

In order to evaluate the applicability of the extracted ultimate resistance values, it is important to consider how well the fitted curve parameters represent the recorded data. Figures 7.6, 7.7, and 7.8 show the extracted $p-y$ curves for five depths for each of the three piles. As shown, for the first few layers below the ground surface, the ultimate resistance

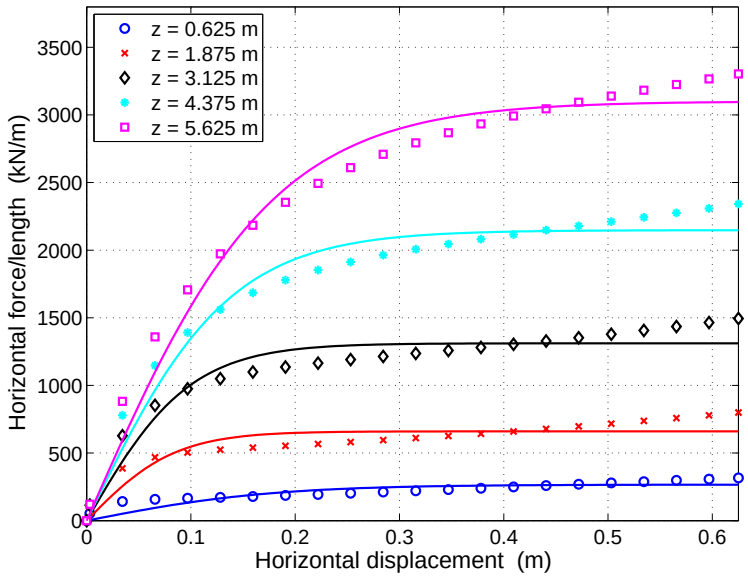

Figure 7.6: Comparison of $p-y$ data extracted from the 2.5 m pile with the fitted hyperbolic tangent functions for the first five pile nodes below the ground surface.

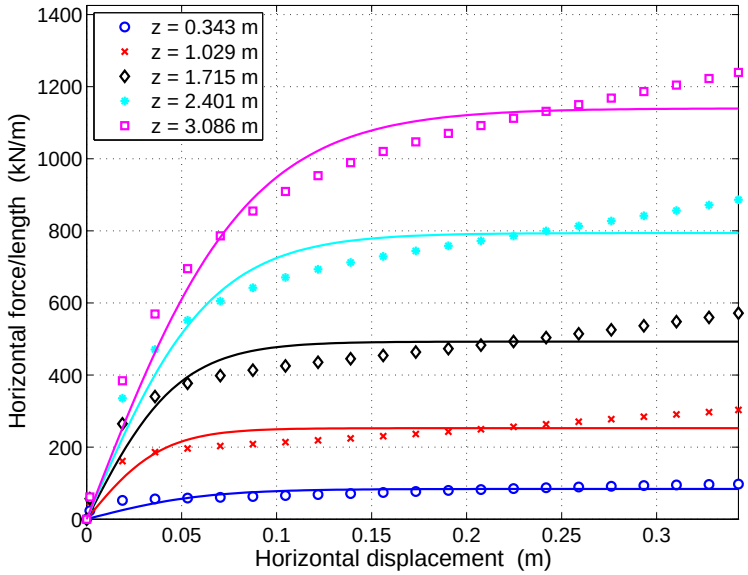

Figure 7.7: Comparison of $p-y$ data extracted from the 1.3716 m pile with the fitted hyperbolic tangent functions for the first five pile nodes below the ground surface.

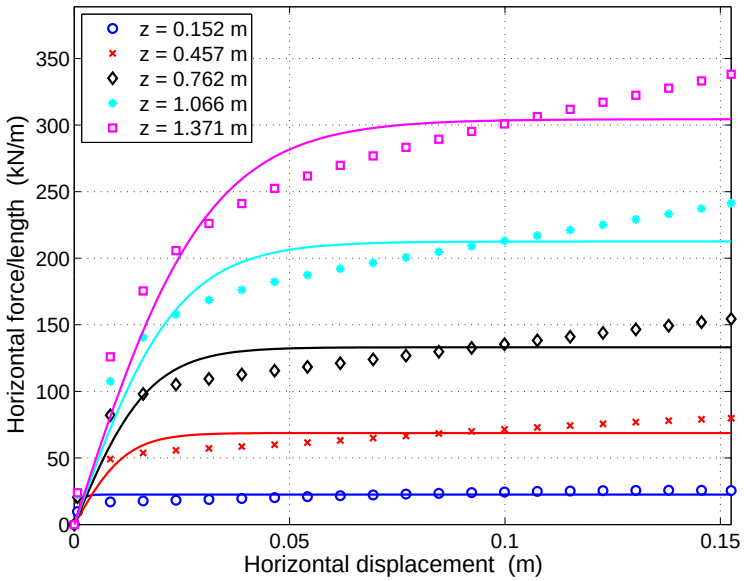

Figure 7.8: Comparison of $p-y$ data extracted from the 0.6096 m pile with the fitted hyperbolic tangent functions for the first five pile nodes below the ground surface.

of the soil appears to have been activated and is appropriately reflected in the fitted parameters. As depth increases, it can no longer be assumed that the ultimate resistance has been achieved. This indicates that with the exception of the near–surface layers, the distributions of p_u returned from the finite element models are extrapolations made by the curve–fitting procedure. The fitted curves underestimate the ultimate resistance with depth and the degree to which p_u is underestimated tends to increase with depth. Figure 7.9 further supports this observation. In this figure, the distribution of stresses in the direction of pile motion is shown at the ultimate displacement of the pile. As shown, the soil elements at shallower depths have reached a limiting value of stress during the deformation process, indicative of yielding in the soil, while the deep elements continue to gain stress, indicating that these elements have not yet experienced failure, nor activated an ultimate resistance.

The observation that the deeper curves do not display results indicating failure of the soil makes sense in the context of the Drucker–Prager soil model. The confining pressure increases with depth. An increase in confining pressure leads to an increased yield strength in the soil model. The limitations of the current model are such that it is not possible to push

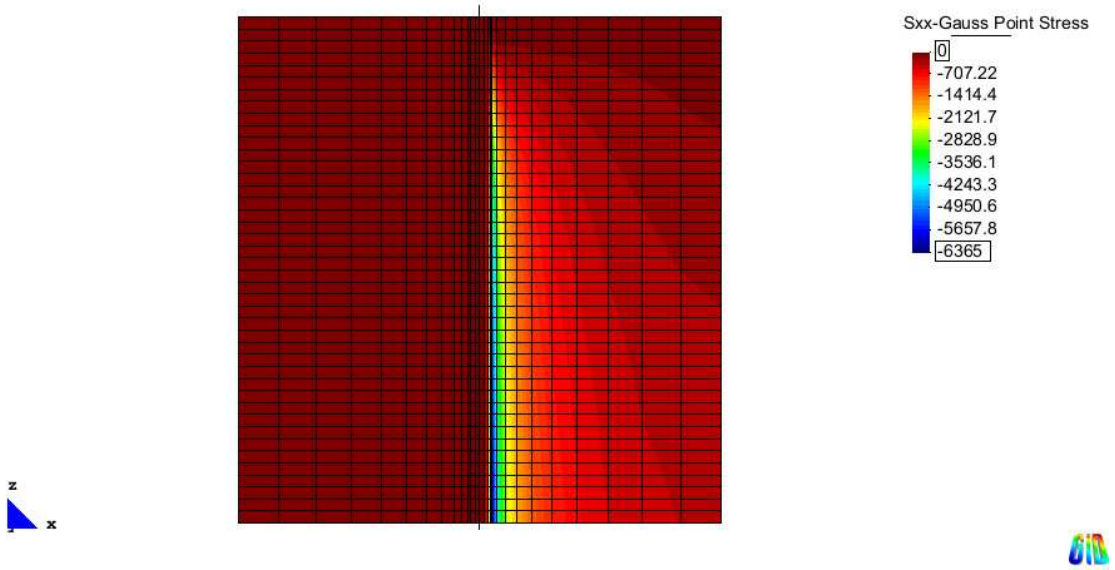

Figure 7.9: Distribution of stress in the direction of loading at the full displacement of the 0.6096 m pile in the rigid pile kinematic case.

the pile sufficiently far as to activate the ultimate resistance at increased depths without suffering mesh distortion and failure of the simulation. Moreover, the small strain/deformation assumption already reaches its limits under the considered deformations. The region over which there is confidence in the ultimate lateral resistance distributions corresponds to the depths at which the FEA results are similar to the estimated p_u distributions. This observation identifies the need for further resolution in the finite element models at shallow depths. To accomplish this, near–surface models are generated and analyzed. The results are presented and discussed in the next section.

7.5 Near–Surface Models

In an effort to gain better insight in the results near the surface, a series of new meshes are generated which only consider the first ten meters below the surface. The ten meter depth is selected due to the observation made in the initial stiffness results that each of the piles behaves initially elastic beyond this depth. Modeling only the upper ten meters allows the analyses to focus on the zone of pronounced plasticity in the soil. Due to lessons learned

about selective mesh refinement (discussed in Section 6.3), the soil and pile elements in the near–surface models are uniformly sized in the vertical direction. Because these models have reduced volume as compared to the default full–sized models, an increase in vertical mesh refinement can be incorporated without increasing the number of degrees–of–freedom or the corresponding computational cost. These alternative models share the same 10–pile–diameter–by–20–pile–diameter footprint present in the full–sized models. This, along with the differential diameters of the piles, necessitates the creation of three such models, one for each pile design. The generated mesh for the 1.3716 m pile near–surface case is shown in Figure 7.10 as a reference.

Rigid pile cases are run using the near–surface models for both elastic and elastoplastic soil elements in order to establish representative $p-y$ curves. These simulations are similar to those previously discussed, however, in an effort to better capture the ultimate resistance, the piles are pushed further into the soil. This, along with the changes in the mesh produces slightly different results than those obtained using the standard models. Figure 7.11 shows the initial stiffness and ultimate resistance distributions resulting from both the default and near–surface meshes. As shown, there are differences between the two models, however, these differences are relatively minor. With respect to initial stiffness, only the results from

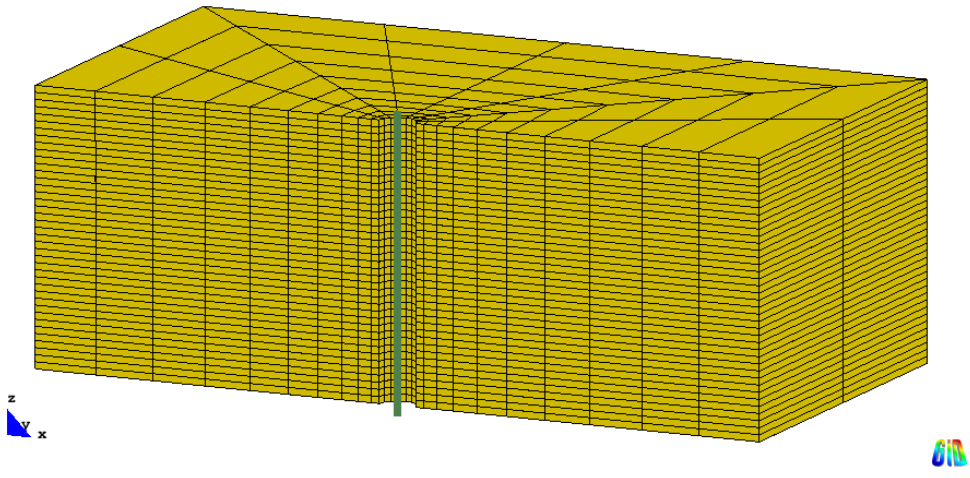

Figure 7.10: The near–surface mesh for the 1.3716 m pile.

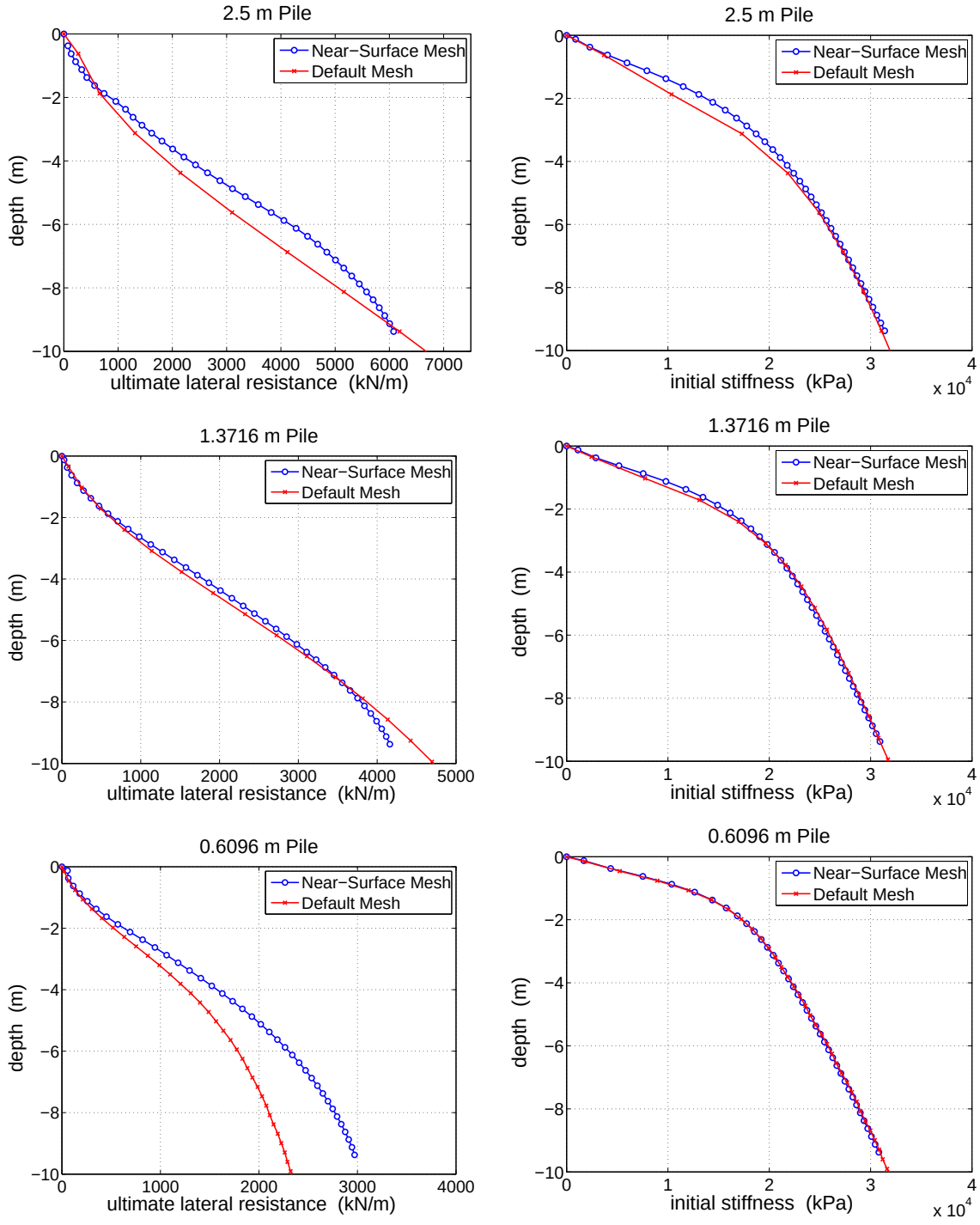

Figure 7.11: Comparison of extracted distributions for the default and near–surface meshes over the first 10 m below the ground surface.

the 2.5 m pile see significant change. This is likely due to the increase in mesh refinement present in the near–surface models, which is much more significant in this model than for the other piles.

The changes in meshing likely affect the ultimate resistance distributions to a degree as well. While the piles in the near–surface models are pushed further into the soil than in the standard models, this extra deformation only seems to benefit the results for the 0.6096 m pile. The larger piles displace too much soil upwards in front of the piles at this higher level of lateral displacement. The contact elements modeling the pile-soil interface lose contact due to this upward movement of soil, and the results beyond this point become meaningless. For the 2.5 m and 1.3716 m piles, the point at which contact is lost is approximately equal to the ultimate pile displacement specified in the previous models. In the 0.6096 m model, the associated soil heave is much smaller in magnitude and contact is not lost. The resulting ultimate lateral resistances from the near–surface mesh for this pile are larger than in the standard mesh due to the increased soil deformation. In this case, more of the soil elements have reached an ultimate state and the extracted resistance distribution represents the true soil response in a better manner.

7.5.1 Initial Stiffness Distributions in Near–Surface Models

The initial stiffness distributions extracted from the near–surface models are only slightly different from those obtained from the standard models. The results from the 1.3716 and 2.5 m piles show slight increases in stiffness at shallow depths, likely due to the increased mesh refinement in these models. The benefit of the near–surface models with respect to initial stiffness can be seen in Figure 7.12, which shows the distributions resulting from the models for each of the piles. The differences between the initial stiffnesses in the plastic zone can clearly be seen. As the pile diameter increases, the amount of plasticity in the soil at shallow depth similarly increases. The extracted initial stiffness distributions demonstrate this mechanism, as the larger piles experience smaller initial soil stiffnes than the smaller piles at corresponding depths. Also of note is the observation that all three of the models reach the elastic stiffness at the same depth. This expected behavior is due to the fact that

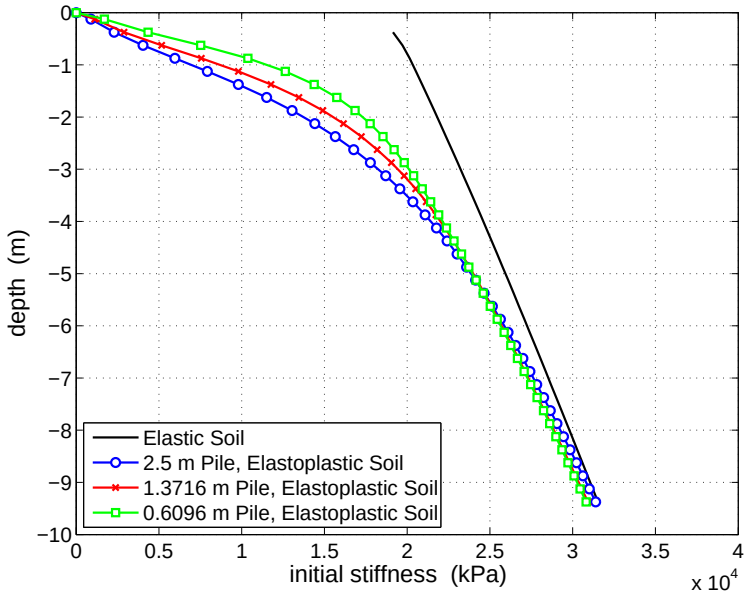

Figure 7.12: Distributions of initial stiffness extracted from the near–surface models for each of the three pile designs using both elastoplastic and elastic soil elements.

the state of stress in the soil which defines the size of the elastic regime is independent of the size of the pile and merely dependent upon the weight of the overlaying soil.

7.5.2 Ultimate Lateral Resistances in Near–Surface Models

The distributions of ultimate lateral resistance in the near–surface models offer a better glimpse into the behavior of the soil at shallow depths. The near–surface models are created such that the pile nodes for each of the three pile diameters are located at the same series of depths, thus, direct comparisons can be made between the p_u distributions resulting from each pile model. Figure 7.13 shows the distributions of ultimate lateral resistance extracted from each of the pile models, illustrating the relative differences in magnitude due to changes in pile diameter. This figure clearly shows that as the pile diameter increases, the corresponding ultimate soil resistance to the passage of that pile also increases. As depth increases, this effect becomes more pronounced. This observation seems to be logical. It should take a much larger effort to push a larger pile through soil than it would take to push a smaller pile through the same soil. The ultimate resistance of that soil should increase

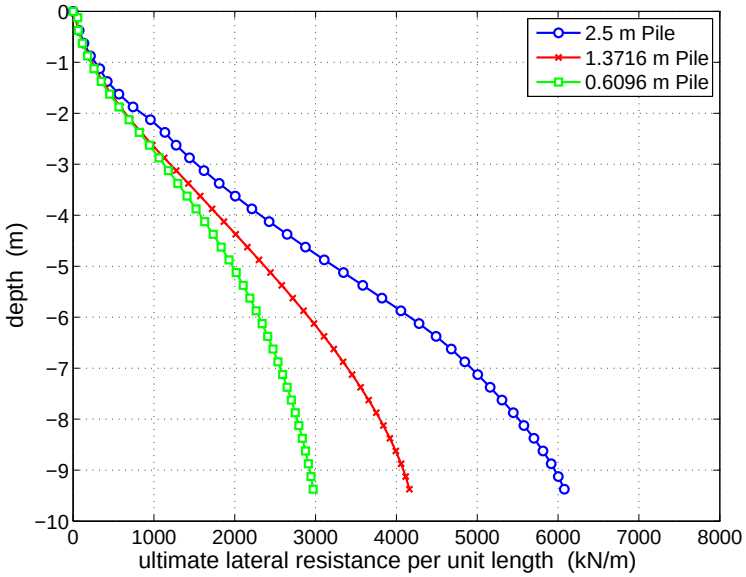

Figure 7.13: Distributions of ultimate lateral resistance extracted from the near–surface models for each of the three piles.

with increasing pile diameter and with increasing overburden pressure, exactly as observed from the results of the near–surface models.

The near–surface p_u distributions are compared to the methods of Broms, Fleming et al., Reese and Van Impe, and Brinch Hansen in Figure 7.14. A full discussion on these methods for estimating an ultimate resistance of a given soil is presented in Section 7.2. Figure 7.14 shows that the extracted p_u distributions are similar to the estimated distributions at shallow depths. The length of correlation is proportional to pile diameter. Beyond this initial zone of correlation, the FEA results become larger than any of the predictive methods before eventually becoming less than the distribution estimated by the method of Reese and Van Impe (2001) [23] at increased depths.

As is observed for the full–size (default) meshes in Section 7.4, the ultimate resistance of the soil does not become fully activated at advanced depths in the FEA. In an effort to gain a better estimate of this value with depth, the piles are pushed further into the soil in the near–surface models. As previously discussed, loss of contact between the larger piles and the soil due to a meshing issue renders this extra deformation meaningless for those models,

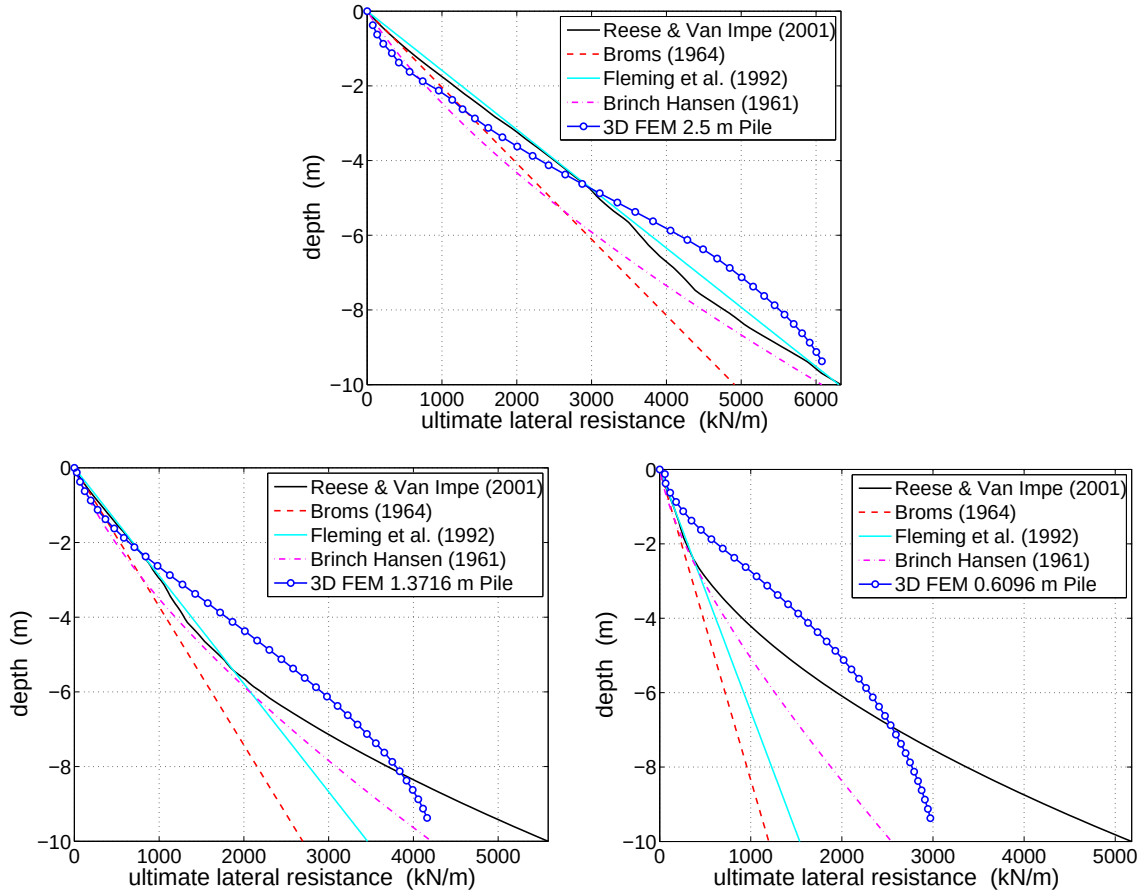

Figure 7.14: Comparison of extracted ultimate resistance distributions with considered estimated methods.

however, the 0.6096 m pile sees increased values of p_u over the results obtained from the standard model because of the extended lateral pile displacement. Though the results from the larger pile models do not see the benefits of the extra push, there is an increase in the number of adequately estimated points on the p_u distribution curves due to the decreased mesh size in the near–surface models as compared to the full–sized (default) counterparts.

Figures 7.15, 7.16, and 7.17 show the extracted $p-y$ data from each of the three pile models along with the fitted hyperbolic tangent curves for a series of depths. The recommended $p-y$ curves per the API (1987) [2] for corresponding pile diameters and depths are also shown for comparison. The API recommended curves have initial stiffnesses and ulti-

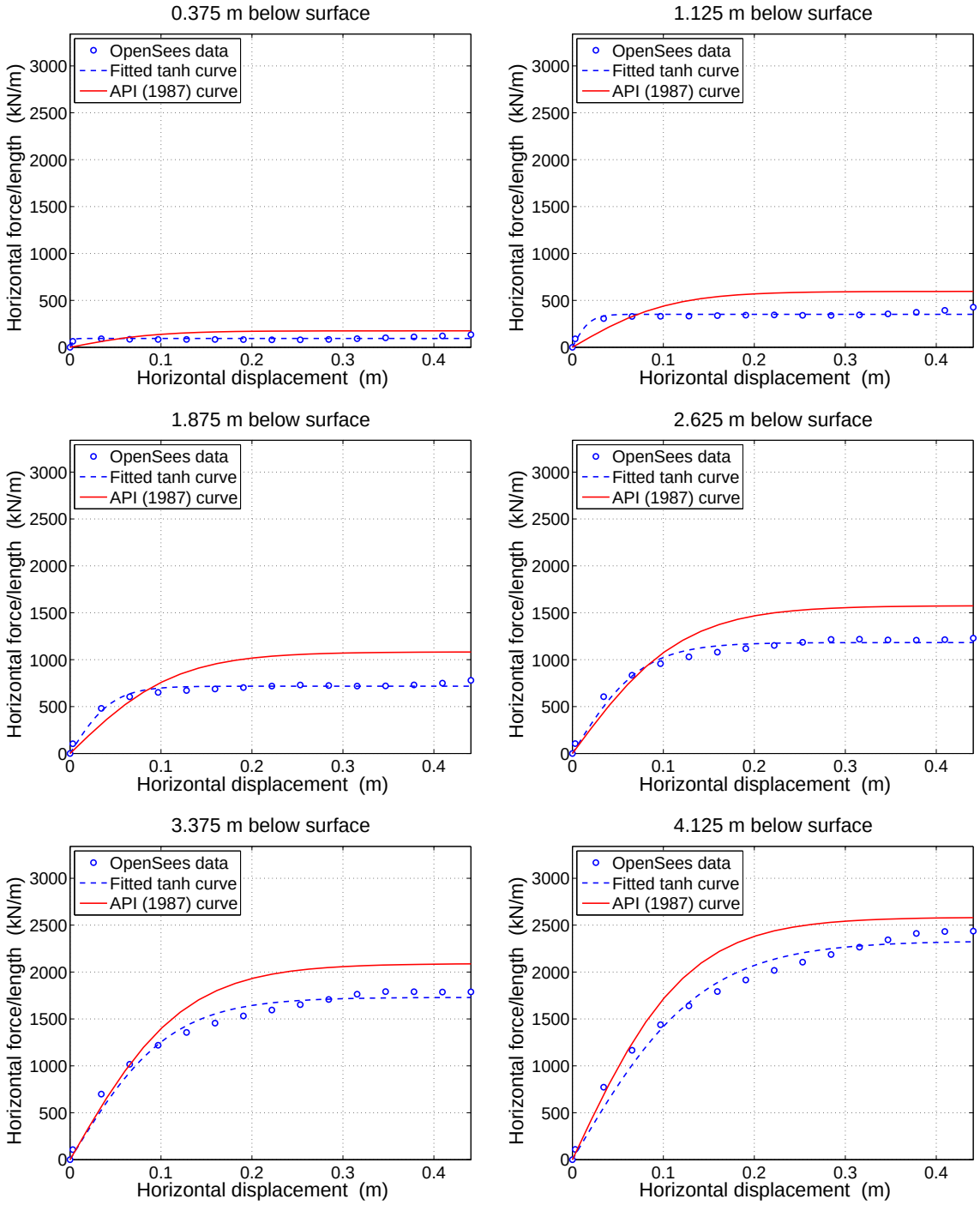

Figure 7.15: Extracted $p-y$ data for 2.5 m pile model for several depths shown with the fitted hyperbolic tangent function and the recommended API (1987) [2] $p-y$ curve for each corresponding depth.

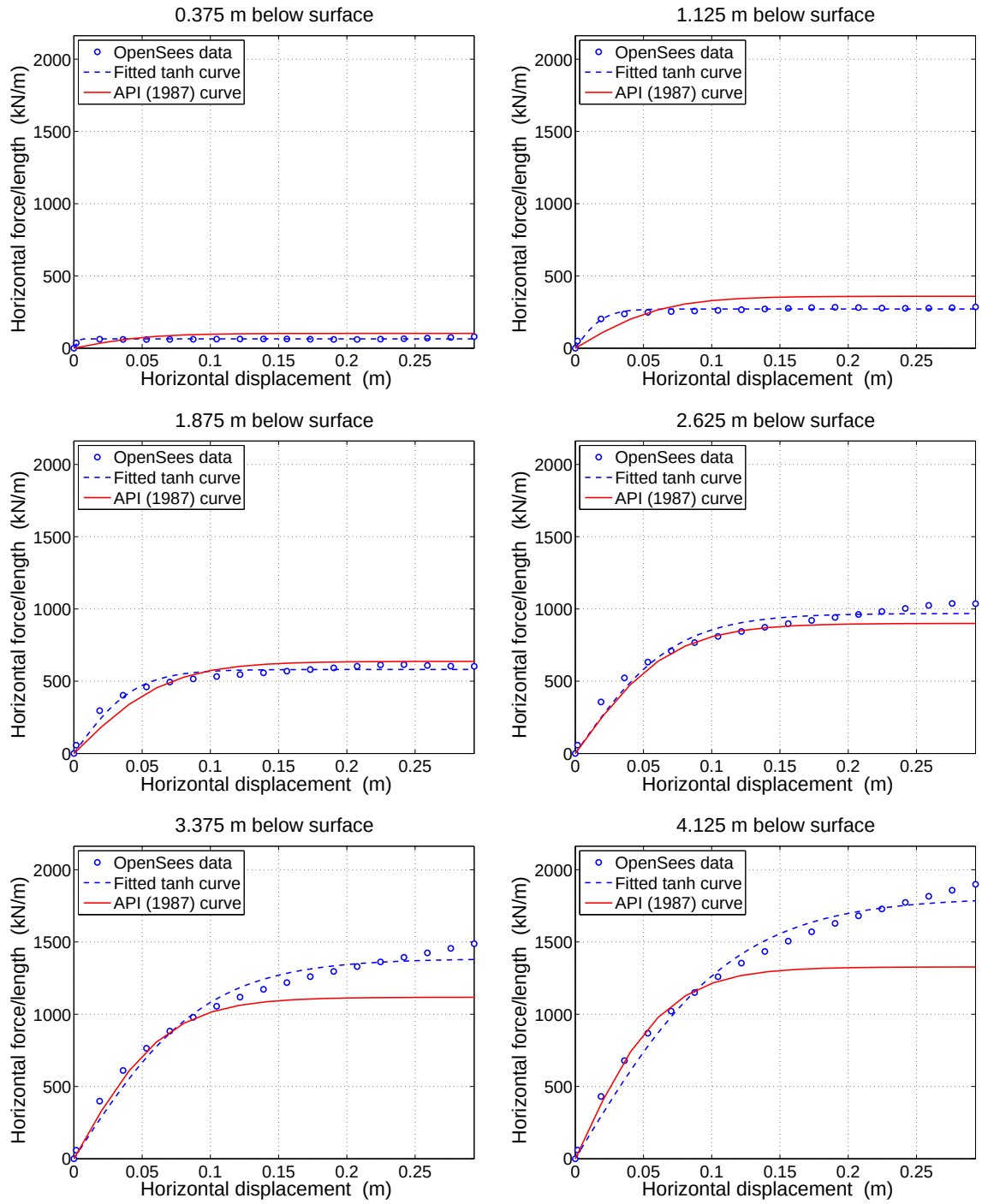

Figure 7.16: Extracted $p-y$ data for 1.3716 m pile model for several depths shown with the fitted hyperbolic tangent function and the recommended API (1987) [2] $p-y$ curve for each corresponding depth.

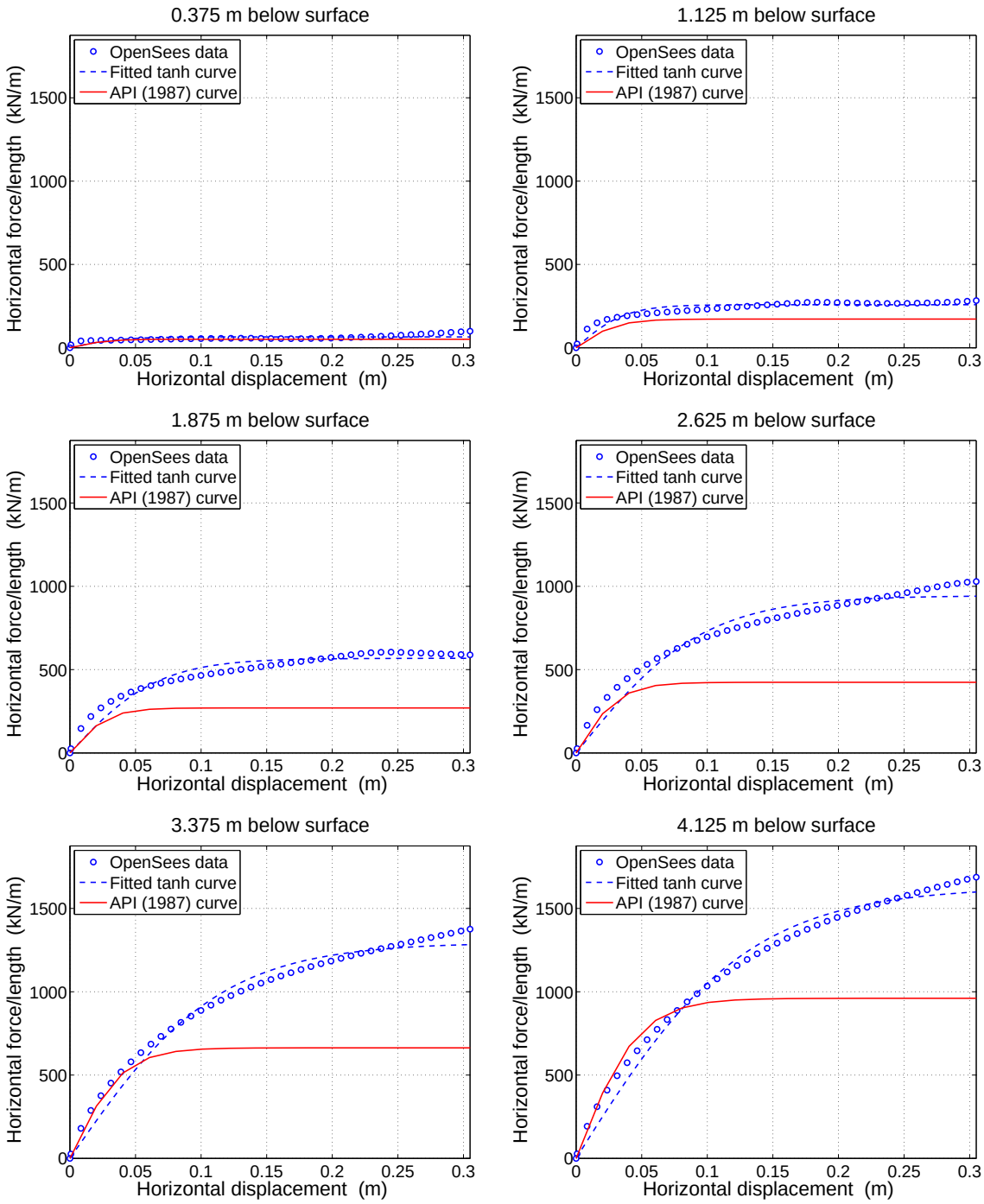

Figure 7.17: Extracted $p-y$ data for 0.6096 m pile model for several depths shown with the fitted hyperbolic tangent function and the recommended API (1987) [2] $p-y$ curve for each corresponding depth.

mate resistances predicted by the methods presented in Reese and Van Impe (2001) [23], however, the shape of the curves is slightly different. Reese and Van Impe recommend curves which have several sections defined by various linear and parabolic functions while the API recommended curves use the hyperbolic tangent function given in Equation (7.13).

The API recommended curves shown in Figures 7.15, 7.16, and 7.17 are generated using the Reese and Van Impe recommended p_u distributions shown in Figure 7.14 and computed using the lesser result of (7.4a) and (7.4b) as discussed in Section 7.4. As is expected based upon comparisons between the distributions of initial stiffness and ultimate lateral resistance, the $p-y$ curves estimated using these methods are comparable to the extracted curves at shallow depths, while differing substantially at greater depths.

Figure 7.17 illustrates the effects of the increased pile displacement on the extracted values of p_u for the 0.6096 m pile. There is a definite increase in the values of p_u returned using the extended pile displacement in the near–surface model for this pile, as noted in Figure 7.11. The plotted $p-y$ curves of Figure 7.17 show that these values are still less than the true ultimate resistance of the soil at depth. With the current mesh and element formulations used in this research, it seems unlikely that the models will be able to capture the ultimate lateral resistance at all depths along the length of the pile. The observations made here are still valuable, as they show that there is a discrepancy both between the various methods of predicting p_u and between the estimated and extracted results.

7.6 Plane Strain Models

In the method proposed by Reese and Van Impe (2001) [23] for determining the ultimate lateral resistance for a given soil, there are two considered failure mechanisms. At shallow depths, a wedge–type failure of the soil is assumed and at greater depths, a plane strain failure mode is assumed. In the finite element models, it is observed that a similar wedge–type failure occurs near the ground surface. It is unclear, however, how similar the results at increased depths are to the assumed plane strain condition. In order to discern how close the conditions at increased depth in the finite element model are to a plane strain condition, and also to analyze the $p-y$ curves resulting from such a condition, a plane strain model is created.

As this is only a validation exercise, only a single plane strain model is created. This model considers the 2.5 m pile design embedded in a soil continuum. As with the near–surface models, the plane strain mesh shares a footprint with the corresponding standard mesh, however, the plane strain soil mesh is only one element thick in the vertical direction. The pile is reduced in length down to two elements with the middle pile node located at the center of the thickness of the layer of soil elements. In order to compare the results of the plane strain model with other results, a method of simulating depth is devised which employs the surface load element developed for use in OpenSees during this research. A detailed discussion of these elements is provided in Section 2.5.

In order to obtain a distribution of results with depth at a minimum of modeling effort, a series of five depths is established. These depths are selected such that the resulting data provides a general sense of the $p-y$ curve parameter distributions over the full length of the pile. Appropriate overburden pressures corresponding to each of these depths are applied to the meshes via the surface load elements in order to determine the resulting displacements of the upper surface of the soil elements. When running the plane strain model, the upper nodes of the soil layer are slowly moved via displacement control through these recorded displacements, creating a depth–appropriate initial stress state in the soil elements, and then held fixed in the vertical direction as the pile is pushed into the soil layer. In this manner, the response of the soil for each of the selected depths is established for the plane strain condition.

The results obtained from the plane strain model are evaluated via comparisons with the results obtained from the default full–sized mesh for the 2.5 m pile and with the series of predictive methods from the literature. In the plane strain model, there is no free surface. The early plasticity observed in the regular mesh at shallow depths should not occur. Therefore, it is expected that the initial stiffnesses obtained from the plane strain models should exceed those obtained from the standard mesh at shallow depths. At increased depths, the stiffnesses obtained from either model should be approximately equal. Assuming the conditions in the default mesh at greater depths are nearly plane strain, the increase in elastic stiffness from the plane strain condition should not be significant. The ultimate lateral resistances obtained from the plane strain model should be larger than those

extracted from the standard model at corresponding depths, especially near the surface where the assumption of a plane strain failure mode is poor. The plane strain condition allows significantly larger confining pressures to develop in the soil elements, leading to a corresponding increase in strength. For this reason, the ultimate resistances extracted from the plane strain model should represent the largest possible resistances that the soil can provide for the lateral displacement of a pile.

Figure 7.18 shows the $p-y$ curve parameter distributions obtained from the 2.5 m pile plane strain model. As expected, the initial stiffnesses near the surface are in excess of those obtained from the default model, and at depth, the stiffnesses are nearly identical. This confirms that the plane strain model is created correctly and the data is processed in an appropriate manner. The p_u distribution obtained from the plane strain case also displays the expected behavior. At each depth, the value of p_u resulting from the plane strain condition is greater in magnitude than the corresponding value from the default mesh case. The degree to which these values are exceeded decreases with depth. At a depth of 1 m, where the default models have shown that the plane strain assumption is not applicable, the ultimate resistance in the plane strain model is approximately ten times larger than the previous result, while at 50 m below the surface, the plane strain resistance is about 1.3 times larger.

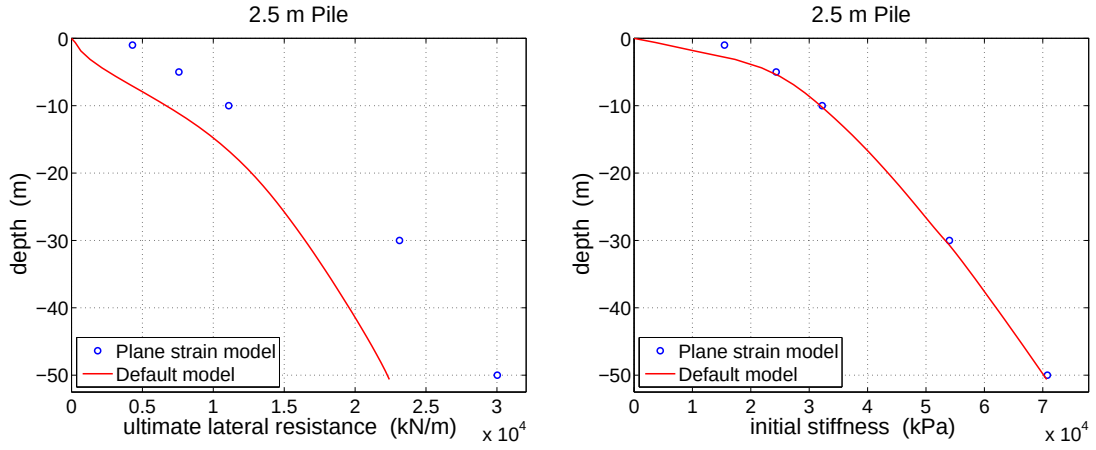

Figure 7.18: Comparison parameter distributions for the standard and plane strain finite element models for the 2.5 m pile.

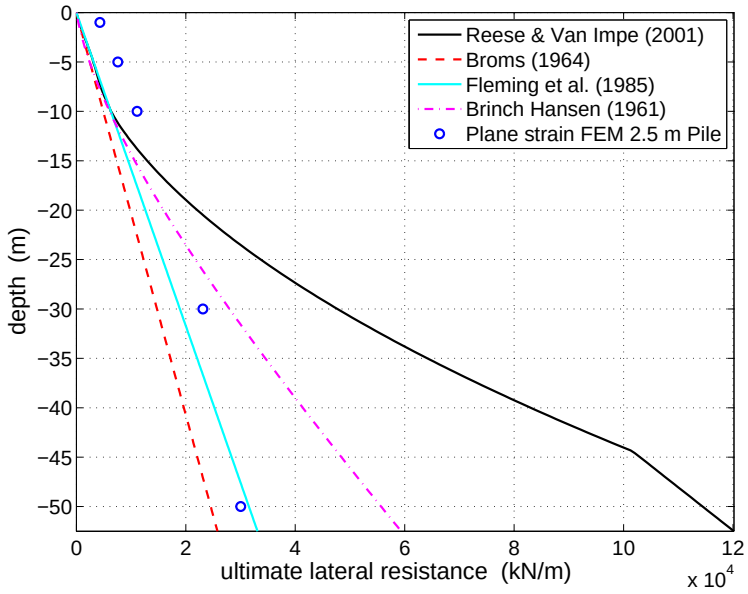

Figure 7.19: Comparison of ultimate lateral resistances extracted from the 2.5 m pile plane strain model with corresponding distributions established using the four considered predictive methods.

As previously mentioned, the method of Reese and Van Impe (2001) [23] for estimating a distribution of ultimate lateral resistance for a given soil/pile combination uses an assumption of plane strain at great depths. It is of interest to see how this estimated distribution, and those estimated using the other methods discussed in Section 7.2, compares to the results of the plane strain simulation. Figure 7.19 shows these estimated distributions alongside the distribution of p_u obtained from the plane strain FEA. As shown, the extracted values of p_u at depth are significantly less than those predicted using the method of Reese and Van Impe and are more similar to those predicted by the method of Fleming et al. (1985) [10].

7.7 Effects of a Liquefied Layer on the Soil Response

When a layered soil profile exists such that a softer soil layer is located between two relatively stronger layers, the presence of the softer layer can affect the responses of the adjacent layers to laterally applied loads. The three–layer soil profile discussed extensively in this thesis in which a liquefiable layer is located between two denser layers of sand is a perfect example of

such a case. Once liquefied, the shear strength of the middle layer is reduced significantly and the interfaces of this layer with the adjacent solid layers now act in a similar manner to the free–surface located at the top of the soil profile. The solid soil at the liquefied interface is now able to squeeze into the softer layer during the application of a lateral load, effectively reducing the strength of the solid layers in the vicinity of the liquefied layer. This process is explored through comparisons between the results of 3D FEA run both with and without the presence of a liquefied layer.

The magnitude and spatial extents of the strength reduction imparted upon the solid layers by their proximity to the liquefied layer depends upon several factors. Among these factors are the thickness of the liquefied layer and the depth at which it is located. In this research, only the affects of increasing liquefied layer depth are examined. This is accomplished through the use of overburden pressures, p_{vo}, applied at the ground surface. This method creates stress states equivalent to those which would occur had the models been extended vertically with significantly less effort. The surface load elements developed for use in OpenSees during this research (see Section 2.5) are utilized in order to apply constant overburden pressure to the surface of each model. A series of five pressures are selected based upon hypothetical additional soil layers having thicknesses equal to 0, 5, 10, 15, and 20 diameters of the 1.3716 m pile, resulting in overburden pressures of 0, 116.6, 233.2, 349.8, and 466.4 kPa, respectively, for a soil unit weight of $\gamma = 17$ kN/m^3.

7.7.1 Evaluation of Finite Element Analysis Results

Figure 7.20 presents a comparison of the ultimate resistance and initial stiffness distributions resulting from the homogenous and liquefied cases for the 1.3716 m pile with no additional overburden pressure (i.e. $p_{vo} = 0$ kPa). These results are typical of all the considered cases, and have been smoothened to account for variations in mesh size using the procedure discussed in Section 6.3. As shown, the effects of the liquefied layer on the adjacent solid layers are more evident in the distribution of p_u, though the initial stiffnesses are affected as well. The curve data obtained from within the liquefied layer is not always of a form which lends itself well to a hyperbolic tangent curve fit. For this reason, values of p_u cannot be

extracted at some of these nodes. The general trends are still apparent, however, and that is the more important consideration.

As shown in Figure 7.20, the ultimate resistances in both the upper and lower solid layers are significantly affected by the presence of the liquefied middle layer. These results are obtained from using the rigid pile kinematic case discussed in Section 6.1.1. The strength reduction lessens in magnitude with increasing distance from the liquefied interface. Near the top and bottom of the soil profile, the homogenous and liquefied cases display nearly identical results. The observed reductions in ultimate resistance and initial stiffness are due to a similar behavior as that observed and discussed at shallow depths in Section 7.5. As the pile is pushed laterally into the soil profile, the soil from the solid layers is able to be pushed into the adjacent weaker layer more easily than it can be compressed laterally. This behavior is illustrated in Figure 5.4 (page 91) which shows the deformed shape of the soil elements in the vicinity of the liquefied layer. When the soil is able to expand in this manner it results in a decrease in the confining pressure in the areas adjacent to the liquefied layer and a subsequent decrease in the elastic regime for those elements. The soil in these locations yielding sooner and thus cannot offer as much resistance to the passage of the pile before reaching its ultimate state.

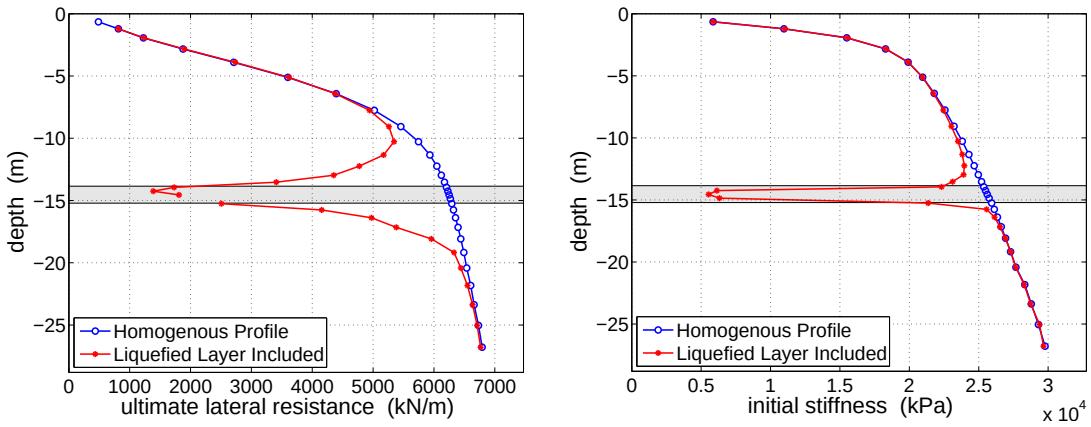

Figure 7.20: Distributions of ultimate lateral resistance and initial stiffness for the homogenous and liquefied soil profiles for the 1.3716 m pile with no additional overburden pressure ($p_{vo} = 0$ kPa).

It is of interest to evaluate the differences in effects of the liquefied layer on the two solid layers. The plots of Figure 7.20 provide a good visual comparison between the results obtained from each soil profile, however, it is difficult to gauge relative reductions. In order to provide a better measure of the relative differences between the homogenous and liquefied soil profiles, the ratios of the ultimate resistance and initial stiffness in the liquefied case are taken with respect to the homogenous case. These ratios are plotted for the 1.3716 m pile in Figures 7.21 and 7.22 for the five considered overburden pressures, representing five different locations of the liquefiable layer, discussed previously. Again, these presented results are typical of those obtained for all three piles.

In Figures 7.21 and 7.22 the location of the liquefied layer is indicated by the shaded region. The soil compacts under the applied overburden pressure and self–weight resulting in settlements. The diagrams are shown on the deformed soil body. As the applied overburden pressure increases, the zone of reduced ultimate resistance tends to decrease in thickness, meaning that a lesser extent of the solid layers are affected by the liquefied layer.

This is illustrated well through the comparison of the p_u ratios for all five overburden pressures at lower right in Figure 7.21. As the overburden pressure increases, corresponding to a deeper location for the liquefied layer, the reduction in ultimate lateral resistance decreases. At increased overburden pressures, there is increased shear strength in the upper and lower solid layers which creates a smaller plastic zone. The two layers appear to be affected approximately equally at all five overburden pressures. This is a significant observation given the fact that conventional methods employed in the $p-y$ method for accounting for the presence of a soft soil layer, such as that proposed by Georgiadis (1983) [11], only consider the effects of a soft layer on the underlaying solid layer. The observation that both surrounding layers are affected by a weaker middle layer confirms a similar observation made by Yang and Jeremic (2005) [27].

When the five initial stiffness ratios are shown together in the lower right plot of Figure 7.22, it is observed that there is little difference in the reductions in initial stiffness for increasing overburden pressures. The reduction in initial stiffness is also not nearly as widespread or as significant as the observed reduction in p_u. It appears that for a given liquefied layer thickness, the effects of this layer on the initial response of the surround-

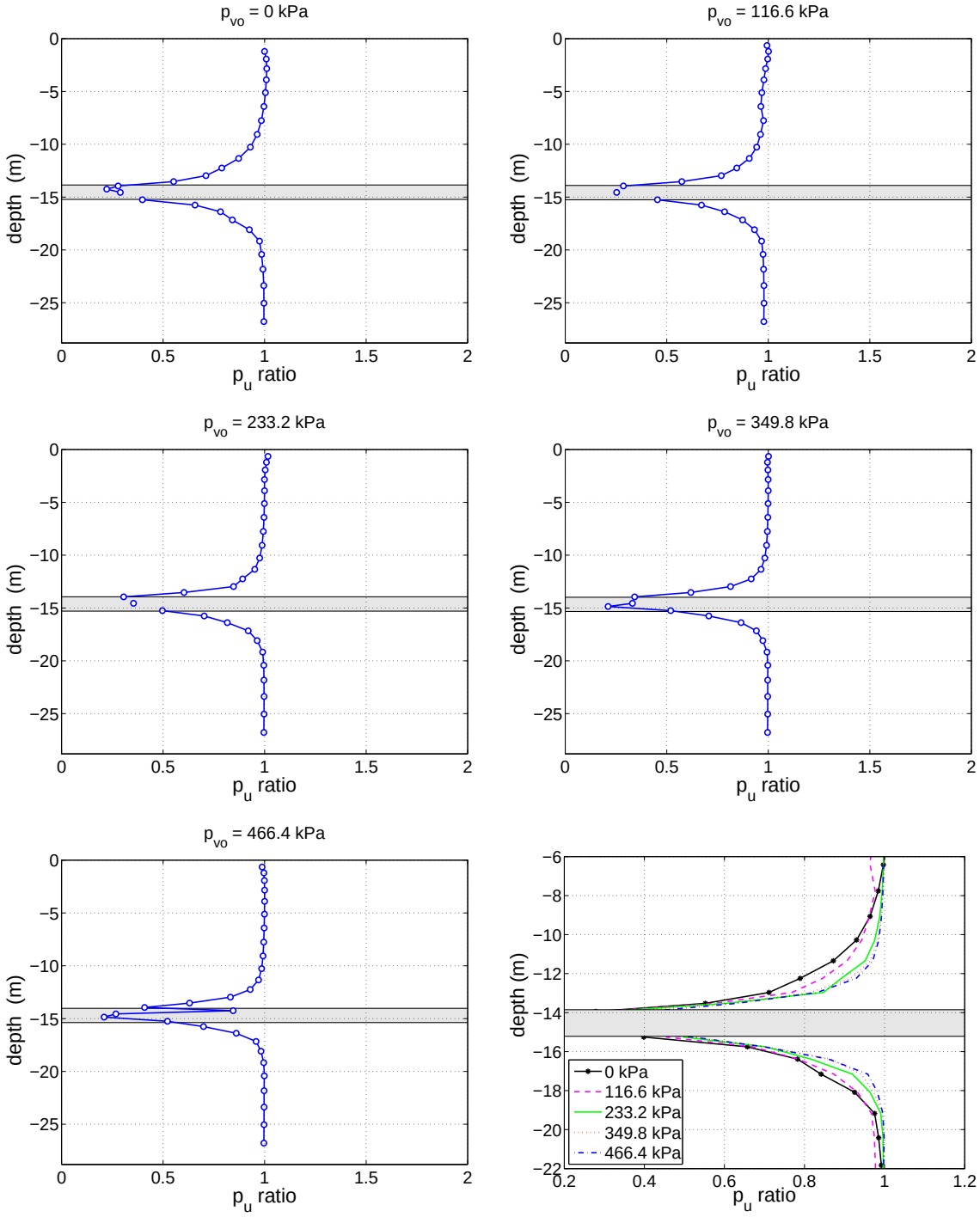

Figure 7.21: Ratios of ultimate lateral resistance extracted from 1.3716 m pile models with liquefied layers to those with homogenous soil profiles for a series of overburden pressures, p_{vo}. The five cases are compared at lower right.

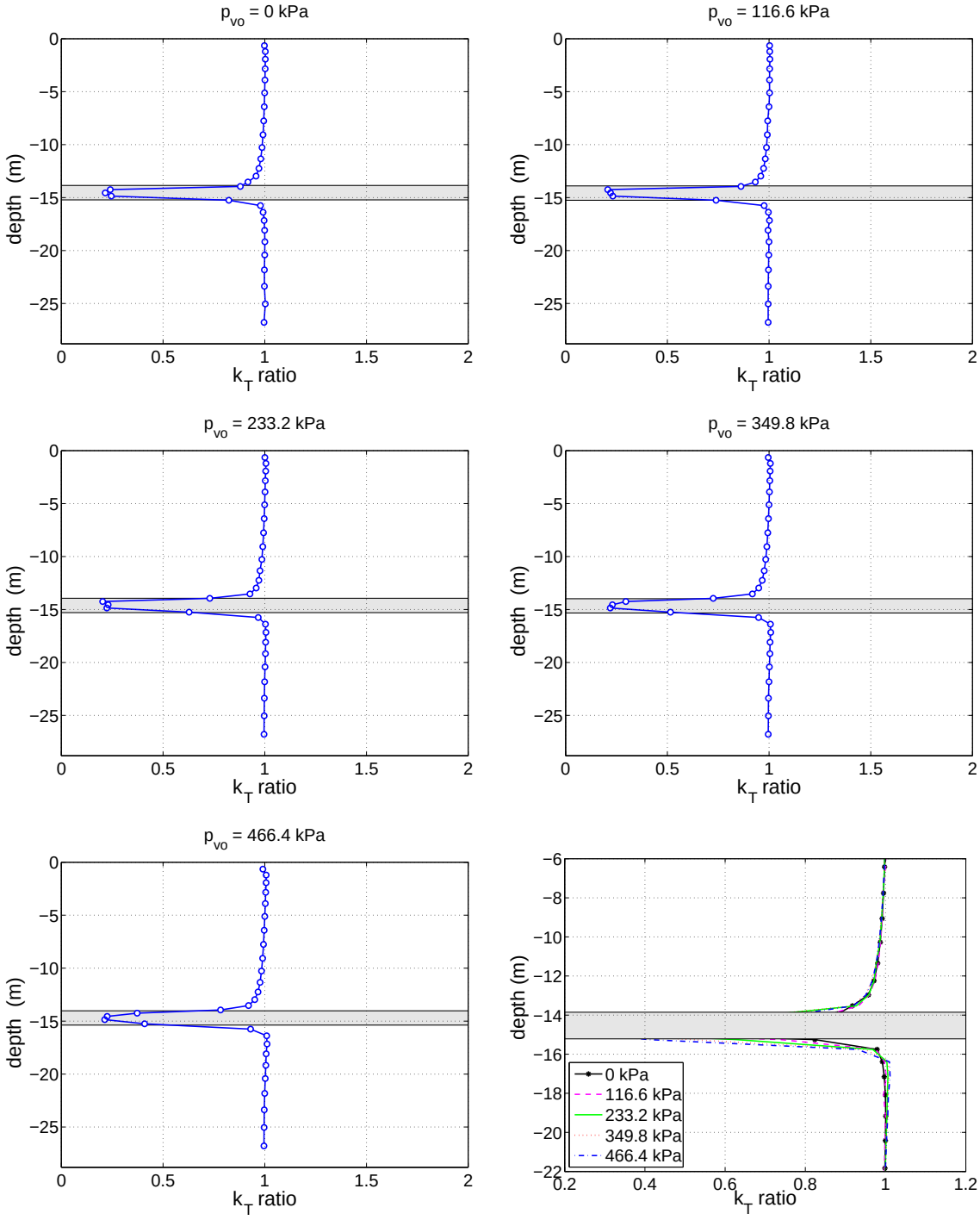

Figure 7.22: Ratios of initial stiffness extracted from 1.3716 m pile models with liquefied layers to those with homogenous soil profiles for a series of overburden pressures, p_{vo}. The five cases are compared at lower right.

ing solid layers is relatively consistent, though more investigations would need to be made before this could be taken as truth.

7.7.2 Summary

The three–dimensional finite element analyses conducted using liquefied soil profiles are able to demonstrate the effects of a weak middle layer on the surrounding solid layers. The ultimate resistances of the soil elements adjacent to the liquefied layer are reduced by up to a factor of one–half for corresponding depths within a completely homogenous layer. Both solid layers appear to be affected relatively equally and the extents of the zone of strength reduction decrease with increasing overburden pressure, though the magnitudes of the reduction do not display a tangible decrease. The initial stiffness of the soil in the vicinity of the liquefied layer is reduced as well, though not to the same degree as the distributions of ultimate lateral resistance.

7.8 One–Dimensional Beam–Spring Lateral Spreading Models

A final evaluation of the extracted and conventional $p-y$ curves in the context of the lateral spreading problem is conducted using a series of one–dimensional models. These models utilize the same beam elements used in the three–dimensional models to represent the piles. In lieu of a soil continuum, the response of the soil is modeled using nonlinear springs attached to each pile node. There are two series of 1D models. In the first, the springs have behavior defined using the $p-y$ curves extracted from the 3D simulations. In the other, the springs are defined using curves established using conventional methods. The results of these one–dimensional simulations are compared to each other and the bending responses of the piles in each are compared to the benchmark three–dimensional results discussed in Chapter 5.

The $p-y$ curves are defined in OpenSees using zero–length elements and the provided *PySimple1* constitutive model, which allows for the definition of $p-y$ curves for both cohesive and cohesionless soils. The *PySimple1* constitutive model is based upon the work of Boulanger et al. (1999) [4] in modeling seismic soil–pile–structure interaction. This constitutive model has an initially linear force density–displacement relationship, with a slope

defined similarly to that discussed in Section 7.3, and plastic force density–displacement behavior described by

$$p = p_u - (p_u - p_o)\left[\frac{cy_{50}}{cy_{50} + |\, y^p - y_o^p|}\right]^n \tag{7.14}$$

in which p_u is the ultimate lateral resistance, y_{50} is the the lateral displacement at which one–half of p_u has been mobilized during monotonic loading, and p_o and y_o^p are the values of p and y^p at the beginning of the current plastic loading cycle, respectively. The constant, c, controls the tangent modulus at the onset of plastic yielding and the constant, n, controls the sharpness of the p - y curve. In order to closely approximate the API (1985) [2] recommended curves for drained sand, Boulanger et al. (1999) [4] recommend setting $c = 0.5$ and $n = 2$. These are the default values for the *PySimple1* material model within OpenSees and were left unchanged for these analyses.

In order to employ the *PySimple1* constitutive model, appropriate values of p_u and y_{50} must be defined as input values at each pile node. The method recommended by the API (1985) [2] is selected as the conventional means for $p-y$ curve definition due to its similarity to the extracted curves. Using the method presented by Reese and Van Impe (2001) [23], which has been adopted by the API, described in Sections 7.2 and 7.3, the initial stiffness and ultimate lateral resistance are defined over the length of the piles. A value of the subgrade reaction coefficient of $k_{py} = 5000$ kN/m^3 is used to define the initial stiffness of the API curves. This value is representative of a loose sand with a low relative density as is indicated by the elastic parameters assigned to the soil constitutive model. This assignment tends to create stiffnesses which are smaller than the FEA stiffnesses at shallow depths and larger than the FEA at deeper depths. This is illustrated in Figure 7.23 which shows the initial stiffness distributions extracted from the near–surface models for all three piles plotted alongside the distribution defined by $k_{py} = 5000$ kN/m^3.

The established p_u values can be used directly in OpenSees, however, the necessary values of y_{50} are not inherently defined. Sensible values of this parameter are determined from (7.13) by solving for the displacement at which the force is equal to one–half of p_u, resulting in

$$y_{50} = \frac{p_u}{k_{py} z} \operatorname{atanh} 0.5 \tag{7.15}$$

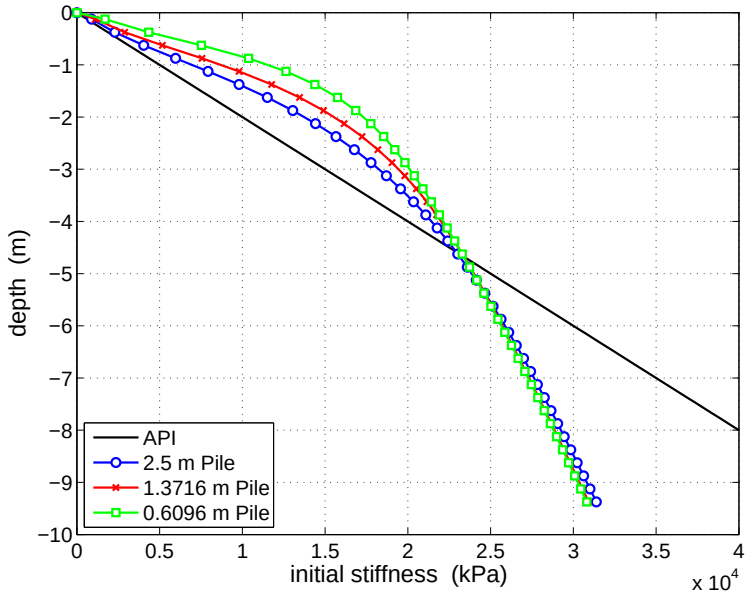

Figure 7.23: Comparison of extracted initial stiffness distributions with the linear distribution recommended by the API (1985) [2] using $k_{py} = 5000$ kN/m^3.

which defines y_{50} in terms of the known values of k_{py}, z, and p_u at each depth. A similar procedure is utilized to obtain suitable values of the parameter y_{50} for the extracted p–y curves, using the fitted hyperbolic tangent function discussed in Section 6.1.2. It is important to note that in the *PySimple1* model, the input values of p_u must be in units of force instead of the commonly–used units of force/length. Appropriate values are obtained through multiplication with the tributary lengths discussed in Section 6.1.

In order to model the lateral spreading kinematic with the one–dimensional models, there are three sets of nodes which exist in the same set of locations. There are the pile nodes, which are connected to each other via beam elements, and two sets of spring nodes. The nodes on the pile side of the springs are slave nodes to the pile nodes, sharing equal displacement (no rotation) with those nodes. The other side of the springs, the soil nodes are initially held fixed. To simulate a lateral spreading event, an imposed displacement profile, matching that used in the three–dimensional models and depicted in Figure 2.2 (page 13), is applied to the soil end of the nonlinear springs. A schematic illustrating the one–dimensional beam–spring model is provided in Figure 7.24.

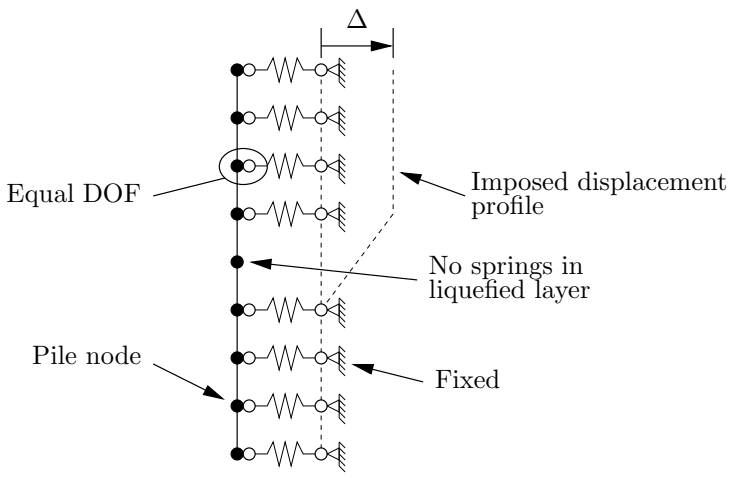

Figure 7.24: Schematic representation of the one–dimensional beam–spring model.

7.8.1 Results of the One–Dimensional Lateral Spreading Models

Using two sets of $p-y$ curves, one conventionally defined and the other extracted from three–dimensional numerical simulations, two models are created for each of the piles. These six models are analyzed in two separate cases:

1. No reduction in strength due to the presence of the liquefied layer in the soil profile is considered (unreduced case).

2. Curves are reduced to account for observed reduction in strength due to proximity to the liquefied layer (reduced case).

In the unreduced case, the extracted $p-y$ curves are obtained from simulations with homogenous soil profiles and the conventional curves are obtained in a normal fashion. The reduced case accounts for a reduction in strength due to proximity to the liquefied layer as observed in Section 7.7. The extracted curves for the reduced case are obtained from rigid pile kinematic analyses run with a liquefied layer in the soil profile. The conventional curves are reduced using the initial stiffness and ultimate lateral resistance ratios discussed in Section 7.7. In both cases the soil stiffness is assumed to be negligible in the liquefied layer and thus is set to zero. All of these cases are analyzed two times, once with elastic beam

Table 7.2: Overview of the considered one–dimensional beam–spring cases for each pile.

	Extracted FEA Curves		API Recommended Curves	
	Reduced	Unreduced	Reduced	Unreduced
Elastic Pile	X	X	X	X
Elastoplastic Pile	X	X	X	X

elements and once with elastoplastic beam elements, creating a grand total of twenty–four distinct cases. A brief overview of the considered cases is presented in Table 7.2.

The results of the considered cases are summarized in Tables 7.3, 7.4, and 7.5, which show the magnitudes of the maximum shear force demand, $\max V$, maximum bending moment demand, $\max M$, and maximum curvature demand, $\max \phi$, on the pile. Additionally, these tables summarize the maximum pile deflection, $\max U$, and the effective length factor, L_{eff}, which is the distance between the extreme moment demands in each of the solid soil layers. The shear force, bending moment, and curvature demands returned using the API curves tend to be at times significantly larger than those returned by the FEA. As the pile diameter decreases, the results become more similar, however, the API curves still predict larger demands for the smallest pile. The effective lengths obtained using the API–recommended $p-y$ curves tend to be smaller than those returned by the extracted curves, indicative of larger extreme bending demands on the piles.

In the elastoplastic pile cases, the maximum bending moments returned using the two sets of $p-y$ curves are similar due to the fact that the piles are reaching their moment capacity, however, the curvature demands placed upon the piles using the API curves are significantly larger and the effective lengths tend to be shorter. Both of these results indicate that the bending demands on the piles using the API curves are much more severe than those obtained using the FEA curves.

The one–dimensional results are also compared to the corresponding results obtained from the three–dimensional modeling effort discussed in Chapter 5. Tables 7.6, 7.7, and 7.8 show the relative error between the one–dimensional pile demands and the three–dimensional

Table 7.3: Summary of 2.5 m pile results in one–dimensional models.

Elastic Pile Cases

Curve Type	$\max V$ (kN)	$\max M$ (kNm)	$\max \phi$ (m^{-1})	$\max U$ (m)	L_{eff} (m)
FEA, homogenous	50900	285100	0.0015	1.65	16.30
FEA, reduced	46700	278900	0.0014	1.64	16.40
API, homogenous	175000	950100	0.0048	1.96	13.10
API, reduced	150000	920600	0.0047	1.94	13.20

Elastoplastic Pile Cases

Curve Type	$\max V$ (kN)	$\max M$ (kNm)	$\max \phi$ (m^{-1})	$\max U$ (m)	L_{eff} (m)
FEA, homogenous	46200	219600	0.0031	1.59	15.70
FEA, reduced	42300	217200	0.0030	1.59	15.80
API, homogenous	92800	240000	0.0882	1.35	9.10
API, reduced	78900	240200	0.0665	1.18	10.10

Table 7.4: Summary of 1.3716 m pile results in one–dimensional models.

Elastic Pile Cases

Curve Type	$\max V$ (kN)	$\max M$ (kNm)	$\max \phi$ (m^{-1})	$\max U$ (m)	L_{eff} (m)
FEA, homogenous	11900	29400	0.0059	0.87	8.25
FEA, reduced	10700	28800	0.0058	0.86	8.30
API, homogenous	25500	60000	0.0120	1.00	6.45
API, reduced	20900	56700	0.0114	1.00	6.60

Elastoplastic Pile Cases

Curve Type	$\max V$ (kN)	$\max M$ (kNm)	$\max \phi$ (m^{-1})	$\max U$ (m)	L_{eff} (m)
FEA, homogenous	4190	6170	0.0378	0.50	5.40
FEA, reduced	3980	6210	0.0955	0.67	5.05
API, homogenous	5870	6240	0.1532	0.46	3.25
API, reduced	5410	6180	0.2950	0.69	3.30

Table 7.5: Summary of 0.6096 m pile results in one–dimensional models.

Elastic Pile Cases

Curve Type	$\max V$ (kN)	$\max M$ (kNm)	$\max \phi$ (m^{-1})	$\max U$ (m)	L_{eff} (m)
FEA, homogenous	2170	2550	0.0108	0.40	3.70
FEA, reduced	1870	2450	0.0104	0.40	3.80
API, homogenous	2700	4040	0.0171	0.49	3.40
API, reduced	2150	3790	0.0161	0.48	3.50

Elastoplastic Pile Cases

Curve Type	$\max V$ (kN)	$\max M$ (kNm)	$\max \phi$ (m^{-1})	$\max U$ (m)	L_{eff} (m)
FEA, homogenous	1290	975	0.0508	0.32	2.80
FEA, reduced	1120	950	0.0424	0.33	3.00
API, homogenous	1420	980	0.2640	0.33	2.30
API, reduced	1200	1000	0.0156	0.34	2.65

pile demands. The elastic pile cases are compared to the results of the free–head 3D Series 3 cases which consider elastic piles in elastoplastic soil. The elastoplastic 1D cases are compared to the free–head 3D Series 4 cases which model elastoplastic piles in elastoplastic soil. As a reference, the 3D results for both the Series 3 and 4 cases are summarized in Tables 5.2 through 5.4.

Theoretically, the errors for the 1D results using the FEA–extracted $p-y$ curves should be small, however, there are several known sources of induced error in the extracted curves as well as different kinematics and missing three–dimensional effects. As previously discussed, the initial stiffness represented by the hyperbolic tangent functions fit to the FEA data is generally less than the true initial stiffness indicated by the recorded soil response. The values of p_u at depth are extrapolated by the curve–fitting procedure, and tend to under–represent the ultimate resistance suggested by the FEA data. Additionally, the $p-y$ curves generated by the *PySimple1* constitutive model merely approximates the form of the hyperbolic tangent curves. The introduced errors make it appear as if the curves representing a

Table 7.6: Relative error in 2.5 m pile results in 1D models as compared to 3D models.

Elastic Pile Cases	Relative Error			
Curve Type	$\max V$ (%)	$\max M$ (%)	$\max \phi$ (%)	L_{eff} (%)
FEA, homogenous	5.80	5.10	3.20	1.20
FEA, reduced	13.7	7.20	5.30	1.50
API, homogenous	223	216	222	18.7
API, reduced	177	206	212	18.1
Elastoplastic Pile Cases	Relative Error			
Curve Type	$\max V$ (%)	$\max M$ (%)	$\max \phi$ (%)	L_{eff} (%)
FEA, homogenous	5.30	3.30	14.0	3.75
FEA, reduced	13.2	4.40	17.9	4.40
API, homogenous	90.2	5.60	2350	40.0
API, reduced	61.7	5.70	1750	33.4

Table 7.7: Relative error in 1.3716 m pile results in 1D models as compared to 3D models.

Elastic Pile Cases	Relative Error			
Curve Type	$\max V$ (%)	$\max M$ (%)	$\max \phi$ (%)	L_{eff} (%)
FEA, homogenous	1.00	3.86	3.18	9.20
FEA, reduced	11.1	5.97	5.30	10.3
API, homogenous	111	95.9	97.3	14.4
API, reduced	73.3	85.1	86.4	12.8
Elastoplastic Pile Cases	Relative Error			
Curve Type	$\max V$ (%)	$\max M$ (%)	$\max \phi$ (%)	L_{eff} (%)
FEA, homogenous	15.7	6.20	63.8	13.3
FEA, reduced	19.9	5.55	8.71	6.78
API, homogenous	18.1	5.17	46.5	31.7
API, reduced	8.87	6.02	182	30.4

Table 7.8: Relative error in 0.6096 m pile results in 1D models as compared to 3D models.

Elastic Pile Cases	Relative Error			
Curve Type	$\max V$ (%)	$\max M$ (%)	$\max \phi$ (%)	L_{eff} (%)
FEA, homogenous	7.25	0.83	0.94	2.41
FEA, reduced	7.45	4.59	4.70	5.02
API, homogenous	33.3	57.3	57.2	6.82
API, reduced	6.07	47.6	47.4	4.03
Elastoplastic Pile Cases	**Relative Error**			
Curve Type	$\max V$ (%)	$\max M$ (%)	$\max \phi$ (%)	L_{eff} (%)
FEA, homogenous	2.92	0.59	14.7	2.08
FEA, reduced	11.0	2.90	4.36	5.65
API, homogenous	13.0	0.42	496	20.6
API, reduced	4.43	1.96	253	7.34

homogenous soil profile provide a better approximation of the three–dimensionally–obtained pile demands than those which have been reduced to account for the presence of the liquefied layer.

Tables 7.6, 7.7, and 7.8 show that the bending demands placed upon the piles in the 1D simulations using the extracted set of $p-y$ curves correspond fairly well with the 3D modeling effort, while the pile demands obtained using the API curves tend to be significantly larger than the 3D FEA results. This result verifies that the observed differences between the $p-y$ curves recommended by conventional means and the soil response returned by the model are manifested as significantly different results when applied to a laterally spreading pile analysis. The effects of these differences can be seen in a comparison of the deformed shapes of the 1.3716 m elastic pile shown in Figure 7.25. When the extracted curves are applied to the 1D model, the base of the pile is able to cut backwards into the soil, just as is observed in the 3D modeling effort. When this occurs, the pile has a degree of rigid body rotation in its deformation profile, lessening the curvature demands incurred during the lat-

eral spreading event. Using the API curves, as shown in Figure 7.25(b), the overestimated curve parameters lead to a condition in which the base of the pile is held firmly in place during the lateral spreading event, increasing the curvature demands on the pile, especially in the lower solid layer.

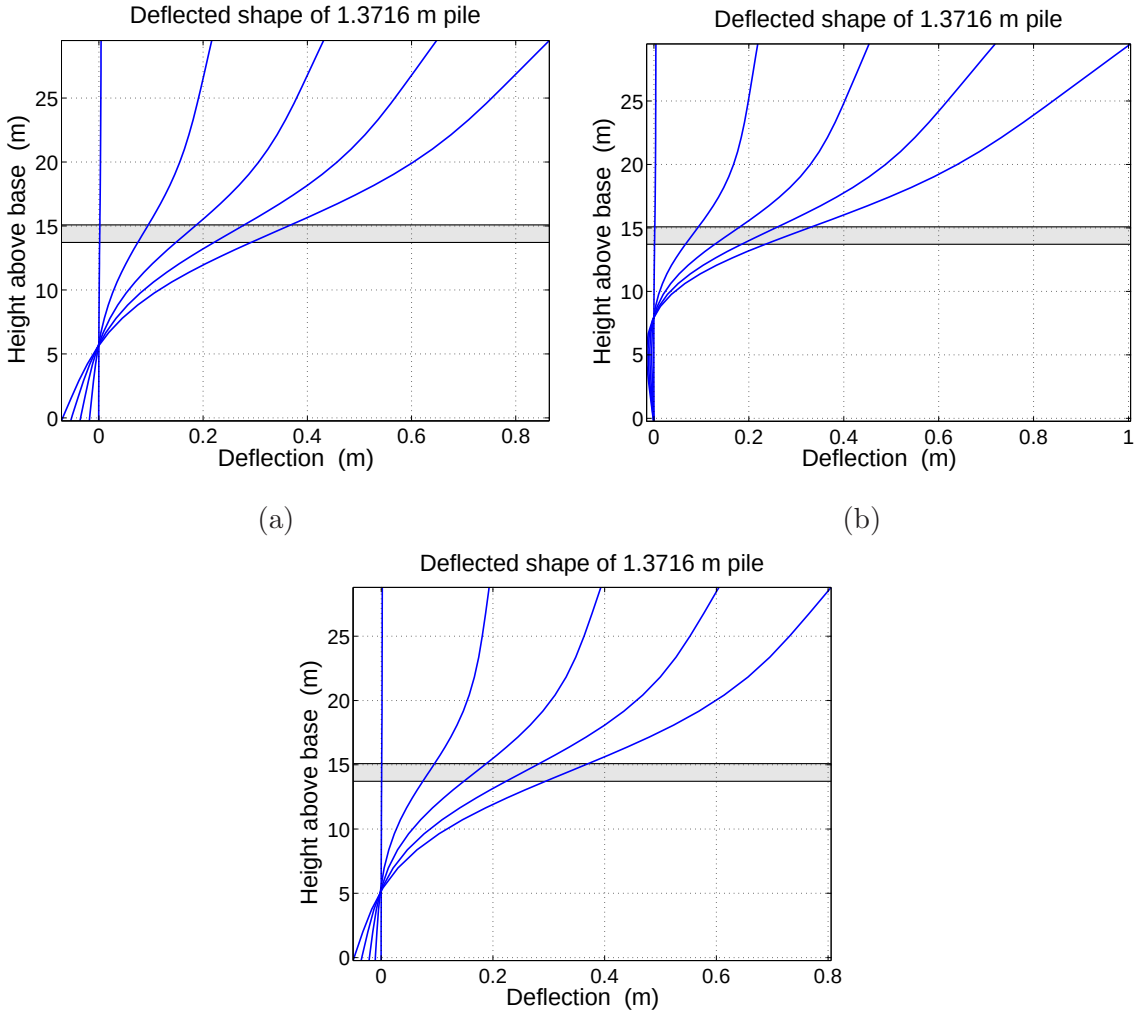

Figure 7.25: Deformed shapes of 1.3716 m elastic piles in 1D analyses using curves reduced for the presence of the liquefied layer. (a) 1D FEA curves. (b) 1D API curves. (c) 3D analysis.

The pile summary plots of Figures 7.26 and 7.27 further demonstrate the differences in pile response for the two sets of $p-y$ curves. As indicated in Figure 7.26, with soil response curves defined using the extracted 3D results, the pile has just reached its moment capacity towards the end of the lateral spreading event and the deformation of the pile is spread out over an effective length of about 16 m. When the API curves are utilized, as shown in Figure 7.27, the pile reaches its moment capacity at a much lower level of soil displacement and incurs a much larger curvature demand. In this case, the plastic hinges which develop in the pile form closer to the liquefied interface and move closer to this interface as the deformation increases. This behavior concentrates the deformation of the pile into a smaller length and greatly increases the shear demand on the pile.

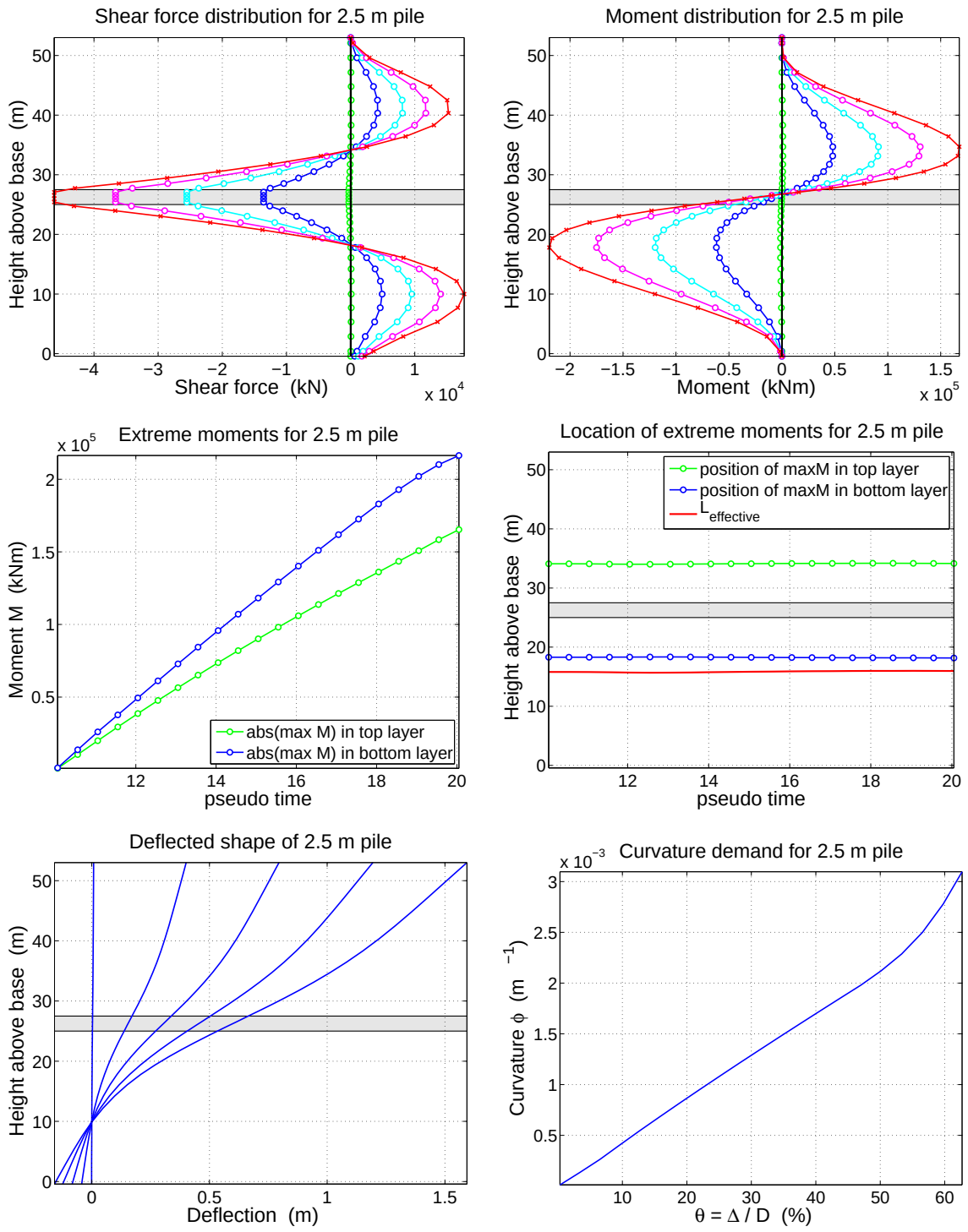

Figure 7.26: Pile summary plots for the 2.5 m elastoplastic pile in the 1D analysis case using FEA $p-y$ curves not reduced for the presence of the liquefied layer. The liquefied layer is the shaded region.

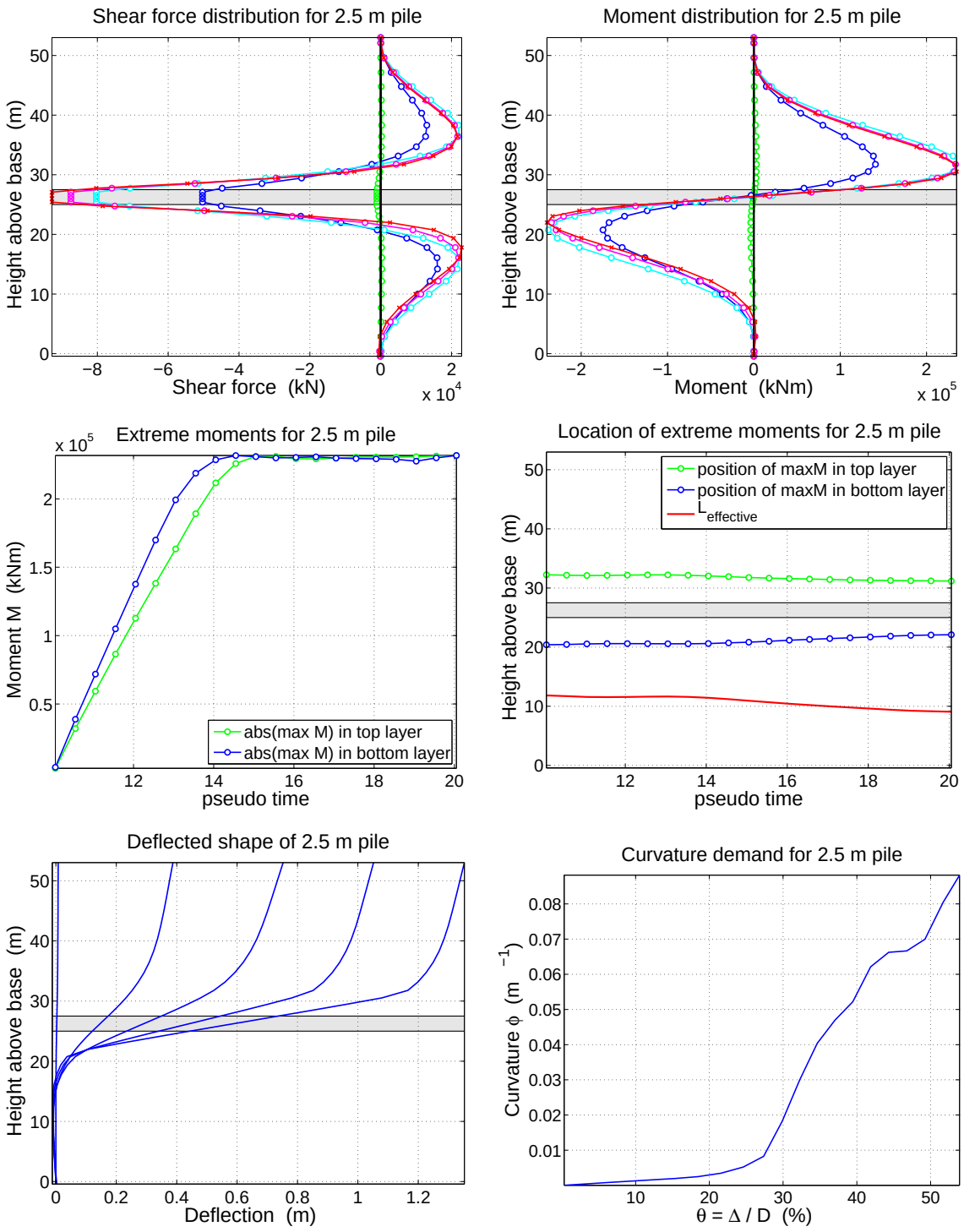

Figure 7.27: Pile summary plots for the 2.5 m elastoplastic pile in the 1D analysis case using API $p-y$ curves not reduced for the presence of the liquefied layer. The liquefied layer is the shaded region.

7.9 Summary

The problem of a single pile embedded in a laterally spreading layered soil system is complex. In order to accurately model such an event using a simplified procedure, great care must be taken in defining proper input parameters for the model. Appropriate distributions of initial stiffness and ultimate lateral resistance must be obtained along the length of the pile for a given soil profile. These parameters vary due to depth effects as well as due to proximity to the liquefied layer. Measures must be taken in order to account for reductions in the ultimate resistance in the solid soil layers due to the presence of the liquefied layer. Both the upper and lower layers are affected by these reductions, and the extents of the weakened zones decrease in length with increasing depth to the liquefied layer. The initial stiffness of the soil in the solid layers is also affected by the weaker layer, however, this parameter is affected to a lesser degree.

In current practice, the $p-y$ method is commonly employed in the analysis of piles subject to lateral loads. Some conventional methods which may be employed in the definition of parameters appropriate for use in $p-y$ curves have been compared. It is observed that there are significant differences in the distributions of ultimate lateral resistance estimated by these methods at depths beyond the first few pile diameters below the surface. It is also observed that the distributions of p_u extracted from the 3D finite element models generally do not correlate well in their form with any of the predictive methods, though the magnitudes of the resistances are relatively similar to the softer of the considered predictive methods. The distributions of initial stiffness recommended for use in $p-y$ curves are entirely linear and appear to be more appropriately applied to near–surface depths where the effects of early soil yield are observed. At increased depth, the full elastic stiffness of the soil is initially active. These values are significantly less than those suggested by conventional methods.

The method for obtaining ultimate resistances presented by Reese and Van Impe (2001) [23] is the most commonly employed method in the construction of $p-y$ curves for cohesionless soil. This method is based essentially upon a single series of field tests in which the piles are loaded at or above the ground surface. As discussed in Section 6.2, the pile kinematics

greatly influence the recorded soil response, suggesting that results obtained from a top–pushover kinematic are not necessarily applicable to alternative load cases. Reese and Van Impe mention that there is more confidence in the form of the predicted results than in the magnitude, which appears to be a fairly valid conclusion as the plane strain FEA results provide further evidence that the predicted magnitudes may be excessive. It is important to note that in the top–pushover case, an overestimation of the ultimate lateral resistance at depth is relatively harmless. The pile is not undergoing deflections large enough to activate the ultimate resistance due to the kinematics of the loading. However, this is of great significance for the lateral spreading problem and cannot be ignored. It appears that more research is necessary in order to obtain an estimate of the ultimate lateral resistance at depth which is suitable for use in the lateral spreading kinematic case.

When applied to one–dimensional beam–spring models, the $p-y$ curves extracted from the 3D FEA return pile demands which are reasonably similar to three–dimensional lateral spreading simulations. There is a relatively small amount of error which can be attributed to inaccuracies in the curve extraction procedure and the transfer of these extracted curves into the nonlinear spring models. Using $p-y$ curves established using the procedure recommended by the American Petroleum Institute (API) (1985) [2], the piles in the 1D models are subject to significantly larger curvature demands than those returned by the 3D modeling effort. These conventional curves are derived based upon tests of piles loaded at or near the ground surface only, and it has been shown that $p-y$ curves established in this manner are not applicable to the alternative kinematic of the lateral spreading case in which pile displacements occur with depth.

Chapter 8

SUMMARY, CONCLUSIONS, AND RECOMMENDATIONS FOR FUTURE WORK

8.1 General

This thesis presents a kinematic analysis of a single pile embedded in a laterally spreading layered soil profile and includes a discussion of the relevancy of conventional analysis models to this load case.

The research encompasses the creation of three–dimensional finite element models using the OpenSees finite element analysis platform. These models consider a single pile embedded in a layered soil continuum. Three reinforced concrete pile designs are considered which represent a range of pile diameters and bending stiffnesses. The piles are modeled using displacement–based beam elements and are assigned elastoplastic constitutive behavior through the use of fiber section models. The soil continuum is modeled using brick elements and a Drucker–Prager constitutive model. Additional cases are investigated using linear elastic formulations for both the piles and the soil. The interface between the beam and brick elements is modeled using beam–solid contact elements. The developed finite element models are used to evaluate the response of the piles and the soil to the lateral spreading kinematic as well as to two additional lateral load cases. Through the extraction of force density–displacement ($p-y$) curves representative of the soil response, the FEA results are used to evaluate the adequacy of several conventional analysis methods in modeling the lateral spreading case.

8.2 Summary and Conclusions

A summary of the work and associated conclusions of this research is presented in terms of the following items: finite element model development, lateral spreading analysis, representative $p-y$ curve extraction, and evaluation of conventional analysis methods.

Finite Element Model Development

Chapters 2, 3, and 4 presented the majority of the finite element model development necessary to this research. Additional variations on the main template model which consider increased lateral extents, near–surface effects, and a plane strain condition were developed and discussed in Chapters 6 and 7. Each individual component of the models was validated to ensure that verifiably–correct behavior is observed when simple load cases are applied. The main aspects of this work are summarized as follows.

- A three–dimensional soil–pile interaction model was created for the case of a single pile embedded in a soil continuum. This model employs beam–column elements to model the piles, solid brick elements for the soil, and beam–solid contact elements to define the soil–pile interaction.

- Fiber section models were created for three template reinforced concrete pile designs. These models define the elastoplastic constitutive behavior for the beam–column elements used to model the piles. The moment–curvature response of these fiber section models were verified by several means.

- The Drucker–Prager constitutive model used to define the elastoplastic behavior for the cohesionless soils in the lateral spreading model was verified through the applications of stress paths which simulate commonly–used geotechnical tests. It was confirmed that the Drucker–Prager model is able to produce predictable responses to the application of these stress paths.

- Variations in the main soil–pile interaction model were made in order to analyze specific behaviors in greater detail. Models with extended lateral extents were developed and used to evaluate the effects of the fixed boundary in the standard model. Near–surface and plane strain models were developed and analyzed in order to validate observations made using the standard mesh.

Lateral Spreading Analysis

As discussed in Chapter 5, twenty four distinct analysis cases were considered for the lateral spreading kinematic. These cases were divided into four analysis Series depending upon the combination of constitutive models assigned for the pile and soil elements. These four Series were analyzed for two boundary conditions at the head of the pile, fixed and free, resulting in eight analysis cases for each of the three pile designs. Several findings were made based upon this modeling effort.

- For a pile subjected to the kinematic demands of the lateral spreading case, the maximum shear force demand develops at the center of the liquefied layer and there are two extreme moment demands, one in each solid soil layer. The maximum moment demand exists in the lower layer for all but one of the twenty four considered cases. The distance between the extreme moments defines the effective length factor for the pile, L_{eff}, a parameter which provides an indication of the severity of the bending demand.

- The liquefied interface acts similarly to a free–surface and the adjacent solid soil is able to be pushed into the weaker center layer during the application of lateral loads. This effectively reduces the strength of the solid soil in the regions adjacent to the liquefied layer.

- Plastic hinges form in the pile at the locations of extreme moment in each layer. The plastic deformation/rotation in these locations becomes concentrated over an increasingly smaller length of the pile as the pile–to–soil stiffness ratio decreases.

- The fixity of the pile head is an important consideration. Cases analyzed using a fixed boundary condition at the top of the pile return larger bending moment demands in the piles than corresponding cases analyzed with a free–head condition. Additionally, the maximum moment demand does not generally exist at the point of fixity, but rather, occurs further down in the soil profile. This location depends upon the thickness of the top layer, soil stiffness, and the bending stiffness of the pile.

- The consideration of elastoplastic soil behavior leads to larger estimated maximum moments in the pile than occur with linear elastic soil elements due to the failure of the soil. This observation has been confirmed through the use of two simple beam models which can be solved by hand in a relatively simple manner. Elastoplastic soil behavior must be considered in order to obtain appropriate maximum moment and shear demands for piles.

Representative $p-y$ Curve Extraction

The soil response obtained from the soil–pile interaction models is evaluated through the extraction of representative force density–displacement ($p-y$) curves at each pile node as discussed in Chapters 6 and 7. Smooth curves are fit to the recorded data using a least square fit. Two functional forms are used, one to establish the initial tangent of the $p-y$ curves and the other to define the complete shape of the curves. In addition to the lateral spreading case, two alternative pile kinematic cases are considered: a top–pushover case and a rigid pile case in which there is a uniform displacement profile with depth. The effects of model–specific phenomena on the extracted results are explored through investigations of variations in the meshing and fixed boundaries. Several conclusions may be drawn from this extraction process.

- The force density–displacement ($p-y$) data returned by the three–dimensional models can be fit reasonably well using a hyperbolic tangent function, though the use of this functional form tends to underpredict the initial stiffness displayed by the FEA data. Initial stiffness can be established using a polynomial curve fit.

- The kinematics of the pile plays an essential role in defining the obtained soil response and can significantly affect the extracted $p-y$ curves. The top–pushover and lateral spreading cases produce pile displacement profiles which vary in magnitude over the length of the piles. At nodes for which the pile displacement is small, not only is the soil response insufficiently activated, the comparably larger displacements which occur at adjacent nodes influence the soil response at these nodes, leading to $p-y$ curves

which are not representative of the true soil response. The rigid pile kinematic case must be utilized in order to obtain sensible local $p-y$ curves over the length of the pile.

- Selective mesh refinement results in soil elements which have varying stiffnesses over the length of the pile. This inconsistent stiffness manifests itself as fluctuations in the recorded soil responses. Models with uniformly–sized meshes are analyzed and the inconsistent results obtained from the selectively refined meshes can be smoothened through multiplication with a ratio obtained using the uniform mesh results.

- The fixed boundaries in the model can influence the soil response at large drift. This is confirmed through the use of an additional model created with increased lateral extents in the direction of pile loading. In the default meshes, the proximity of the pile to the boundary causes confining stresses to develop in the deeper portions of the soil which are too large. This effect can be partially alleviated through the use of non–associative plasticity in the soil constitutive model.

- The presence of a liquefied layer in the soil profile reduces the initial stiffness and ultimate lateral resistance of the solid soil layers in the areas adjacent to the weaker liquefied middle layer. These effects are more tangible and widespread with respect to the ultimate resistances, though it is observed that there is a slight reduction in the initial stiffnesses adjacent to the liquefied interface as well. Both the upper and lower solid layers appear to be affected equally by this strength reduction. The extent of these effects decreases as the overburden pressure above the liquefied layer increases.

Evaluation of Conventional Analysis Methods

The representative $p-y$ curves extracted from the three–dimensional models using the procedures described in Chapter 6 were used in order to evaluate several conventional means for describing soil response and establishing $p-y$ curves. The evaluation of the extracted parameter distributions and comparisons with the conventional methods were discussed in Chapter 7. The considered methods encompass several commonly referenced methods for

the definition of distributions of ultimate resistance and initial stiffness with depth. Several observations were made from these comparisons and about the extracted parameter distributions and the following conclusions are drawn.

- The depth appropriate soil failure modes must be considered in the distributions of both the initial stiffness and ultimate lateral resistance of the soil. Near the surface, the lack of overburden pressure leads to the early onset of yield while at depth, the increased overburden pressure leads to the expansion of the elastic regime in the soil. Both of these factors significantly influence both the initial stiffness and ultimate resistance of the extracted $p-y$ curves.

- The magnitudes of the extracted FEA curves are similar to several of the considered methods at different depths, however, the general form of the results is not reflected in the predicted distributions. It is noted that the current model is not capturing the true ultimate resistance of the soil at depths beyond a few meters. The extracted values beyond this point are extrapolated by the curve–fitting procedure.

- The linear initial stiffness distribution assumed by the investigated conventional methods appears to be based upon an extrapolated elastoplastic state. The predicted stiffness at shallow depths correlates fairly well with the extracted results, though there is a diameter–dependence which is missing. At increased depths, there is no clear correlation between the extracted and estimated results.

- The method most commonly employed when establishing $p-y$ curves for a particular cohesionless soil, that presented by Reese and Van Impe (2001) [23], overestimates both the initial stiffness and ultimate lateral resistance of the soil at depth. This method is based upon field tests in which loads are applied at or above the ground surface. It is likely that the kinematics of the pile in this case contribute to the unrealistically large values which are predicted by this methodology.

8.3 Recommendations for Future Work

There are several avenues for future work which are suggested by this research. Though many findings have been made, there are nearly as many unanswered questions. These recommendations for future work are subdivided into several categories for clarity.

Finite Element Model Development

- The current models are created based upon the dimensions of the piles. Everything from the depth of the soil profile to the thickness of the liquefied layers. It may be advantageous to explore these ideas using models which are all of uniform dimensions.

- The Drucker–Prager constitutive model used in the simulations is a relatively simple model which does not necessarily capture all aspects of the soil behavior. It may prove useful to explore the findings of this research using a soil model which better captures the true soil behavior.

Lateral Spreading Analysis

- Parametric studies considering variations in the thickness and depth of the liquefied layers may prove beneficial to enhancing the understanding of the demands placed upon a pile embedded in a laterally spreading soil system. Additionally, these future parametric studies could include variations in the soil properties which would further alter the pile–soil stiffness ratio.

Experimental Need

- It may enhance the understanding of this problem to devise a way in which to perform a physical lateral spreading test either at full, or nearly full, scale or at a reduced scale using a shaking table or a centrifuge. This would provide a second set of data with which to evaluate the results of the numerical simulations.

- It has been observed that the soil response obtained from the numerical simulations does not correlate with commonly used empirical methods for predicting this response,

especially at depth. Perhaps physical tests, performed using a rigid pile kinematic, along with further numerical simulations can aid in the determination of suitable distributions of initial stiffness and ultimate resistance over the length of the piles.

Soil Response Evaluation

- One of the largest shortcomings of this research is the inability of the current models to extract the full ultimate lateral resistance of the soil at depth. It would be worthwhile to invest some time and effort into creating a model which is capable of activating the ultimate lateral resistance of the soil at all depths. In this manner, a more appropriate distribution of this soil parameter may be obtained.

- This research focused on analyses conducted using a single pile embedded in a soil profile in which all surfaces are perpendicular to the pile and there are only three layers. It would be of interest to evaluate the applicability of these findings to any number of additional cases such as pile groups, battered piles, sloping ground conditions, and increased number of soil layers. Any one of these investigations could prove to be a valuable contribution to the general knowledge of laterally loaded piles.

BIBLIOGRAPHY

[1] ACI Committee 318. *Building Code Requirements for Structural Concrete (ACI 318–05) and Commentary (ACI 318R–05).* American Concrete Institute, Farmington Hills, MI, 2005.

[2] American Petroleum Institute (API). Recommended practice for planning, designing and constructing fixed offshore platforms. *API Recommended Practice 2A(RP–2A)*, 1987.

[3] Z.P. Bazant and E. Becq-Giraudon. Statistical prediction of fracture parameters of concrete and implications for choice of testing standard. *Cement and Concrete Research*, 32(4):529–556, 2002.

[4] R.W. Boulanger, C.J. Curras, B.L Kutter, D.W. Wilson, and A. Abghari. Seismic soil–pile–structure interaction experiments and analyses. *Journal of Geotechnical and Geoenvironmental Engineering, ASCE*, 125(9):750–759, 1999.

[5] J. Brinch Hansen. The ultimate resistance of rigid piles against transversal forces. In *Bulletin No. 12*, pages 5–9. Geoteknisk Institute, Copenhagen, 1961.

[6] B.B. Broms. Lateral resistance of piles in cohesionless soils. *Journal of the Soil Mechanics and Foundations Division, ASCE*, 90(SM3):123–156, 1964.

[7] D.A. Brown and C.F. Shie. Three dimensional finite element model of laterally loaded piles. *Computers and Geotechnics*, 10(1):59–79, 1990.

[8] W.F. Chen and A.F. Saleeb. *Constitutive Equations for Engineering Materials Volume I: Elasticity and Modeling.* Elsevier Science B.V., Amsterdam, 1994.

[9] D.C. Drucker and W. Prager. Soil mechanics and plastic analysis or limit design. *Quarterly of Applied Mathematics*, 10(2):157–165, 1952.

[10] W.G.K. Fleming, A.J. Weltman, M.F. Randolph, and W.K. Elson. *Piling Engineering.* Surrey University Press, London, 1985.

[11] M. Georgiadis. Development of p–y curves for layered soils. In *Proceedings of the Geotechnical Practice in Offshore Engineering*, pages 536–545. ASCE, 1983.

[12] Peter Helnwein. Some remarks on the compressed matrix representation of symmetric second-order and fourth-order tensors. *Computer Methods in Applied Mechanics and Engineering*, 190(22-23):2753 – 2770, 2001.

[13] M.F. Kaplan. Crack propogation and the fracture of concrete. *Journal of the American Concrete Institute*, 58(5):591–610, 1961.

[14] D.C. Kent and R. Park. Flexural members with confined concrete. *Journal of the Structural Mechanics Division, ASCE*, 97(ST7):1969–1990, 1971.

[15] I. Lam, P. Arduino, and P. Mackenzie-Helnwein. Opensees soil–pile interaction study under lateral spread loading. In *International Foundation Congress & Equipment Expo*, Orlando, FL, May 2009.

[16] H. Matlock and L.C. Reese. Generalized solutions for laterally loaded piles. *Journal of the Soil Mechanics and Foundations Division, ASCE*, 86(SM5):63–91, 1960.

[17] S. Mazzoni, F. McKenna, M.H. Scott, and G.L. Fenves. *OpenSees Command Language Manual*. Pacific Earthquake Engineering Research Center, University of California, Berkeley, 2007.

[18] B. McClelland and J. Focht. Soil modulus for laterally loaded piles. *Transactions, ASCE*, 123:1049–1086, 1958.

[19] T.H.G. Megson. *Structural and Stress Analysis*. Elsevier Butterworth Heinemann, Amsterdam, 2005.

[20] R. Park and T. Paulay. *Reinforced Concrete Structures*. Wiley & Sons, New York, 1975.

[21] K.A. Petek. *Development and Application of Mixed Beam–Solid Models for Analysis of Soil–Pile Interaction Problems*. Ph.d. thesis, University of Washington, 2006.

[22] L.C. Reese, W.R. Cox, and F.D. Koop. Analysis of laterally loaded piles in sand. In *Proceedings of the 6th Offshore Technology Conference*, volume 2, pages 473–483, Houston, 1974.

[23] L.C. Reese and W.F. Van Impe. *Single Piles and Pile Groups Under Lateral Loading*. A.A. Balkema, Rotterdam, Netherlands, 2001.

[24] R.F. Scott. *Foundation Analysis*. Prentice–Hall, Englewood Cliffs, NJ, 1981.

[25] S.T. Wang and L.C. Reese. Design of pile foundations in liquefied soils. In *Geotechnical Earthquake Engineering and Soil Dynamics III*, pages 1331–1343. ASCE, 1998.

[26] S. Xu and X. Zhang. Determination of fracture parameters for crack propagation in concrete using an energy approach. *Engineering Fracture Mechanics*, 75(15):4292–4308, 2008.

[27] Z. Yang and B. Jeremic. Study of soil layering effects on lateral loading behavior of piles. *Journal of Geotechnical and Geoenvironmental Engineering*, 131(6):762–770, 2005.